Satellite remote sensing of riverine freshwater contribution in Hudson Bay marine system

by:

Atreya Basu

আত্রেয় বসু

A Thesis submitted to the

Faculty of Graduate and Postdoctoral Studies

of the University of Manitoba

in partial fulfillment of the degree of

Doctor of Philosophy

Department of Environment and Geography

Clayton H. Riddell Faculty of Environment, Earth and Resources

University of Manitoba

Winnipeg

Copyright © 2026 by Atreya Basu

Supervised by

Assoc. Prof. Dr. **Jens Ehn**
Department of Environment and Geography
Clayton H. Riddell Faculty of Environment, Earth, and Resources
The University of Manitoba
Winnipeg, MB R3T 2N2, Canada

Internal examiner 1

Dr. **Greg McCullough *(Retd.)***
Department of Environment and Geography
Clayton H. Riddell Faculty of Environment, Earth, and Resources
The University of Manitoba
Winnipeg, MB R3T 2N2, Canada

Internal examiner 2

Prof. Dr. **Simon Bélanger (*Adjunct*)**
Department of Environment and Geography
Clayton H. Riddell Faculty of Environment, Earth, and Resources
The University of Manitoba
Winnipeg, MB R3T 2N2, Canada

Internal examiner 3

Prof. Dr. **David Lobb**
Department of Soil Science
Faculty of Agriculture, and Food Sciences
The University of Manitoba
Winnipeg, MB R3T 2N2, Canada

External Examiner

Prof. Dr. Anu Noorma
Faculty of Science and Technology
The University of Tartu, Estonia

Abstract

Freshwater regulates stratification in marine systems, a key driver of circulation, productivity, and exchange processes. This is especially important in the Arctic Ocean, where nearly one-fifth of global freshwater drains, and an intensifying hydrological cycle increases freshwater input. However, Hudson Bay, an Arctic marginal sea that receives three times as much river runoff yield per unit area as the Arctic Ocean, remains one of the least observed components of the Arctic freshwater system. This thesis therefore develops satellite-based approaches, supported by field data, to map seasonal distributions of river water (RW) and sea-ice melt (SIM), the main freshwater sources in the Hudson Bay marine system.

The third chapter examined the dispersion of the combined Nelson and Hayes River plume into southwestern Hudson Bay using satellite-derived chromophoric dissolved organic matter (CDOM) and total suspended solids (TSS). A new method showed that quantile concentrations of CDOM declined exponentially from the river mouth and varied with river discharge, whereas TSS did not, demonstrating CDOM as an effective river plume tracer. Wind forcing further regulated plume transport, with anticyclonic winds driving riverine CDOM towards central Hudson Bay and cyclonic winds promoting eastward alongshore transport.

The fourth chapter used satellite-derived salinity and CDOM to map RW and SIM fractions in the surface waters of Hudson Bay and James Bay (HJB), based on RW, SIM, and seawater (SW) fractions derived from salinity–oxygen isotope ratios. Satellite retrievals reproduced known freshwater patterns, with RW dominating southern and eastern regions, particularly in James Bay, which receives the largest riverine inputs within the Hudson Bay marine system. Satellite retrieved SIM prevailed in central Hudson Bay and declined through summer. From 2011 to 2019, RW fractions increased while SIM fractions declined across HJB.

Since RW and SIM are evolving in the surface waters of HJB, the fifth chapter determined which freshwater type controls stratification by analyzing salinity, temperature, and oxygen-isotope profiles. Results show that RW dominates stratification year-round, from coastal waters to northern HJB. Projected increases in wintertime RW discharge will likely enhance stratification and may impede deep-water renewal. Therefore, by combining satellite-based ocean color data, salinity, and isotope-based analyses, this thesis advances understanding of freshwater distribution, and stratification in the understudied Hudson Bay marine system.

Land Acknowledgements

The University of Manitoba campuses and research spaces are located on original lands of Anishinaabeg, Ininiwak, Anisininewuk, Dakota Oyate, Dene and Inuit, and on the National Homeland of the Red River Métis.

The University of Manitoba recognizes that the Treaties signed on these lands are a lifelong, enduring relationship, and we are dedicated to upholding their spirit and intent. We acknowledge the harms and mistakes of the past and the present. With this understanding, we commit to supporting Indigenous excellence through active Reconciliation, meaningful change, and the creation of an environment where everyone can thrive. Our collaboration with Indigenous communities is grounded in respect and reciprocity and this guides how we move forward as an institution.

Personal Acknowledgements

I express my sincerest gratitude to my supervisor, Dr. Jens Ehn. His commitment to science has been a constant source of inspiration. I am grateful for his unwavering belief in my scientific potential and for his teachings on how to do science simply and communicate it clearly. I thank him for his support, teaching, and guidance throughout my PhD.

I am grateful to all my advisory committee members for their support, guidance, suggestions, and encouragement throughout my doctoral studies. I thank Dr. Simon Bélanger, whose scientific guidance and thoughtful feedback on my manuscripts helped me strengthen my remote sensing, critical thinking, and writing skills. I also sincerely thank Dr. Greg McCullough for his advice and for generously sharing his deep knowledge of the Hudson Bay system. My gratitude extends to Dr. David Lobb for his valuable advice during the annual progress report meetings. I also acknowledge my PhD external examiner, Dr. Anu Noorma, for her thoughtful evaluation of my thesis and constructive comments and suggestions, which helped improve its quality.

I would also like to express my heartfelt appreciation to Dr. Zou Zou Kuzyk for her scientific guidance and for the James Bay fieldwork opportunity, which provided the essential data needed to complete my PhD. I am grateful for the funding support from Dr. Ehn and Dr. Kuzyk. I am thankful to Dr. Mats Granskog, Dr. C. J. Mundy, Dr. Tim Papakyriakou and Dr. David Capelle for their assistance with field data. My gratitude extends to the crew members aboard the CCGS Des Groseilliers, M/V Strait Signet, CCGS Amundsen, and R/V William Kennedy, whose collaboration was critical to the successful completion of my PhD.

The Centre for Earth Observation Science (CEOS) at the University of Manitoba is close to my heart, where I had the opportunity to complete my doctoral research. A heartfelt thank you to all the faculty, technicians, and support staff for your continued support. A special thanks to Celia Mellinger, Graduate Program and Alumni Coordinator of the Department of Environment and Geography, C. H. R. Faculty of Earth, Environment and Resources for her help and administrative support throughout my doctoral studies.

Friends are an integral part of life, and their presence has been invaluable throughout my PhD journey. My friends from India, Sayan Mukhopadhaya, Raja Das, Madhumita Chakraborty, Soham Mukherjee, Satyananda Maiti, Gaurav Chakraborty, Subhangan Basu, Agnijeet Roy, Moinak

Banerjee, Nilanjan Sammadar, Biswadeep Bandopadhyay, Chandrima Chakrabarty, Shaini Naha, and Anirban Mukhopadhyay, have been a constant source of motivation and encouragement. A special mention goes to Arpan Nandi, who proficiently troubleshot my laptop whenever technical issues arose, helping me keep my research and thesis work moving forward.

I would also like to thank my friends and colleagues in Canada, Yanique Campbell, Emma Ausen, Madison Harasyn, Kaushik Gupta, Agoston Fischer, Allesia Guzzi, Stephen Ciastek, Aura Diaz, Dave Babb, Satwant Kaur, Lisa Matthes, Chris Peck, Brock Edwards, Claire Herbert, Wayne Chan, Esdoorn Wilcox, Monojit Saha, Debangshu Banerjee, Fowzia Ahmed, Rei Shibue, Kate Yezhova, Nolan Snyder, Jang Han Lee, Lucas Barbedo De Freitas, Laura Dalman, Durell Desmond, Nabanita Das, Yudhisthir Reddy, Veronica Coppolaro, Claire Hornby, Nathalie Thériault, David Landry, Tonya Burgers, and Zakhar Kazmiruk.

My family has always been a steadfast pillar in my life, with a commitment to education, culture and learning passed down through generations. I pay homage to my ancestors, Ramdeb Basu, Ramram Basu, Nidhiram Basu, Gorachand Basu, Keshablal Basu, Surendranath Basu and Nistarini Basu. The legacy carried forward by by my grandparents Sachindranath Basu and Annapurna Basu, Nikhilnath Basu and Renuka Basu, Sachidananda Basu and Dipali Basu, Paritosh Sarkar and Jharna Sarkar, and Debotosh Sarkar and Bharati Sarkar who nurtured my curiosity and scientific mindset from a young age. I fondly remember my maternal grandparents Lily Mitra and Ramchandra Mitra. Their collective values and commitment to education have remained with me throughout my academic journey and helped me become the first in my family to earn a PhD.

Throughout this journey, I have been fortunate to draw strength and encouragement from my extended family. I am deeply grateful to my aunts, Tapati Basu, Samita Biswas, Nandita Mitra, the late Mohua Dutta, Kuheli Ghosh, Mitali Ghosh, Madhumita Das, Paramita Mitra, Nabanita Sarkar, Srabani Basu, Sanghamitra Basu, the late Debosree Basu, Smriti Ghosh, and the late Sunanda Sen, for their encouragement throughout my PhD. I am equally grateful to my uncles, the late Sukalyan Basu, the late Abhijit Basu, Chinmay Basu, Sanmay Basu, Shibaprashad Basu, Utpal Basu, the late Ashoke Mitra, Tripti Kumar Ghosh, the late Niren Kumar Ghosh, Kanailal Dutta, Pradip Kumar Biswas, Nitish Mitra, Shaktipada Das, Abhijit Mitra, the late Shyamal Kanti Ghosh, and the late Tapas Sen, for supporting and encouraging me in the career path I chose to pursue.

I am thankful to my cousins, Arindam Bose, Aditi Dutta, Mohua Sarkar, Aritra Basu, Satarupa Basu, Trina Basu, Jyoti Prakash Mitra, the late Samrat Kanti Ghosh, Samipriya Das, Madhuparna Das, Anushka Mitra, Arshia Mitra, Antara Ghosh Dhar, Emon Dhar, Nilanjana Bhowmick, Kanakendu Bhowmick, Krishnendu Ghosh, Debanjan Dutta, Tapobrata Sen, Arpita Sen, and Gitanjali Sen, who have been a constant source of encouragement and support throughout this journey. I especially thank my cousin, Dr. Subhabrata Sen, whose dedication to research and pursuit of a PhD inspired my own path towards a life in scientific research. I also cherish the love and support of my nephews, Hitangshu Bose and Soumil Sen, and my nieces, Sinjini Bhowmick, Sambrita Bhowmick, and Ashmi Sarkar. As my PhD journey approached its final years, I was fortunate to have the support of my in-laws, Sanghamitra Goswami, Debasis Goswami, and Indrasish Goswami, for which I am sincerely thankful.

I pay my respect to the late Dr. David Barber, the principal project investigator of the Hudson Bay System Study (BaySys) project, under which this research was conducted in collaboration with Manitoba Hydro and NSERC, Canada. I sincerely thank the Faculty of Graduate and Postdoctoral Studies at the University of Manitoba for providing me with the opportunity to pursue my doctoral research and for their support throughout my PhD program.

This Ph.D. thesis is dedicated to the sacrifices of

my mother (মা) ***Chaitali Basu*** *and father (বাবা)* ***Smarajit Basu,***

unwavering belief and patience of my wife ***Debamitra Basu (পায়েল)***

and motivation from my feisty daughter ***Dridha Basu (প্লাইও)***

As often recited by my grandfather Sachindranath Basu

The woods are lovely, dark and deep,
But I have promises to keep,
And miles to go before I sleep,
And miles to go before I sleep

Robert Frost

Table of Contents

Abstract ..... **i**
Land Acknowledgements ..... **ii**
Personal Acknowledgements ..... **iii**
Dedication ..... **v**
List of tables ..... **xi**
List of figures ..... **xiii**
List of acronyms ..... **xxiii**
Use of copyrighted material ..... **xxv**
1. Chapter – Introduction **1**
1.1. Motivation 1
1.2. Thesis objectives 2
1.3. Thesis outline 3
2. Chapter – Background **5**
2.1. Freshwater sources in the Arctic marine systems 5
2.1.1. Rivers 5
2.1.2. Sea Ice 6
2.1.3. Land Ice 7
2.1.4. Pacific Ocean 8
2.1.5. Precipitation 8
2.2. Freshwater distribution in the Arctic marine systems 10
2.2.1. Amerasian Basin 10
2.2.2. Eurasian Basin 11
2.2.3. Hudson Bay 12
2.3. Freshwater circulation in Arctic marine systems 15
2.3.1. Alongshore boundary current 15
2.3.2. Wind driven circulation 16
2.3.3. Circumpolar boundary current 16
2.4. Importance of freshwater in Arctic marine systems 19
2.4.1. Sea ice variability 20
2.4.2. Biological and biogeochemical impact 20

2.4.3. Ecological impact 21
2.5. Freshwater tracers in Arctic marine systems 22
2.5.1. Physical tracers 22
2.5.2. Chemical tracers 22
2.5.3. Biogeochemical tracers 24
2.6. Freshwater tracing using satellite remote sensing 25
2.6.1. Salinity and sea surface temperature 25
2.6.2. Sea surface height 26
2.6.3. Gravity anomaly 27
2.6.4. Chromophoric dissolved organic matter and suspended solids 28
2.6.4.1. Ocean color remote sensing 28
2.6.4.2. Empirical detection 29
2.6.4.3. Inversion-based detection 29
3. Chapter – Plume dispersion from the Nelson and Hayes rivers into Hudson Bay using satellite remote sensing of CDOM and suspended sediment 30
Abstract 31
3.1. Introduction 32
3.2. Data and method 34
3.2.1. Study area 34
3.2.2. In situ CDOM and TSS measurements 37
3.2.3. Remote sensing 39
3.2.4. Satellite-derived river runoff distribution and directionality 41
3.3. Results and discussion 43
3.3.1. In situ CDOM and TSS versus salinity gradient 43
3.3.2. Evaluation of optical relationships 46
3.3.3. Dilution of $a_{CDOM}\,(412)$ 48
3.3.4. Dilution of TSS 50
3.3.5. River plume directionality and wind 56
3.4. Conclusion 60
Data availability 62
Supplementary materials 63

4. Chapter – Satellite data trace seasonal freshwater dispersion in Hudson and James Bays 67
Abstract 67
4.1. Introduction 67
4.2. Data and method 70
4.2.1. Field data 70
4.2.2 Satellite Remote Sensing 71
4.2.2.1 CDOM and River Water Fraction 71
4.2.2.2. Sea surface salinity, freshwater, and sea-ice melt fractions 72
4.3. Results 73
4.3.1. In situ CDOM and salinity variability 73
4.3.2. Satellite-derived freshwater fraction 73
4.3.3. Satellite-derived river water fraction 74
4.3.4. Satellite-derived sea-ice melt fraction 75
4.1. Discussion 77
4.1.1. Relationship between in situ $a_{CDOM}^{lab}(412)$ and in situ river water fraction 77
4.1.2. Satellite-derived river water dispersion 78
4.1.3. Satellite-derived sea-ice melt dispersion 80
4.2. Conclusion 81
Data availability 82
Supplementary materials 82
5. Chapter – River water control of stratification in Arctic marginal seas 93
Abstract 93
5.1. Introduction 93
5.2. Data and methods 94
5.3. Results 98
5.3.1. Salinity and temperature controls on density stratification 98
5.3.2. Sources of freshwater and their control on haline stratification 99
5.3.3. Regional variability of freshwater sources and their control on haline stratification 100
5.4. Discussion 104
5.5. Conclusion 105
Data availability 106

Supplementary materials 107
6. Chapter – Summary and conclusions **114**
6.1. Importance and main contribution 114
6.2. Summary 115
6.2.1. Plume dispersion from the Nelson and Hayes rivers into Hudson Bay using satellite remote sensing of CDOM and suspended sediment 115
6.2.2. Satellite data trace seasonal freshwater dispersion in Hudson and James Bays 116
6.2.3. River water control of stratification in Arctic marginal seas 117
6.3. Limitations and future works 118
References **119**
Contribution of collaborating authors **156**

List of tables

Table 3.1. Mean values of decay rate, extent, and concentration of satellite-retrieved absorption of chromophoric dissolved organic matter (a_{CDOM}) at 412 nm and total suspended solids (TSS)……..……53

Table 3.2. Mean $a_{CDOM}^{river}(412)$-weighted direction (*Az*), relative vorticity (*rv*), zonal wind speed (*u*), meridional wind speed (*v*), wind direction (wd) and speed (ws) for different wind regimes, along with correlation coefficients[a] between wind metrics and plume direction in brackets…….60

Table S3.1. List of in situ sampling stations, time and date of sampling, tidal flow stage, and optical application for algorithm development and matchup……....63

Table S3.2. List of satellite data used for Nelson/Hayes River plume dispersion study, and discharge type, tidal flow, and wind regime……..65

Table S4.1. Statistics of match-up analysis……...90

Table S4.2. Laboratory measured absorption of chromophoric dissolved organic matter (CDOM) and salinity in Hudson and James Bay (HJB)……...……...91

Table S4.3. Monthly River discharge (m^3s^{-1}) stations (2011–2019) for western and eastern Hudson Bay (WHB and EHB) (https://wateroffice.ec.gc.ca/search/historical_e.html).....92

Table 5.1. Seasonal contribution of salinity gradient ($\Delta S/\Delta z$; S m^{-1}) and temperature gradient ($\Delta\theta/\Delta z$; °C m^{-1}) to potential density gradient ($\Delta\rho_\theta/\Delta z$; kg m^{-3} m^{-1}) across water columns of Hudson and James Bays (HJB), evaluated using simple linear regression analyses……...99

Table 5.2. Seasonal contribution of river water ($|\Delta RW/\Delta z|$; fraction m^{-1}) and sea-ice melt ($|\Delta SIM/\Delta z|$; fraction m^{-1}) gradients to salinity gradients ($\Delta S/\Delta z$; S m^{-1}) at the depth of maximum salinity gradient (z_{SGM}; m), across the Hudson and James Bay (HJB) evaluated using simple linear regression analyses……...100

Table S5.1: Seasonal contribution of salinity gradient ($\Delta S/\Delta z$; S m^{-1}) and temperature gradient ($\Delta\theta/\Delta z$; °C m^{-1}) to potential density gradient ($\Delta\rho_\theta/\Delta z$; kg m^{-3} m^{-1}) across water columns of Hudson and James Bays (HJB), evaluated using multiple linear regression analysis……....107

Table S5.2. Seasonal contribution of river water ($|\Delta RW/\Delta z|$; fraction m^{-1}) and sea-ice melt ($|\Delta SIM/\Delta z|$; fraction m^{-1}) gradients to salinity gradients ($\Delta S/\Delta z$; S m^{-1}) at the depth of maximum salinity gradient (z_{SGM}; m), across the Hudson and James Bay (HJB) evaluated using multiple linear regression analyses…….....107

Table S5.3: Seasonal characteristics of the halocline in James Bay and south of 60° N in Hudson Bay……...108

Table S5.4: Seasonal characteristics of the halocline north of 60° N in Hudson Bay and for Hudson Bay combined north and south…….109

List of figures

Figure 2.1. a. Arctic Ocean bathymetry from the international bathymetric chart of the Arctic Ocean updated database (Jakobsson et al., 2008). The projection is Lambert Equal Area and the 200 m, 500 m, 2,000 m, and 4,000 m isobaths are shown. Adapted from Rudels et al. (2012). Map drawn by Martin Jakobsson. AB = Amerasian Basin. AR = Alpha Ridge. EB = Eurasian Basin. FJL = Franz Josef Land. GR = Gakkel Ridge. GSR = Greenland Scotland Ridge. LR = Lomonosov Ridge. LS = Lancaster Sound. MR = Mendeleev Ridge. NS = Nares Strait. SZ = Severnaya Zemlya. FB = Foxe Basin. HB = Hudson Bay. JB = James Bay. HS = Hudson Strait. b. The circulation of the upper layers of the Arctic Ocean. Warm Atlantic currents are indicated by red arrows, cold less saline polar and Arctic currents by blue arrows. Low salinity transformed currents are indicated by green arrows. The thick blue arrows show circulation from the Canadian Arctic Archipelago into Foxe Basin, which continues as cyclonic circulation in Hudson Bay (shown by thick violet arrows), exiting through Hudson Strait into the Labrador Sea. The annual mean maximum ice extent is shown in blue and the annual minimum in red (late twentieth century conditions). The minimum in 2007, the second absolute minimum to date, is shown in dark red. AC = Anadyr Current. ACC = Alaskan Coastal Current. BC = Baffin Island Current. BIC = Bear Island Current. LCC = Labrador Coastal Current. BG = Beaufort Gyre. EGS = East Greenland Current. EIC = East Iceland Current. ESC = East Spitsbergen Current. IC = Irminger Current. JMC = Jan Mayen Current. MC = Murman Current. NAD = North Atlantic Drift. NAC = Norwegian Atlantic Current. NCC = Norwegian Coastal Current. SB = Siberian branch (of the Transpolar Drift). SCC = Siberian Coastal Current. TPD = Transpolar Drift. WGC = West Greenland Current. WSC =West Spitsbergen Current from Rudels and Carmack (2022)..……..……..……...9

Figure 2.2. The Arctic Ocean's two "lids": sea ice and the halocline. Sea ice growth in winter adds salt to the surface ocean, driving penetrative convection to form the winter mixed layer (WML). In summer, freshwater (FW) is added to the mixed layer through seasonal contributions of sea-ice melt, terrestrial runoff (RO) and the balance of precipitation-evaporation (P-E), which strongly stratify the surface ocean. This stratification limits the depth of wind mixing, allowing formation of a shallow summer mixed layer (SML). Below the SML, fractions of the previous season's processes may remain; specifically, a cool remnant winter water (RWW) immediately above the

base of the WML from the previous year. In the presence of sea ice with sufficient open water, a near-surface temperature maximum (NSTM) may form immediately below the SML by solar heating, capped by the cold, low salinity surface layer. These exchanges between the surface ocean layer and the sea ice "lid" occur across the Arctic Ocean, however, the additional FW associated with Pacific water (PW) enhances surface stratification in the Amerasian Basin (AB) and contributes to the difference between the halocline "lid" within the deep AB and that of the Eurasian Basin (EB); represented conceptually in (a, b), respectively. In both the Pacific and Atlantic sectors of the Arctic Ocean, warm Atlantic-derived waters (AW) form the base of the halocline. The water column above is comprised of multiple layers that define the seasonal and permanent haloclines, constrained by the horizontal interleaving of seasonally modified FW inputs. a. In the Pacific sector halocline, PW inputs from the Bering Sea interflow, increasing stratification, and further constraining the depth of convection. Here, the winter convection penetrates down to the base of the Pacific Summer Water (PSW) and the sub-surface temperature maximum (T_{max}), which in turn lies above the Pacific Winter Water (PWW) and the sub-surface temperature minimum (T_{min}). Below PW lies lower halocline water (LHW), which likely forms on Siberian shelves. b. In the Atlantic sector, the thickness and distribution of halocline layers is highly variable across the EB, but includes a cold halocline layer (CHL) and LHW layer above the warm AW layer. Both form as a consequence of sea ice formation and winter convective mixing events; CHL mostly within the basin and LHW on mostly on shelves with subsequent drainage into the basins from Brown et al. (2020)…….13

Figure 2.3. A conceptual diagram showing generally the mixing and deep convection in a. late winter and b. water mass structure (HSSML = Homogenous Summer Surface Mixed Layer; SSML = Summer Surface Mixed Layer; WSML= Winter Surface Mixed Layer) late summer in Hudson Bay from Granskog et al., (2011)……14

Figure 2.4. Schematic representation of potential buoyancy-driven boundary flows driven by continental discharge among the northern coastline around North America and Eurasia from Carmack et al. (2015)…….15

Figure 2.5. a. Freshwater accumulates in the Arctic Ocean under high-pressure conditions, leading to enhanced storage in the Amerasian Basin and the formation of a strong Beaufort Gyre. During this phase, Eurasian river runoff is transported eastward along the Arctic shelves. b. Under weaker

high-pressure conditions, the Beaufort Gyre weakens, releasing freshwater that is transported into the Transpolar Drift along with Eurasian runoff. The 1893–1896 drift of *Fram* is shown by the white track, while the red track represents the 2014–2015 drift of the hovercraft *Sabvabaa* from Hall and Kristoffersen et al. (2025)…….18

Figure 2.6. Schematics of average spring/summer and fall surface flow patterns that are based on Aviso satellite altimetry data and model output from Ridenour et al. (2019a)……19

Figure 3.1. The study domain was separated into circular sections 10 km wide, with the initial section being 50 km from the Nelson River mouth (denoted by a star) to offshore Hudson Bay (500 km). The study domain corresponding to 10-m bathymetries was excluded from the model domain to avoid bias because of extremely high nearshore values of chromophoric dissolved organic matter (CDOM) and total suspended solids (TSS). For each section, quantiles $Q_{0.05}$–$Q_{0.95}$ were calculated for the retrieved concentrations of CDOM and TSS to estimate Nelson/Hayes runoff mixing. The location of Hudson Bay within Canada is shown in the inset, along with Nelson River (dark grey) and Hayes River (red) drainage basins, Lake Winnipeg, and Manitoba (sky blue)…….36

Figure 3.2. The Red-Green-Blue (RGB) image of the European Space Agency's Sentinel-2A satellite (August 6, 2016; 10-m spatial resolution) shows reflective turbid waters of Nelson River and dark waters of Hayes River rich in chromophoric dissolved organic matter (CDOM). In situ sampling stations of CDOM and total suspended solids (TSS) are denoted by their names. The dashed line represents the approximate location of the Nelson River fresh surface layer; the fresh surface layer of the Hayes River is located around Silver Goose (SG; Manitoba Hydro, 2014)……..……38

Figure 3.3. a. Power-law relationship between in situ absorption of chromophoric dissolved organic matter at 412 nm, $a_{CDOM}(412)$, and the blue (488 nm) to red (667 nm) remote sensing reflectance (R_{rs}) band ratio and b. exponential relationship between in situ total suspended solids (TSS) and R_{rs} at 667 nm. The annotated a and b values in the figures represent regression coefficients, as shown in Equations 3.4 and 3.5……..40

Figure 3.4. Quantile concentrations $Q_{0.05}$–$Q_{0.95}$ of satellite-retrieved a–c. absorption of chromophoric dissolved organic matter, $a_{CDOM}(412)$, and d–f. total suspended solids (TSS) for three different types of daily Nelson and Hayes river (NHR) discharge into Hudson Bay. The red lines represent the $Q_{0.95}$ thresholds, which represents marine waters with the highest CDOM or TSS. Concentrations below the threshold represent water in the offshore domain. Distance corresponding to 50% and 75% dilution of the CDOM and TSS values at the river mouth are represented by blue and green lines, respectively.……...43

Figure 3.5 a. The decrease of in situ absorption of chromophoric dissolved organic matter, $a_{CDOM}(412)$, with salinity along the Nelson River transect was best described with the power-law fit, shown by the solid line, while the higher $a_{CDOM}(412)$ along the Hayes River transect underwent a linear decrease, shown by the dashed line. b. Similar trends were observed for total suspended solids (TSS), where the higher TSS of the Nelson River transect decreased faster than TSS along the Hayes River transect, described by fits like those for CDOM. The inset figure on a logarithmic scale highlights TSS suspension in the Nelson River estuary and TSS settling in the coastal waters (salinity >20) of Hudson Bay. Hayes River TSS settles within the Nelson River plume at a salinity between approximately 15 and <20.……46

Figure 3.6. a. The blue to red band ratio retrieved absorption of chromophoric dissolved organic matter, $a_{CDOM}(412)$, with higher accuracy (Equation 3.4) and b. lower accuracy was obtained for total suspended solids (TSS) using a single red band (Equation 3.5). The black solid and dashed lines represent regression fits and 1:1 scatter line, respectively……..……..48

Figure 3.7. Satellite-derived river-influenced a. absorption of chromophoric dissolved organic matter (a_{CDOM}) at 412 nm and b. total suspended solids (TSS) in southwestern Hudson Bay with increasing distance from the mouth of the Nelson River. The river water fraction is separated for three daily discharge conditions: low (1500–4200 $m^3 s^{-1}$), mid (>4200–6500 $m^3 s^{-1}$), and high (>6500–9000 $m^3 s^{-1}$). The dashed lines and dotted lines show the estimated 50% dilution (0.50 river CDOM/TSS water fraction) and 75% dilution (0.25 river CDOM/TSS water fraction) of river water with seawater, respectively.……..51

Figure 3.8. a. Variability in the decay rate of absorption of chromophoric dissolved organic matter, a_{CDOM} (412), with daily Nelson/Hayes river (NHR) discharge, Q; b. variability of a_{CDOM} (412) with NHR discharge; (c) co-variability trend of the a_{CDOM} (412) decay rate (b_{CDOM}) and a_{CDOM} (412), shown by a solid black line; and (d) co-variability trend of the NHR discharge-normalized a_{CDOM} (412) decay rate (b'_{CDOM}) and discharge-normalized a_{CDOM} (412) (a'_{CDOM} (412)), shown by a solid black line. Dark grey squares, light grey triangles, and black circles in panels a and b represent data points corresponding to 50%, 75%, and 100% decay, respectively, of river CDOM values for each image. Lines in panels a and b, color-coded to 50%, 75%, and 100% decay of river CDOM values, represent the trends of the variability of CDOM decay rate and concentration with discharge. Inset symbols *, **, ^, and ^^ represent statistical significance at $p \leq$ 0.5, 0.01, 0.001, and 0.0001, respectively. ……...…….52

Figure 3.9. Satellite-derived images of chromophoric dissolved organic matter and total suspended solids in southwestern Hudson Bay. Moderate resolution imaging Spectroradiometer (MODIS)-derived images of river-influenced (a, c, e, g) absorption of colored dissolved organic matter, a_{CDOM} (412), and b, d, f, h total suspended solids (TSS) at extents of 50%, 75%, and 100% dilution (represented by red, green, and black contours, respectively) for (a and b) low discharge, (c and d) mid discharge, (e and f) high discharge, and (g and h) high tide. Panels a–f also represent the extent of ebb tidal flow. The grey shading denotes the region flagged for shallow water pixels……..……54

Figure 3.10. Variability of the decay rate constant, b_{CDOM}, for satellite-retrieved absorption of chromophoric dissolved organic matter, a_{CDOM} (412), and its concentration as a function of discharge during (a and c) ebb tidal flow and (b and d) flood tidal flow. Dark grey squares represent data points corresponding to 50% decay of river-a_{CDOM} (412) values corresponding to 10 flood and 12 ebb tide images. Light grey triangles, and black circles represent data points corresponding to 75%, and 100% decay, respectively, of river-a_{CDOM} (412) values corresponding to 16 flood and 18 ebb tide images. Lines color-coded to 50%, 75%, and 100% decay of river-a_{CDOM} (412) values represent the trends of the variability of a_{CDOM} (412) decay rate and concentration with discharge. Inset symbols *, **, ^, and ^^ represent statistical significance at $p \leq 0.5$, 0.01, 0.001, and 0.0001, respectively.……...……55

Figure 3.11. Variability of the total suspended solids (TSS) decay rate, b_{TSS}, with Nelson/Hayes daily river discharge, Q, for a. all 33 satellite images used in this analysis, b. ebb tide images, and c. flood tide images. Variability of TSS concentration with Q for d. all 33 images, e. ebb tide images, and f. flood tide images. The dark grey squares, light grey triangles, and black circles represent data points corresponding to 50%, 75%, and 100% decay, respectively, of river TSS values for each image. Lines color-coded to 50%, 75%, and 100% decay of river TSS values represent the trends of the variability of TSS decay rate and concentration with discharge. Inset symbols *, **, ^, and ^^ represent statistical significance at $p \leq 0.5$, 0.01, 0.001, and 0.0001, respectively.……...……56

Figure 3.12. a. River plume directions measured as a weighted function of satellite-retrieved river-water absorption of chromophoric dissolved organic matter, $a_{CDOM}^{river}(412)$ for different wind regimes based on relative wind vorticity. The grey shading represents plume direction within one standard deviation. In both panel a. and b., the red, green, and blue lines represent mean plume direction for cyclonic, weak, and strong anticyclonic winds, respectively; the black line denotes the mean plume direction. b. The plus symbol represents the Nelson River mouth, serving as the reference for the calculation of pixel bearings. Each grey circular line corresponds to the distance from the freshest point of 10-km width, with the first line at approximately 50 km from the river mouth. Dominant wind direction with speed is shown in the inset. c. Mean satellite-retrieved absorption coefficient of colored dissolved organic matter (a_{CDOM}) at 412 nm for 50% (0.50 *RCWF*), 75% (0.25 *RCWF*), and 100% (0.00 *RCWF*) dilution of the Nelson and Hayes river CDOM values, where *RCWF* stands for river-influenced CDOM water fraction……...58

Figure 3.13. a. Shoreward plume direction, based on satellite-retrieved river-water absorption of chrmophoric dissolved organic matter, $a_{CDOM}^{river}(412)$ was associated with lower relative vorticity (*rv*) and vice versa. b. Weak meridional southerly winds (*v*), c. strong easterly zonal winds (*u*), and d. high wind speeds (*ws*) were associated with strong anticyclonic wind regime. Inset symbols *, **, ^, and ^^ represent statistical significance at $p \leq 0.5$, 0.01, 0.001, and 0.0001, respectively……...…….59

Figure 4.1. a. Hudson and James Bay (HJB) study area showing bathymetry, sampling stations, major rivers, key regions, and features: NWHB, SWHB, SHB, SEHB, and CHB (northwestern,

southwestern, southern, southeastern, and central Hudson Bay [HB]), Belcher Islands (BI), Hudson Strait (HS), Kivalliq Polynya, Mid Bay Bank, Winisk Trough, and Henrietta Maria Ridge. The inset map shows the location of HJB (black square) within Canada. b. Relationship between in situ salinity (S^{lab}) and in situ oxygen isotope ratio ($\delta^{18}O^{lab}$) in HJB. Dashed green and red lines show salinity (32.5) and $\delta^{18}O^{lab}$ (−2.16‰) seawater endmembers, respectively. c. Relationships between in situ colored dissolved organic matter concentration measured at 412 nm, a_{CDOM}^{lab} (412), and in situ S^{lab} in HJB. d. Linear relationship between in situ river water fraction (RW) and in situ a_{CDOM}^{lab} (412) in Hudson Bay (solid black line). Dotted and dashed black lines show mixing using in situ a_{CDOM}^{lab} (412) of 2.5 m^{-1} (this study) and 6.4 m^{-1} (Granskog et al., 2007, 2009) at RW = 1, respectively. e. Non-linear relationship between in situ RW and in situ a_{CDOM}^{lab} in James Bay (solid black and long-dashed curved line extrapolated to zero intercept). Dotted linear line shows mixing using in situ a_{CDOM}^{lab}= 25 m^{-1} at RW = 1. f. Matchup between in situ a_{CDOM}^{lab} (412), and satellite-derived a_{CDOM}^{sat} (412), employing red to blue band ratio, Multiple Linear Regression, and Quasi Analytical Algorithm, v.6 (QAA). The gold line shows fit for a_{CDOM}^{BR} (412) and the gray dotted line shows fit for corrected a_{CDOM}^{BR} (412). g. Matchup between in situ RW fraction and satellite-derived RW^{sat} fraction, with the solid black line showing the fit. h. Matchup between in situ S^{lab} and satellite-derived S^{sat} in HB, with the solid black line showing the fit and the red dashed line showing the corrected S^{sat} fit for $S^{lab} \leq 27$. i. Matchup between in situ sea-ice melt fraction (SIM) and satellite-derived SIM^{sat} fraction, with fit shown by the solid black line. The black diagonal dashed lines in panels f–i indicate the 1:1 fit……..……..69

Figure 4.2. a. Box plots showing monthly distribution FW^{sat}, RW^{sat}, and SIM^{sat} across Hudson and James Bay (HJB) for June (JUN), July (JUL), August (AUG), and September (SEP). Per-pixel monthly mean (2011–2019) of satellite-derived fractions of b–e. freshwater ($\overline{SIM^{sat}}$), f–i. river water ($\overline{RW^{sat}}$), and j–m. sea-ice melt ($\overline{SIM^{sat}}$) in HJB. For panels b–m, dotted contours show satellite-derived salinity (S^{sat}), white and gray areas indicate missing data and $-\overline{SIM^{sat}}$, respectively, and pixels ≤ 10 m depth are masked (beige)……76

Figure 4.3. Mean (June–September) satellite-derived fractions of a. freshwater ($\overline{FW^{sat}}$), b. river water ($\overline{RW^{sat}}$), and c. sea-ice melt ($\overline{SIM^{sat}}$) across Hudson and James Bay (HJB), western Hudson

Bay (WHB), and eastern Hudson Bay (EHB) from 2011 to 2019. Solid and dashed black lines indicate significant ($p < 0.05$) and non-significant ($p > 0.05$) trends for HJB, respectively……...……77

Figure S4.1. Satellite-derived mean fractions of a–d. freshwater ($\overline{\mathrm{FW}}^{\mathrm{sat}}$); g–h. river water ($\overline{\mathrm{RW}}^{\mathrm{sat}}$); i–l. sea-ice melt ($\overline{\mathrm{SIM}}^{\mathrm{sat}}$), in Hudson and James Bay (HJB), western Hudson Bay (WHB) and eastern Hudson Bay (EHB) from 2011 to 2019 for the months of June, July, August and September……..86

Figure S4.2. Per-pixel coefficient of variation (2011–2019) of satellite-derived fractions of a–d. freshwater ($\mathrm{FW}^{\mathrm{sat}}$), e–h. river water ($\mathrm{RW}^{\mathrm{sat}}$) and i–l. sea-ice melt ($\mathrm{SIM}^{\mathrm{sat}}$) in Hudson and James Bay (HJB) for June (JUN), July (JUL), August (AUG) and September (SEP). Dotted contours show satellite-derived salinity ($\mathrm{S}^{\mathrm{sat}}$). White and grey areas indicate missing data and $-\mathrm{SIM}^{\mathrm{sat}}$ pixels, respectively. Coastal pixels < 10 m depth are masked (beige)…….87

Figure S4.3. Monthly changes in mean satellite-derived fractions of a–b. freshwater ($\overline{\mathrm{FW}}^{\mathrm{sat}}$), e–f. river water ($\overline{\mathrm{RW}}^{\mathrm{sat}}$) and g–h. sea-ice melt ($\overline{\mathrm{SIM}}^{\mathrm{sat}}$) in July (JUL), August (AUG) and September (SEP) from their preceding month for western and eastern Hudson Bay (WHB and EHB), respectively, from 2011–2019……88

Figure S4.4. Relationship (solid black line) between satellite-derived per pixel mean (2011–2019) freshwater fractions ($\overline{\mathrm{FW}}^{\mathrm{sat}}$) and satellite-derived per pixel mean (2011–2019) fractions of a–d. river water ($\overline{\mathrm{RW}}^{\mathrm{sat}}$) and e–h. sea-ice melt ($\overline{\mathrm{SIM}}^{\mathrm{sat}}$) for June (JUN), July (JUL), August (AUG) and September (SEP) for all pixels of western (when latitude $>$ 83° W) and eastern Hudson Bay (when latitude $\leq$ 83° W), color coded by coefficient of variance (CV %)……...89

Figure S4.5. a–b. Monthly changes in river discharge change in July (JUL), August (AUG) and September (SEP) from their preceding month for western and eastern Hudson Bay (WHB and EHB) from 2011–2019. c–d. River discharge for June to September from 2011–2019. dashed lines represent non-significant ($p > 0.05$) trends……....90

Figure 5.1: Hudson and James Bay (HJB) study area. Discrete water-sampling stations in coastal (<100 m deep; pale yellow) and offshore (≥100 m deep; light green) waters during early summer (June–July), late summer (August–September), and fall (October) are shown in the map. Stations with ≥ 3 depth samples are shown with filled symbols, whereas stations with fewer samples are

shown with transparent symbols. Stations with both salinity and temperature measurements are marked with black outline. Samples from southern regions include James Bay (JB), southeastern Hudson Bay (SEHB), Winisk Trough (WT), southern Hudson Bay (SHB), southwestern Hudson Bay (SWHB), and central Hudson Bay (CHB). Samples from northern regions include northwestern Hudson Bay (NWHB), northern Hudson Bay (NHB), northeastern Hudson Bay (NEHB), and the Narrows. Major islands shown include Southampton Island (SI), Coats Island (CI), and Mansel Island (MI) in the north, as well as the Belcher Islands (BI) in SEHB and Akimiski Island (AI) in JB. Subsurface waters at station 5 near SI and station BS07 in SWHB, indicated by black plus symbols, exhibit negative salinity gradients during late summer. The inset map highlights the HJB study area (red outline) within Canada, with Foxe Basin (FB) to the north, connected to the Arctic Ocean, and Hudson Strait (HS) to the northeast, linking HJB to the Labrador Sea (LS) in the North Atlantic Ocean and to Baffin Bay (BB), which also connects to the Arctic Ocean……...97

Figure 5.2. a–c. z_{SGM}, with the yellow contours showing the salinity. d–f. Salinity gradient ($\Delta S/\Delta z$; S m^{-1}), with the black contours indicating the salinity difference (ΔS) between the halocline top and bottom boundaries. g–i. Larger of absolute values of river water gradients ($|\Delta RW/\Delta z|$; fraction m^{-1}) and sea-ice melt gradients ($|\Delta SIM/\Delta z|$; fraction m^{-1}) determine dominance on haline stratification. White contours in panels g–i show the apparent river water influence (i.e., $|RW|/(|RW| + |SIM|)$), and pink dashed contours mark regions with negative SIM, whereas the remaining $|\Delta SIM/\Delta z|$-dominated regions correspond to positive sea-ice melt contribution. In panels a–i, solid contours (yellow, black, and white) denote areas well supported by observations, whereas dashed contours indicate extrapolated regions obtained using inverse-distance-weighted interpolation (1.5° radius) and subsequently smoothed with a 3×3 kernel. Grey masks in panels b, e, h indicate subsurface waters at station 5 near SI and station BS07 in SWHB that exhibit negative salinity gradients and were therefore excluded from the gridded fields…102

Figure 5.3. Examples of vertical profiles of salinity, river water (RW), sea-ice melt (SIM), and freshwater (FW = RW + SIM) across Hudson Bay and James Bay (HJB) during early summer, late summer, and fall. a–b. James Bay, c–d. southeastern Hudson Bay (SEHB), and e–f. northeastern Hudson Bay (NEHB). Shaded envelopes show ±1 standard deviations for each

variable. Thick segments within vertical profiles denote the halocline layer. Black circles in panels a., c., and e. mark the depth of the maximum salinity gradient (z_{SGM}; m)…….103

Figure S5.1: Vertical profiles of salinity, river water (RW), sea-ice melt (SIM), and freshwater (FW = RW + SIM) during early summer, late summer, and fall in a–b. Winisk Trough, c–d. southern Hudson Bay (SHB), and e–f. southwestern Hudson Bay (SWHB). Shaded envelopes show ±1 standard deviations for each variable. Thick segments within vertical profiles denote the halocline layer. Black circles in panels a, c, and e. mark the depth of the salinity gradient maximum (z_{SGM}; m)……..111

Figure S5.2: Vertical profiles of salinity, river water (RW), sea-ice melt (SIM), and freshwater (FW = RW + SIM) during early summer, late summer, and fall in a–b. central Hudson Bay (CHB), and c–d. northern Hudson Bay (NHB). Shaded envelopes show ±1 standard deviations for each variable. Thick segments within vertical profiles denote the halocline layer. Black circles in panels a, and c mark the depth of the salinity gradient maximum (z_{SGM}; m)……..112

Figure S5.3: Vertical profiles of salinity, river water (RW), sea-ice melt (SIM), and freshwater (FW = RW + SIM) during early summer, late summer, and fall in a–b. northwestern Hudson Bay (NWHB), and c–d. Narrows. Shaded envelopes show ±1 standard deviations for each variable. Thick segments within vertical profiles denote the halocline layer. Black circles in panels a, and c mark the depth of the salinity gradient maximum (z_{SGM}; m)……113

List of acronyms

Acronym	Full form
ADT	Absolute Dynamic Topography
AOPs	Apparent Optical Properties
AVISO	Archiving, Validation and Interpretation of Satellite Oceanographic Data
BaySys	Hudson Bay System Study
BEC	Barcelona Expert Center
BR	Band Ratio
CCGS	Canadian Coast Guard Ship
CDOM	Chromophoric Dissolved Organic Matter
CNES	Centre National d'Études Spatiales
CSA	Canadian Space Agency
CTD	Conductivity–Temperature–Depth
DAAC	Distributed Active Archive Center
DLR	Deutsches Zentrum für Luft- und Raumfahrt
DOC	Dissolved Organic Carbon
DOM	Dissolved Organic Matter
DOT	Dynamic Ocean Topography
ECMWF	European Centre for Medium-Range Weather Forecasts
EOSDIS	Earth Observing System Data and Information System
ERA5	ECMWF Reanalysis v5
ERS	European Remote Sensing
ESA	European Space Agency
FW	Freshwater Fraction
GFZ	German Research Centre for Geosciences
GIOP	Generalized Inherent Optical Property
GRACE	Gravity Recovery and Climate Experiment
GRACE-FO	Gravity Recovery and Climate Experiment Follow-On
GSM	Garver–Siegel–Maritorena
HD	High Discharge
HJB	Hudson Bay and James Bay
IAPSO	International Association for the Physical Sciences of the Oceans
ICESat	Ice, Cloud, and land Elevation Satellite
IOCCG	International Ocean Colour Coordinating Group
IOPs	Inherent Optical Properties
KaRIn	Ka-band Radar Interferometer
LAADS	Level-1 and Atmosphere Archive and Distribution System
LCC	Labrador Coastal Current

Acronym	Full form
LD	Low Discharge
MD	Mid Discharge
MLR	Multiple Linear Regression
MODIS	Moderate Resolution Imaging Spectroradiometer
MUMM	Management Unit of the North Sea Mathematical Models
NAP	Non-Algal Particles
NASA	National Aeronautics and Space Administration
NHR	Nelson and Hayes Rivers
NIR	Near-Infrared
NPP	National Polar-orbiting Partnership
NSERC	Natural Sciences and Engineering Research Council of Canada
NTU	Nephelometric Turbidity Unit
OACs	Optically Active Constituents
PACE	Plankton, Aerosol, Cloud, ocean Ecosystem
POC	Particulate Organic Carbon
QAA	Quasi-Analytical Algorithm
RCWF	River CDOM-Influenced Water Fraction
RMSE	Root-Mean-Square Error
ROFI	Region of Freshwater Influence
R/V	Research Vessel
RW	River Water
SeaDAS	SeaWiFS Data Analysis System
SIM	Sea-Ice Meltwater
SMAP	Soil Moisture Active Passive
SMOS	Soil Moisture and Ocean Salinity
SSH	Sea-Surface Height
SST	Sea-Surface Temperature
SW	Seawater
SWIR	Shortwave Infrared
SWOT	Surface Water and Ocean Topography
TA	Total Alkalinity
TEOS-10	Thermodynamic Equation of Seawater – 2010
TSS	Total Suspended Solids
TWF	Turbid Water Fraction

Use of copyrighted material

Figure 2.1. Adapted from of Rudels, B., and E. Carmack. 2022. Arctic ocean water mass structure and circulation. *Oceanography* 35(3–4):52- 65. This is an open access article made available under the terms of the Creative Commons Attribution 4.0 International License (https://creativecommons.org/licenses/by/4.0/).

Figure 2.2. Reprinted from Brown, K. A., Holding, J. M., & Carmack, E. C. (2020). Understanding Regional and Seasonal Variability Is Key to Gaining a Pan-Arctic Perspective on Arctic Ocean Freshening. *Frontiers in Marine Science, 7,* 606. This is an open-access article distributed under the terms of the Creative Commons Attribution License (CC BY).

Figure 2.3. Reprinted from Granskog, M. A., Kuzyk, Z. Z. A., Azetsu-Scott, K., & Macdonald, R. W. (2011). Distributions of runoff, sea-ice melt and brine using δ18O and salinity data—A new view on freshwater cycling in Hudson Bay. *Journal of Marine Systems, 88*(3), 362–374, with permission from Elsevier (License number: 6273251275880; May 20, 2026)

Figure 2.4. Reprinted from Carmack, E., Winsor, P., & Williams, W. (2015). The contiguous panarctic Riverine Coastal Domain: A unifying concept. *Progress in Oceanography*, *139*, 13–23, with permission from Elsevier (License number: 6273260714924; May 20, 2026)

Figure 2.5. Reprinted from Hall, J., & Kristoffersen, Y. (2025). Exploring Air Cushion Travel for Science Missions Over Arctic Sea Ice and Antarctic Ice Shelves, 2008–2025. *Oceanography*, *38*(4), 30–39. This is an open access article made available under the terms of the Creative Commons Attribution 4.0 International License (https://creativecommons.org/licenses/by/4.0/).

Figure 2.6. Reprinted from Ridenour, N. A., Hu, X., Sydor, K., Myers, P. G., & Barber, D. G. (2019b). Revisiting the Circulation of Hudson Bay: Evidence for a Seasonal Pattern. *Geophysical Research Letters*, *46*(7), 3891–3899. Copyright (2019); American Geophysical Union. This is an open-access article distributed under the terms of the Creative Commons Attribution License (CC BY).

Chapter 3 of this thesis is reproduced with minor modifications from Basu, A., McCullough, G., Bélanger, S., Mukhopadhyay, A., Doxaran, D., Sydor, K., et al. (2023). Plume dispersion from the Nelson and Hayes rivers into Hudson Bay using satellite remote sensing of CDOM and suspended sediment. *Elementa: Science of the Anthropocene*, **11**(1), 00076. Copyright (2026); the authors hold the copyright of this article. This is an open access article made available under the terms of the Creative Commons Attribution 4.0 International License (https://creativecommons.org/licenses/by/4.0/).

Chapter 4 of this thesis is reproduced with minor modifications from Basu, A., Bélanger, S., Kuzyk, Z. Z. A., Singh, R. K., Mukherjee, S., Larouche, P., Guzzi, A. C., Ausen, E. L., McCullough, G., & Ehn, J. K. (2026). Satellite data trace seasonal freshwater dispersion in Hudson and James Bays. *Geophysical Research Letters, 53*(2). Copyright (2026); the authors hold the copyright of this article. This is an open-access article distributed under the terms of the Creative Commons Attribution License (CC BY).

1. Chapter – Introduction

1.1. Motivation

The Hudson Bay and James Bay system (HJB) is the third-largest Arctic marginal sea (~0.9 million km²), following the Bering and Barents Seas. It is an inland marine system located along the southern margin of the Arctic Ocean in North America (Martini, 1986; Pelletier, 1986; Figure 2.1a).

HJB receives over 700 km³ of freshwater annually from more than 40 rivers (McCullough et al., 2019). About 46% (323 km³) of the HJB runoff is discharged into James Bay, a shallow inland sea in the southeastern corner of Hudson Bay (Figure 2.1a). Besides river runoff, seasonal sea-ice melt adds to the freshwater inventory of the shallow HJB basin (150 m; Peltier, 1986), making it a freshwater-influenced marine system (Dunbar, 1993).

Freshwater-induced density gradients, bathymetry, and the Coriolis force contribute to the geostrophic, cyclonic circulation of HJB (Ridenour et al., 2019a). Wind-driven circulation facilitates cross-shelf Ekman exchange of freshwater, with offshore transport in summer and onshore transport in fall (St-Laurent et al., 2011; Ridenour et al., 2019a; Ahmed et al., 2020). River water has an estimated residence time of approximately three to seven years in HJB (St-Laurent et al., 2011), although a more recent modelling study estimated a residence time of approximately 32 years, whereas sea-ice meltwater exhibits a much shorter residence time on seasonal timescales (Ridenour et al., 2019b). In winter, sea-ice formation and associated brine rejection promote convective mixing, vertically redistributing freshwater accumulated during summer and contributing to deep-water formation (Mundy et al., 2010). Thus, freshwater plays a central role in regulating stratification, the density-driven layering of seawater, and circulation within the HJB marine system.

Ongoing Arctic warming and hydrological change are altering the HJB marine system (Serreze & Barry, 2011; Rantanen et al., 2022). Rver discharge are increasing, while sea-ice cover is declining (Feng et al., 2021; Crawford et al., 2021; Stroeve et al., 2024). Changes in wind patterns are expected to redistribute freshwater within HJB (Fazel-Rastgar et al., 2020) and alter its export

through Hudson Strait to the Labrador Sea (Straneo and Saucier, 2008). In addition, anthropogenic influences, particularly river regulation for hydroelectric power generation, modify the timing and magnitude of freshwater discharge, including increased regulated flows during late fall and winter to meet hydropower demand (Stadnyk et al., 2020).

Thus, hydrographic changes in freshwater sources ultimately alter stratification. Changes in stratification can propagate across the food web, from microbes (Jacquemot et al., 2021, 2024) and phytoplankton (Matthes et al., 2021; Barbedo et al., 2022; Kitching et al., 2026) to fish (Schembri et al., 2025) and whales (Ausen et al., 2023), with implications for the livelihoods, income, and cultural well-being of coastal communities that depend on these marine resources through fisheries and hunting.

Beyond HJB, freshwater exported through Hudson Strait is transported southward along the Labrador shelf by the Labrador Coastal Current (LCC) (Figure 2.1b). Recirculation near Hamilton Bank in the southeastern Labrador Sea may facilitate the cross-shelf transport of HJB–LCC freshwater into the North Atlantic, with implications for ocean circulation and climate (Lin et al., 2026).

Despite the importance of freshwater in HJB, where river discharge is increasing and regulated and sea-ice cover is declining, the relative contributions of river water and sea-ice meltwater to stratification and deep-water renewal remain poorly constrained because of sparse in situ observations across this remote, seasonally ice-covered marine system. This paucity of field-based observations limits our understanding of how different freshwater sources regulate stratification and influence deep-water formation, motivating the development and application of satellite remote-sensing approaches to trace freshwater sources and assess their contributions to HJB stratification.

1.2. Thesis objectives

The main goal of this thesis is to trace the seasonal dispersion of river water and sea-ice meltwater, the two primary liquid freshwater sources in HJB, using satellite remote sensing and in situ freshwater tracers, including chromophoric dissolved organic matter (CDOM), total suspended solids (TSS), salinity, and oxygen isotopes (^{18}O and ^{16}O) are used to trace these freshwater sources

and determine their influence on water-column stratification. The objectives of the thesis are stated below:

i. Develop a satellite-based method to evaluate the dispersal of CDOM and TSS-rich Nelson/Hayes River (NHR) plume into Hudson Bay.

ii. Assess the extent and directionality of the NHR plume offshore in Hudson Bay using retrieved CDOM from satellite images.

iii. Determine river water and sea-ice melt contribution in the surface water of HJB during summer using satellite-derived CDOM and salinity.

iv. Evaluate satellite-based river water and sea-ice melt retrieval in HJB by assessing spatial and temporal patterns relative to established trends.

v. Assess seasonal and inter-annual variations of satellite-derived river water and sea-ice melt contribution in the surface water of HJB.

vi. Quantify river water and sea-ice melt contributions throughout the water column.

vii. Evaluate how different freshwater types control seasonal stratification within the HJB water column.

1.3. Thesis outline

This thesis comprises six chapters, including this first chapter.

Chapter 2 provided background on traditional and satellite-based approaches for tracing freshwater in marine systems. It synthesized freshwater sources, their distribution, and circulation within polar water masses. The chapter concludes by outlining the impacts of evolving freshwater regimes in the Arctic and HJB.

Chapter 3 addressed the thesis objectives i–ii. Findings were presented in a peer-reviewed research paper and published in the journal *Elementa: Science of the Anthropocene*:

Basu, A., McCullough, G., Bélanger, S., Mukhopadhyay, A., Doxaran, D., Sydor, K., et al. (2023). Plume dispersion from the Nelson and Hayes rivers into Hudson Bay using satellite remote

sensing of CDOM and suspended sediment. *Elementa: Science of the Anthropocene*, 11(1), 00076. https://doi.org/10.1525/elementa.2022.00076

Chapter 4 addressed the thesis objectives iii–v. Findings were presented in a peer-reviewed research paper and published in the journal *Geophysical Research Letters*:

Basu, A., Bélanger, S., Kuzyk, Z. Z. A., Singh, R. K., Mukherjee, S., Larouche, P., Guzzi, A. C., Ausen, E. L., McCullough, G., & Ehn, J. K. (2026). Satellite data trace seasonal freshwater dispersion in Hudson and James Bays. *Geophysical Research Letters*, *53*(2), e2025GL116442. https://doi.org/10.1029/2025GL116442

Chapter 5 addressed the thesis objectives vi–vii. Findings submitted as a research paper for publication in a peer-reviewed journal.

Chapter 6 summarized the key findings of Chapters 3, 4, and 5, identified limitations of the research, and presented recommendations for future work.

2. Chapter – Background

Freshwater plays a fundamental role in Arctic oceanography by regulating stratification and influencing ocean circulation, sea-ice formation, nutrient supply, and primary productivity (Carmack et al., 2016). River runoff, sea-ice melt, glacial and land-ice melt, Pacific Water inflow, and net precipitation (i.e., precipiataion – evaporation) each contribute to the freshwater budget and water-mass structure of the Arctic marine system (Serreze et al., 2006; Haine et al., 2015). Understanding the spatial and temporal distribution of these freshwater sources and their circulation is essential for assessing ongoing changes in the Arctic marine environment under an intensifying hydrological cycle.

2.1. Freshwater sources in the Arctic marine systems

2.1.1. Rivers

The Arctic Ocean and its marginal seas receive 13% of global river discharge from drainage basins that encompass 15% of the global land surface, underscoring the importance of river inputs in these high-latitude marine systems (Carmack et al., 2016). A recent Pan-Arctic assessment estimated river runoff at 5169 $km^3\ yr^{-1}$ for 1984–2018 (Feng et al., 2021), higher than earlier estimates for 1980–2000 (3900 $km^3\ yr^{-1}$) and 2000–2010 (4200 $km^3\ yr^{-1}$) (Serreze et al., 2006; Haine et al., 2015). The runoff estimation by Feng et al. (2021) is comparable to the projected 21st-century estimate of 5500 $km^3\ yr^{-1}$ (Vavrus et al., 2012).

This Pan-Arctic increase in river discharge is primarily driven by the Eurasian rivers (3401 $km^3\ yr^{-1}$), which grew by 0.24 % yr^{-1}, exceeding the Pan-Arctic average (0.22 % yr^{-1}) during 1984–2018 (Feng et al., 2021). The six largest Eurasian rivers, Lena, Ob', Yenisei, Severnaya Dvina, Pechora, and Kolyma, collectively discharged 2028 $km^3\ yr^{-1}$, representing 39% of the total Pan-Arctic runoff (Feng et al., 2021).

In contrast, North American rivers draining into the Arctic Ocean (e.g., Mackenzie) and into Hudson Bay and James Bay (HJB; Nelson, Churchill, and La Grande) contributed 34% (1768 $km^3\ yr^{-1}$) to the Pan-Arctic runoff. North American river discharge increased by 0.19 % yr^{-1} over the same period (Feng et al., 2021). About, 323 $km^3\ yr^{-1}$ of the North American runoff (i.e., 10 % of the Pan-Arctic runoff) enters the much smaller James Bay, yielding 5.5 m of river-derived freshwater layer, whereas 368 $km^3\ yr^{-1}$ (i.e., 11% of the Pan-Arctic runoff) is discharged into the

larger Hudson Bay, corresponding to a runoff yield of 0.5 m (McCullough et al., 2019). Foxe Basin and Hudson Strait contribute an additional 195 km^3 yr^{-1} runoff. The resulting mean runoff yield for the Hudson Bay complex, which includes Hudson Bay, James Bay, Foxe Basin, and Hudson Strait (0.7 m), is nearly twice the Arctic Ocean average (0.4 m) (McCullough et al., 2019; Feng et al., 2021), highlighting the significance of the basin within the Pan-Arctic freshwater budget. Moreover, some of these rivers draining into HJB (Nelson, Churchill, and La Grande) are regulated for hydropower generation, which alters the seasonality of runoff and thereby impacts regional oceanography (Stadnyk et al., 2020).

2.1.2. Sea Ice

The largest source of freshwater in the Arctic Ocean is sea ice. However, the mean Arctic sea ice volume declined from 17,800 km^3 in 1980–2000 to 14,300 km^3 in 2000–2010. Over the same period, perennial ice remained stable at 13,000 km^3, and the multiyear ice decreased from 10,900 km^3 to 7,400 km^3 (Serreze et al., 2006; Haine et al., 2015).

The loss of multiyear ice and shift to thinner, seasonal ice reduced mean ice thickness from 2.3–2.5 m in the early 1980s to 1.1–1.3 m by 2020, representing nearly 50% thinning (Schweiger et al., 2011; Laxon et al., 2013; Wang et al., 2022). Consistent with this thinning, sea ice volume has also declined by 2500 km^3 per decade in April and 3500 km^3 per decade in September since 1979 (Schweiger et al., 2011).

The mean sea ice extent in the Arctic Ocean (1981–2010) has also receded by 2.4–3.5% per decade between October and April, with accelerated reductions observed after 2000 (Stroeve and Notz, 2018). Moreover, the September minimum sea ice extent, a key indicator of the state of the Arctic ice cover, declined linearly from 1979 to 2006, reaching a record low in 2007. However, post-2007, minimum sea ice extent is variable, with no significant long-term trend (Stern, 2024).

In contrast to the Arctic Ocean, long-term records of sea ice volume are scarce for the seasonally ice-covered sub-Arctic HJB. A satellite-based analysis estimated a mean April sea ice volume of 1104 km^3 for 2003–2016 across HJB, corresponding to an average thickness of 1.5 m, comparable to that of the Arctic Ocean (Landy et al., 2017). Similar to the Arctic Ocean, HJB has experienced earlier breakup and later freeze-up over 1970–2021, leading to a lengthening of the ice-free season (Gagnon and Gough, 2002; Hochheim and Barber, 2013; Kowal et al., 2015; Andrews et al., 2018;

Gough, 2024; Stroeve et al., 2024). This trend of shorter sea ice cover period in HJB is projected to continue through 2100 (Crawford et al., 2021). Overall sea ice in the Arctic Ocean and HJB is declining in contrast to river runoff, and the Arctic Ocean is projected to be ice-free during summer by 2050 (Notz and SIMIP community, 2020).

In concert with the long-term decline in sea ice volume, the freshwater input from summer sea-ice melt has also decreased regionally (Mensha et al., 2025), although basin-scale observations in the Arctic Ocean remain limited. Nevertheless, seasonal sea-ice melt contributes 0.6 m of liquid freshwater to the Arctic Ocean, in addition to 0.4 m from river runoff, making it a major component of the freshwater budget (Haine et al., 2015; Perovich et al., 2021).

Recent advances in satellite-based freshwater tracing using sea surface- salinity, temperature, and height provide new insights into the distribution of sea-ice meltwater within the thin near-surface layer (0.1–1 m) of the Arctic Ocean (Smith et al., 2024). For example, in the western Arctic Ocean, sea-ice melt has been linked to freshwater accumulation within the Beaufort Sea Gyre (De Andrés et al., 2025).

In Hudson Bay, satellite-derived estimates of 1253 km^3 of sea ice volume provide a first-order constraint on the potential meltwater reservoir; however, the seasonal evolution of meltwater distribution remains poorly resolved (Landy et al., 2017). Existing field-based estimates in Hudson Bay are largely restricted to single seasons and are regional in extent (Kuzyk et al., 2008; Granskog et al., 2011; Eastwood et al, 2020; Ahmed et al., 2020). Thus, quantitative estimates of sea-ice meltwater concentration and its dispersion remain scarce across these polar marine systems.

2.1.3. Land Ice

Glaciers and ice caps of Greenland, the Canadian Arctic Archipelago, Iceland, Svalbard, and the High Arctic have experienced mass loss from 1190 $km^3\ yr^{-1}$ during 1992–2011 to 2440 $km^3\ yr^{-1}$ during 2012–2017, through surface runoff, basal melting, calving, and subglacial discharge (Gardner et al., 2011; Moholdt et al., 2012; Shepherd et al., 2012; Noël et al., 2020; Foss et al., 2024).

Melting of land ice across the Arctic and sub-Arctic regions contributed approximately 6300 km^3 of freshwater to the Baffin Bay and the North Atlantic Ocean between 1958 and 2016 (Bamber et

al., 2018). Melting of the Greenland Ice Sheet alone contributed more than 465 km^3 yr^{-1} between 2003 and 2010 (Kjeldsen et al., 2015; King et al., 2018; Mankoff et al., 2019), with recent estimates suggesting freshwater fluxes of 1000–1300 km^3 yr^{-1} during 2010–2019, of which 26 km^3 yr^{-1} is attributed to solid ice discharge (Bamber et al., 2018; Solomon et al., 2021).

Although the meltwater volume from land ice is smaller than river runoff and sea-ice melt, it plays a critical role in sea level rise, ocean circulation, air–sea heat exchange, and the redistribution of carbon in high-latitude marine systems (Bhatia et al., 2013; Guardia, Hu and Myers, 2015; Bevis et al., 2019), underscoring the need for improved understanding of meltwater transport from land ice.

2.1.4. Pacific Ocean

The northward flow of Pacific Water into the Arctic Ocean through the Bering Strait is driven by sea-surface height, pressure gradients, and wind forcing between the North Pacific and the Arctic Ocean (Coachman and Aagaard, 1966). These Pacific waters, influenced by the Alaskan Coastal Current, Yukon River runoff, and Anadyr shelf waters (salinity: 32.1−32.6), are relatively fresh compared to Atlantic Water (salinity: 33.8−34.8) entering the Arctic Ocean via the Fram Strait and the Barents Sea (Woodgate and Aagaard, 2005).

Pacific water flux through the Bering Strait into the Arctic Ocean was estimated around 1670 km^3 yr^{-1} prior to 1989 and increased to 2500 km^3 yr^{-1} by 2010 (Aagaard and Carmack, 1989; Serreze et al., 2006; Haine et al., 2015). Because 64% of the Bering Strait flow exits the Arctic toward the North Atlantic, Pacific-origin freshwater constitutes a significant contribution to the Arctic (Yang and Cessi, 2024).

A portion of the Pacific Water entering the Arctic Ocean (90 km^3 yr^{-1}) flows through Fury and Hecla Strait in the Canadian Arctic Archipelago into Foxe Basin. From Foxe Basin, the water flows southward into Hudson Bay, primarily through Roes Welcome Sound in northwestern Hudson Bay, and east of Southampton Island in northern Hudson Bay (McCullough et al., 2019).

2.1.5. Precipitation

Observational records of precipitation over the Arctic Ocean and surrounding sub-Arctic seas remain sparse. Consequently, atmospheric reanalysis products, despite their uncertainties, suggest

a decadal intensification of net precipitation over the polar oceans and seas (Barrett et al., 2020; Walsh et al., 2023). Estimates indicate that net precipitation over the Arctic Ocean increased from 990 km^3 yr^{-1} prior to 1989 to 2200 km^3 yr^{-1} by 2010 (Aagaard and Carmack, 1989; Serreze et al., 2006; Haine et al., 2015), and is projected to increase further due to sea ice loss, enhanced poleward moisture transport, and rising air temperatures (Bintanja et al., 2020; McCrystall et al., 2021).

Precipitation over the central Arctic Ocean occurs predominantly as snowfall during winter; however, increasing summer rainfall has been reported. The Arctic is projected to transition toward a rainfall-dominated regime in the future (Bintanja and Andry, 2017; McCrystall et al., 2021; Dou et al., 2022; Cast et al., 2026).

Freshwater contribution from precipitation into the Arctic Ocean is comparable to the Bering Strait through-flow. In contrast, over the Hudson Bay and James Bay system, the net precipitation contribution is smaller and poorly contrained ranging from −190 to >330 km^3 yr^{-1} (St-Laurent et al., 2011; cf. McCullough et al., 2019).

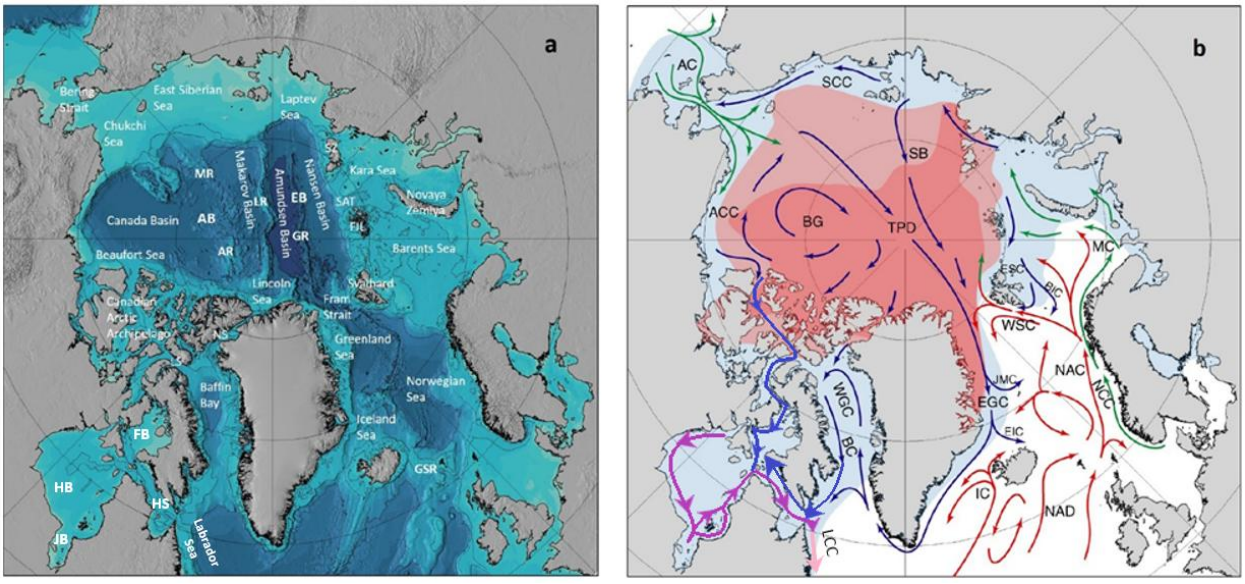


Figure 2.1. a. Arctic Ocean bathymetry from the international bathymetric chart of the Arctic Ocean updated database (Jakobsson et al., 2008). The projection is Lambert Equal Area and the 200 m, 500 m, 2,000 m, and 4,000 m isobaths are shown. Adapted from Rudels et al. (2012). Map drawn by Martin Jakobsson. AB = Amerasian Basin. AR = Alpha Ridge. EB = Eurasian Basin. FJL = Franz Josef Land. GR = Gakkel Ridge. GSR = Greenland Scotland Ridge. LR = Lomonosov Ridge. LS = Lancaster Sound. MR = Mendeleev Ridge. NS = Nares Strait. SZ = Severnaya

Zemlya. FB = Foxe Basin. HB = Hudson Bay. JB = James Bay. HS = Hudson Strait. b. The circulation of the upper layers of the Arctic Ocean. Warm Atlantic currents are indicated by red arrows, cold less saline polar and Arctic currents by blue arrows. Low salinity transformed currents are indicated by green arrows. The thick blue arrows show circulation from the Canadian Arctic Archipelago into Foxe Basin, which continues as cyclonic circulation in Hudson Bay (shown by thick violet arrows), exiting through Hudson Strait into the Labrador Sea. The annual mean maximum ice extent is shown in blue and the annual minimum in red (late twentieth century conditions). The minimum in 2007, the second absolute minimum to date, is shown in dark red. AC = Anadyr Current. ACC = Alaskan Coastal Current. BC = Baffin Island Current. BIC = Bear Island Current. LCC = Labrador Coastal Current. BG = Beaufort Gyre. EGS = East Greenland Current. EIC = East Iceland Current. ESC = East Spitsbergen Current. IC = Irminger Current. JMC = Jan Mayen Current. MC = Murman Current. NAD = North Atlantic Drift. NAC = Norwegian Atlantic Current. NCC = Norwegian Coastal Current. SB = Siberian branch (of the Transpolar Drift). SCC = Siberian Coastal Current. TPD = Transpolar Drift. WGC = West Greenland Current. WSC =West Spitsbergen Current from Rudels and Carmack (2022).

2.2. Freshwater distribution in the Arctic marine systems

2.2.1. Amerasian Basin

The Amerasian Basin, comprising the Canada Basin and Makarov Basin, is the principal freshwater reservoir of the Arctic Ocean (Carmack et al., 2016; Figure 2.1a). The Canada Basin lies north of the Chukchi and Beaufort Seas and is bounded by the Alpha–Mendeleev Ridge. The Makarov Basin lies to the west of the Alpha–Mendeleev Ridge (Figure 2.1a; Jakobsson et al., 2012). These basins receive freshwater inputs from North American (e.g., the Mackenzie River) and East Siberian rivers (e.g., the Kolyma River), Pacific inflow through the Bering Strait, sea-ice melt, and precipitation.

River discharge and sea-ice melt contribute to upper-ocean stratification, characterized by a summer mixed layer (20–30 m) overlying colder, dense winter waters (Figure 2.2; Peralta-Ferriz and Woodgate, 2015). Beneath the remnant winter water lies Pacific Summer Water (−1 to 3 °C), which gets modified by sea ice formation on the Chukchi shelf (Figure 2.2a). These colder (−1.8 °C) and denser Pacific Winter Waters sink beneath the fresher Pacific Summer Water, occupying depths of 100–200 m. Together, these Pacific water masses form the halocline (30–200 m) in the

Amerasian Basin, which isolates the warm Atlantic Water from the cold surface ocean (Figure 2.2a; Brown et a., 2020).

The halocline in the Canada Basin, which separates the cold surface waters from the warmer, deeper Atlantic Water, contains a temperature maximum associated with Pacific Summer Water and a temperature minimum associated with Pacific Winter Water (Steele et al., 2004; Shimada et al., 2005; Woodgate et al., 2010). While the halocline in the Canada Basin is strongly influenced by Pacific-derived waters, the Makarov Basin halocline is primarily dominated by dense waters formed along the East Siberian shelves (Aagaard et al., 1981; Rudels et al., 1996).

Below the halocline, Atlantic water contributes to the formation of intermediate waters (300–2000 m) (Rudels, 2012). In the Canada Basin, this intermediate water mass exhibits a distinct deep temperature minimum associated with the lateral spreading of colder waters from the Makarov Basin across the Mendeleev Ridge (Rudels and Carmack, 2022). However, the Makarov Basin lacks a temperature minimum and cools toward the bottom, reflecting intermittent spillover and mixing with colder deep waters from the Eurasian Basin (Jones et al., 1995; Rudels, 2012).

The deepest waters below 2000 m are relatively homogeneous and weakly stratified, with temperatures near −0.5 °C and salinities around 34.9–35. These deep waters are isolated from surface forcing and are renewed slowly through inter-basin exchanges. Geothermal heating may promote convective mixing and warming of the abyssal layer (Jones et al., 1995).

Recent observations indicate that the freshwater content in the Amerasian Basin has increased substantially since the early 2000s (Haine et al., 2015). Also, regional weakening of the halocline associated with increased upward heat flux from Atlantic Waters highlight the evolving role of the freshwater in the Amerasian Basin (Polyakov et al., 2020; Timmermans and Marshall, 2020).

2.2.2. Eurasian Basin

The Nansen and Amundsen Basins form the Eurasian sector of the Arctic Ocean (Figure 2.1a). The Nansen Basin lies to the north of the Barents and Kara Seas, while the Amundsen Basin lies to the north of the Laptev Sea. They are separated by the Gakkel Ridge, and the Lomonosov Ridge separates the Amundsen Basin from the Makarov Basin, marking the boundary between the Eurasian and Amerasian sectors (Figure 2.1a; Jakobsson et al., 2012).

Freshwater in the Eurasian Basin is supplied by Siberian rivers (Ob, Yenisei, and Lena), sea-ice melt, and precipitation, forming a stratified surface layer approximately 20–40 m thick (Figure 2.2b). Below this surface layer, dense shelf waters from the Kara and Laptev Seas sink and contribute to the formation of the halocline (Figure 2.2b; Steele and Boyd, 1998). The halocline is relatively weaker in the Nansen Basin, where warmer Atlantic Water promotes vertical mixing, and stronger in the Amundsen Basin, where cold, dense shelf waters contribute to its maintenance. Overall, the Eurasian Basin has a weaker and thinner halocline than the Amerasian Basin because it contains less freshwater and is more strongly influenced by Atlantic Water (Rudels et al., 2012).

Waters below the halocline in the Amundsen Basin are among the coldest deep waters in the Arctic, with temperatures near −0.94 °C and salinity around 34.94, whereas Nansen Basin deep water is slightly warmer and less saline (Rudels, 2012). Below 1,000 m, temperature and salinity increase, which may indicate geothermal heating of the deepest waters (Rudels, 2012; Carmack et al., 2012).

2.2.3. Hudson Bay

Freshwater in Hudson Bay, gets distributed within a shallow, semi-enclosed basin like the Arctic Ocean (average depth 150 m; Peltier, 1984). In spring and summer, large river inputs from the Nelson, Churchill, Winisk, and other rivers form a fresh surface layer (30–60 m) along the southern and western coasts (Prinsenberg, 1986a, b; Granskog et al., 2009). This surface layer, composed of river water and sea-ice melt, overlies a colder winter mixed layer formed during sea ice production (Figures 2.3a, b).

Brine-enriched waters (Kuzyk et al., 2008; Granskog et al., 2011), contributions from Foxe Basin and Hudson Strait (Jones and Anderson, 1994), and river water (Mundy et al., 2010) are found below the winter mixed layer in Hudson Bay. Nevertheless, deep-water formation in Hudson Bay and James Bay remains underexplored; however it is expected that river water may be mixed to the bottom in the shallow James Bay.

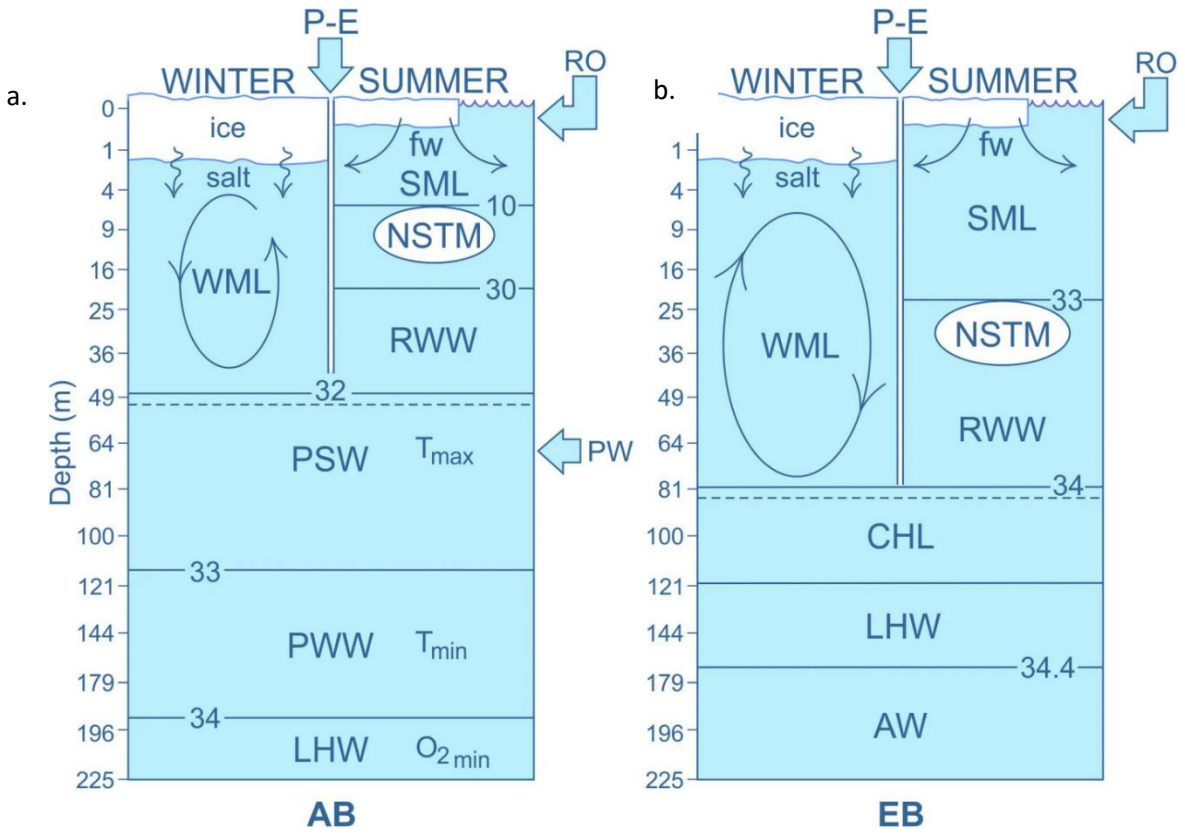


Figure 2.2. The Arctic Ocean's two "lids": sea ice and the halocline. Sea ice growth in winter adds salt to the surface ocean, driving penetrative convection to form the winter mixed layer (WML). In summer, freshwater (FW) is added to the mixed layer through seasonal contributions of sea-ice melt, terrestrial runoff (RO) and the balance of precipitation-evaporation (P-E), which strongly stratify the surface ocean. This stratification limits the depth of wind mixing, allowing formation of a shallow summer mixed layer (SML). Below the SML, fractions of the previous season's processes may remain; specifically, a cool remnant winter water (RWW) immediately above the base of the WML from the previous year. In the presence of sea ice with sufficient open water, a near-surface temperature maximum (NSTM) may form immediately below the SML by solar heating, capped by the cold, low salinity surface layer. These exchanges between the surface ocean layer and the sea ice "lid" occur across the Arctic Ocean, however, the additional FW associated with Pacific water (PW) enhances surface stratification in the Amerasian Basin (AB) and contributes to the difference between the halocline "lid" within the deep AB and that of the Eurasian Basin (EB); represented conceptually in (a, b), respectively. In both the Pacific and Atlantic sectors of the Arctic Ocean, warm Atlantic-derived waters (AW) form the base of the

halocline. The water column above is comprised of multiple layers that define the seasonal and permanent haloclines, constrained by the horizontal interleaving of seasonally modified FW inputs. a. In the Pacific sector halocline, PW inputs from the Bering Sea interflow, increasing stratification, and further constraining the depth of convection. Here, the winter convection penetrates down to the base of the Pacific Summer Water (PSW) and the sub-surface temperature maximum (T_{max}), which in turn lies above the Pacific Winter Water (PWW) and the sub-surface temperature minimum (T_{min}). Below PW lies lower halocline water (LHW), which likely forms on Siberian shelves. b. In the Atlantic sector, the thickness and distribution of halocline layers is highly variable across the EB, but includes a cold halocline layer (CHL) and LHW layer above the warm AW layer. Both form as a consequence of sea ice formation and winter convective mixing events; CHL mostly within the basin and LHW on mostly on shelves with subsequent drainage into the basins from Brown et al. (2020)

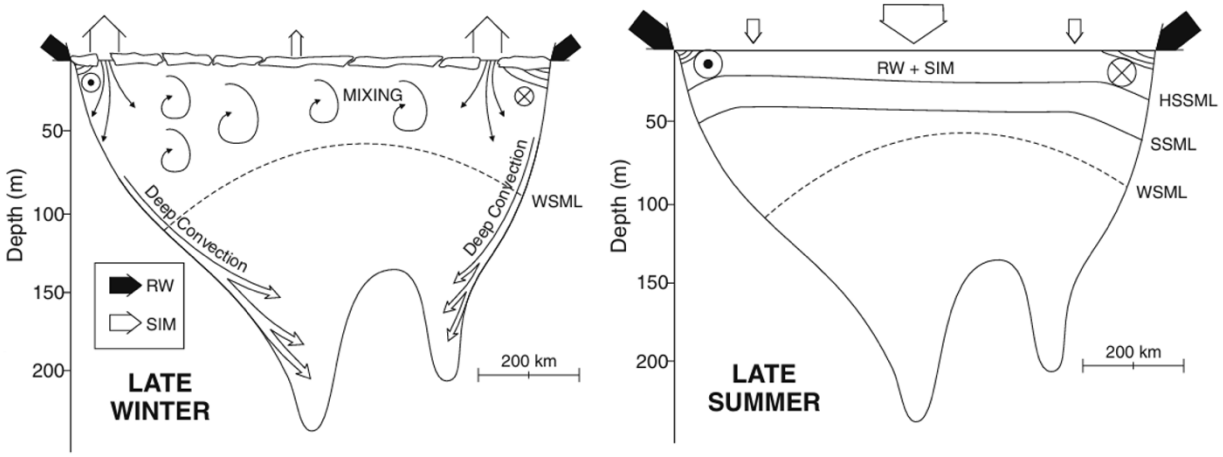


Figure 2.3. Water mass structure of the Hudson Bay. A conceptual diagram showing generally the mixing and deep convection in a. late winter and b. water mass structure (HSSML = Homogenous Summer Surface Mixed Layer; SSML = Summer Surface Mixed Layer; WSML= Winter Surface Mixed Layer) late summer in Hudson Bay from Granskog et al., (2011).

2.3. Freshwater circulation in Arctic marine systems

2.3.1. Alongshore boundary current

Surface circulation in the Arctic Ocean is controlled by density gradients generated by freshwater inputs from river discharge and sea-ice melt. River runoff from major Eurasian and North American rivers forms buoyant plumes that occupy the upper 10–20 m of the water column over the continental shelves (e.g., Osadchiev et al., 2017, 2021, 2023; Ehn et al., 2019). These river plumes merge to form a contiguous coastal river water domain that extends 10 – 20 km along the Arctic continental margins (Figure 2.2; Carmack et al., 2015).

The shallow shelf geometry and Earth's rotation transport river water eastward from the Barents Sea to the Laptev Sea along the continental margin, continuing into the East Siberian Sea and Chukchi Sea (Figures 2.1b; 2.2) as a boundary current. Likewise, river water from the Yukon and Mackenzie rivers flows eastward along the Canadian Arctic Archipelago.

This coastal riverine domain, rich in terrestrial sediments and CDOM, can be traced using satellite remote sensing, as demonstrated in the Arctic Ocean (e.g., Fichot et al., 2013), and remains poorly studied in Hudson Bay and James Bay.



Figure 2.4. Schematic representation of potential buoyancy-driven boundary flows driven by continental discharge among the northern coastline around North America and Eurasia from Carmack et al. (2015).

2.3.2. Wind driven circulation

A high-pressure system over the Arctic drives wind-induced anticyclonic circulation, transporting a portion of the coastal boundary current and shelf waters into the Amerasian Basin. This circulation enhances Ekman convergence in the Beaufort Sea, leading to freshwater accumulation within the Beaufort Gyre (Figure 2.5a; Proshutinsky & Johnson, 1997). As a result, liquid freshwater storage increased by 60–65% between the late 20th and early 21st centuries (Haine et al., 2015), accompanied by a rise in sea surface height observed from satellite altimetry (Giles et al., 2012).

Under high-pressure (anticyclonic) conditions, Eurasian river runoff remains confined to the alongshore boundary current, which gets transported eastward along the Siberian shelves into the East Siberian and Chukchi seas. In contrast, a low-pressure (cyclonic) system or weak high-pressure system drives Pacific and North American river water stored in the Beaufort Gyre, together with Eurasian river runoff, toward the Fram Strait through the Transpolar Drift (Figure 2.5b; Steele et al., 2004; Proshutinsky et al., 2009; Charette et al., 2020).

Similarly, anticyclonic circulation in early summer in eastern Hudson Bay drives fresh coastal waters offshore. In contrast, cyclonic circulation in fall transports freshwater along the southern coast of Hudson Bay and through Hudson Strait into the Labrador Sea (Granskog et al., 2009; Straneo and Saucier, 2008; Ridenour et al., 2019b; Dmitrenko et al., 2020; Figure 2.3).

2.3.3. Circumpolar boundary current

Warm Atlantic Water melts sea ice across Svalbard and the Barents Sea, contributing to water-column stratification (Kong et al., 2025). Earth's rotation (Coriolis effect) then transports these stratified waters along the continental slope from the Barents Sea through the Kara Sea and Laptev Sea into the East Siberian Sea and Chukchi Sea (Rudel, 2012). Cross-shelf transport driven by density gradients, tidal mixing, brine-induced freshwater entrainment, wind mixing, and mesoscale

eddies adds river water, sea-ice melt, and Pacific waters to the boundary current, enhancing stratification.

Along the continental slope of the Canada Basin, the boundary current known as the Beaufort Jet forms due to strong lateral density gradients between the fresh interior and saltier outer waters of the Beaufort Gyre (Manucharyan & Spall, 2016). However, cyclonic circulation in the Eurasian Basin weakens the Beaufort Jet, which drives river water and Pacific waters from the Beaufort Gyre into the Fram Strait via the Transpolar Drift (Proshutinsky et al., 2009).

In contrast to the fresh and stratified surface layer, the deep waters of the boundary current consist of salty Atlantic water that propagates eastward along the continental slope together with the surface layer (Rudels, 2012). During this circumpolar transport, these deep waters get mixed with dense, cold waters formed on Arctic shelves by brine rejection and eventually exit the Arctic Ocean through the Fram Strait (Rudels, 2012). Thus, the export of fresh surface waters and deep Atlantic-sourced waters into the North Atlantic Ocean via Fram Strait makes the Arctic Ocean a "double estuary" system (Carmack and Wassmann, 2006).

Similarly, in Hudson Bay, freshwater from major rivers (e.g., Nelson, Churchill, La Grande) forms a buoyant coastal layer that is advected eastward along the margins as a coastal boundary current (Figure 2.6), and is seasonally modulated by winds and sea ice processes (Figure 2.6; Prinsenberg, 1986; Granskog et al., 2009; Dmitrenko et al., 2020).

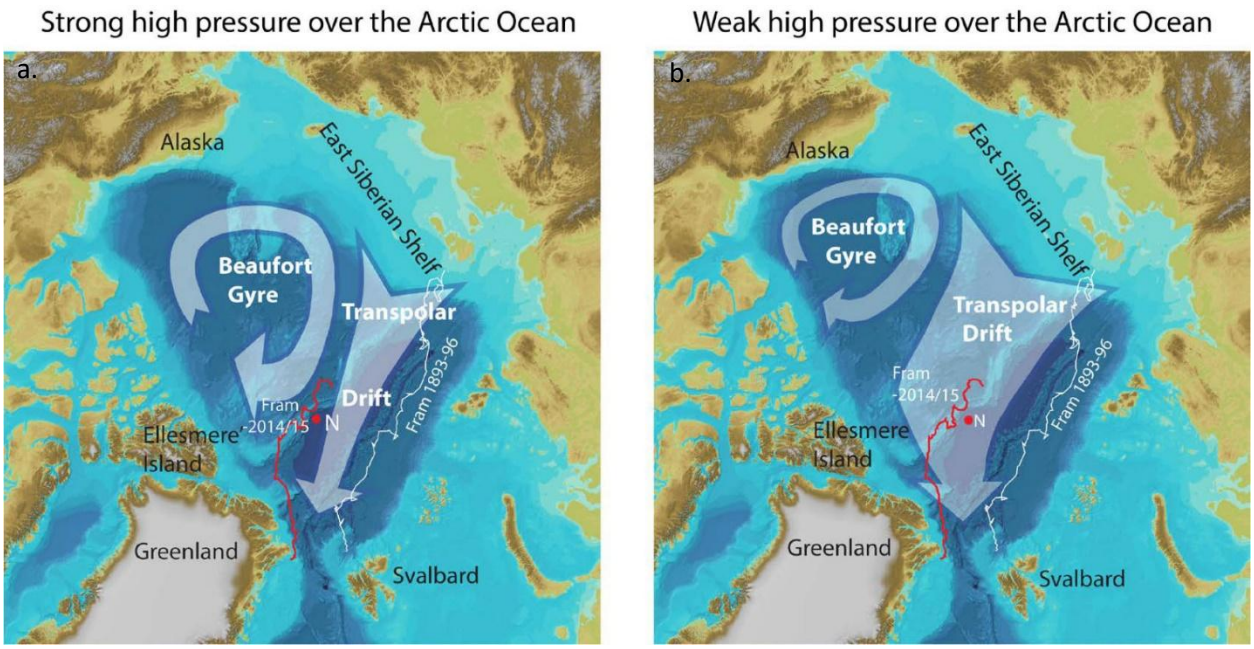


Figure 2.5. a. Freshwater accumulates in the Arctic Ocean under high-pressure conditions, leading to enhanced storage in the Amerasian Basin and the formation of a strong Beaufort Gyre. During this phase, Eurasian river runoff is transported eastward along the Arctic shelves. b. Under weaker high-pressure conditions, the Beaufort Gyre weakens, releasing freshwater that is transported into the Transpolar Drift along with Eurasian runoff. The 1893–1896 drift of *Fram* is shown by the white track, while the red track represents the 2014–2015 drift of the hovercraft *Sabvabaa* from Hall and Kristoffersen et al. (2025).

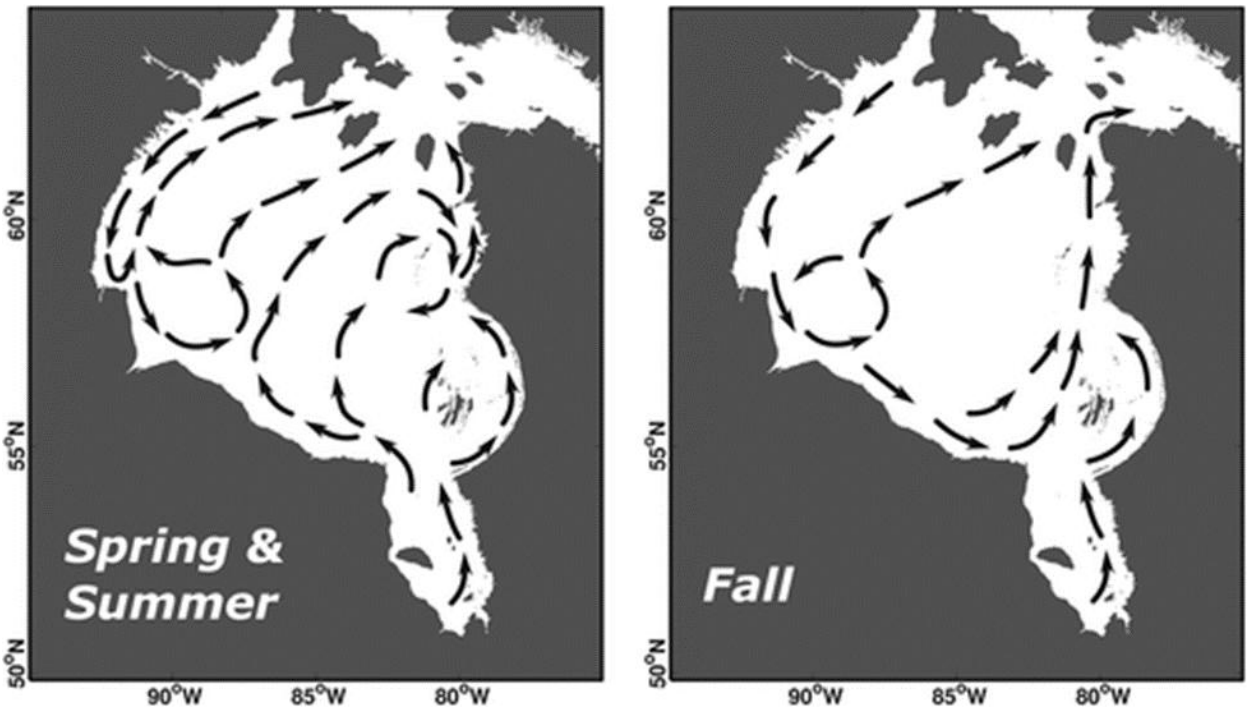


Figure 2.6. Schematics of average spring/summer and fall surface flow patterns that are based on Aviso satellite altimetry data and model output from Ridenour et al. (2019b)

2.4. Importance of freshwater in Arctic marine systems

The Arctic Ocean and the Hudson Bay marine system are projected to freshen throughout the twenty-first century due to increasing river discharge, precipitation, and Pacific inflow (Kattsov et al., 2007; Vihma et al., 2016; MacDonald et al., 2018; Shu et al., 2018). However, the relative contributions of increasing riverine freshwater input and changes in the net freshwater contribution from sea-ice formation and melt remain uncertain. Nevertheless, changes in freshwater input, storage, and redistribution are expected to alter upper-ocean stratification and modify exchanges between surface and deeper waters, as well as freshwater transport among basins. These changes will influence sea-ice processes, underwater light availability, biogeochemical cycling, primary production, ocean acidification and the functioning of Arctic marine ecosystems, necessitating continuous monitoring of different freshwater sources and their distribution across Pan-Arctic marine systems (refer to section 2.5–2.6 for freshwater tracing approaches).

2.4.1. Sea ice variability

In the Amerasian Basin, increased freshwater accumulation in the Beaufort Gyre enhanced stratification (Pemberton and Nilsson, 2016; Wang et al., 2025), which promoted sea-ice formation (Ivanova et al., 2026). In contrast, shoaling Atlantic Water weakened stratification and enhanced upward oceanic heat flux, thereby contributing to sea-ice decline and delaying freeze-up in the Eurasian Basin (Challet et al., 2025). Additional heat input from increased Pacific Water (Woodgate, 2018; Danielson et al., 2020) further amplified sea-ice loss in the Eurasian Basin (Polyakov et al., 2012; Cheng et al., 2025). Recent observations also indicate weakening stratification in the Makarov Basin associated with increased Atlantic Water influence (Polyakov et al., 2025). As sea ice retreats, Arctic surface waters are projected to warm, with sea surface temperatures increasing by up to 10°C by 2300 (Carton et al., 2015).

2.4.2. Biological and biogeochemical impact

Freshwater-driven stratification can limit nutrient supply from deeper waters, thereby impeding primary production in nutrient-depleted regions. For example, parts of the Canada Basin have shown declining nutrient inventories in the upper ocean, leading to reduced productivity (Ardyna and Arrigo, 2020). Moreover, increased delivery of TSS and CDOM can attenuate light, thereby preventing phytoplankton blooms (Holmes et al., 2012; Tank et al., 2012; Matsuoka et al., 2013). In contrast, the decline of sea ice in the Eurasian Basin enhances light penetration and extends the open-water growing season, which stimulates phytoplankton blooms. In the Barents Sea, reduced ice cover combined with Atlantic heat inflow has promoted higher productivity (Arrigo et al., 2008; Oziel et al., 2017; Lewis et al., 2020).

Freshening also lowers total alkalinity and carbonate ion concentrations, reducing carbonate saturation states (Ω), thus increasing the vulnerability of Arctic waters to ocean acidification (Yamamoto-Kawai et al., 2009). In river-influenced regions such as the Canada Basin and HJB, aragonite undersaturation ($\Omega_{ar} < 1$) has been observed, particularly during summer when freshwater inputs are highest (Yamamoto-Kawai et al., 2009; Else et al., 2013). These acidified waters are corrosive to calcifying organisms, posing a threat to marine ecosystems.

Although increased stratification and expanding open-water conditions can initially enhance oceanic CO_2 uptake, this capacity may eventually become limited (Woosley and Millero, 2020).

Stronger stratification suppresses vertical mixing and reduces the resupply of nutrients to surface waters, potentially limiting primary production and biological carbon uptake. At the same time, enhanced microbial remineralization can increase CO_2 concentrations within the water column, further lowering pH (Cai et al., 2010; Else et al., 2008a, b; Else et al., 2013; Ahmed et al., 2021) and potentially reducing the export and long-term sequestration of carbon in deeper waters. Thus, while freshening and expanding open-water conditions may initially favour greater atmospheric CO_2 uptake, continued freshening and stratification may ultimately constrain the capacity of the Arctic Ocean to act as a long-term carbon sink.

2.4.3. Ecological impact

Stratification in Hudson Bay influences marine trophic levels, from microbes to higher organisms. Microbial communities are highly sensitive to salinity gradients, with river-influenced systems supporting distinct freshwater, estuarine, and marine assemblages (Morency et al., 2022). Freshwater-driven stratification favors smaller, mixotrophic, and heterotrophic microbial communities in nutrient-depleted surface waters, while diatom-dominated assemblages persist below the subsurface chlorophyll maximum where nutrients remain available (Jacquemot et al., 2022, 2024). Increased terrestrial organic matter delivered by rivers further stimulates heterotrophic microbial activity and alters carbon processing pathways (Vonk et al., 2013; Kazmiruk et al., 2021).

Changes in stratification also impact marine food webs. Shifts in phytoplankton composition and reduced nutrient availability affect the quality of prey for zooplankton and fish. Consequently, changes in zooplankton and fish community structure have been observed in Hudson Bay, with implications for higher predators such as beluga whales (Estrada et al., 2012; Schembri et al., 2022, 2023, 2025; Ausen et al., 2023).

In addition, sea-ice loss modifies bloom timing and increases the likelihood of mismatches between primary producers and grazers (Ardyna et al., 2014; Wassmann and Reigstad, 2025). The loss of sea-ice habitat across the Arctic Ocean and its marginal seas affects ice-dependent species such as Arctic cod, seals, and polar bears by altering feeding grounds, migration patterns, and reproductive success (Grebmeier et al., 2006; Laidre et al., 2015; McGeachy et al., 2024; Stroeve et al., 2024). These ecological changes also affect the livelihoods and cultural well-being of Arctic

coastal communities that depend on marine resources for food, income, and cultural practices. Collectively, these impacts highlight freshwater variability as a central control on the future of Arctic marine ecosystems and the communities that depend on them under an intensifying hydrological cycle.

2.5. Freshwater tracers in Arctic marine systems

Freshwater from different sources mixes with ambient seawater, making its origin and distribution difficult to determine. Freshwater sources in Arctic and sub-Arctic marine systems can therefore be identified and quantified using tracers that reflect differences in their physical, chemical, and biogeochemical properties. This section reviews the field-based tracers used to distinguish freshwater sources and examine their distribution in marine systems.

2.5.1. Physical tracers

Freshwater content (FW; fraction) in seawater is derived from salinity (S; dimensionless), measured using a calibrated salinometer or a Conductivity–Temperature–Depth (CTD) profiler, and expressed relative to a marine endmember salinity (S_{ref}) (Equation 2.1). For the Arctic Ocean, a reference salinity of 34.8 is commonly used, while 32.1–32.8 is typically used for the Hudson Bay system (e.g., Aagaard & Carmack, 1989; Granskog et al., 2011; Ahmed et al., 2020).

$$FW = 1 - \left(\frac{S}{S_{ref}}\right) \tag{2.1}$$

Salinity is a conservative tracer of freshwater in the ocean, and temperature (T; °C) provides complementary information that helps distinguish freshwater types in the marine system. River water enters polar marine systems as relatively warm freshwater in summer. In contrast, sea-ice melt and glacial meltwater add cold, near-freezing freshwater to the surface ocean (e.g., Granskog et al., 2011; Rooijakkers et al., 2025). These distinct thermal signatures, together with salinity, allow freshwater from rivers, sea, and glacial ice to be distinguished, providing insight into the distribution of freshwater sources in polar marine systems.

2.5.2. Chemical tracers

In marine systems, the oxygen-isotope ratio (^{18}O /^{16}O, expressed as $\delta^{18}O$; ‰) is widely used as a chemical tracer to differentiate freshwater sources from ambient seawater. At low latitudes,

evaporation transfers almost exclusively lighter oxygen isotopes (^{16}O) into the vapor phase, with some ^{18}O incorporated into the vapor. As this vapor is transported poleward, successive condensation and precipitation remove the remaining heavy ^{18}O, leaving the remaining vapor progressively depleted in ^{18}O. As a result, Arctic and sub-Arctic precipitation, and the river runoff derived from it, are isotopically light, with $\delta^{18}O$ typically ranging from −10‰ to −30‰ (e.g., Yamamoto-Kawai et al., 2005; Guzzi et al., 2024).

River ice, formed directly from the meteoric freshwater, retains depleted isotopic signatures (−15‰). In contrast, marine ice forms from isotopically heavier seawater ($\delta^{18}O$: −2‰) and becomes enriched in ^{18}O during freezing, resulting in less negative to positive $\delta^{18}O$ (−1‰ to +5‰). This enrichment occurs because sea-ice formation preferentially incorporates heavier isotopes into the ice lattice, while salty brine that is isotopically heavier (+2.6‰) than the surrounding seawater is expelled into the underlying water column (Macdonald et al., 1995; Kuzyk et al., 2008; Granskog et al., 2009). As sea ice melts during summer, the freshwater released to the surface ocean exhibits $\delta^{18}O$ values close to 0‰, distinct from isotopically lighter river water. Together, the combined use of salinity and $\delta^{18}O$ enables identification of freshwater sources in marine systems (Östlund & Hut, 1984).

In addition to the $\delta^{18}O$ tracer, other isotopic tracers, such as hydrogen ($\delta^{2}H$), radium (^{223}Ra, ^{224}Ra, ^{226}Ra, ^{228}Ra), radon (^{222}Rn), tritium–helium (^{3}H–^{3}He), carbon ($\delta^{13}C$ or ^{14}C), and strontium ($^{87}Sr/^{86}Sr$), are used to characterize freshwater sources, pathways, and residence times in marine systems. However, these chemical tracers have limitations for freshwater estimation. $\delta^{2}H$ mostly mirrors $\delta^{18}O$ (e.g., Voelker et al., 2015). Radioactive isotopes such as radium and radon are non-conservative and spatially heterogeneous (e.g., Bhatia et al., 2011; Kipp et al., 2019). Tritium–helium remains useful for water mass age but is constrained by its very low concentrations in seawater which increases analytical costs (Ekwurzel et al., 2001). Carbon and strontium isotopes are sensitive to biological and chemical transformations, which limit their application for quantifying freshwater fractions (e.g., Griffith et al., 2012; Tank et al., 2012).

Similarly, non-isotopic chemical tracers such as total alkalinity (TA), which can trace riverine inputs from distinct watersheds, are non-conservative and are influenced by biological and carbonate processes (Lansard et al., 2012). Major ions (e.g., Na^{+}, Cl^{-}, Ca^{2+}) largely scale with salinity (Tank et al., 2012). Barium (Ba) enriched river waters behave quasi-conservatively at low

salinities and are affected by sediment interactions on shelves (Guay et al., 2009). Overall, these chemical tracers provide insights into freshwater sources and processes but are less robust than salinity– $\delta^{18}O$ approaches for freshwater source partitioning.

2.5.3. Biogeochemical tracers

Dissolved organic carbon (DOC) serves as a biogeochemical tracer of terrestrial freshwater in marine systems as long as it remains conservative and is not substantially degraded by photochemical or microbial processes. DOC originates primarily from wetland-rich watersheds underlain by permafrost that store large organic carbon pools across the Arctic and sub-Arctic regions (1460–1600 Pg) (Hugelius et al., 2014; Schuur et al., 2015; Kåresdotter et al., 2021).

Ongoing warming has accelerated permafrost thaw, increasing the mobilization of soil organic carbon and enhancing riverine DOC fluxes to marine systems (Biskaborn et al., 2019; Capelle et al., 2020). Globally, riverine DOC export to the oceans is estimated at 190–208 Tg yr^{-1}, of which the Arctic Ocean receives about 16%–19% (Raymond et al., 2007; Holmes et al., 2012; Tank et al., 2012). Sub-Arctic systems such as HJB also receive significant DOC inputs (5–6 Tg yr^{-1}) (Capelle et al., 2020).

DOC in water samples filtered through a 0.2–0.7 μm filter is generally measured by high-temperature catalytic oxidation or wet-chemical methods (Sharp et al., 1995, 2002). In addition, chromophoric dissolved organic matter (CDOM; refer to Chapter 3 for methods), the light-absorbing fraction of DOC, is widely used as an optical proxy, particularly in river-influenced coastal waters (Bricaud et al., 1981; Matsuoka et al., 2017).

Alongside DOC, rivers deliver 5.7 Tg of particulate organic carbon (POC) and 315 Tg of total suspended solids (TSS; refer to Chapter 3 for methods) to the Arctic Ocean annually. POC and TSS fluxes have been increasing due to warming and enhanced precipitation (McClelland et al., 2016; Tian et al., 2026).

Additionally, rivers supply dissolved nutrients (e.g., nitrate, phosphate, silicate) that regulate primary productivity and biogeochemical cycling, making them useful tracers of river water (Holmes et al., 2012; Lee et al., 2023; Guzzi et al., 2024). Together, with salinity-oxygen isotope these biogeochemical tracers provide insight into freshwater sources, transport, and ecosystem impacts in Arctic and sub-Arctic marine systems.

2.6. Freshwater tracing using satellite remote sensing

Satellite remote sensing provides spatially comprehensive and continuous observations of freshwater tracers across remote and seasonally ice-covered Arctic and sub-Arctic marine systems, where field observations are sparse. Freshwater can be detected from satellites through variations in surface salinity and temperature or indirectly through changes in water surface elevation and optically active constituents such CDOM and TSS in the water column. This section reviews satellite-based approaches for freshwater tracing using microwave, thermal-infrared, radar and lidar altimetry, and ocean color remote sensing.

2.6.1. Salinity and sea surface temperature

Sea-surface salinity (S_{sat}) can be retrieved from passive L-band (1.4 GHz) microwave radiometers onboard satellites, including the European Space Agency's (ESA) Soil Moisture and Ocean Salinity (SMOS) mission and NASA's Soil Moisture Active Passive (SMAP) and Aquarius missions (Supply et al., 2020; Tang et al., 2020). At L-band frequencies, the microwave emissivity of the sea surface depends on the dielectric properties of seawater, which vary primarily with salinity and temperature. Satellite radiometers measure the brightness temperature emitted from the ocean surface, from which surface emissivity and subsequently S_{sat} are retrieved after accounting for sea-surface temperature, surface roughness, and atmospheric effects (Martinez et al., 2022). The retrieved S_{sat} for each pixel can then be used to estimate surface freshwater content relative to a reference salinity (Equation 2.2).

$$FW_{sat} = 1 - \left(\frac{S_{sat}}{S_{ref}}\right) \tag{2.2}$$

S_{sat} observations, complemented by space-based thermal infrared (10.5–12.5 μm) measurements of sea surface temperature (SST_{sat}, °C), from the Moderate Resolution Imaging Spectroradiometer (MODIS) and the Visible Infrared Imaging Radiometer Suite onboard the Aqua and Suomi NPP satellites of NASA, enable discrimination between relatively warm river plumes and colder sea-ice or glacial melt (e.g., Nghiem et al., 2012; Jia & Minnett, 2020).

2.6.2. Sea surface height

Satellite altimetry is used to estimate freshwater storage and transport by measuring variations in sea-surface elevation, as the accumulation of relatively low-density freshwater can elevate sea-surface height relative to ambient saline waters.

Conventional radar altimeters transmit microwave pulses towards the ocean surface and determine the distance between the satellite and sea surface from the travel time of the returned signal. This measured distance and the satellite's orbital altitude enable estimation of sea-surface elevation relative to a reference ellipsoid, a smooth mathematical approximation of Earth's shape. The difference between the sea-surface elevation measured by radar altimetry and the geoid, an equipotential surface of Earth's gravity field, represents dynamic ocean topography (DOT), or sea-surface height (SSH). Horizontal gradients in DOT are used to estimate surface geostrophic currents and thereby examine freshwater redistribution and export.

In the Arctic Ocean, radar altimeters onboard the European Remote Sensing satellites (ERS-1 and ERS-2) and Envisat provided measurements of SSH through openings in the sea-ice cover (Peacock and Laxon, 2004). Using these satellites, Giles et al. (2012) identified freshwater storage in the western Arctic Ocean associated with wind-driven circulation in the Beaufort Gyre. ESA's CryoSat-2 provides improved coverage of the Arctic Ocean, enabling studies of Arctic freshwater storage and surface geostrophic circulation (Kwok and Morison, 2016; Armitage et al., 2016). More recently, the Surface Water and Ocean Topography (SWOT) mission, developed jointly by the Centre National d'Études Spatiales (CNES, France) and NASA, with contributions from the Canadian Space Agency (CSA) and United Kingdom Space Agency, extends conventional radar altimetry through the use of Ka-band radar interferometry. Its Ka-band Radar Interferometer (KaRIn) measures water-surface elevation across a wide swath, providing high-resolution two-dimensional observations of surface topography over oceans and inland waters (e.g., Fu et al., 2024).

Radar altimetry has been applied to the Hudson Bay system. Ridenour et al. (2019) used Absolute Dynamic Topography (ADT) and surface geostrophic velocities from the CNES-AVISO satellite altimetry product to examine seasonal circulation in Hudson Bay. The study revealed a dual seasonal circulation regime, contrary to the traditionally assumed cyclonic circulation of Hudson Bay.

Lidar altimetry uses laser pulses rather than microwave radiation to measure surface elevation. NASA satellite lidar missions, including the Ice, Cloud, and land Elevation Satellite (ICESat) retrieve SSH from leads within the sea-ice cover and provide high-resolution measurements of sea-ice freeboard, ice-sheet and glacier elevation, and surface-water elevation (Kwok and Morison, 2011; Kwok et al., 2019).

Lidar and radar altimetry can be used together because of their complementary measurement capabilities. Radar can operate through clouds and during polar darkness, providing greater temporal coverage, whereas lidar provides precise measurements of surface elevation and sea-ice freeboard but is limited by cloud cover. In addition, radar and lidar signals interact differently with snow and sea ice, providing information for constraining sea-ice freeboard, snow depth, ice thickness, and ultimately ice volume (Saha et al., 2023). In the Hudson Bay system, Landy et al. (2017) combined CryoSat-2 with ICESat to quantify variations in sea-ice thickness and volume, providing information on freshwater stored in sea ice and subsequently released during melting.

2.6.3. Gravity anomaly

The Gravity Recovery and Climate Experiment (GRACE), a joint mission of NASA and the Deutsches Zentrum für Luft- und Raumfahrt (DLR, Germany), measured temporal variations in Earth's gravity field using two satellites travelling in the same orbit and separated by a fixed nominal distance. As the leading satellite approached a region of greater mass and therefore stronger gravitational attraction, it accelerated slightly away from the trailing satellite, increasing the distance between them. After passing over the region, the leading satellite decelerated while the trailing satellite experienced the same gravitational attraction, producing a corresponding change in their separation. These changes in satellite-to-satellite distance were measured using a microwave ranging system and used to determine spatial and temporal variations in Earth's gravity field (Tapley et al., 2004; Wahr et al., 2004).

Because changes in water and ice storage redistribute mass at Earth's surface, temporal gravity anomalies can be converted to changes in equivalent water mass. GRACE observations were therefore used to estimate changes in terrestrial water storage, ice-sheet and glacier mass, and ocean mass, providing information on freshwater storage and fluxes in Arctic and sub-Arctic regions (e.g., Syed et al., 2007; Giles et al., 2012). The Gravity Recovery and Climate Experiment

Follow-On (GRACE-FO), launched in 2018 as a partnership between NASA and the German Research Centre for Geosciences (GFZ), continues the GRACE record.

2.6.4. Chromophoric dissolved organic matter and suspended solids

2.6.4.1. Ocean color remote sensing

Ocean color remote sensing detects water color and its variability based on the interaction of solar radiation (100–2500 nm) with optically active constituents (OACs) in the water column, including CDOM, suspended solids, phytoplankton, and water itself (Morel & Prieur, 1977). These interactions with OACs are described spectrally in terms of inherent optical properties (IOPs), such as absorption ($a(\lambda)$; m^{-1}) and scattering ($b(\lambda)$; m^{-1}) (Gordon et al., 1975).

CDOM strongly absorbs light in the blue wavelengths (400–500 nm) and is a negligible scatterer (Bricaud et al., 1981). Suspended solids, including inorganic sediments as well as phytoplankton cells and aggregates, scatter light across the visible to near-infrared (NIR; 400–1300 nm) spectrum, with enhanced scattering at longer wavelengths (Bricaud & Morel, 1986; Morel, 1987). Phytoplankton pigments dominate absorption in the blue (440 nm) and red (675 nm) regions of the spectrum (Sathyendranath et al., 1989). Pure water absorbs at longer wavelengths and contributes modestly to scattering (Pope & Fry, 1997; Twardowski et al., 2007). Shortwave infrared (SWIR; 1300–2500 nm) radiation is strongly absorbed by pure water, resulting in near-zero water-leaving radiance over most aquatic environments. Consequently, SWIR bands are commonly used for atmospheric correction, particularly in turbid coastal and inland waters where conventional near-infrared atmospheric correction assumptions may fail (Wang & Shi, 2007).

IOPs and the ambient light field determine the apparent optical properties (AOPs) of the water column. Among these, remote sensing reflectance ($R_{rs}(\lambda)$; sr^{-1}) is defined as the ratio of water-leaving radiance ($L_w(\lambda)$; W m^{-2} sr^{-1} nm^{-1}) to down welling irradiance just above the sea surface ($E_d(\lambda)$; W m^{-2} nm^{-1}), and is the primary quantity measured by satellite sensors (Equation 2.3; Gordon et al., 1975).

$$R_{rs}(\lambda) = \frac{L_w(\lambda)}{E_d(\lambda)} \approx g \frac{b_{bw}(\lambda) + b_{bp}(\lambda)}{a_w(\lambda) + a_{CDOM}(\lambda) + a_{phy}(\lambda) + a_{NAP}(\lambda) + b_{bw}(\lambda) + b_{bp}(\lambda)}, \quad (2.3)$$

where,

- $b_{bw}(\lambda)$ is the backscattering coefficient of pure water (m^{-1}),

- $b_{bp}(\lambda)$ is the backscattering coefficient of particles, primarily suspended solids (m^{-1}),
- $a_w(\lambda)$, $a_{CDOM}(\lambda)$, $a_{phy}(\lambda)$, and $a_{NAP}(\lambda)$ are the absorption coefficients (m^{-1}) of pure water, CDOM, phytoplankton pigments, and non-algal particles (NAP, i.e., inorganic sediments), respectively, and
- g is a geometry-dependent proportionality factor (Gordon et al., 1988).

2.6.4.2. Empirical detection

CDOM and TSS in coastal waters vary with river discharge, thereby altering $R_{rs}(\lambda)$. Empirical relationships between $R_{rs}(\lambda)$ and these tracers enable satellite-based (e.g., Aqua-MODIS; Sentinel-2, 3) mapping of river water dispersion in marine systems. For example, blue-to-red R_{rs} band ratios are commonly used to retrieve CDOM in coastal waters (Doxaran et al., 2005; Bélanger et al., 2008; Campanelli et al., 2017), where red bands offset suspended sediment effects in the blue wavelengths (Nechad et al., 2010). CDOM sources can also be characterized using their spectral slope (S; nm^{-1}) (e.g., $S_{350–500}$; Babin et al., 2003).

However, empirical optical algorithms are region-specific and depend on local optical conditions and constituent composition. Their performance degrades outside calibration regions due to variability in absorption and scattering, limiting their robustness for global freshwater mapping.

2.6.4.3. Inversion-based detection

In contrast to empirical approaches, inverse bio-optical models decompose $R_{rs}(\lambda)$ measured by space-based ocean color sensors into absorption and backscattering components, enabling estimation of CDOM and TSS across a wide range of optical conditions (Gordon et al., 1988). These models rely on *a priori* knowledge of constituent spectral behavior to constrain the inversion. For example, CDOM absorption is represented by an exponential decrease in longer wavelengths (Equation 2.4; Bricaud et al., 1981),

$$a_{CDOM}(\lambda) = a_{CDOM}(\lambda_0)\, e^{-S(\lambda-\lambda_0)}, \quad (2.4)$$

where $a_{CDOM}(\lambda_0)$ is the absorption coefficient at a reference wavelength (typically 412 or 443 nm) and S (nm^{-1}) is the CDOM spectral slope.

Particle backscattering, dominated by suspended solids, follows a power-law dependence on wavelength (Equation 2.5; Morel, 1987; Stramski et al., 2004),

$$b_{bp}(\lambda) = b_{bp}(\lambda_0)\left(\frac{\lambda}{\lambda_0}\right)^{-\eta}, \quad (2.5)$$

where the dimensionless slope η is related to particle size distribution and composition, with lower values indicating dominance of larger, mineral-rich particles typical of river plumes.

Widely used inverse models include the Quasi-Analytical Algorithm (QAA), which sequentially derives total absorption and backscattering from reflectance spectra and partitions them into constituent components using semi-analytical relationships (Lee et al., 2002). The Garver–Siegel–Maritorena (GSM) model, which inverts reflectance to estimate chlorophyll-a, CDOM absorption, and particle backscattering through nonlinear optimization (Maritorena et al., 2002). The Generalized Inherent Optical Property (GIOP) framework further extends these approaches by allowing flexible parameterizations of absorption and scattering components and multiple solution schemes (Werdell et al., 2013). Arctic-specific implementations, decompose CDOM and non-algal particles to enable estimation of DOC and freshwater distributions in Arctic marine systems (Matsuoka et al., 2013).

However, deterministic inversions are sensitive to uncertainties in model assumptions and optical parameterizations, particularly in optically complex Arctic coastal waters. Bayesian inverse approaches address these limitations by incorporating prior knowledge and uncertainty in key parameters (e.g., $a_{CDOM}(\lambda)$ and S, $b_{bp}(\lambda)$, and $a_{phy}(\lambda)$) and updating them using satellite-derived $R_{rs}(\lambda)$ to obtain posterior estimates with quantified uncertainty (e.g., Mukherjee et al., 2026).

3. Chapter – Plume dispersion from the Nelson and Hayes rivers into Hudson Bay using satellite remote sensing of CDOM and suspended sediment

This chapter was published in the peer-reviewed journal *Elementa: Science of the Anthropocene*. The citation for this manuscript is:

Basu, A., McCullough, G., Bélanger, S., Mukhopadhyay, A., Doxaran, D., Sydor, K., et al. (2023). Plume dispersion from the Nelson and Hayes rivers into Hudson Bay using satellite remote sensing of CDOM and suspended sediment. *Elementa: Science of the Anthropocene*, 11(1), 00076. https://doi.org/10.1525/elementa.2022.00076

Abstract

Changes in the dispersion patterns of Arctic river plumes due to climate change and hydroelectric regulation are challenging to monitor, calling for synoptic, continuous observation using satellite remote sensing. Algorithms for chromophoric dissolved organic matter (CDOM) and total suspended solids (TSS) were applied to moderate resolution imaging spectroradiometer (MODIS) imagery to study the dispersion of the combined Nelson River and Hayes River plume into southwestern Hudson Bay, employing quantile regressions to capture dispersion variability along a freshwater–marine gradient. MODIS-derived CDOM and TSS quantile concentrations ($Q_{0.05}$–$Q_{0.95}$) decreased exponentially with distance from the Nelson River mouth. The $Q_{0.95}$ asymptote marked the offshore extent of the river plume and was used to determine the marine and river water fractions of surface water in southwestern Hudson Bay. At about 125 km from the mouth of the Nelson River, CDOM was reduced by 75% relative to its river mouth values. Owing to the significant co-variability between CDOM dilution and river discharge, a 0.25 river water fraction was estimated at this distance, which varied by ±35 km during flood and ebb flows. Anti-cyclonic winds transported the river plume along the 54° azimuth towards central Hudson Bay, while cyclonic winds propagated the plume eastward along the south shore. Particle settling in the coastal waters and resuspension events from mudflats and/or bank erosion caused non-significant relationships between TSS and river discharge. This non-conservative behavior renders TSS a less useful optical tracer of Nelson and Hayes river water in southwestern Hudson Bay. The novel quantile regression approach for defining boundaries of river water dilution in transitional waters may provide useful information for coastal management at spatial scales of tens to hundreds of kilometers, ranging from near-real-time monitoring to seasonal and multi-year studies.

3.1. Introduction

River water flowing into coastal waters often forms a "river plume," a buoyant surface layer that overlies the more saline marine water. As the river water in the plume propagates offshore, it gradually becomes more saline as it mixes with the ambient seawater (Hetland, 2005). This mixing creates a transitional salinity zone referred to as a region of freshwater influence (ROFI) (Horner-Devine et al., 2015). Several factors, which include river discharge, tidal amplitude and velocity, coastal bathymetry, coastline geometry, wind stress, ocean circulation, water mass stratification, presence of sea ice, and Coriolis force, determine the properties of the ROFI (e.g., Kuzyk et al., 2008; Pimenta et al., 2011; Osadchiev and Sedakov, 2019).

The buoyant layer of river water in the ROFI forms due to a density difference between fresh and salty ocean water (Garvine, 1995). The offshore propagation of this buoyant layer results primarily from the tidal and wind-forced drift of the surface plume and mixing with the underlying ocean water (Garvine, 1999). Ultimately, the balance between stratification and mixing determines the spread and dispersion of river plumes in the open ocean. Due to higher river inflow per unit area and ice-meltwater, freshwater content exerts greater control over upper-water-column stratification in the Arctic Ocean than in other oceans (Aagaard and Carmack, 1989; Carmack, 2007; Ehn et al., 2019).

Various tracers can be used to characterize the extent and shape (directionality) of a river plume. As a critical factor in density gradients, salinity is the most widely used physical tracer for characterizing of river plumes and ROFI. However, plume definitions vary as to the salinity difference from offshore ocean water that delineates their extents, e.g., Mississippi River plume (salinity: 32–36), Congo River plume (<30–36), Ganges/Brahmaputra River plume (<26–34), Amazon River plume (30–36), Mekong River plume (32–33) and the Arctic Lena River plume (16-28) (Fournier and Lee, 2021; Zhuk and Kubryakov, 2021). Temperature may be used as a physical tracer of river plumes, but it also varies by the geographical and climatological setting of the rivers (e.g., Otero et al., 2009; Palacios et al., 2012; Hopkins et al., 2013). Other dissolved minor and trace constituents, such as barium (Ba; e.g., Guay and Falkner, 1997; Guay et al., 2009), phosphate (PO4; e.g., Ikeda et al., 2018), nitrate (NO3; e.g., Hsiao et al., 2014), aluminum (Al), and silica (Si; e.g., Middag et al., 2009; Bergeron and Tremblay, 2014), are also used to trace sources of riverine freshwater depending on their source concentration.

The rivers that debouch into the Arctic Ocean contribute significantly to the higher total alkalinity of the surface polar mixed layer (Anderson et al., 2004). Therefore, alkalinity serves as a fluvial water tracer (e.g., Lansard et al., 2012). The non-conservative nature of these chemical tracers, except for dissolved organic carbon (DOC; e.g., Guégen et al., 2011; Milleur et al., 2023), renders them less reliable compared to the more conservative proxies of salinity and temperature.

Poleward depletion of the oxygen-18 (^{18}O) isotope relative to oxygen-16 (^{16}O) in precipitation has enabled the use of this isotope ratio $^{18}O/^{16}O$ ($\delta^{18}O$; ‰), a chemical tracer, and salinity to discern polar ROFI, which embeds river runoff (e.g., van Donk and Mathieu, 1969; Östlund and Hut,1984; Granskog et al., 2009; Granskog et al., 2011). Logistical inaccessibility to Arctic/sub-Arctic coastal waters and the expense and time required for these methodologies further limit the widespread use of these chemical tracers in addressing questions about the spatial and temporal variability of river plumes.

The synoptic coverage of modern space-based optical sensors has proven an efficient means of characterizing river runoff using optical proxies (e.g., Schroeder et al., 2012). Optical tracking of river runoff in Arctic waters effectively uses the concentration of chromophoric dissolved organic matter (CDOM) because it is conservative (e.g., Matsuoka et al., 2012; Fichot et al., 2013). Similarly, the satellite-derived concentration of total suspended solids (TSS) has also been used to study the Mackenzie River plume in the Beaufort Sea (Doxaran et al., 2012), but with significant drawbacks, such as the inability of optical signatures to distinguish between river-derived sediments and resuspended bed sediments, and between vertical settling and horizontal dispersion of sediments.

River plume dynamics in Hudson Bay are poorly understood, yet essential to understanding the impact of climate change and river regulation on the Hudson Bay marine system. Given the significance of cumulative fluvial discharges into Hudson Bay (710 $km^3\ yr^{-1}$, including James Bay, 1984–2013; Déry et al., 2016; McCullough et al., 2019), knowledge of river plume dynamics is essential to understanding basin-scale oceanographic processes and associated ecological regimes.

Because Hudson Bay remains ice-covered for more than half the year, from winter to early summer, when runoff is high, previous studies have focused on the spread of river plumes under sea ice. Such plume dispersion can be more extensive than in open water due to reduced mixing by winds and waves (e.g., Messier et al., 1986; Ingram and Larouche, 1987; Li and Ingram, 2007;

Peck et al., 2022). However, optical satellite observations for river plume detection are not possible when sea ice is present in significant amounts. Therefore, to date, satellite remote sensing techniques have not been used to investigate river plumes in Hudson Bay.

Here, we study the dispersion of freshwater from the Nelson and Hayes Rivers (NHR) in southwestern Hudson Bay during the ice-free period using a satellite-based approach. The runoff from Nelson River, augmented by Hayes River, supplies more than half the freshwater loading from the southwestern watershed of Hudson Bay (Déry et al., 2011) and is a significant source of terrestrial dissolved organic matter (DOM) and particulates to the region (Guéguen et al., 2011; Guéguen et al., 2016; Capelle et al., 2020). The objectives of this study are threefold:

i. Evaluate the retrieval of CDOM and TSS from satellite imagery of the NHR estuary using available in situ data;
ii. Develop a satellite-based method to evaluate the dispersal of CDOM and TSS-rich NHR plume into Hudson Bay;
iii. Assess the extent and directionality of the NHR plume offshore in Hudson Bay using retrieved CDOM from satellite images.

3.2. Data and method

3.2.1. Study area

The Nelson River and Hayes River flow northward through Manitoba (Canada) into a shared estuary in southwestern Hudson Bay (Figure 3.1). The NHR estuary is a seasonally ice-covered, mesotidal estuary with a characteristic funnel shape (Wang et al., 2012). With a mean annual discharge of 109 km^3 (in 1984–2013; Déry et al., 2016), the Nelson River is one of the largest rivers draining into Hudson Bay. It drains a watershed of 1.1 million km^2 across central and western Canada (inset in Figure 3.1). It transports significant amounts of suspended sediments and DOM from the Canadian Shield and the Canadian Interior Plains into Hudson Bay (Rosenberg et al., 2005). Large lakes, such as Lake Winnipeg along the river course, and coastal mudflats act as both sinks and sources of sediments and terrestrial and algal CDOM (Goharrokhi et al., 2022).

Since 1978, flow diverted from Churchill River has contributed 24 $km^3\ yr^{-1}$ to the flow in the lower Nelson River (i.e., one quarter of the total discharge). Also, since 1978, the level of 23,750 km^2 of

Lake Winnipeg has been regulated to provide seasonal storage (State of Lake Winnipeg, 2020), allowing for increased river discharge during the winter (Déry and Wood, 2005), reducing the spring and summer peak inflow into the lake (McCullough et al., 2019). Furthermore, over the post-diversion and regulation period, the discharge of the Nelson River increased by about 42%, from 92 $km^3\ yr^{-1}$ in the decade 1984–1993 to 131 $km^3\ yr^{-1}$ during 2004–2013 (Déry et al., 2016), due to increased runoff driven by climate change in the upper watershed (Clair et al., 1998).

The Hayes River, originating from Northern Manitoba, drains an entirely Precambrian Shield watershed into the same estuary as the Nelson River (inset in Figure 3.1; Rosenberg et al., 2005). It is an unregulated river with an annual mean discharge of 19 $km^3\ yr^{-1}$ during 1984–2013 (Déry et al., 2016). The Hayes River discharge has also increased over the last three decades, but by a smaller amount (28%) compared to the Nelson River (Déry et al., 2016). Over the same three decades, the two rivers accounted for 61% of the 210 $km^3\ yr^{-1}$ discharge into Hudson Bay between the mouth of Churchill River and the entrance to James Bay (table 2 in McCullough et al., 2019).

Since it drains through the northern wetlands and peatlands, Hayes River has higher CDOM and lower TSS than the Nelson River, as shown in satellite imagery (Figure 3.2). Other significant rivers draining into the southwestern Hudson Bay are the Churchill and Seal Rivers, located north of the Nelson River. The combined mean annual discharge volume of the Churchill and Seal Rivers was determined to be 35% of the NHR discharge for the same 1984–2013 period (Déry et al., 2016), thus highlighting the significance of NHR discharge into southwestern Hudson Bay. A geostrophic anticlockwise (cyclonic) circulation regime prevails off the southwest coast, transporting a portion of terrestrial freshwater toward eastern Hudson Bay (Prinsenberg, 1986; Ridenour et al., 2019a).

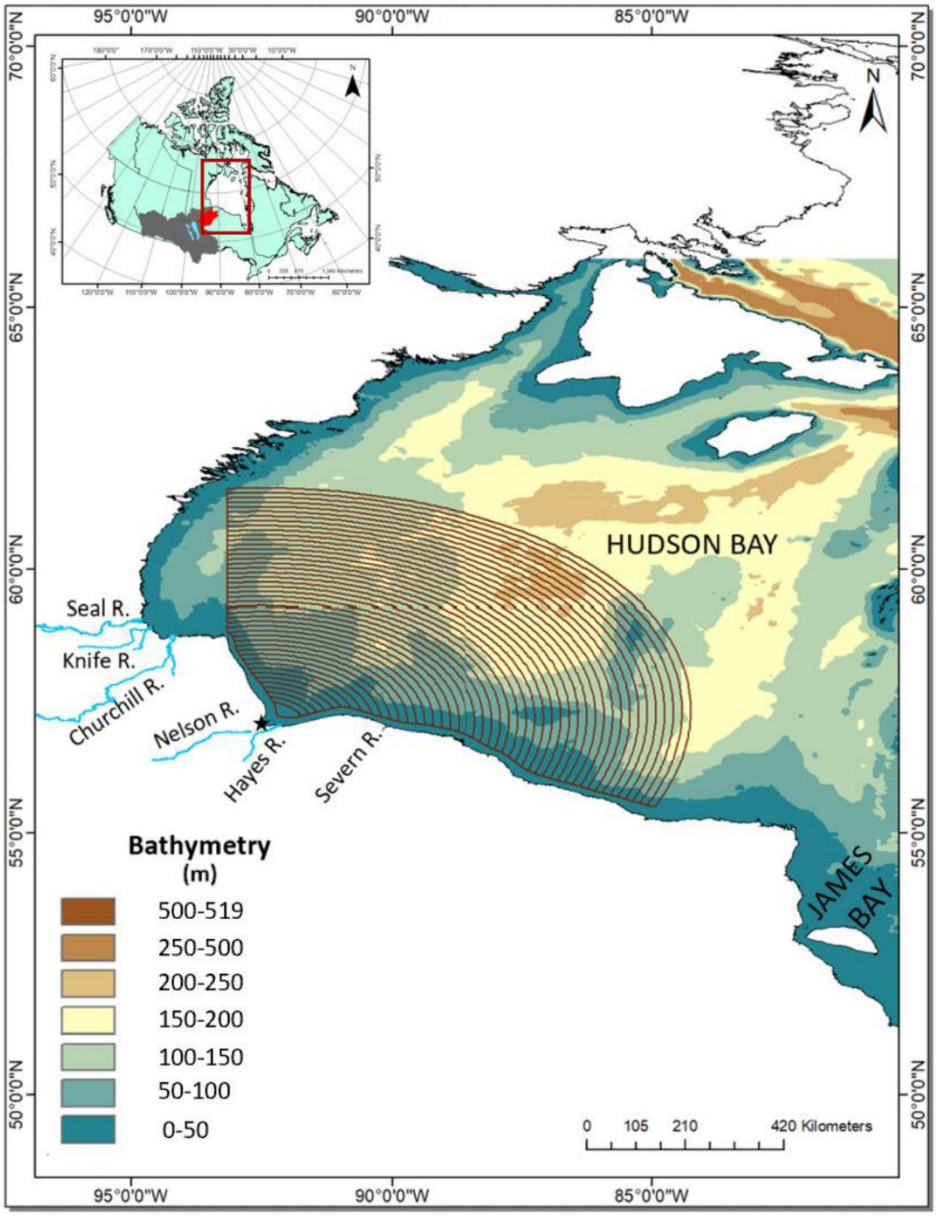


Figure 3.1. The study domain was separated into circular sections 10 km wide, with the initial section being 50 km from the Nelson River mouth (denoted by a star) to offshore Hudson Bay (500 km). The study domain corresponding to 10-m bathymetries was excluded from the model domain to avoid bias because of extremely high nearshore values of chromophoric dissolved organic matter (CDOM) and total suspended solids (TSS). For each section, quantiles $Q_{0.05}$–$Q_{0.95}$ were calculated for the retrieved concentrations of CDOM and TSS to estimate Nelson/Hayes runoff mixing. The location of Hudson Bay within Canada is shown in the inset, along with Nelson River (dark grey) and Hayes River (red) drainage basins, Lake Winnipeg, and Manitoba (sky blue).

3.2.2. In situ CDOM and TSS measurements

Surface water samples for CDOM and TSS analysis were collected from 40 stations in the NHR estuary onboard a barge launched from the M/V Strait Signet from August 7 to 12, 2006 (except August 11, 2006; Figure 3.2; Table S3.1). Water samples filtered through a 0.7-μm Whatman 25-mm glass fiber filter were scanned for CDOM spectral absorption in the 275–800 nm wavelength range using an Ocean Optics S2000 spectrophotometer equipped with 10-cm long quartz cuvettes. Light transmittance (T) through the samples was converted to absorbance spectra (A) using Equation 3.1.

$$A = -\log_{10}(T) \tag{3.1}$$

After baseline correction at 685 nm (Babin et al., 2003), the raw absorbance spectra were converted to spectral absorption coefficients using the following equation:

$$a_{CDOM}(\lambda) = \ln(10) \times \frac{A_{CDOM}(\lambda)}{d} \tag{3.2}$$

where a_{CDOM} is the CDOM spectral absorption coefficient (m^{-1}) at a wavelength λ (nm). A_{CDOM} is the CDOM absorbance (unitless fraction), and d is the path length (m) of the cuvette (0.1 m) used for the spectrophotometric measurements. Finally, the CDOM absorption spectra were modeled using Equation 3.3 to obtain the spectral absorption coefficient at 412 nm, $a_{CDOM}(412)$, and the exponential slope, *S*, between 300 and 600 nm (Bricaud et al., 1981).

$$a_{CDOM}(\lambda) = a_{CDOM}(412) \times e^{-S(\lambda-412)} \tag{3.3}$$

The CDOM absorption at the 412-nm reference wavelength was used in this study to measure CDOM when describing water properties.

TSS (mg L^{-1}) was determined by filtering a known volume of the water sample through pre-weighed 0.7-μm Whatman glass fiber filters (47 mm in diameter). After filtration, the filters were rinsed three times with Milli-Q water to remove salt particles. The processed filter papers were oven-dried at 105°C for 24 hours. After drying, the filters were placed in a desiccator to cool to room temperature and weighed. This process was repeated three times to ensure complete moisture loss. The difference between pre- and post-filtering dry weights, divided by the filtered water volume, provided the TSS (Van der Linde, 1998).

These in situ data were used to determine empirical relationships between CDOM and TSS and water surface remote sensing reflectance (Section 3.2.3) to enable satellite-based retrieval for NHR runoff characterization.

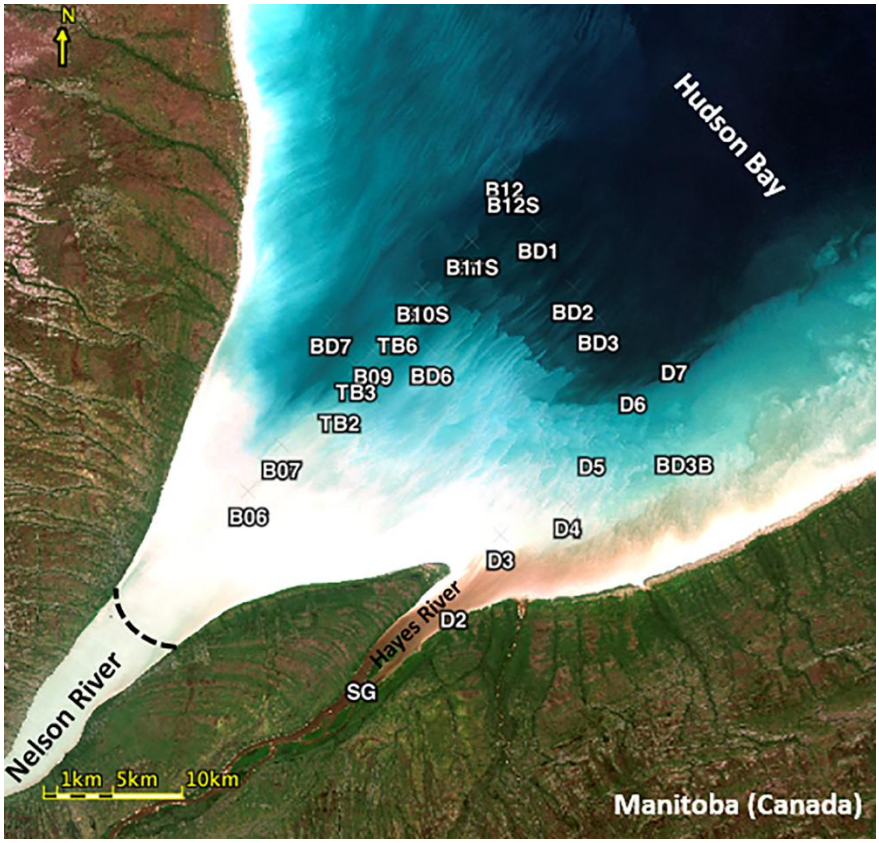


Figure 3.2. The Red-Green-Blue (RGB) image of the European Space Agency's Sentinel-2A satellite (August 6, 2016; 10-m spatial resolution) shows reflective turbid waters of Nelson River and dark waters of Hayes River rich in chromophoric dissolved organic matter (CDOM). In situ sampling stations of CDOM and total suspended solids (TSS) are denoted by their names. The dashed line represents the approximate location of the Nelson River fresh surface layer; the fresh surface layer of the Hayes River is located around Silver Goose (SG; Manitoba Hydro, 2014).

3.2.3. Remote sensing

In situ spectral remote sensing reflectance, $R_{rs}(\lambda)$, the ratio of outgoing spectral radiance to incident spectral solar irradiance, was measured at 12 stations on August 8–9, 2006 (Table S3.1) using an Analytical Spectral Device FieldSpec 4. Surface water was sampled simultaneously for water quality analysis. Optical sampling was carried out continuously at a 1.4-nm bandwidth over the wavelength range of 400–900 nm. The incident irradiance was measured using a calibrated Spectralon panel (placed horizontally) with known reflectance properties. Radiance was recorded at 2- or 4-second intervals using a 15° fore-optic positioned vertically downwards, about 2 m from the barge and 2 m above water, switching between over-water and over-panel (Spectralon) at five observation intervals. The R_{rs} spectrum calculated for each station is the median of at least 25 over-water observations from this series. These spectra were corrected for sun-glint using the similarity-spectrum-based approach of Ruddick et al. (2006). They were the first and, so far, the only available in situ remote sensing dataset collected for the NHR estuary region.

A blue (488 nm) to red (667 nm) R_{rs} band ratio (i.e., MODIS bands 10 and 13) was used to formulate an empirical relationship with in situ CDOM absorption at 412 nm using a non-linear regression approach (Doxaran et al., 2005; Campanelli et al., 2017):

$$a_{CDOM}^{\text{in situ}}(412) = 2.21 \left[\frac{R_{rs}^{\text{in situ}}(488)}{R_{rs}^{\text{in situ}}(667)}\right]^{-1.24} \quad (3.4)$$

Following Nechad et al. (2010), non-linear empirical relationships were established for TSS retrieval using a single red band of R_{rs} 667 nm:

$$TSS^{\text{in situ}} = 5.49 \exp\left[53.31\, R_{rs}^{\text{in situ}}(667)\right] \quad (3.5)$$

The fits of the data to these two relationships are shown in Figures 3.3a and b, respectively. These simple empirical relationships (Equations 3.4 and 3.5) were used to retrieve CDOM and TSS from geolocated Moderate Resolution Imaging Spectroradiometer (MODIS) images (on NASA's Earth Observing System Aqua and Terra satellites). Level 1A radiance to R_{rs} conversion was carried out using the Management Unit of the North Sea Mathematical Models (MUMM) atmospheric correction module (Ruddick et al., 2000). This conversion was performed using the l2-gen processor of NASA's SeaDAS image processing platform. The cloud-albedo threshold of 0.40 was

used in the l2-gen processor instead of the default 0.20 to avoid flagging of highly reflective turbid waters of the NHR estuary as cloud pixels (Matsuoka et al., 2016). A match-up analysis, centered on station locations, was performed to assess the retrieval efficacy of the empirical relationships, yielding 15 match-up points with <2-hour differences between in situ sampling and satellite overpasses.

Thirty-three clear-sky and ice-free MODIS scenes obtained for August over the 2000–2010 period (Table S3.2) were used in this study for the NHR plume characterization. Clear-sky and ice-free scenes were available for August of each year, except in 2004, when mobile ice floes were present at the NHR estuary. Consequently, 2004 August was excluded from the analysis. As Equations 3.4 and 3.5 were formulated based on August in situ R_{rs} alone, this study focuses exclusively on this month to limit uncertainty arising from variations in the solar incidence angle, the presence of sea ice, and the paucity of in situ observations.

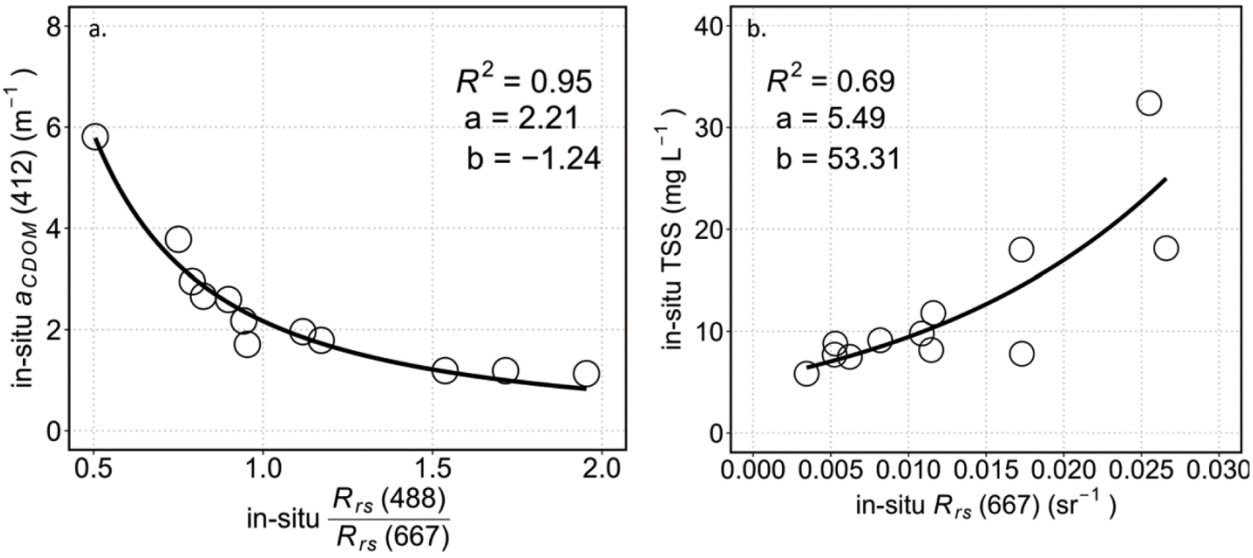


Figure 3.3. a. Power-law relationship between in situ absorption of chromophoric dissolved organic matter at 412 nm, a_{CDOM} (412), and the blue (488 nm) to red (667 nm) remote sensing reflectance (R_{rs}) band ratio and b. exponential relationship between in situ total suspended solids

(TSS) and R_{rs} at 667 nm. The annotated a and b values in the figures represent regression coefficients, as shown in Equations 3.4 and 3.5.

3.2.4. Satellite-derived river runoff distribution and directionality

Distributions of CDOM and TSS were derived from satellite imagery within an area extending 500 km offshore from the undiluted river water in the Nelson River mouth (57.07°N, 92.51°W; Figure 3.1; dashed line in Figure 3.2). The salinity within this region ranges from 0 to approximately 29 based on field observations (Granskog et al., 2007, 2009; Granskog, 2012; Guéguen et al., 2016). With the river mouth as the point of origin, the study domain was divided into circular sections 10 km wide (Figure 3.1). The initial section was set to 50 km from the river mouth to avoid the hydrodynamic complexity near the river mouth and a data gap in the available satellite images. For each section, quantile concentrations for the 5%–95% probability range ($Q_{0.05}$–$Q_{0.95}$) of CDOM and TSS were retrieved (e.g., Figure 3.4).

Building on the work of Gangloff et al. (2017) on turbid plume thresholding, this study extends the use of $Q_{0.95}$ asymptotes (red lines in Figure 3.4) to partition river and marine surface waters in southwestern Hudson Bay using a quantile range. The $Q_{0.95}$ asymptotes (hereafter "threshold") represents the concentration of the most CDOM- or TSS-rich offshore waters of southwestern Hudson Bay. Pixels with CDOM or TSS below this threshold are considered offshore marine waters with less than 5% possible river influence. Water with CDOM or TSS above the threshold is defined as belonging to the ROFI.

We used the threshold to estimate the dilution of NHR discharge as a function of distance from the river mouth. The quantile values equalling the threshold for each circular section were determined for CDOM and TSS. For example, in Figure 3.4c, the threshold line crosses the $Q_{0.50}$ values in the section located approximately 110 km from the river mouth. Thus, at 110 km from the NHR mouth, 50% of CDOM exceeds the threshold (i.e., $\frac{0.50}{0.95}$ or 0.53 marine water fraction). Therefore, we calculate a river-influenced water fraction of $1 - \frac{0.50}{0.95}$ or 0.53 at 110 km. Similar calculations were performed for all semi-circular sections within the CDOM and TSS imagery to model the dispersion of river CDOM/TSS-influenced waters. These satellite images corresponded to three daily discharge conditions: low discharge (LD; 1500–4200 $m^3\ s^{-1}$), mid

discharge (MD; >4200–6500 $m^3 s^{-1}$), high discharge (HD; >6500–9000 $m^3 s^{-1}$), and tidal stages (flood and ebb).

The NHR discharge data were obtained from Manitoba Hydro at the Long Spruce generating station. Tidal stages in MODIS images were determined from the Canadian Hydrographic Service's modeled water level data. Based on a current speed of 3 m s^{-1} for the Nelson River (Wang et al., 2012), the water discharged from Long Spruce station was estimated to take approximately 15 hours to flow the 162 km distance to the NHR estuary. Therefore a minimum of 2-day-averaged discharge of NHR was used for correlation studies involving the river-influenced water fraction (0.50, 0.25, and 0.00) and their corresponding $a_{CDOM}^{Q_{0.95}}$ and TSS.

Finally, the NHR runoff directionality was derived in two steps. First, the bearing of each pixel (within the study domain) from the Nelson River mouth was determined. The weighted mean bearing for each semi-circular section was calculated from these values after binning at 3° within each section. CDOM representing its riverine fraction, i.e., corrected for the marine background using $Q_{0.95}$ thresholds (Equation 3.6), was used as the weight parameter. Negative values of $a_{CDOM}^{river}(412)$ indicated pure marine pixels were precluded as weights for estimating the NHR plume direction.

$$a_{CDOM}^{river}(412) = a_{CDOM}(412) - a_{CDOM}^{Q_{0.95}\,threshold}(412) \quad (3.6)$$

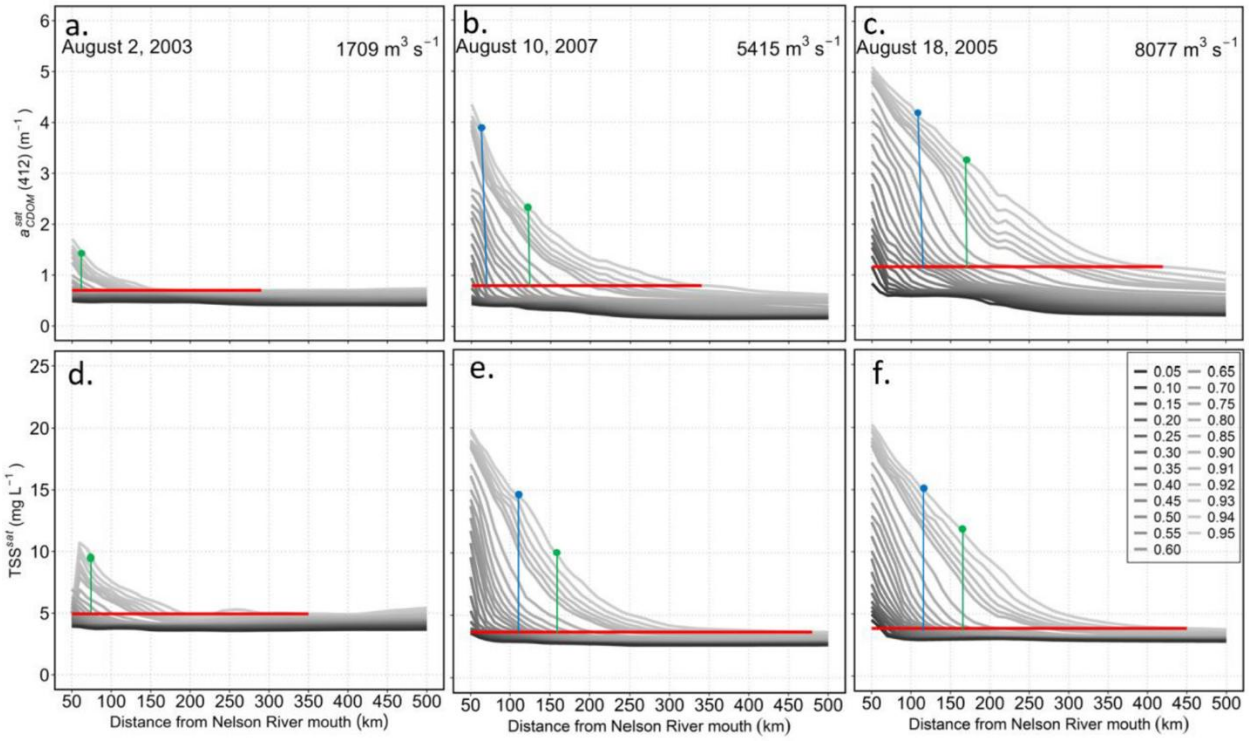


Figure 3.4. Quantile concentrations $Q_{0.05}$–$Q_{0.95}$ of satellite-retrieved a–c. absorption of chromophoric dissolved organic matter, a_{CDOM} (412), and d–f. total suspended solids (TSS) for three different types of daily Nelson and Hayes river (NHR) discharge into Hudson Bay. The red lines represent the $Q_{0.95}$ thresholds, which represents marine waters with the highest CDOM or TSS. Concentrations below the threshold represent water in the offshore domain. Distance corresponding to 50% and 75% dilution of the CDOM and TSS values at the river mouth are represented by blue and green lines, respectively.

3.3. Results and discussion

3.3.1. In situ CDOM and TSS versus salinity gradient

Higher values of CDOM (a_{CDOM} (412), range of 1.07–7.69 m^{-1}) were measured in the estuarine samples near the Hayes River mouth compared to the Nelson River estuary (0.72–5.99 m^{-1}; Figure 3.5a). The Hayes River drains through peat bogs of Northern Manitoba, which are a source of high CDOM (Rosenberg et al., 2005). At the confluence zone of the rivers (salinity of 19–20), a_{CDOM} (412) dropped to 1.04–1.5 m^{-1}, while a minimum of 0.72 m^{-1} was observed beyond a

salinity of 20 (coastal waters). These CDOM trends along the salinity gradient were consistent with those reported by Guéguen et al. (2011), which also reported that Hayes River samples had 1.19 times more CDOM (at 355 nm) than the Nelson River estuary.

Coastal waters of Hudson Bay have been reported to have a mean CDOM (at 355 nm) of 1.81 m^{-1} at a salinity of 27, with values around 2 m^{-1} for southern Hudson Bay (Granskog et al., 2007), which are equivalent to 0.61 m^{-1} and 0.68 m^{-1} at 412 nm, respectively (calculated using Equation 3.3 and $S_{250–400}$ = 0.019 nm^{-1}). These values are consistent with our minimum observed in the coastal waters of southwestern Hudson Bay.

Xi et al. (2013) reported Hudson Bay mean summer and fall a_{CDOM} (412) to be around 0.24 m^{-1} and 0.25 m^{-1}, respectively (calculated using $S_{350–500}$ = 0.019 nm^{-1} and 0.0174 nm^{-1}). For comparison, the Mackenzie River, draining into the southern Beaufort Sea, had a_{CDOM} (412) values within the range of 0.03–1.89 m^{-1} (calculated using $S_{400–800}$ = 0.02 nm^{-1}; Matsuoka et al., 2011). CDOM in the Mackenzie River contributed to 94% of the total non-water absorption at 412 nm (Bélanger et al., 2008). Such a range of CDOM absorption was also observed in European coastal waters (Babin et al., 2003). Therefore, coastal a_{CDOM} (412) (0.72–7.69 m^{-1}; $S_{300–600}$ = 0.0176 nm^{-1}) of southwestern Hudson Bay was comparable to that of the Arctic and European coastal waters, highlighting the regional and global applicability of NHR runoff studies.

The mean (± standard deviation) TSS was higher for the Nelson River estuary samples (12.42 ± 13 mg L^{-1}, n = 26) than in the Hayes River (6.67 ± 3.71 mg L^{-1}, n = 14), with a maximum of 67 mg L^{-1} and 16 mg L^{-1}, respectively (Figure 3.5b). Around the river confluence zone and beyond, a mean TSS of 9 mg L^{-1} and 5 mg L^{-1} was observed for Nelson and Hayes rivers, respectively. Compared to the Hayes River, which drains entirely through the Shield watershed, the Nelson is a much larger river (about 6× greater discharge) with a watershed that extends beyond the Shield into the sedimentary Interior Plains. Moreover, Nelson River remains affected by bank erosion from large impoundments and diversion projects supporting hydroelectric generation (Environment Canada and Department of Fisheries and Oceans, 1992; Rosenberg et al., 2005; Goharrokhi et al., 2022).

Published TSS measurements in Hudson Bay are scarce. Xi et al. (2014) reported that the highest inorganic particle load in Hudson Bay was observed in coastal waters near the Nelson River

estuary. TSS maxima of 2.5 mg L^{-1} and 1.8 mg L^{-1} were observed in Hudson Bay in September 2005 and July 2010, respectively, with mean values of 0.74 mg L^{-1} and 0.55 mg L^{-1} (Xi et al., 2013). However, this study excluded the estuarine TSS values of the Nelson River. The TSS minimum (3 mg L^{-1}) measured in the coastal waters of southwestern Hudson Bay closely matches the fall maximum reported by Xi et al. (2013). Seasonal variability of TSS inside the Nelson River estuary peaks during the spring freshet, with turbidity measurements of 500 NTU (272 mg L^{-1}), decreasing in late summer to 200 NTU (88 mg L^{-1}; Wang et al., 2012). The turbidity-equivalent TSS was calculated empirically using a linear slope of 0.61 mg L^{-1} NTU^{-1} and a bias of 35 mg L^{-1} (personal communication from Greg McCullough).

Both CDOM and TSS were diluted at increasing salinity (Figure 3.5). While there were enough samples (n = 26) to suggest the power-law decay of Nelson River CDOM (R^2 = 0.81), the data points from Hayes River showed a linear decay (R^2 = 0.93; Figure 3.5a). (We use "decay" in its mathematical sense, and not to imply chemical decay.) Since Nelson River had a lower CDOM relative to Hayes River, it decayed relatively faster (0.72 m^{-1} $salinity^{-1}$) than Hayes River CDOM (0.39 m^{-1} $salinity^{-1}$). This enhanced decay rate might be attributed to the higher hydrodynamic forcing of the larger Nelson River. Guéguen et al. (2016) found that CDOM photodegradation decreases with increasing salinity. Therefore, in the context of this study, CDOM with salinity >20 will be least affected by photodegradation and can thus serve as a conservative tracer of river water. Such conservative mixing of CDOM in the coastal waters of Hudson Bay was also reported by Granskog et al. (2007).

Similarly, for TSS, a higher decay rate was observed for the Nelson River (0.83 mg L^{-1} $salinity^{-1}$; R^2 = 0.58) than for the Hayes River (0.34 mg L^{-1} $salinity^{-1}$; R^2 = 0.33; Figure 3.5b). The higher standard deviation of TSS samples suggests greater variability in the particulate domain, indicating non-conformance with a single source. It is well known that suspended solids are not generally conservative tracers of freshwater flowing into marine waters. They will tend to settle out as sediment transport capacity decreases, and, particularly in estuaries, the finer particles will tend to flocculate, forming larger particles marked by higher settling velocities (e.g., Kranck, 1984; Burban et al., 1989; Manning et al., 2010; Bainbridge et al., 2012; Many et al., 2016). Moreover, sediment dynamics in the Nelson and Hayes estuary are complicated by wave and tidal erosion of widespread mudflats, which provide an additional source brought into suspension by

turbulence in the fluvial-marine mixing zone (inset in Figure 3.5b). Hence, the non-conservative nature of TSS decay with increasing salinity in the NHR estuary (Figure 3.5b) limits TSS's value as a river runoff tracer in our study area.

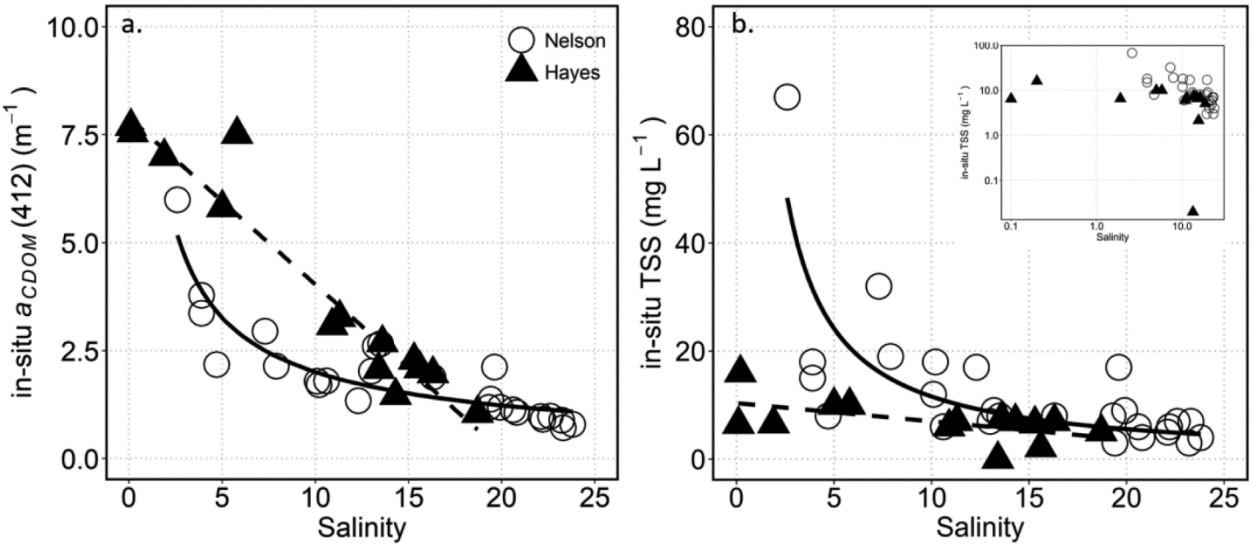


Figure 3.5. a. The decrease of in situ absorption of chromophoric dissolved organic matter, a_{CDOM} (412), with salinity along the Nelson River transect was best described with the power-law fit, shown by the solid line, while the higher a_{CDOM} (412) along the Hayes River transect underwent a linear decrease, shown by the dashed line. b. Similar trends were observed for total suspended solids (TSS), where the higher TSS of the Nelson River transect decreased faster than TSS along the Hayes River transect, described by fits like those for CDOM. The inset figure on a logarithmic scale highlights TSS suspension in the Nelson River estuary and TSS settling in the coastal waters (salinity >20) of Hudson Bay. Hayes River TSS settles within the Nelson River plume at a salinity between approximately 15 and <20.

3.3.2. Evaluation of optical relationships

Because of reduced ice cover in Hudson Bay, which led to higher evaporation of surface waters, an increase in cloud cover over southern Hudson Bay was recorded for 1998–2018 (Fazel-Rastgar, 2020). The frequent cloud cover poses a significant challenge to obtaining cloud-free optical satellite data and matchups with the only in situ data in our study area during late summer. Nevertheless, of the 40 in situ data points collected on August 7–12, 2006, 28 were available

(excluding the 12 data points from August 8 and 9 used to formulate the empirical relationships) for the retrieval assessment of the empirical optical relationships (Equations 3.4 and 3.5).

A single clear-sky MODIS satellite image was obtained for each day between August 7 and 10, 2006 (no sampling occurred on August 11, and no cloud-free images were obtained for August 12; Table S3.2). Among the 21 in situ data points (excluding the 7 data points of August 12, 2006), stations D5, D6, and D7 of August 7, 2006, and B10, B11, and B12 of August 8, 2006, were precluded from the matchup analysis, as these points were sampled beyond the ±2-hour time frame of satellite data acquisition. The choice of this timeframe for matchup analysis was based on the study by Bailey and Werdell (2006) and accounted for the approximate 12-hour tidal period observed for the Nelson River. Therefore, 15 data points were used to validate the optical algorithm.

The satellite-retrieved a_{CDOM} (412) (a_{CDOM}^{sat} (412); Equation 3.3) agreed well with the in situ observations (R^2 = 0.74; slope = 0.60; Figure 3.6a), despite the interfering presence of high TSS. The root-mean-square error (RMSE) of 1.11 m^{-1} accounts for the intercept of 0.51 m^{-1}. The linear statistical relationship for TSS (Equation 3.4) was weaker than for a_{CDOM} (412) with R^2 of 0.69 and slope of 0.23, possibly due to its higher spatial-temporal variability caused by estuarine TSS dynamics (settling, resuspension, lateral flow; Figure 3.6b). The high y-intercept of 7.13 mg L^{-1} can account for a higher RMSE of 12.34 mg L^{-1}, which may be due to the low variability in the TSS training data set (not subject to spatial-temporal misfits between optical and water quality data). Also, some combination of spatial resolution bias of satellite sensors, uncertainty in atmospheric correction approaches (Dorji and Fearns, 2017), and the TSS retrieval algorithm itself (Balasubramanian et al., 2020) might cause retrieval errors.

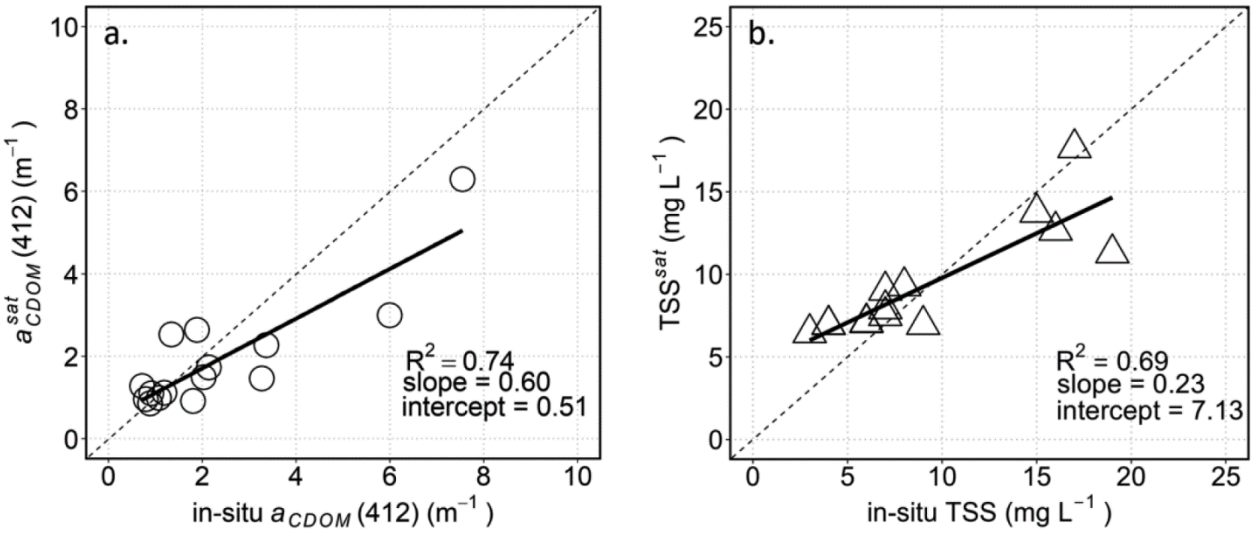


Figure 3.6. a. The blue to red band ratio retrieved absorption of chromophoric dissolved organic matter, a_{CDOM} (412), with higher accuracy (Equation 3.4) and b. lower accuracy was obtained for total suspended solids (TSS) using a single red band (Equation 3.5). The black solid and dashed lines represent regression fits and 1:1 scatter line, respectively.

3.3.3. Dilution of a_{CDOM} (412)

The river CDOM-influenced water fraction (hereafter *RCWF*), estimated from a^{sat}_{CDOM} (412), based on the quantile statistics (Section 2.4) obtained for each semi-circular section (Figure 3.1), decreased exponentially with increasing distance from the Nelson River mouth (Figure 3.7a). The exponential decay constants (b_{CDOM}; km^{-1}) were calculated using the following equation:

$$RCWF = e^{-b_{CDOM} \times d} \quad (3.7)$$

where d is the distance (km) from the Nelson River mouth. The modeled b_{CDOM} in Equation 3.7 correlated negatively with daily discharge ranging from 1500 to 9000 m^3 s^{-1} (Figure 3.8a), indicating that the NHR plume expanded offshore with increasing discharge. Therefore, instances with higher discharge were marked by extended offshore limits relative to the lower discharges shown by the black contours in Figures 3.9a, c, and e. For all 33 images, the mean extent of 0.50 and 0.25 *RCWF* (i.e., at 50% and 75% river CDOM dilution) was 88 km and 125 km, respectively (Table 3.1).

Moreover, the offshore depletion of CDOM covaried positively with NHR discharge (Figure 3.8b), mainly observed for the 50% and 75% attenuation of the river CDOM values (e.g., Figure 3.4a–c). This trend showed that NHR discharge contributes significantly to CDOM in southwestern Hudson Bay.

However, only 13% of the variability of a_{CDOM} (412) could be explained by b_{CDOM} variability (Figure 3.8c). As b_{CDOM} and a_{CDOM} (412) were functions of NHR discharge, their discharge-based normalizations were warranted. The variability of discharge-normalized CDOM ($a'_{CDOM} = \frac{a_{CDOM}(412)}{Q}$; s m^{-4}) in ROFI accounted for 67% variance ($p < 0.001$) of discharge-normalized b_{CDOM} ($b'_{CDOM} = \frac{b_{CDOM}}{Q}$; s km^{-1} m^{-3}; Figure 3.8d). Furthermore, together with NHR discharge (Q), b'_{CDOM} variability explained about 79% of variance ($p < 0.001$; Equation 3.8).

$$b'_{CDOM} = -\alpha \cdot Q + \beta\, a'_{CDOM} + \varepsilon \quad (3.8)$$

where α and β are regression coefficients of Q and a'_{CDOM} respectively, and ε is the constant. In a simplified way, a'_{CDOM} is an inverse measure of CDOM load (discharge volume × CDOM). Therefore, the offshore decrease in CDOM is influenced by both the CDOM load and the hydrodynamic forcing associated with NHR discharge. Thus, from Equation 3.8, one can conclude that high NHR discharges will substantially load the coastal waters of southwestern Hudson Bay with increased volumes of CDOM. This river water disperses relatively farther into the bay, as indicated by the reduced decay rate of CDOM (b_{CDOM}) and a high $Q_{0.95}$ CDOM threshold (offshore CDOM maximum; Figure 3.9e).

Similarly, modeled b_{CDOM} for flood and ebb tidal flows correlated negatively with Q (Figure 3.10a and b) and vice versa for CDOM (Figure 3.10c and d). An enhanced rate of b_{CDOM} was obtained for flood tide relative to ebb tidal flow, resulting in reduced extents of river CDOM-influenced waters in coastal Hudson Bay (Table 1; Figure 3.9g). For 100% dilution, ebb tidal-dilution rate and CDOM correlated strongly with NHR discharge (Figure 3.10a and c) and vice versa for flood tidal flows (Figure 3.10b and d). The tidal stage of the images, represented in terms of hours remaining until the next high tide, was not a statistically significant parameter in describing the variability of b'_{CDOM}, possibly an artifact of spring and neap water level variation influencing CDOM dilution.

3.3.4. Dilution of TSS

The turbid water fraction (hereafter *TWF)* in southwestern Hudson Bay, estimated from TSS^{sat}, also decayed exponentially with increasing distance from the Nelson River mouth (Figure 3.7b).

$$TWF = e^{-b_{TSS} \times d} \quad (3.9)$$

However, unlike b_{CDOM}, b_{TSS} was poorly and non-significantly correlated with Q, except for 0.25 *TWF*, which was statistically significant (Figure 3.11a). This trend was reflected in the invariant *TWF* extents estimated for the different discharge conditions (Figures 3.9b, d, and f; Table 3.1).

Similarly, TSS was also poorly and non-significantly correlated with the NHR discharge (Figure 3.11d). Therefore, the traced TSS was not exclusively of riverine origin. Significant suspension of sediment is known to occur within the NHR estuary due to shallow bathymetry and the presence of mudflats (Figure 3.5b; Wang et al., 2012). Also, finer particles are flocculated into larger particles as river water enters the marine domain with relatively higher salinity, leading to an enhanced settling rate, as observed in Figure 3.5b. These factors contributed to the poor, non-significant correlation with river discharge, which was also observed for ebb tides (Figures 3.11b and e) and flood tides (Figures 3.11c and f). Reduced turbid plume extents and lower TSS were estimated for flood tides, unlike CDOM (Figure 3.9h; Table 3.1).

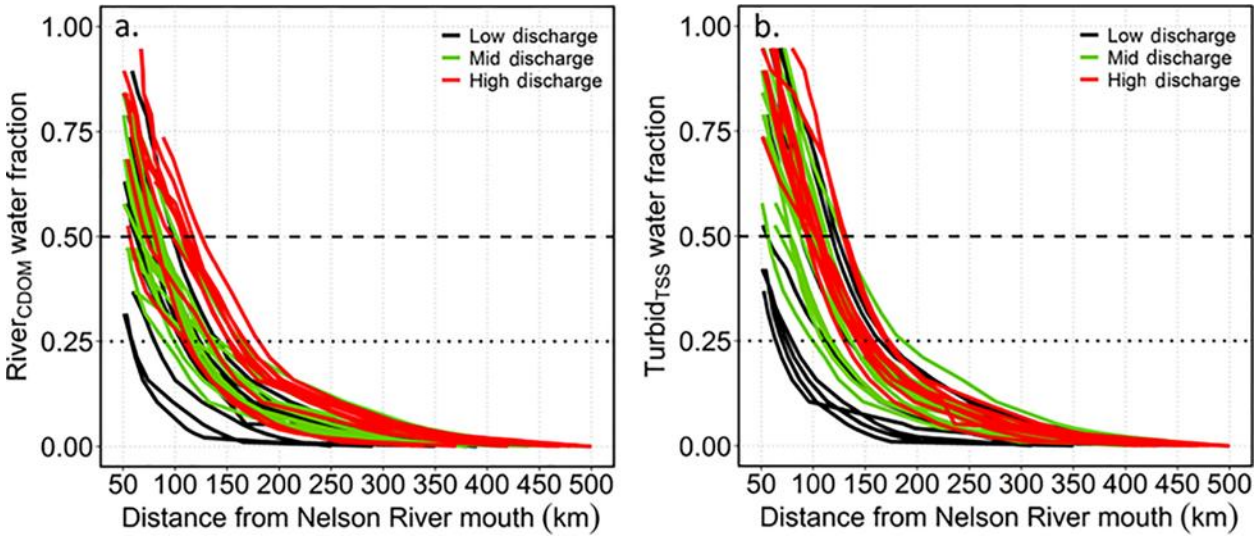


Figure 3.7. Satellite-derived river-influenced a. absorption of chromophoric dissolved organic matter (a_{CDOM}) at 412 nm and b. total suspended solids (TSS) in southwestern Hudson Bay with increasing distance from the mouth of the Nelson River. The river water fraction is separated for three daily discharge conditions: low (1500–4200 $m^3 s^{-1}$), mid (>4200–6500 $m^3 s^{-1}$), and high (>6500–9000 $m^3 s^{-1}$). The dashed lines and dotted lines show the estimated 50% dilution (0.50 river CDOM/TSS water fraction) and 75% dilution (0.25 river CDOM/TSS water fraction) of river water with seawater, respectively.

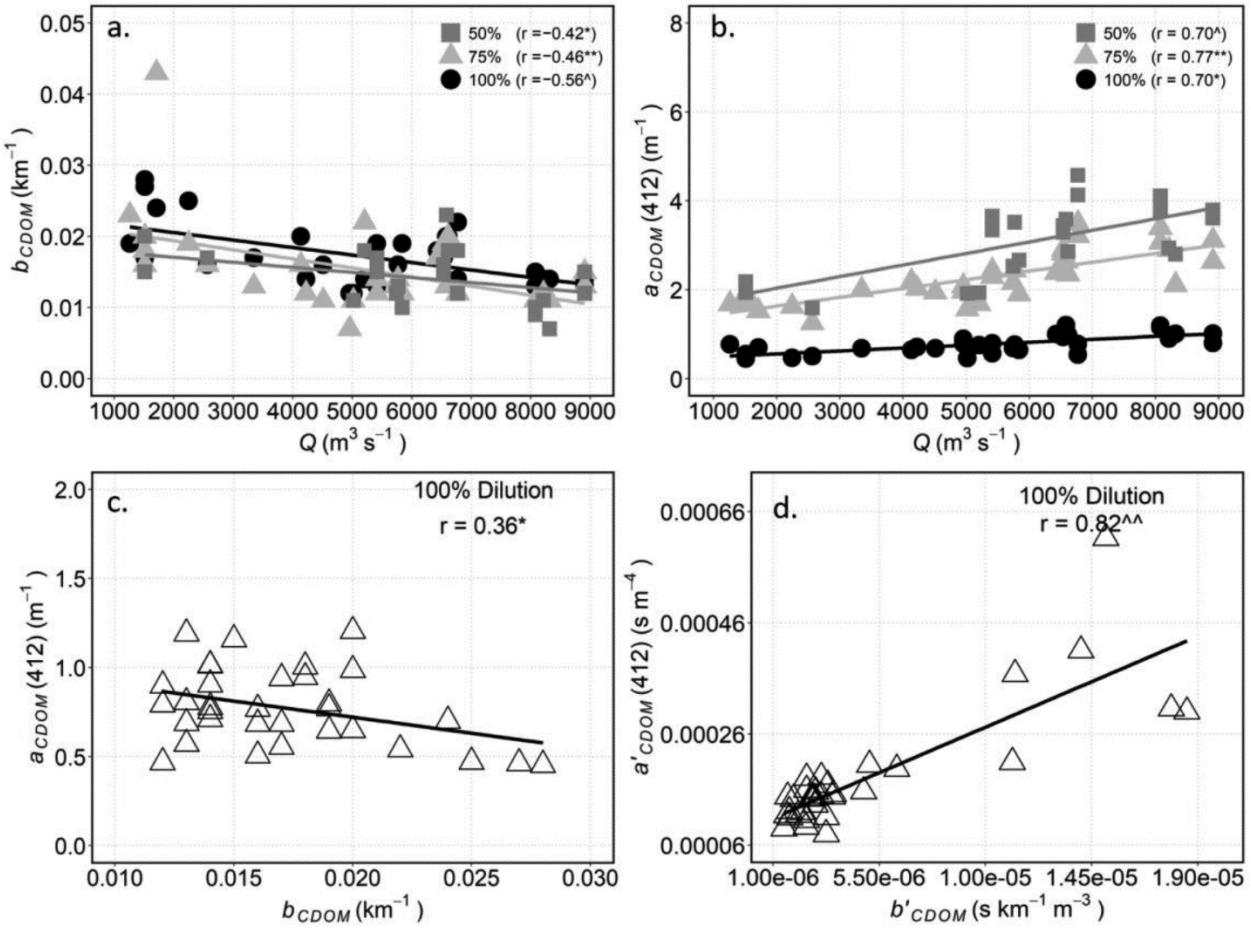


Figure 3.8. a. Variability in the decay rate of absorption of chromophoric dissolved organic matter, a_{CDOM} (412), with daily Nelson/Hayes river (NHR) discharge, Q; b. variability of a_{CDOM} (412) with NHR discharge; (c) co-variability trend of the a_{CDOM} (412) decay rate (b_{CDOM}) and a_{CDOM} (412), shown by a solid black line; and (d) co-variability trend of the NHR discharge-normalized a_{CDOM} (412) decay rate (b'_{CDOM}) and discharge-normalized a_{CDOM} (412) (a'_{CDOM} (412)), shown by a solid black line. Dark grey squares, light grey triangles, and black circles in panels a and b represent data points corresponding to 50%, 75%, and 100% decay, respectively, of river CDOM values for each image. Lines in panels a and b, color-coded to 50%, 75%, and 100% decay of river CDOM values, represent the trends of the variability of CDOM decay rate and concentration with discharge. Inset symbols *, **, ^, and ^^ represent statistical significance at $p \leq 0.5$, 0.01, 0.001, and 0.0001, respectively.

Table 3.1 Mean values of decay rate, extent, and concentration of satellite-retrieved absorption of chromophoric dissolved organic matter (a_{CDOM}) at 412 nm and total suspended solids (TSS)

	a_{CDOM} (412) dilution (%)						**TSS dilution (%)**					
	50			**75**			**50**			**75**		
Scenarios[a]	***b*[b]**	**E[c]**	**C[d]**	***b*[b]**	**E[c]**	**C[d]**	***b*[b]**	**E[c]**	**C[e]**	***b*[e]**	**E[c]**	**C[e]**
LD	0.017	81	1.93	0.02	101	1.77	0.013	98	16.6	0.019	116	13.39
MD	0.014	79	2.92	0.014	123	2.2	0.012	94	15.6	0.015	138	12.55
HD	0.014	99	3.62	0.013	150	2.89	0.013	107	16.7	0.014	152	13.27
FT	0.017	76	3.18	0.018	109	2.27	0.012	94	15.4	0.017	127	12.34
ET	0.013	94	2.99	0.014	134	2.28	0.013	103	16.7	0.015	142	13.44
All	0.014	88	3.05	0.015	125	2.28	0.013	99	16.2	0.016	136	13.02

[a] Low discharge (LD), mid discharge (MD), high discharge (HD), flood tide (FT), and ebb tide (ET).

[b] Slope (km^{-1}).

[c] Extent (km).

[d] Concentration (m^{-1}).

[e] Concentration ($mg\ L^{-1}$).

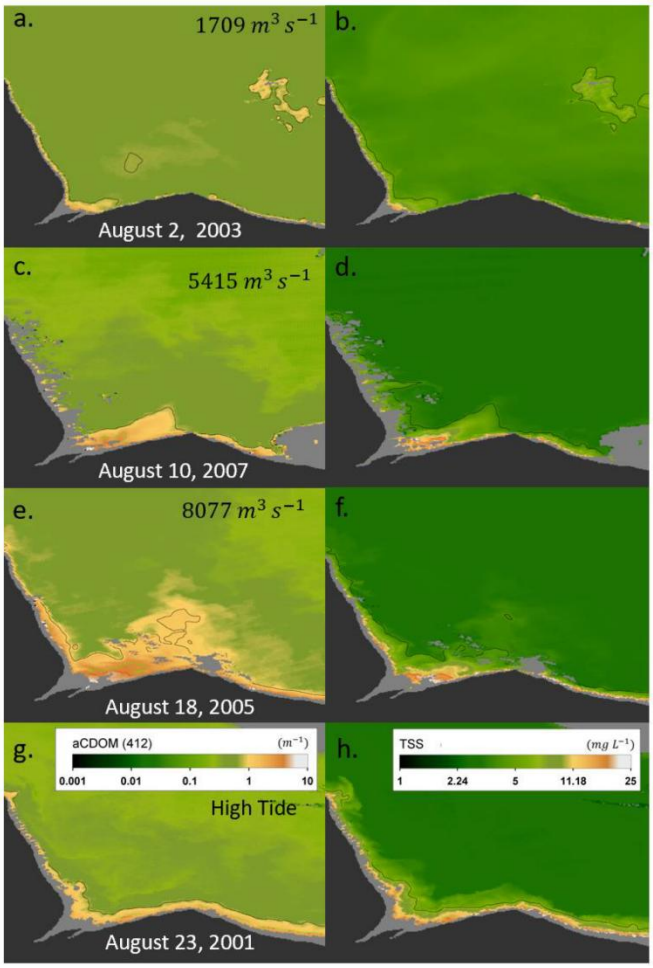


Figure 3.9. Satellite-derived images of chromophoric dissolved organic matter and total suspended solids in southwestern Hudson Bay. Moderate resolution imaging Spectroradiometer (MODIS)-derived images of river-influenced (a, c, e, g) absorption of colored dissolved organic matter, a_{CDOM} (412), and b, d, f, h total suspended solids (TSS) at extents of 50%, 75%, and 100% dilution (represented by red, green, and black contours, respectively) for (a and b) low discharge, (c and d) mid discharge, (e and f) high discharge, and (g and h) high tide. Panels a–f also represent the extent of ebb tidal flow. The grey shading denotes the region flagged for shallow water pixels.

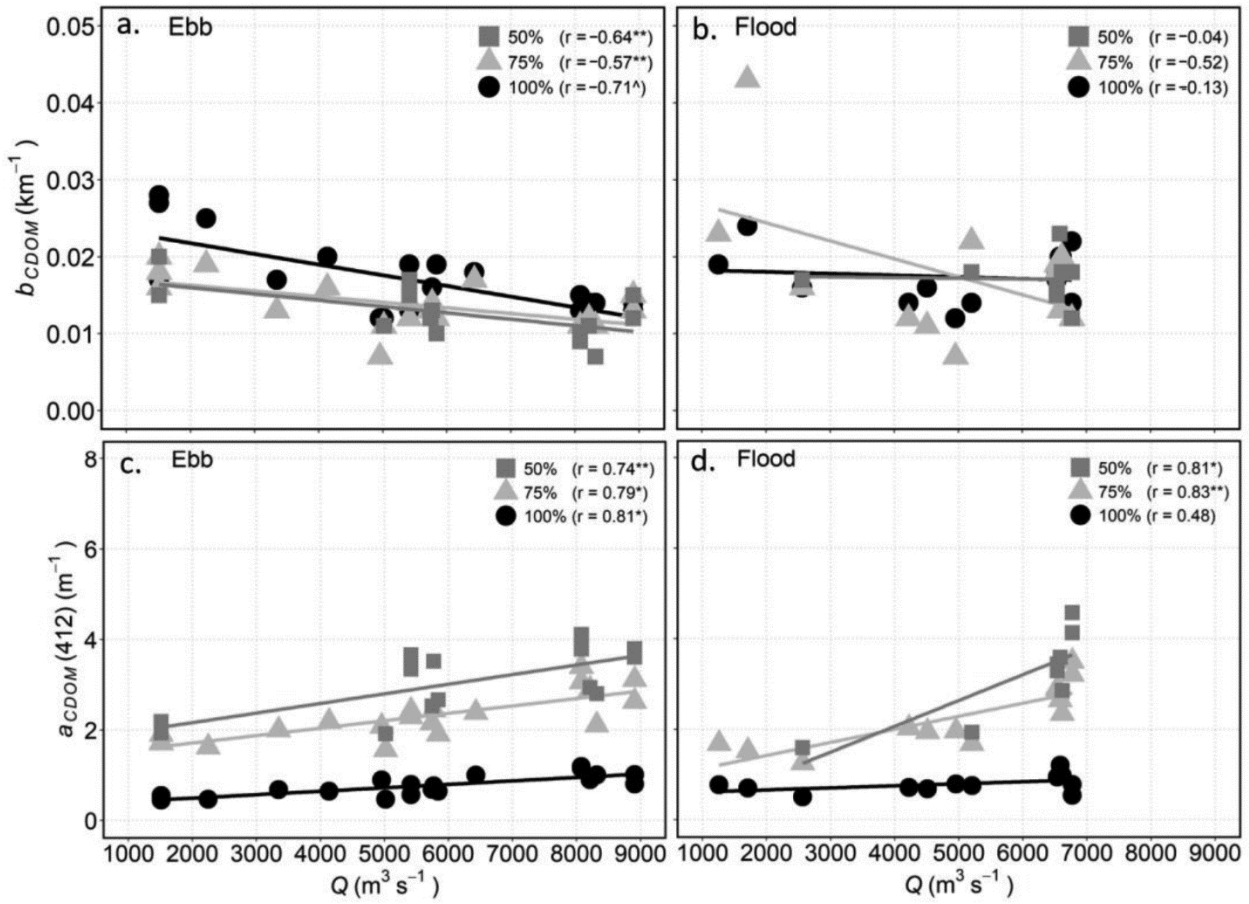


Figure 3.10. Variability of the decay rate constant, b_{CDOM}, for satellite-retrieved absorption of chromophoric dissolved organic matter, a_{CDOM} (412), and its concentration as a function of discharge during (a and c) ebb tidal flow and (b and d) flood tidal flow. Dark grey squares represent data points corresponding to 50% decay of river-a_{CDOM} (412) values corresponding to 10 flood and 12 ebb tide images. Light grey triangles, and black circles represent data points corresponding to 75%, and 100% decay, respectively, of river-a_{CDOM} (412) values corresponding to 16 flood and 18 ebb tide images. Lines color-coded to 50%, 75%, and 100% decay of river-a_{CDOM} (412) values represent the trends of the variability of a_{CDOM} (412) decay rate and concentration with discharge. Inset symbols *, **, ^, and ^^ represent statistical significance at $p \leq 0.5$, 0.01, 0.001, and 0.0001, respectively.

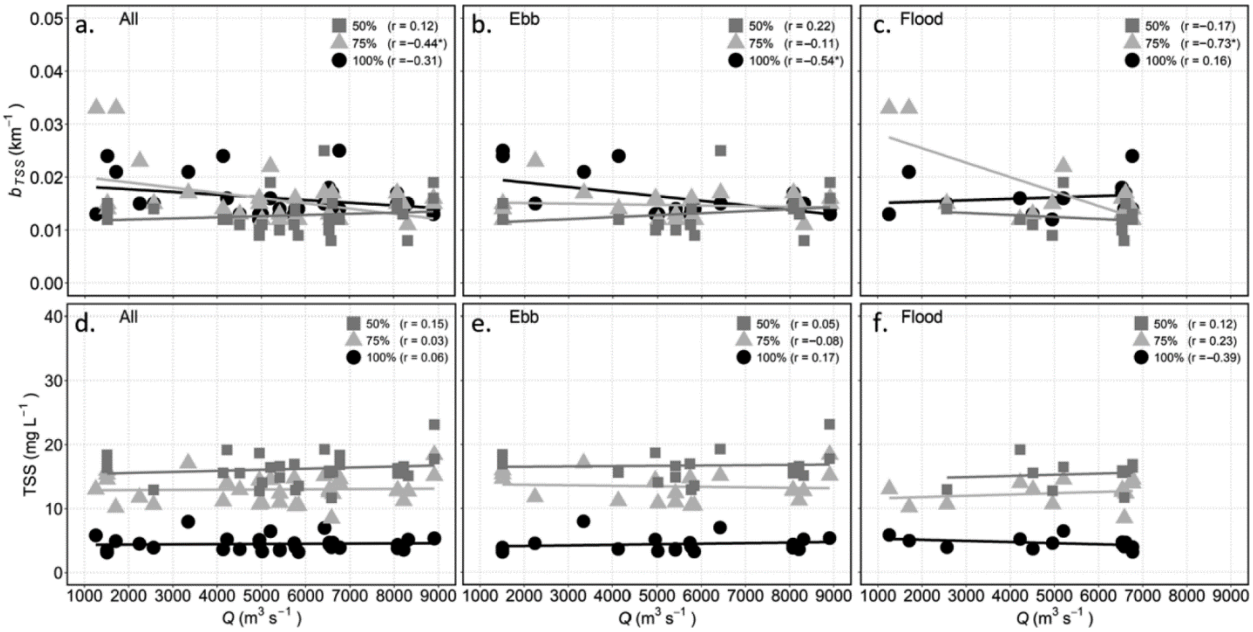


Figure 3.11. Variability of the total suspended solids (TSS) decay rate, b_{TSS}, with Nelson/Hayes daily river discharge, Q, for a. all 33 satellite images used in this analysis, b. ebb tide images, and c. flood tide images. Variability of TSS concentration with Q for d. all 33 images, e. ebb tide images, and f. flood tide images. The dark grey squares, light grey triangles, and black circles represent data points corresponding to 50%, 75%, and 100% decay, respectively, of river TSS values for each image. Lines color-coded to 50%, 75%, and 100% decay of river TSS values represent the trends of the variability of TSS decay rate and concentration with discharge. Inset symbols *, **, ^, and ^^ represent statistical significance at $p \leq 0.5$, 0.01, 0.001, and 0.0001, respectively.

3.3.5. River plume directionality and wind

Once the NHR plume extents have been calculated, providing a spatial estimate of ROFI, the determination of their flow direction seeks to understand river water transport pathways in southwestern Hudson Bay. The NHR river waters propagated offshore with a mean azimuth of 54° from the river mouth (Figure 3.12a), that is, closely following the southern shore of Hudson Bay. However, an overall range of 3–85° was observed within $a_{CDOM}^{river}(412)$ azimuths for the semi-circular sections (Figure 3.12b). This range suggests that NHR waters often flowed straight into the bay and also propagated southeast towards James Bay. Thus, 0.25 and 0.50 RCWF, marked by

higher $a_{CDOM}(412)$, aligned along the southern coast of Hudson Bay, while the NHR plume threshold was relatively offshore (Figure 3.12c). Therefore, the role of winds was envisaged to explain this variability as a function of atmospheric vorticity (Dmitrenko et al., 2020).

The averages of the 33 NHR plume azimuth (*Az*) ranged from 36° to 67°. Northerly (184°) and anticyclonic (clockwise; relative vorticity ($\overline{rv}$) = $-1.8e^{-6}$ s^{-1}) winds, obtained from ERA5, prevailed in southwest Hudson Bay. The zonal and meridional winds were predominantly easterly ($\bar{u}$ = −4.1 m s^{-1}) and southerly (= 0.34 m s^{-1}) with a mean wind speed of 5 m s^{-1}. Three classes of *rv* were obtained for 33 images: strong anticyclonic wind ($\overline{rv} = -5.3e^{-6}$ s^{-1}), weak anticyclonic wind ($\overline{rv} = -1.3e^{-6}$ s^{-1}, and cyclonic wind ($\overline{rv} = 8.2e^{-6}$ s^{-1}). Strong and weak anticyclonic winds were classified based on the mean negative *rv*.

Table 3.2 shows that the most angular $\overline{Az}$ was associated with cyclonic winds (Figure 3.12a). The cyclonic (anticlockwise) wind rotation generates a cyclonic oceanic gyre, which forces offshore waters towards land through Ekman pumping (Dmitrenko et al., 2021), forcing the NHR water eastward along the southern shore of Hudson Bay. A strong, significant ($p < 0.001$) relationship was obtained between *Az* and intensified clockwise wind rotation (Figure 3.13a). Such wind reversal reverses the flow direction of the oceanic gyre, carrying onshore waters towards central Hudson Bay (Ridenour et al., 2019a). The offshore displacement of NHR water lowers the plume azimuth (Table 3.2; Figure 3.12a). With the reduction in the intensity of anticyclonic wind rotation, the plume azimuth became relatively shoreward, though NHR water still made its way into central Hudson Bay (Table 3.2; Figure 3.12a). Under the prevailing anticyclonic wind regime, this effect was observed from the mean plume azimuth of all 33 images (Figures 3.12a and b).

The shoreward plume deflection during cyclonic winds was associated with strengthened southerly meridional winds (Figure 3.13b), while stronger easterly zonal winds accompanied by higher wind speeds resulted in the offshore displacement of the NHR waters (Figures 3.13c and d; Table 3.2). Such exchange of river water with central Hudson Bay was reported by St-Laurent et al. (2011) and Granskog et al. (2009). Also, wind-induced plume transport occurs beyond Cape Tatnam (approximately 110 km from the Nelson River mouth) with a riverine regime preceding it (Figure 3.12a), suggesting the role of coastal geometry in NHR plume propagation.

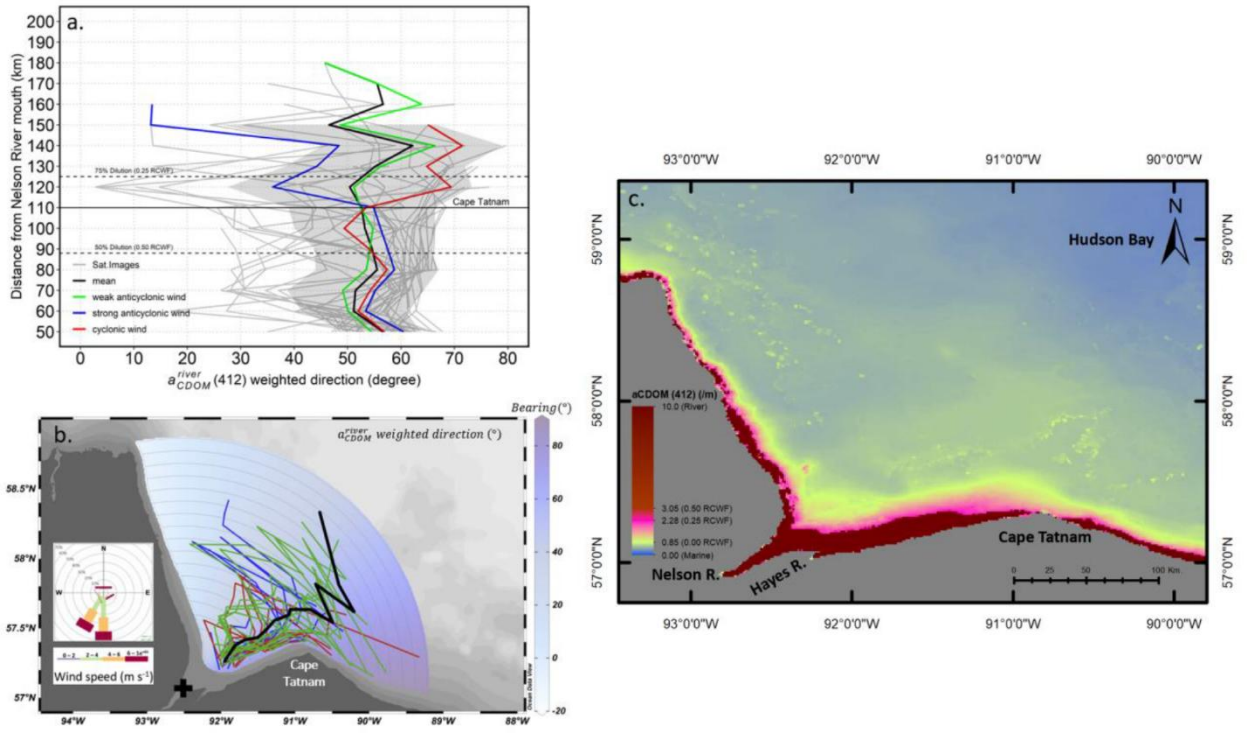


Figure 3.12. a. River plume directions measured as a weighted function of satellite-retrieved river-water absorption of chromophoric dissolved organic matter, $a^{river}_{CDOM}(412)$ for different wind regimes based on relative wind vorticity. The grey shading represents plume direction within one standard deviation. In both panel a. and b., the red, green, and blue lines represent mean plume direction for cyclonic, weak, and strong anticyclonic winds, respectively; the black line denotes the mean plume direction. b. The plus symbol represents the Nelson River mouth, serving as the reference for the calculation of pixel bearings. Each grey circular line corresponds to the distance from the freshest point of 10-km width, with the first line at approximately 50 km from the river mouth. Dominant wind direction with speed is shown in the inset. c. Mean satellite-retrieved absorption coefficient of colored dissolved organic matter (a_{CDOM}) at 412 nm for 50% (0.50 *RCWF*), 75% (0.25 *RCWF*), and 100% (0.00 *RCWF*) dilution of the Nelson and Hayes river CDOM values, where *RCWF* stands for river-influenced CDOM water fraction.

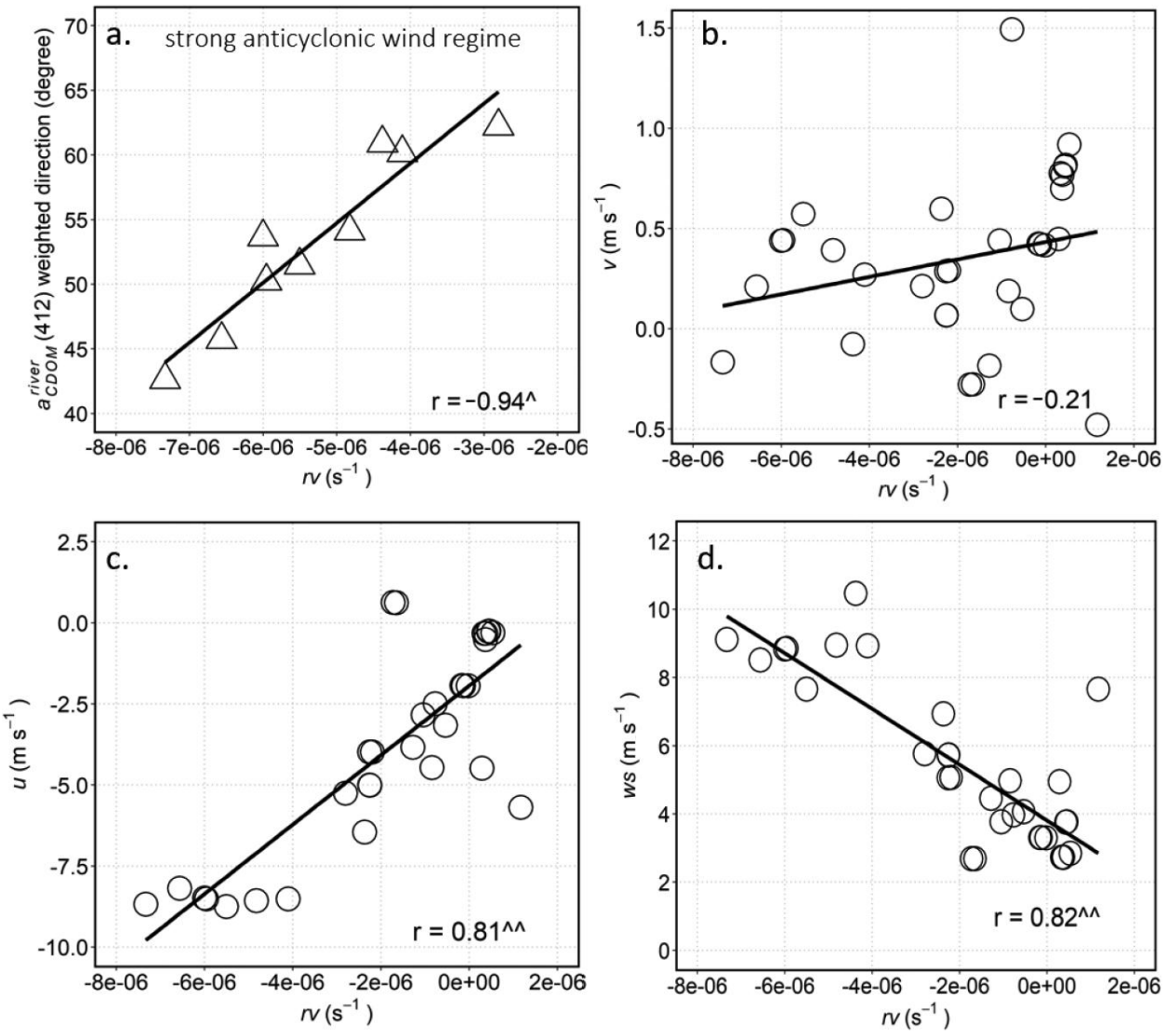


Figure 3.13. a. Shoreward plume direction, based on satellite-retrieved river-water absorption of chrmophoric dissolved organic matter, $a_{CDOM}^{river}(412)$ was associated with lower relative vorticity (*rv*) and vice versa. b. Weak meridional southerly winds (*v*), c. strong easterly zonal winds (*u*), and d. high wind speeds (*ws*) were associated with strong anticyclonic wind regime. Inset symbols *, **, ^, and ^^ represent statistical significance at $p \leq 0.5$, 0.01, 0.001, and 0.0001, respectively.

Table 3.2. Mean $a_{CDOM}^{river}(412)$)-weighted direction (*Az*), relative vorticity (*rv*), zonal wind speed (*u*), meridional wind speed (*v*), wind direction (wd) and speed (ws) for different wind regimes, along with correlation coefficients[a] between wind metrics and plume direction in brackets

Wind regime[b]	***Az* (°)**	***rv* (s^{-1})**	***u* (m s^{-1})**	***v* (m s^{-1})**	**wd (°)**	**ws (m s^{-1})**
SA	53	-5.3×10^{-6} [−0.94^]	−8.35 [−0.22]	0.26 [0.08]	151.48 [0.29]	8.57 [−0.18]
WA	54	-1.3×10^{-6} [0.44*]	−3.05 [0.75**]	0.27 [0.48]	195.71 [0.54*]	4.34 [0.75**]
CYC	60[c]	8.2×10^{-7} [0.07*]	−1.46 [−0.16]	0.55 [−0.15]	195.91 [0.29]	3.77 [−0.25]

[a] Where * indicates $p \leq 0.05$; **, $p \leq 0.01$; and ^, $p \leq 0.001$.

[b] Strong anticyclonic (SA), weak anticyclonic (WA), and cyclonic (CYC).

[c] Excluding flood tide.

3.4. Conclusion

Dispersion of the Nelson and Hayes river plume from the Nelson River estuary into southwestern Hudson Bay was investigated using satellite-derived chromophoric dissolved organic matter and total suspended solids. The quantile concentration of CDOM and TSS ($Q_{0.05}$–$Q_{0.95}$) declined exponentially with distance from the river mouth. Based on paired in situ salinity and $a_{CDOM}(412)$ observations, $a_{CDOM}^{sat}(412)$ and its dilution over the distance from the Nelson River mouth correlated well to NHR discharge and river water fraction. So, within the NHR plume, the defined $a_{CDOM}^{river}(412)$ influenced water fraction decayed exponentially with distance. Higher river discharge was associated with higher $a_{CDOM}^{sat}(412)$ in the inner plume region, an extended offshore boundary, and a higher offshore CDOM maximum. The river water was diluted by about 75% at 125 km, ranging ±25 km due to discharge variability and ±35 km during the greatest flood and ebb tides.

Based on pixel bearings of maximum $a_{CDOM}^{sat}(412)$ in each quantile, wind vorticity contributes significantly to the NHR plume direction in Hudson Bay. Clockwise winds carry the NHR plume towards central Hudson Bay, while anticlockwise winds force alongshore eastward transport. Such geostrophic river water transport occurs elsewhere in the Arctic (Proshutinsky et al., 2009; Giles et al., 2012; Morison et al., 2012; Carmack et al., 2015).

Unlike CDOM, TSS did not correlate significantly with NHR discharge. Hence, the offshore TSS maximum corresponds to the turbid plume boundary, distinct from the NHR CDOM and river water plume boundary. The turbid plume carries sediments sourced from nearshore mudflats and/or bank erosion, as well as from the NHR watershed, and is reduced by settling. That is, TSS in southwestern Hudson Bay is not a conservative tracer of river water and, in any case, is not solely sourced from the NHR. Hence, TSS is disregarded as an optical tracer of NHR water dispersion. Nevertheless, because both CDOM and TSS exhibit similar absorption characteristics across the visible spectrum, the distribution of TSS needs to be understood so that CDOM retrieval from satellite images can account for its signature.

Due to time constraints and logistical difficulties, field measurements of Arctic estuaries are limited to a few transects throughout the freshwater-marine salinity gradient. These measurements are influenced by river discharge, tidal, wind, and ocean background current variability (Horner-Devine et al., 2015). We have demonstrated a novel satellite-based quantile regression approach for analyzing complex two-dimensional river water dispersion into the ocean at an estuary/coastal scale, thereby addressing these issues.

Arctic and sub-Arctic river runoff is expected to increase due to increasing precipitation driven by climate change (Gagnon and Gough, 2002; Peterson et al., 2002; Serreze et al., 2006; Haine et al., 2015; Carmack et al., 2016; McCrystall et al., 2021). Our plume-mapping approach can compensate for the scarcity of in situ data and advance our understanding of how river plume dynamics respond to increasing freshwater discharge into Arctic, sub-Arctic, North Atlantic, and European coastal waters.

Further studies on CDOM persistence and residence time are necessary to support integrating the time dimension into river plume tracking via CDOM dilution. Furthermore, due to the poor quality

of sea surface brightness temperatures near landmasses, satellite-based sea surface salinity products such as ESA Soil Moisture and Ocean Salinity (SMOS) are not well suited for estuaries and nearshore waters (Oliva et al., 2012; Martín-Neira et al., 2016). Thus, a salinity data gap across the land-ocean continuum prevents continuous, synoptic river plume tracking from space. By adopting this technique based on the CDOM-salinity relationship, salinity can be mapped in nearshore waters, thereby addressing estuarine and coastal salinization and desalinization and informing coastal management. Space-based mapping of river water mixing with seawater aims to deliver on the Ocean Decade Challenges 1 and 2 (https://oceandecade.org/challenges/) and Sustainable Development Goal 14 of the United Nations.

Data availability

Primary remote sensing dataset: Level 1 MODIS Terra and Aqua were obtained from NASA EODIS LAADS DAAC.

Primary wind dataset: ERA5 reanalyzed hourly wind data were acquired from Copernicus ECMWF.

Secondary dataset: In situ CDOM, TSS, salinity, remote sensing data, have been provided as supplemental material Excel files listed under Supplemental material in the web-version of the paper.

Supplementary materials

Table S3.1. List of in situ sampling stations, time and date of sampling, tidal flow stage, and optical application for algorithm development and matchup

Station	Location	Latitude (°)	Longitude (°)	Date and Time (CST)	Tidal flow	Optical Use
D3	Hayes	-92.13	57.09	2006 Aug 07 15:01	Ebb	Matchup
D5	Hayes	-92.02	57.15	2006 Aug 07 16:40	Ebb	Unused
D6	Hayes	-91.97	57.19	2006 Aug 07 18:40	Ebb	Unused
D7	Hayes	-91.92	57.21	2006 Aug 07 17:40	Ebb	Unused
B06	Nelson	-92.43	57.12	2006 Aug 08 12:58	Ebb	Matchup
B07	Nelson	-92.39	57.15	2006 Aug 08 12:04	Ebb	Algorithm
B08	Nelson	-92.33	57.18	2006 Aug 08 10:42	Ebb	Algorithm
B09	Nelson	-92.28	57.21	2006 Aug 08 09:54	Flood	Unused
B10	Nelson	-92.22	57.25	2006 Aug 08 08:55	Flood	Unused
B11	Nelson	-92.16	57.28	2006 Aug 08 08:20	Flood	Unused
B12	Nelson	-92.12	57.33	2006 Aug 08 15:03	Ebb	Matchup
TB2	Nelson	-92.32	57.18	2006 Aug 08 13:38	Ebb	Matchup
TB3	Nelson	-92.3	57.2	2006 Aug 08 13:46	Ebb	Matchup
TB6	Nelson	-92.25	57.23	2006 Aug 08 14:03	Ebb	Matchup
B09	Nelson	-92.27	57.22	2006 Aug 09 16:20	Ebb	Algorithm
B12	Nelson	-92.12	57.33	2006 Aug 09 11:36	Ebb	Algorithm
BD1	Coastal	-92.08	57.29	2006 Aug 09 12:04	Ebb	Algorithm
BD2	Coastal	-92.04	57.25	2006 Aug 09 12:34	Ebb	Algorithm
BD3	Coastal	-92.01	57.23	2006 Aug 09 13:01	Ebb	Algorithm
BD4	Coastal	-92.06	57.81	2006 Aug 09 14:39	Ebb	Algorithm
BD6	Coastal	-92.21	57.21	2006 Aug 09 15:48	Ebb	Algorithm
BD7	Coastal	-92.33	57.23	2006 Aug 09 16:44	Ebb	Algorithm
B10S	Nelson	-92.22	57.25	2006 Aug 09 13:21	Ebb	Matchup
B11S	Nelson	-92.16	57.28	2006 Aug 09 12:40	Ebb	Matchup
D5	Hayes	-92.02	57.15	2006 Aug 09 14:09	Ebb	Algorithm

D6	Hayes	-91.97	57.19	2006 Aug 09 14:29	Ebb	Algorithm
B12S	Nelson	-92.11	57.32	2006 Aug 09 11:46	Ebb	Matchup
B12	Nelson	-92.11	57.32	2006 Aug 10 12:00	Ebb	Matchup
BD1	Coastal	-92.08	57.29	2006 Aug 10 12:43	Ebb	Matchup
BD2	Coastal	-92.04	57.26	2006 Aug 10 13:36	Ebb	Matchup
BD3	Coastal	-92.01	57.23	2006 Aug 10 14:16	Ebb	Matchup
BD3B	Coastal	-91.91	57.15	2006 Aug 10 15:39	Ebb	Matchup
D6	Hayes	-91.961	57.189	2006 Aug 10 14:58	Ebb	Matchup
D5	Hayes	-92.02	57.153	2006 Aug 12 13:10	Ebb	Unused
D6	Hayes	-91.964	57.187	2006 Aug 12 13:29	Ebb	Unused
D7	Hayes	-91.916	57.214	2006 Aug 12 13:51	Ebb	Unused
D2	Hayes	-92.187	57.052	2006 Aug 12 11:52	Flood	Unused
D3	Hayes	-92.131	57.086	2006 Aug 12 12:17	Flood	Unused
D4	Hayes	-92.057	57.109	2006 Aug 12 12:41	Flood	Unused
SG	Hayes	-92.297	57.006	2006 Aug 13 10:36	Flood	Unused

Table S3.2. List of satellite data used for Nelson/Hayes River plume dispersion study, and discharge type, tidal flow, and wind regime

Discharge Type	MODIS Data	Tidal flow	Wind Regime	Optical Application
Low[a]	T2000232172500	Flood	CYC[d]	Plume
Low	A2002232184000	Low	WA[e]	Plume
Low	T2002217173500	Ebb	SA[f]	Plume
Low	A2003234175500	Low	WA	Plume
Low	A2003234193500	Low	WA	Plume
Low	T2003214181000	Flood	SA	Plume
Low	T2003215171500	Flood	SA	Plume
Low	T2003218174500	Low	SA	Plume
Low	T2003228164500	Flood	WA	Plume
Low	T2003234174500	Ebb	WA	Plume
Mid	T2000231182000	High	WA	Plume
Mid[b]	T2001226180500	Ebb	SA	Plume
Mid	T2001235180000	Flood	CYC	Plume
Mid	A2006217180500	Low	WA	Plume
Mid	A2006236183500	Ebb	CYC	Plume
Mid	T2006236164500	High	CYC	Plume
Mid	A2007222193000	Ebb	SA	Plume
Mid	T2007221170000	Ebb	SA	Plume
Mid	T2007222174000	Ebb	SA	Plume
Mid	A2008224185000	Low	CYC	Plume
Mid	T2010222165000	Ebb	SA	Plume
High[c]	A2005230180000	Ebb	WA	Plume
High	A2005230194000	Ebb	WA	Plume
High	A2005233183000	Ebb	WA	Plume
High	A2005234173500	Ebb	WA	Plume
High	A2005242182500	Ebb	WA	Plume
High	T2005242164000	Ebb	WA	Plume

High	A2009238191500	Flood	CYC	Plume
High	A2009239182000	Flood	CYC	Plume
High	T2009239180500	Flood	CYC	Plume
High	T2009240171000	Flood	CYC	Plume
High	A2007231192500	Flood	WA	Plume
High	T2007231173500	Flood	WA	Plume
Mid	A2006219175000	Ebb	-	Matchup
Mid	A2006220183500	Ebb	-	Matchup
Mid	A2006221174000	Ebb	-	Matchup
Mid	A2006222182000	Ebb	-	Matchup

[a] Low-: 1500-4200 $m^3 s^{-1}$.

[b] Mid: > 4200-6500 $m^3 s^{-1}$.

[c] High: > 6500–9000 $m^3 s^{-1}$.

[d] CYC: Cyclonic wind regime.

[e] WA: Weak anti-cyclonic wind regime.

[f] SA: Strong anti-cyclonic wind regime.

4. Chapter – Satellite data trace seasonal freshwater dispersion in Hudson and James Bays

This chapter was published in the peer-reviewed journal *Geophysical Research Letters*. The citation for this manuscript is:

Basu, A., Bélanger, S., Kuzyk, Z. Z. A., Singh, R. K., Mukherjee, S., Larouche, P., Guzzi, A. C., Ausen, E. L., McCullough, G., & Ehn, J. K. (2026). Satellite data trace seasonal freshwater dispersion in Hudson and James Bays. *Geophysical Research Letters*, *53*(2), e2025GL116442. https://doi.org/10.1029/2025GL116442

Abstract

Freshwater dispersal controls stratification, circulation, and biogeochemical processes in Hudson and James Bay (HJB); however, limited field observations hinder understanding of how different freshwater types drive change. This study uses the Aqua-Moderate Resolution Imaging Spectroradiometer and the Soil Moisture and Ocean Salinity-Microwave Imaging Radiometer using Aperture Synthesis data to distinguish and map river water (RW) and sea-ice melt (SIM), the two main freshwater types in HJB. Satellite-derived RW and SIM agree with in situ tracers, filling field data gaps that support future freshwater research. Higher RW fractions up to 0.40 in southern HJB and a seasonal SIM decline from 0.35 to 0.00 in central HJB match observed patterns. RW spreads offshore in July, contracts in August, and forms a coastal band in September, sustained by cyclonic winds despite reduced discharge. From 2011 to 2019, RW fractions increased (0.0048 yr^{-1}) while SIM fractions declined (−0.003 yr^{-1}) across HJB.

4.1. Introduction

River water (RW) and sea-ice melt (SIM) are the primary freshwater sources in the coastal Arctic, including Hudson and James Bays (HJB, Figure 4.1a), where they influence circulation, stratification, and biogeochemical processes (Deschepper et al., 2023; Prinsenberg, 1986a, 1986b; Ridenour et al., 2019a, 2019b). While salinity quantifies total freshwater, distinguishing RW and SIM contributions requires additional tracers. In the Arctic Ocean and HJB, oxygen isotope ratio ($\delta^{18}O$) combined with salinity distinguishes isotopically light RW from heavy SIM (Ahmed

et al., 2020; Granskog et al., 2011; Kuzyk et al., 2008; Östlund & Hut, 1984). Other tracers, including alkalinity, salinity, and temperature, were used to trace freshwater in HJB (Jones & Anderson, 1994). Several other studies have incorporated, alongside salinity and $\delta^{18}O$, in situ measurements of chromophoric dissolved organic matter (CDOM), as this is an effective tracer of freshwater derived from the CDOM-rich HJB watershed (Évrard et al., 2023; Granskog, 2012; Granskog et al., 2007, 2009; Guéguen et al., 2011, 2016). However, these approaches rely on sparse, late summer ship-based observations, which limit the spatiotemporal assessment of freshwater variability in HJB, despite documentation of opposing trends in river discharge (increasing) and sea ice extent (decreasing) in HJB (Crawford et al., 2021; Feng et al., 2021; McCullough et al., 2019; Tivy et al., 2011).

In contrast to field data, satellite remote sensing offers synoptic and temporal tracing of surface water properties. Satellite-derived sea surface salinity (S^{sat}) supports freshwater monitoring in high latitude seas but cannot distinguish RW from SIM (Supply et al., 2020). In HJB, S^{sat} and altimetry have been used to quantify freshwater stored in sea ice in April (Landy et al., 2017). Here, we combine ocean color observations with S^{sat} to separate CDOM-rich RW from CDOM-poor SIM during summer, similar to an approach applied in the Beaufort Sea (Matsuoka et al., 2016). However, HJB is particularly well suited for satellite-based freshwater tracing due to its large river inflows, high CDOM import and export, seasonal ice cover, shallow bathymetry (<350 m), isolation from other oceans, and large spatial extent (>800,000 km^2) (Martini, 1986; Pelletier, 1986; Figure 4.1a, Text S4.1).

The objectives of the study are the following:

1. Determine RW and SIM fractions in the surface water of HJB during summer using satellite-derived CDOM and S^{sat}, referenced to fractions calculated using in situ (salinity-$\delta^{18}O$) methods.

2. Evaluate satellite-based RW and SIM tracing in HJB by assessing spatial and temporal patterns relative to established trends.

3. Assess seasonal and inter-annual variations of satellite-derived RW and SIM fractions in the surface water of HJB from 2011 to 2019 as a basis for establishing a robust baseline, which could be used to assess change in future decades.

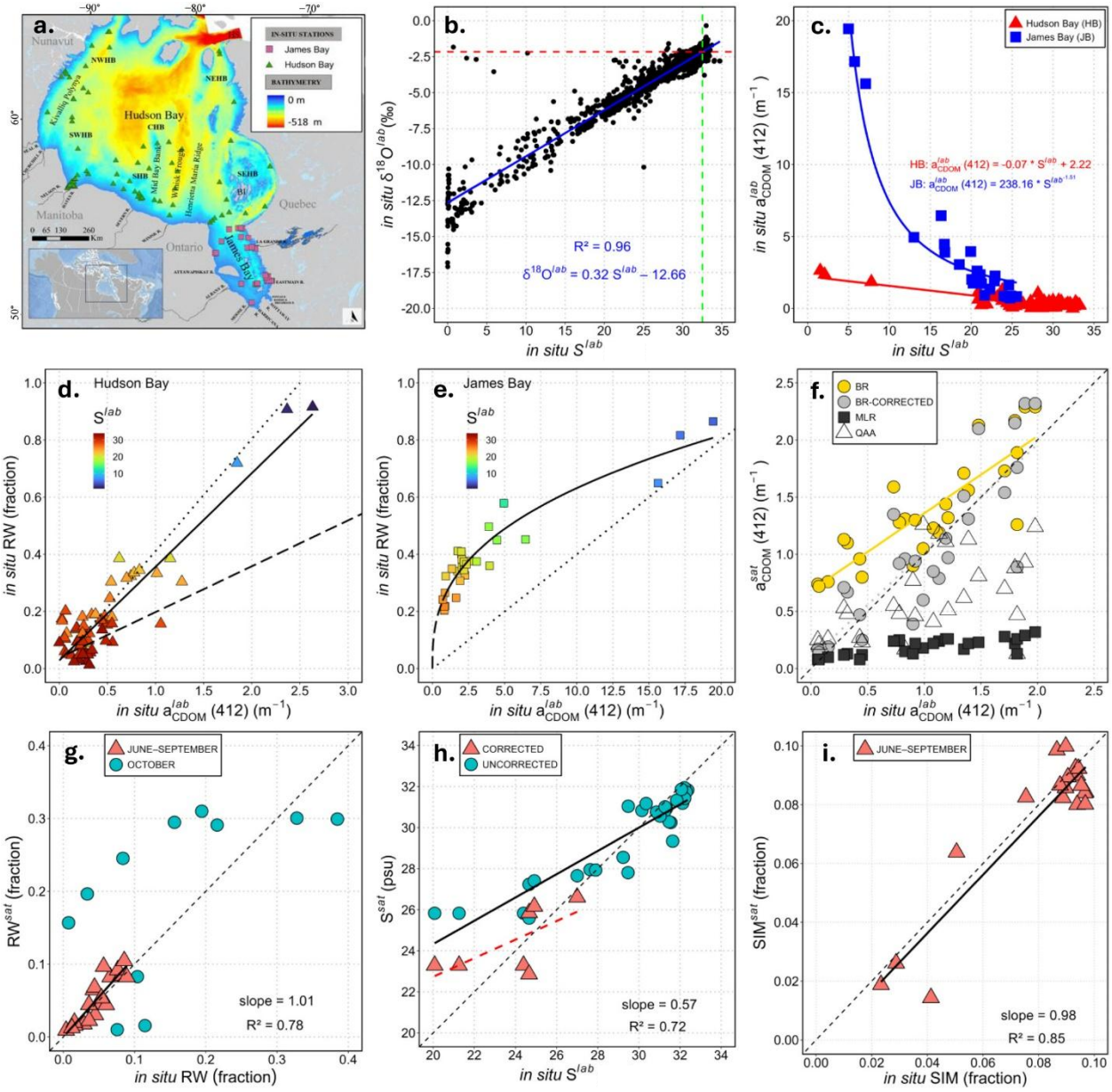


Figure 4.1. a. Hudson and James Bay (HJB) study area showing bathymetry, sampling stations, major rivers, key regions, and features: NWHB, SWHB, SHB, SEHB, and CHB (northwestern,

southwestern, southern, southeastern, and central Hudson Bay [HB]), Belcher Islands (BI), Hudson Strait (HS), Kivalliq Polynya, Mid Bay Bank, Winisk Trough, and Henrietta Maria Ridge. The inset map shows the location of HJB (black square) within Canada. b. Relationship between in situ salinity (S^{lab}) and in situ oxygen isotope ratio ($\delta^{18}O^{lab}$) in HJB. Dashed green and red lines show salinity (32.5) and $\delta^{18}O^{lab}$ (−2.16‰) seawater endmembers, respectively. c. Relationships between in situ colored dissolved organic matter concentration measured at 412 nm, a_{CDOM}^{lab} (412), and in situ S^{lab} in HJB. d. Linear relationship between in situ river water fraction (RW) and in situ a_{CDOM}^{lab} (412) in Hudson Bay (solid black line). Dotted and dashed black lines show mixing using in situ a_{CDOM}^{lab} (412) of 2.5 m^{-1} (this study) and 6.4 m^{-1} (Granskog et al., 2007, 2009) at RW = 1, respectively. e. Non-linear relationship between in situ RW and in situ a_{CDOM}^{lab} in James Bay (solid black and long-dashed curved line extrapolated to zero intercept). Dotted linear line shows mixing using in situ a_{CDOM}^{lab}= 25 m^{-1} at RW = 1. f. Matchup between in situ a_{CDOM}^{lab} (412), and satellite-derived a_{CDOM}^{sat} (412), employing red to blue band ratio, Multiple Linear Regression, and Quasi Analytical Algorithm, v.6 (QAA). The gold line shows fit for a_{CDOM}^{BR} (412) and the gray dotted line shows fit for corrected a_{CDOM}^{BR} (412). g. Matchup between in situ RW fraction and satellite-derived RW^{sat} fraction, with the solid black line showing the fit. h. Matchup between in situ S^{lab} and satellite-derived S^{sat} in HB, with the solid black line showing the fit and the red dashed line showing the corrected S^{sat} fit for $S^{lab} \leq 27$. i. Matchup between in situ sea-ice melt fraction (SIM) and satellite-derived SIM^{sat} fraction, with fit shown by the solid black line. The black diagonal dashed lines in panels f–i indicate the 1:1 fit.

4.2. Data and method

4.2.1. Field data

Surface waters collected from HJB between 2005 and 2021 onboard several cruises (n = 110, Figure 4.1a; Text S4.2) were analyzed in the laboratory for CDOM absorption coefficient at 412 nm (a_{CDOM}^{lab}, m^{-1}; Bricaud et al., 1981), salinity (S^{lab}), and $\delta^{18}O^{lab}$ (‰) (Text S4.2).

Linear relationship between $\delta^{18}O^{lab}$ and S^{lab} (Figure 4.1b, R^2 = 0.91, p < 0.001, $\delta^{18}O^{lab}$ = 0.32 S^{lab} − 12.66) was used to estimate $\delta^{18}O^{lab}$ sea water (SW) endmember. Mass balance Equations 4.1-4.3 were solved for in situ RW, SIM, and SW fractions within each sample, using appropriate S^{lab} and $\delta^{18}O^{lab}$ endmembers (Östlund & Hut, 1984) (Text S4.3).

$$RW + SIM + SW = 1 \quad (4.1)$$

$$RW\ S_{RW} + SIM\ S_{SIM} + SW\ S_{SW} = S^{lab} \quad (4.2)$$

$$RW\ \delta^{18}O_{RW} + SIM\ \delta^{18}O_{SIM} + SW\ \delta^{18}O_{SW} = \delta^{18}O^{lab} \quad (4.3)$$

A Type I regression linked $a_{CDOM}(412)$ with $\delta^{18}O^{lab}$-estimated RW fractions in Hudson Bay (i.e., for stations north of 55°N latitude as shown by Equation 4.4 and Figure 4.1d), and a power law fit described the relationship for James Bay (i.e., for stations south of 55°N latitude as shown by Equation 4.5 and Figure 4.1e).

$$RW = 0.32\ a^{lab}_{CDOM}(412) + 0.02, \text{ when latitude} > 55°N \quad (4.4)$$

$$RW = 0.26\ \left(a^{lab}_{CDOM}(412)\right)^{0.37}, \text{ when latitude} < 55°N \quad (4.5)$$

4.2.2 Satellite Remote Sensing

4.2.2.1 CDOM and River Water Fraction

Satellite-derived CDOM absorption coefficients (a^{sat}_{CDOM} m^{-1}) at 412 nm were obtained using an empirical blue (488 nm) to red (667 nm) remote sensing reflectance (R_{rs}, sr^{-1}) band ratio (BR) (Basu et al., 2023; Doxaran et al., 2005). The red band (667 nm) in BR compensates for suspended solids contamination in the blue band (448 nm), enabling CDOM retrieval (Basu et al., 2023). BR was applied on the NASA Aqua Satellite's Moderate Resolution Imaging Spectroradiometer (MODIS) imagery (n = 1,377 days, 1 km resolution, June–October, 2011–2019). R_{rs} was computed from MODIS Level 1A radiance data and atmospherically corrected using a spectral shape parameter-based algorithm for coastal waters implemented in SeaDAS (Singh & Shanmugam, 2014; Singh et al., 2019).

A match-up analysis between $a^{sat}_{CDOM}(412)$ and $a^{lab}_{CDOM}(412)$ was conducted for 26 stations with a <2-hr difference between satellite overpass and field sampling (Bailey and Werdell, 2006). The match-up analysis revealed a positive bias relative to in situ CDOM, necessitating bias correction using Equation 4.6 (Text S4.4, Table S4.1, and Figure 4.1f).

$$a^{sat}_{CDOM}(412) = 1.39\ a^{BR}_{CDOM}(412) - 0.86 \quad (4.6)$$

Within HJB, the corrected a_{CDOM}^{BR} (Equation 4.6) was used to retrieve satellite-based RW fraction (RW^{sat}), applying Equation 4.7 for pixels >55°N and Equation 4.8 for pixels ≤55°N at 1 km resolution. This regional approach of RW^{sat} retrieval was based on the in situ relationships between a_{CDOM}^{lab} (412) and RW (Equations 4.4 and 4.5, Figures 4.1d and 4.1e).

$$RW = 0.32\ a_{CDOM}^{sat}(412) + 0.02, \text{ when latitude} > 55°N \quad (4.7)$$

$$RW = 0.26\ (a_{CDOM}^{sat}(412))^{0.37}, \text{ when latitude} < 55°N \quad (4.8)$$

Three-day composites of RW^{sat} (to compensate for missing pixels due to cloud and sea ice cover) were validated against concurrent in situ RW fractions from June (n = 11), August (n = 6), September (n = 2), and October (n = 10). The results showed agreement with in situ RW fractions, except for October (Text S4.5 and Table S4.1, Figure 4.1g).

4.2.2.2. Sea surface salinity, freshwater, and sea-ice melt fractions

The Soil Moisture and Ocean Salinity (SMOS) satellite's Microwave Imaging Radiometer using Aperture Synthesis sensor maps sea surface salinity (S^{sat}) using L-band interferometry (1.4 GHz, 21 cm). This study used 3-day-averaged S^{sat} at 25 km resolution from the Barcelona Expert Center (BEC) Arctic-SMOS v3 product (2011–2019; Martínez et al., 2022) to estimate surface freshwater content in HJB. It was validated against S^{lab} from 32 stations (2016, 2018, and 2019) in Hudson Bay, showing good agreement for $S^{lab} > 27$ (Figure 4.1h, Equation 4.9). For $Slab \leq 27$, overestimations in southern and southeastern Hudson Bay required correction using Equation 4.10, obtained from the slope and intercept of the match-up (Figure 4.1h and Table S4.1).

$$S^{sat} = S_{BEC}^{sat}, \text{ when } S_{BEC}^{sat} > 27, \quad (4.9)$$

$$S^{sat} = 1.82\ S_{BEC}^{sat} - 23.7, \text{ when } S_{BEC}^{sat} < 27, \quad (4.10)$$

Satellite-derived surface freshwater fraction (FW^{sat}) of each pixel was estimated from corrected S_{BEC}^{sat} at 25 km resolution:

$$FW^{sat} = 1 - \frac{S^{sat}}{32.5}, \quad (4.11)$$

which is based on the linear relationship between in situ FW (RW + SIM) and S^{lab} (i.e., $FW = 1 - S^{lab}/32.5$). Resampled RW^{sat} was subtracted from FW^{sat} to deduce the SIM fraction (SIM^{sat}) at 25 km resolution:

$$SIM^{sat} = FW^{sat} - RW^{sat}, \quad (4.12)$$

Pixels with unrealistic RW^{sat}, indicated by $-SIM^{sat}$, were excluded, assuming errors were due to retrieval uncertainties, autochthonous CDOM, and brine from sea ice formation. Three-day composites of SIM^{sat} agreed well against concurrent in situ SIM fractions from June, August, and September (Table S4.1, Figure 4.1i).

4.3. Results

4.3.1. In situ CDOM and salinity variability

The surface waters of James Bay had higher a_{CDOM}^{lab} (412) and lower S^{lab} than Hudson Bay, consistent with previous studies (Évrard et al., 2023; Granskog, 2012; Granskog et al., 2007, 2011; Guéguen et al., 2011, 2016) (Table S4.2). Furthermore, regional variability of a_{CDOM}^{lab} (412) and S^{lab} (Text S4.6 and Table S4.2), underscores the role of river discharge and circulation in distributing CDOM across HJB, leading to distinct to S^{lab} relationships in Hudson Bay and James Bay (Figure 4.1c). Consequently, separate RW^{sat} retrieval models were applied for each basin (Equations 4.7 and 4.8).

4.3.2. Satellite-derived freshwater fraction

Surface water in HJB exhibited satellite-derived freshwater fractions (FW^{sat}) ranging from 0.04 to 0.71 (Figure 4.2a) and salinities (S^{sat}) ranging between 10 and 32 from June to September. The mean FW^{sat} across HJB was 0.15 ± 0.09, corresponding to a mean S^{sat} of 27.7 ± 2.6. Per pixel mean FW^{sat} ($\overline{FW^{sat}}$; $2011-2019$) was lowest in northwestern Hudson Bay and highest in southeastern Hudson Bay and James Bay, consistent with field salinity data and past studies (Figures 4.2b–4.2e, Table S4.2; Eastwood et al., 2020; Jones & Anderson, 1994). Satellite observations generally showed higher $\overline{FW^{sat}}$ in eastern Hudson Bay compared to the west, except in June and July 2017, when this pattern reversed (Figure 4.3a, Figures S4.1a and S4.1b).

The satellite-based approach enabled the detection of seasonal and interannual FW^{sat} patterns not captured by ship-based observations. $\overline{FW^{sat}}$ in HJB decreased from 0.21 ± 0.10 in June to 0.15 ± 0.07 in September, indicating a typical seasonal decline (Figure 4.2a). In western Hudson

Bay (i.e., west of −83° longitude), $\overline{\mathrm{FW}^{\mathrm{sat}}}$ was generally higher in July than in June, except in 2017 (Figure S4.3a) while eastern Hudson Bay (i.e., east of −83° longitude) $\overline{\mathrm{FW}^{\mathrm{sat}}}$ showed a July decline, with exceptions in 2011 and 2019, (Figure S4.3b S4.1). $\overline{\mathrm{FW}^{\mathrm{sat}}}$ decreased through August and September in both regions, though minor September increases occurred in eastern Hudson Bay in 2011, 2016, and 2017 (Figures S4.3a and S4.3b). Seasonal $\overline{\mathrm{FW}^{\mathrm{sat}}}$ from 2011 to 2019 increased in July but declined in other months (Figures S4.1a–S4.1d), yielding an overall non-significant trend of −0.0003 yr^{-1} ($p > 0.05$) in HJB for June–September combined (Figure 4.3a).

4.3.3. Satellite-derived river water fraction

Surface water in HJB exhibited satellite-based RW fractions ($\mathrm{RW}^{\mathrm{sat}}$) ranging from 0.03 to 0.40 (Figure 4.2a), with a mean $\mathrm{RW}^{\mathrm{sat}}$ of 0.11 ± 0.05 from June to September. Per pixel mean $\mathrm{RW}^{\mathrm{sat}}$ ($\overline{\mathrm{RW}^{\mathrm{sat}}}$; 2011–2019) were higher in the southern and southeastern Hudson Bay and James Bay, with lower values in central and northwestern Hudson Bay, aligning with $\overline{\mathrm{FW}^{\mathrm{sat}}}$ patterns (Figures 4.2f–4.2i). Coefficient of variation of $\overline{\mathrm{RW}^{\mathrm{sat}}}$ ($\mathrm{CV}_{\mathrm{RW}^{\mathrm{sat}}}$; 2011–2019), was lower in southern and southeastern regions, but higher in other regions (Figure 4.1a, Figures S4.2e–S4.2h), mirroring $\mathrm{CV}_{\mathrm{FW}^{\mathrm{sat}}}$ patterns (Figures S4.2a–S4.2d).

Across HJB, $\overline{\mathrm{RW}^{\mathrm{sat}}}$ declined from 0.13 ± 0.03 in June to 0.10 ± 0.02 in July–August, then increased to 0.13 ± 0.02 in September (Figure 4.2a). Eastern Hudson Bay consistently showed higher $\overline{\mathrm{RW}^{\mathrm{sat}}}$ than western Hudson Bay (Figure 4.3b), with peaks in 2015 and 2018 coinciding with $\overline{\mathrm{FW}^{\mathrm{sat}}}$. However, unlike $\overline{\mathrm{FW}^{\mathrm{sat}}}$, $\overline{\mathrm{RW}^{\mathrm{sat}}}$ generally decreased from June to July in western Hudson Bay, except in 2012, 2014, and 2016. From July to August, $\overline{\mathrm{RW}^{\mathrm{sat}}}$ declined in western Hudson Bay in most years, while eastern Hudson Bay showed variability, increasing in some years (e.g., 2012, 2014, 2017, and 2019) and decreasing in others. Between August and September, $\overline{\mathrm{RW}^{\mathrm{sat}}}$ increased in both regions (Figures S4.3c and S4.3d). The correlation between $\overline{\mathrm{RW}^{\mathrm{sat}}}$ and $\overline{\mathrm{FW}^{\mathrm{sat}}}$ progressively weakened through summer, reaching its lowest in September (Figures S4.4a–S4.4d).

Satellite observations further revealed seasonal dispersion of RW. In July, $\overline{\mathrm{RW}^{\mathrm{sat}}}$ indicated offshore spread from southwestern and southern Hudson Bay (Figure 4.2g), which was not observed in August (Figure 4.2h). By September, a distinct band of $\overline{\mathrm{RW}^{\mathrm{sat}}}$ was visible within the

saltier surface waters of these regions (Figure 4.2i). In southeastern Hudson Bay, $\overline{\mathrm{RW}^{\mathrm{sat}}}$ increased west of the Belcher Islands from June to September and persisted along the southeastern coast throughout the season (Figures 4.2f–4.2i), consistent with CDOM field observations and reflecting freshwater input from James Bay, which contributes more than half of HJB's river discharge (cf. Déry et al., 2011). From 2011 to 2019, seasonal $\overline{\mathrm{RW}^{\mathrm{sat}}}$ increased in all months (Figures S4.1e–S4.1h), yielding a significant overall trend of 0.0048 yr^{-1} ($p < 0.05$) in HJB for June–September (Figure 4.3b).

4.3.4. Satellite-derived sea-ice melt fraction

Surface water in HJB showed satellite-derived SIM fractions ($\mathrm{SIM}^{\mathrm{sat}}$) ranging from 0.00 to 0.35 (Figure 4.2a) with a mean $\mathrm{SIM}^{\mathrm{sat}}$ of 0.08 ± 0.03 between June and September. Per pixel mean $\mathrm{SIM}^{\mathrm{sat}}$ ($\overline{\mathrm{SIM}^{\mathrm{sat}}}$; 2011–2019) peaked in July, particularly around central and southeastern Hudson Bay, the Winisk Trough, and James Bay, accompanied by low $\mathrm{CV}_{\mathrm{FW}^{\mathrm{sat}}}$ (Figure 4.2k, Figure S4.2j). By late summer, traces of $\mathrm{SIM}^{\mathrm{sat}}$ remained in southern Hudson Bay, James Bay, and southeast of the Belcher Islands (Figures 4.2l and 4.2m). Anomalous $\overline{\mathrm{SIM}^{\mathrm{sat}}}$ distributions appeared in both western and eastern Hudson Bay, with slightly higher values in the west, except in June 2015 (Figure 4.3c, Figures S4.1i–S4.1l).

Seasonal $\overline{\mathrm{SIM}^{\mathrm{sat}}}$ in HJB increased from 0.08 ± 0.06 in June to 0.12 ± 0.07 in July, then decreased to 0.07 ± 0.05 in August and 0.05 ± 0.03 in September (Figure 4.2a). From June to July, $\overline{\mathrm{SIM}^{\mathrm{sat}}}$ increased in western Hudson Bay but declined in the east, except in 2011 (Figures S4.3e and S4.3f). A July to August decrease of $\overline{\mathrm{SIM}^{\mathrm{sat}}}$ followed in both regions, with exceptions in 2015 (western Hudson Bay) and 2015, 2019 (eastern Hudson Bay) (Figures S4.3e and S4.3f). Between August and September, $\overline{\mathrm{SIM}^{\mathrm{sat}}}$ declined in western Hudson Bay, while minor increases were observed in eastern Hudson Bay during 2014, 2016, 2018, and 2019 (Figures S4.3e and S4.3f). $\overline{\mathrm{SIM}^{\mathrm{sat}}}$ showed the strongest positive correlation with mean $\overline{\mathrm{FW}^{\mathrm{sat}}}$ in July, weakening in later months (Figures S4.4f–S4.4h). From 2011 to 2019, $\overline{\mathrm{SIM}^{\mathrm{sat}}}$ decreased in all months (Figures S4.1i–S4.1l), yielding a significant overall trend of −0.003 yr^{-1} ($p < 0.05$) for June–September combined (Figure 4.3c).

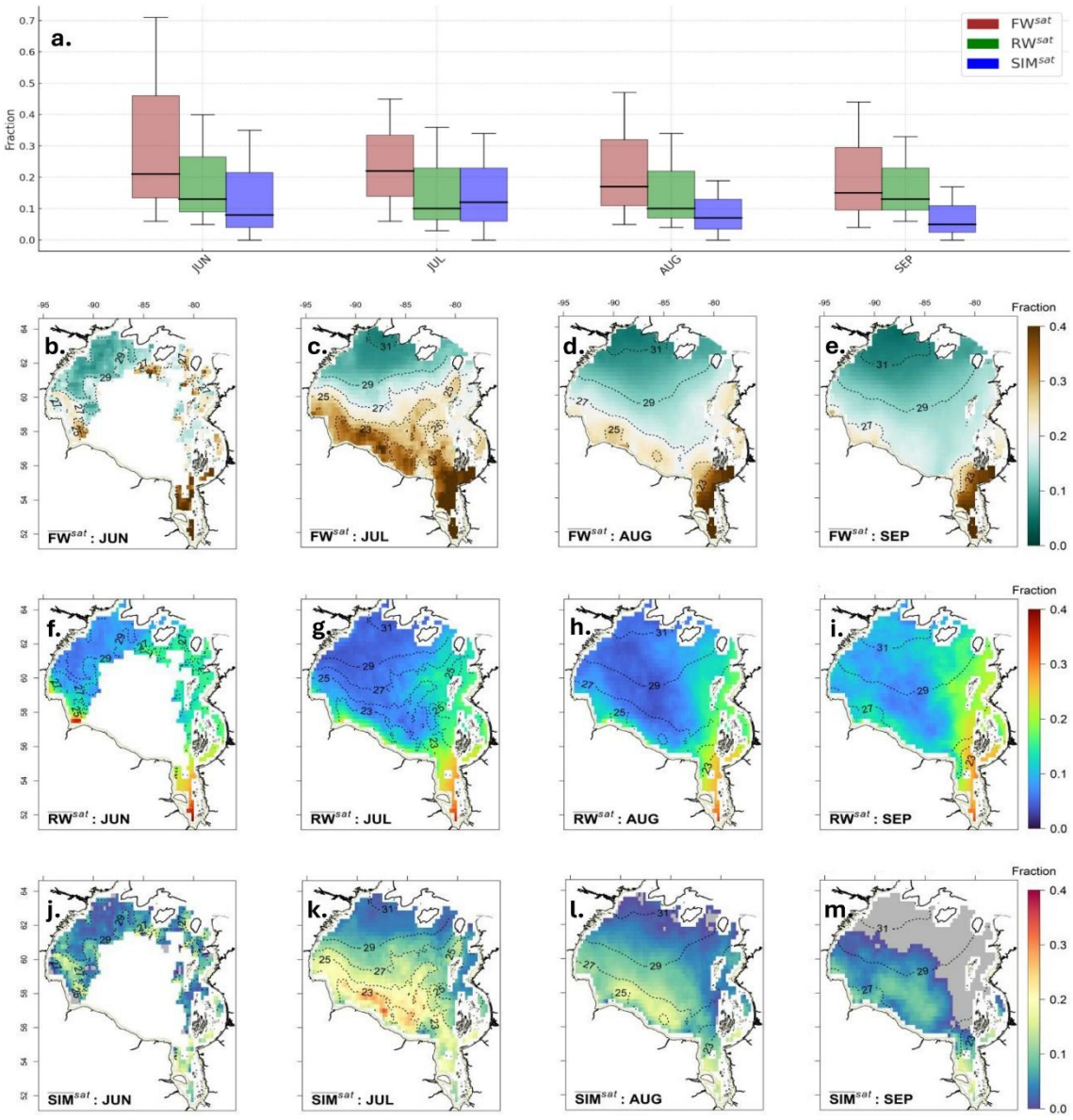


Figure 4.2. a. Box plots showing monthly distribution FW^{sat}, RW^{sat}, and SIM^{sat} across Hudson and James Bay (HJB) for June (JUN), July (JUL), August (AUG), and September (SEP). Per-pixel monthly mean (2011–2019) of satellite-derived fractions of b–e. freshwater ($\overline{SIM^{sat}}$), f–i. river water ($\overline{RW^{sat}}$), and j–m. sea-ice melt ($\overline{SIM^{sat}}$) in HJB. For panels b–m, dotted contours show satellite-derived salinity (S^{sat}), white and gray areas indicate missing data and $-\overline{SIM^{sat}}$, respectively, and pixels ≤ 10 m depth are masked (beige).

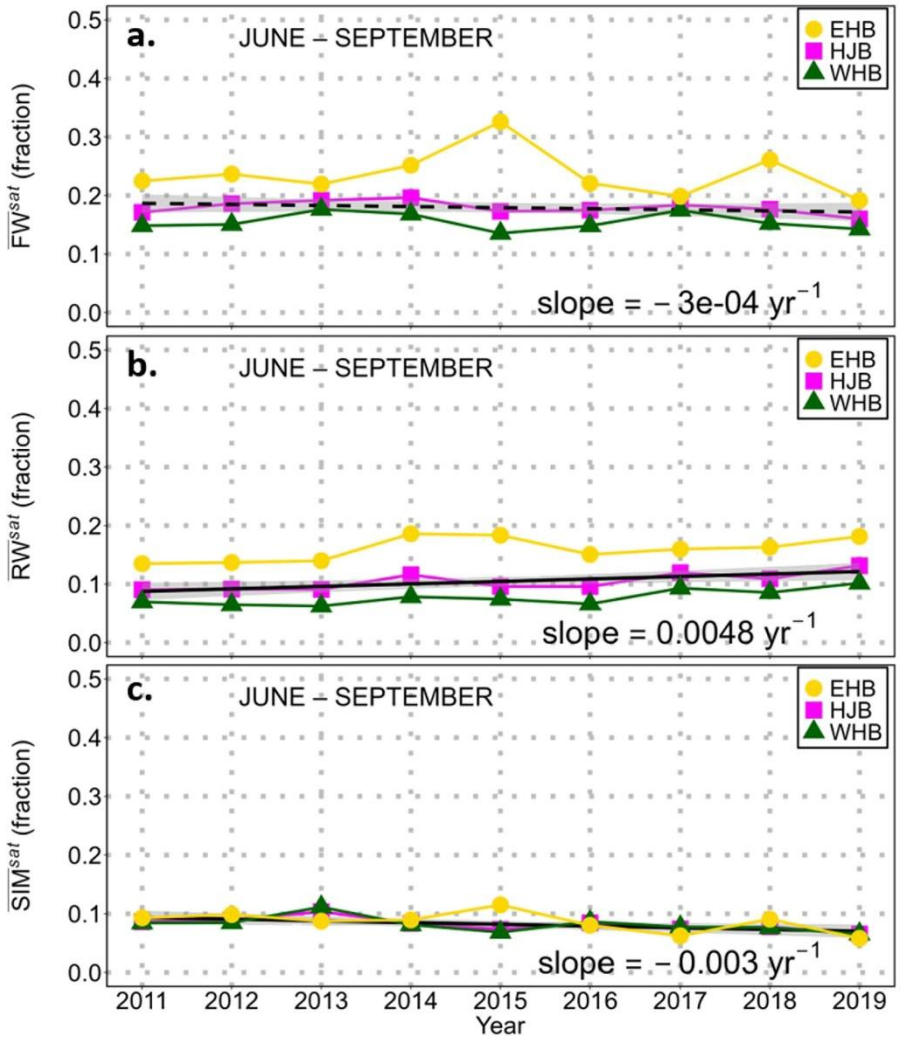


Figure 4.3. Mean (June–September) satellite-derived fractions of a. freshwater ($\overline{\mathrm{FW}^{\mathrm{sat}}}$), b. river water ($\overline{\mathrm{RW}^{\mathrm{sat}}}$), and c. sea-ice melt ($\overline{\mathrm{SIM}^{\mathrm{sat}}}$) across Hudson and James Bay (HJB), western Hudson Bay (WHB), and eastern Hudson Bay (EHB) from 2011 to 2019. Solid and dashed black lines indicate significant ($p < 0.05$) and non-significant ($p > 0.05$) trends for HJB, respectively.

4.1. Discussion

4.1.1. Relationship between in situ $a_{CDOM}^{lab}(412)$ and in situ river water fraction

The conservative relationship between in situ $a_{CDOM}^{lab}(412)$ and in situ RW fractions in Hudson Bay (Figure 4.1d) contrasts with the non-conservative CDOM behavior observed by Granskog

et al. (2009) in southwestern Hudson Bay, which suggested a potential underestimation of RW fractions by 50%–80%. However, the Granskog et al. (2009) study was limited to the anomalous 2005 flood year and focused only on southwestern Hudson Bay, which is dominated by Nelson and Churchill River inputs. The present study benefits from several years of observations and broad geographic coverage, rendering the observed in situ CDOM–RW relationship more representative of typical conditions, consistent with findings from Granskog et al. (2007) and Meilleur et al. (2023).

However, the James Bay-wide field observations indicate very high surface $a_{CDOM}^{lab}(412)$ and a nonlinear relationship with in situ RW fraction (Figure 4.1e). This nonlinearity may reflect contributions from CDOM-poor river inputs, SIM dilution, or CDOM degradation by light and microbes. Despite this nonlinearity, CDOM remains a robust RW tracer in HJB due to its conservative mixing behavior in several Hudson Bay estuaries (e.g., Basu et al., 2023) and relatively small area of James Bay (<70,000 km^2) within the HJB complex.

4.1.2. Satellite-derived river water dispersion

HJB experiences high river discharge during spring freshet, which peaks in May and June (McCullough et al., 2019), is evident from elevated $\overline{RW^{sat}}$ and $\overline{FW^{sat}}$ in June and July (Figure 4.2a). The uneven distribution of RW^{sat} and FW^{sat}, with higher values in southern waters, is due to major rivers draining into southern and southwestern Hudson Bay and James Bay. In contrast, northern Hudson Bay lacks equally large river sources (Déry et al., 2011) and is influenced by saline inflows from the Arctic and Atlantic Oceans (Figures 4.2b–4.2i).

Low variability and strong correlation between $\overline{RW^{sat}}$ and $\overline{FW^{sat}}$ confirm the dominance of RW in the southern coastal waters (Meilleur et al., 2023, Figures S4.2a–S4.2h and S4.4a–S4.4d). Overestimated S^{sat} in southeastern Hudson Bay further indicates higher RW in this region (Figure 4.1h); however, general alignment of RW^{sat} with FW^{sat} in eastern Hudson Bay supports the use of satellite-derived CDOM for RW retrieval in HJB (Figures S4.4a–S4.4d).

Although 9 years of data are insufficient to assess long-term trends, HJB is known to exhibit seasonal and interannual trends in river discharge (cf. Déry et al., 2011), which we expect to translate into trends and spatial patterns in RW^{sat}. RW^{sat} generally declined month-to-month from

June to September across HJB, mirroring the decreasing river discharge, with occasional increases corresponding to discharge peaks (Figures S4.3c, S4.3d, S4.5a, and S4.5b).

At regional scales, RW^{sat} showed a marginal yet significant inter-annual increase over the study period (2011–2019), particularly in the eastern Hudson Bay (Figure 4.3b). Despite declining river discharge in the western Hudson Bay, a post-2016 rise in RW^{sat} aligned with the 2017 discharge peak (Figure 4.3b; Figure S4.5c; Table S4.3). These observations demonstrate that satellite data effectively capture both seasonal and inter-annual RW^{sat} variability linked to river discharge patterns across HJB.

However, regional trends in RW^{sat} over 2011–2019 cannot entirely be explained by river discharge alone. For example, in eastern Hudson Bay, positive RW^{sat} changes from July to August during some years contrast with declining discharge trends (Figures S4.3d and S4.5d). This may be due to the increased influence of CDOM-rich outflow from James Bay, even when August discharge is lower than July, as observed in some unregulated rivers draining into James Bay (see Table 2 of Évrard et al. (2023)).

Furthermore, while RW^{sat} showed a year-to-year increase from 2011 to 2019 in eastern Hudson Bay from June through September (Figures S4.1e–S4.1h), river discharge increased in June and July but declined in August and September (Figure S4.5d and Table S4.3). This suggests a shift in the timing and redistribution of RW^{sat} within the system. These insights further emphasize the importance of using satellite-based methods to trace RW redistribution in HJB.

Circulation driven by wind and sea-surface height gradients redistributes RW^{sat} across HJB (Dmitrenko et al., 2021). In July, RW^{sat} gets transported offshore from southwestern and southern Hudson Bay (Figure 4.2g), but this weakens in August (Figure 4.2h, Basu et al., 2023; St-Laurent et al., 2011). Cyclonic vorticity in late summer drives northward RW^{sat} transport from James Bay to east of the Belcher Islands, sustaining high RW^{sat} in southeastern Hudson Bay despite reduced discharge (Figures 4.2h and 4.2i). This wind-driven transport forms a “riverine corridor” in the saltier waters of southern Hudson Bay, visible in September imagery (Figure 4.2i) and marked by low RW^{sat} and FW^{sat} variability (Figures S4.2d and S4.2h). In contrast, the high variability near the Winisk Trough in August suggests circulation changes linked to wind vorticity reversal (Figures S4.2c and S4.2g). Additionally, variability in RW^{sat} and FW^{sat} in southwestern and

northwestern Hudson Bay (Figures S4.2b and S4.2f) suggests that redistribution of RW^{sat} is consistent with Ridenour et al. (2019a) and Ridenour et al., (2019b). Therefore, RW^{sat} dispersion in HJB aligns with modeled and observed August and September circulation, which transport RW along the eastern coast of Hudson Bay and subsequently along the southern shore of Hudson Strait, into the Labrador Sea in the North Atlantic Ocean (Dmitrenko et al., 2020; Granskog et al., 2011; Ridenour et al., 2019a, 2019b; Straneo & Saucier, 2008).

4.1.3. Satellite-derived sea-ice melt dispersion

Following the peak sea ice volume in late April (Landy et al., 2017), melting likely begins in May and pools in southern Hudson Bay by June, unseen in satellite data due to ice cover. This meltwater spreads into central Hudson Bay, as indicated by SIM^{sat} during July and August (Figures 4.2k and 4.2l), when RW^{sat} in this region remains minimal (Figures 4.2g and 4.2h). The low variability and the strong correlation between $\overline{SIM^{sat}}$ and $\overline{FW^{sat}}$ in July confirm SIM as the main freshwater source in central Hudson Bay at that time, resulting in higher $\overline{FW^{sat}}$ (Figures S4.2j and S4.4f , Figure 4.2a).

In western Hudson Bay, SIM^{sat} peaks in July, exceeding June values, and typically declines through August and September, except in August 2015, when delayed SIM led to a rise (Figure S4.3e, cf. Tang et al., 2020). Generally, northwesterly winds push sea ice away from the Kivalliq polynya (Figure 4.1a) in western Hudson Bay to central and southeastern Hudson Bay (Figure 4.1a), leading to thicker spring sea ice in the east (Bruneau et al., 2021; Kirillov et al., 2020; Landy et al., 2017) and consequently higher SIM additions to its surface waters (Granskog et al., 2011).

However, this study showed that eastern Hudson Bay exhibits slightly lower SIM^{sat} than western Hudson Bay (Figure 4.3c), potentially due to the overestimation of S^{sat} (even after correction) in southeastern Hudson Bay (Figure 4.1h), a region with substantial RW and SIM input from James Bay (Figures 4.2g–4.2i, Eastwood et al., 2020). Additionally, contrary to the expected eastward displacement of sea ice, some studies have reported that sea ice tends to persist longer in southwestern and southern Hudson Bay, while melting ice is continuously replenished by ice transported from northern Hudson Bay (Galbraith and Larouche, 2011; Barber et al., 2021). This north-to-south transport and subsequent melting of sea ice may redistribute SIM towards the

southern and western regions of the bay, likely contributing to the higher SIM^{sat} observed in western Hudson Bay.

Nevertheless, SIM^{sat} in eastern Hudson Bay declined from June through September (Figure 4.3c, Figure S4.1i–S4.1l), following the expected seasonal pattern. However, in 2015, late SIM led to high SIM^{sat} in eastern Hudson Bay during August (Figures S4.1k and S4.3f, cf. Tang et al., 2020). The elevated SIM^{sat} was observed in FW^{sat} during June–August 2015 in eastern Hudson Bay (Figures S4.3a–S4.3c).

Corresponding with the eastward ice displacement, SIM^{sat} was traced in southeastern Hudson Bay later in the season, during August and September (Figures 4.2l and 4.2m). Additionally, the deeper bathymetry (>100 m) southeast of the Belcher Islands (Figure 4.1a) may also contribute to late-season SIM^{sat} in certain years, as longer sea ice persistence in this region can lead to elevated SIM^{sat}.

Cyclonic circulation and tidal and wind-driven mixing disperse SIM^{sat} in HJB, leading to its gradual decline in surface waters during summer and subsequent transport, together with RW, into the Labrador Sea (Granskog et al., 2011; Saucier et al., 2004) (Figures 4.2k–4.2m). Both the SIM and the RW account for 50% of the freshwater transported by the Labrador Current in the North Atlantic Ocean (Straneo & Saucier, 2008). The marginal decline detected in SIM^{sat} between 2011 and 2019 (Figure 4.3c) may be due to anomalous sea ice distribution in western and eastern Hudson Bay.

4.2. Conclusion

Freshwater in HJB sources from river discharge and SIM. Since river input is enriched in CDOM and suspended solids, a blue-to-red Band Ratio is applied to reduce the effects of suspended solids on satellite-based CDOM retrieval, enabling CDOM to serve as a conservative tracer of RW in HJB (Basu et al., 2023). Satellite observations capture seasonal and interannual freshwater variability across HJB.

High RW fractions were observed during the early summer and are redistributed by wind-driven circulations in late summer. SIM declined through the summer. From 2011 to 2019, surface RW increased, and SIM decreased, consistent with rising river discharge and declining sea-ice cover (Crawford et al., 2021; Feng et al., 2021; McCullough et al., 2019; Tivy et al., 2011).

Uncertainty in satellite-based RW estimates arises due to autochthonous CDOM production from phytoplankton degradation in northwestern Hudson Bay (Kitching et al., 2026; Barbedo et al., 2022; Matthes et al., 2021). Other factors, including CDOM photo- and microbial degradation, sea ice cover, cloudiness, air–sea freshwater fluxes, low sea surface temperature, sun angle, and algorithmic limitations (Bélanger et al., 2007; Guéguen et al., 2016; Kazmiruk et al., 2021; Loisel et al., 2013; Martínez et al., 2022; Tang et al., 2020), add to the uncertainty of satellite-based freshwater tracing. Despite these limitations, satellite remote sensing remains essential for monitoring freshwater variability in HJB and its impacts on regional oceanography, primary productivity, and ecology, as well as on North Atlantic circulation and climate (Ausen et al., 2023; Barbedo et al., 2022; Basu et al., 2023; Wu et al., 2023).

Data availability

The Aqua-MODIS Level 1A radiance data at 1 km resolution were obtained from MCST (2017). The BEC Arctic-SMOS V3 sea surface salinity 3-day average product at 25 km resolution are available from sftp://eodata-bec.icm.csic.es (Username: ftpuser, Password: .x8UP(ar.YZ2R), and Port: 22758). In situ data for salinity, oxygen isotope ratio, CDOM absorption at 412 nm, along with data on river water, sea-ice melt, and sea water fractions for Hudson and James Bays were obtained from Basu and Guzzi (2025).

Supplementary materials

Text S4.1.

Annually, Hudson and James Bays (HJB) receive about 900 km^3 of river water (RW) (1984–2018) from both natural and regulated rivers, accounting for about 18% of Arctic runoff (McCullough et al., 2019). This runoff, primarily rich in chromophoric dissolved organic matter (CDOM) and suspended solids, enters along the western and southern coasts, sourced from the Taiga Shield and Hudson Bay Lowlands (Basu et al., 2023; Capelle et al., 2020; Wiken, 1986). Cyclonic circulation along the coasts typically redistributes this freshwater (St-Laurent et al., 2011; Prinsenberg, 1986b), but recent satellite altimetry and coupled models reveal an anticyclonic pattern in southeastern HJB, driving freshwater northeastward into the interior through the Winisk Trough (Figure 4.1a) following spring and summer runoff peaks (Ridenour et al., 2019a).

In addition to river discharge, sea-ice melt (SIM) plays a significant role in HJB's freshwater distribution. At the end of April, the freshwater stored in sea ice (640–740 km³) is comparable to the annual river runoff, potentially diluting the riverine CDOM signal as the ice melts (Landy et al., 2017). The transport of sea ice by winds and cyclonic circulation often creates strong north-south gradients in SIM, with thicker ice accumulating in the southern and eastern regions (Landy et al., 2017), while open waters, like the Kivalliq polynya (Figure 4.1a), form in the northwest (Bruneau et al., 2021). As a result, much of the SIM is released far from its original withdrawal point, complicating freshwater tracing in HJB.

Understanding the seasonal and inter-annual variability of RW and SIM is crucial as changes in river discharge and the length of ice-free days continue to evolve in HJB (Hochheim and Barber, 2014). A 10.4% decrease in sea ice cover from 1968 to 2008, driven by rising air temperatures and wind, impacts the SIM volume in HJB (Tivy et al., 2011), while RW inputs have exhibited variability in temporal trends due to both climate change and regulation (cf., Feng et al., 2021; Déry et al., 2016; 2018).

Together, RW and SIM influence the stratification (e.g., Ahmed et al., 2020), the surface circulation (e.g., St-Laurent et al., 2011) and numerous biogeochemical processes in HJB, such as organic matter and nutrient distribution (e.g., Lee et al., 2023; Capelle et al., 2020; Kuzyk et al., 2009; Lapoussière et al., 2009) , phytoplankton growth (e.g., Barbedo et al., 2022; Matthes et al., 2021), microbial and fish biodiversity (e.g. Schembri et al., 2023; Morency et al., 2022; Jacquemot et al., 2021), beluga habitats (e.g., Ausen et al., 2023), gas exchange (e.g., Ahmed et al., 2020; Else et al., 2008).

Text S4.2.

Surface waters were collected from HJB (n = 110) onboard M/V Strait Signet (8–12 August 2006), CCGS Amundsen (25–30 September 2005; 9–31 July 2010; June 3–July 1, 2018), CCGS Des Groseilliers (September 26–October 3, 2016) and R/V William Kennedy (1–13 August 2021) were subjected to filtration. Filtered waters (0.2 µm / 25 mm polyether sulfone filter) in a 0.1 m quartz cuvette were scanned for light (340–700 nm) absorbance by CDOM (A_{CDOM}^{lab}; unitless) using Perkin-Elmer ultraviolet-visible integrated sphere dual-beam spectrophotometer (IOCCG, 2018). Ultrapure Milli-Q water was used as the blank. A_{CDOM}^{lab} was baseline-corrected by subtracting

absorbance values averaged over 680–700 nm (Babin et al., 2003) and then converted to Napierian absorption coefficient (a_{CDOM}^{lab}; m^{-1}) using equation S4.1, where λ is the wavelength (nm) (Bricaud et al., 1981).

$$a_{CDOM}^{lab}(\lambda) = \ln(10)\, A_{CDOM}^{lab}(\lambda) \,/\, 0.1 \quad \text{(S4.1)}$$

In situ salinity (S^{lab}) of surface water samples were measured with an Autosal Salinometer 8400B calibrated with IAPSO Standard Sea Water. A Picarro L-2120i was used to analyze $\delta^{18}O$ (‰). An additional 1387 water samples (2005–2021), collected from different depths and cruises in HJB, were analyzed for salinity and $\delta^{18}O$. Linear relationship between $\delta^{18}O^{lab}$ and S^{lab} (Figure 4.1b) suggests conservative mixing of fresh RW within salty marine waters of HJB.

Text S4.3.

A salinity of 32.5 was selected as the seawater endmember for HJB. The corresponding seawater oxygen isotope value ($\delta^{18}O$ = –2.16 ‰) was derived from the linear fit shown in Figure 4.1b. Because evaporation in HJB peaks mainly after September (Tang et al., 2020) and our study period spans June–September, the effects of evaporation and sea ice formation are inherently accounted for in the selected seawater endmember. SIM endmembers were adopted from Ahmed et al. (2020), with salinity (S_{sim} = 1.4 ± 0.5) and $\delta^{18}O_{sim}$ = –0.8 ± 0.2 ‰, representing samples collected during the 2018 spring melt in Hudson Bay. The SIM component inherently includes precipitation from snowfall within HJB. For the RW endmember, a $\delta^{18}O_{RW}$ = –12.66 ‰ was assigned based on the same linear fit (Figure 4.1b). The RW endmember accounts for precipitation occurring over land.

Text S4.4.

Empirical blue (488 nm) to red (667 nm) remote sensing reflectance ($R_{rs}; sr^{-1}$) band ratio (BR) derived a_{CDOM}^{BR} (412) (Basu et al., 2023; Doxaran et al., 2005) performed better than the quasi-analytical algorithm (QAA version 6; Lee et al., 2002; IOCCG, 2014) and multiple linear regression (MLR; Mannino et al., 2014) algorithm (both these algorithms underestimated CDOM retrieval) but showed a positive bias (Figure 4.2a; Table S4.1). Hence, a_{CDOM}^{BR} (412) was corrected

using the match-up slope and intercept (Figure 4.1f; Table S4.1; Equation 4.6), to increase the accuracy of satellite-based RW retrieval (RW^{sat}) in HJB.

Text S4.5.

RW^{sat} showed agreement with in situ RW for June, August and September (Table S4.1; Figure 4.1g). However, in October, RW^{sat} was overestimated, likely due to autochthonous CDOM sources common in the Arctic Ocean (e.g. Stedmon et al., 2021) but underexplored in HJB (Figure S4.2b). The variability observed at very low range of $a_{CDOM}^{lab}(412)$ and in situ RW in Hudson Bay (Figure 4.1d) also may be explained by CDOM loss through photobleaching (e.g., Osburn et al., 2009; Helms et al., 2008) and microbial degradation (e.g., Kazmiruk et al., 2018). Lower sun-angle could also contribute to erroneous a_{CDOM}^{sat} estimation, preventing the partitioning of freshwater components using satellite data late in the open water season (i.e. October-November).

Text S4.6.

Surface waters in the southwestern region of Hudson Bay exhibited high in situ $a_{CDOM}^{lab}(412)$ (i.e., high concentration of CDOM measured from field data) and low in situ S^{lab} (i.e., low salinity measured from field data), influenced by major rivers such as the Nelson and Churchill. In contrast, the northwestern part of Hudson Bay, which lacks major rivers inputs, and is influenced by saline inflows from the Arctic and Atlantic Ocean had very low $a_{CDOM}^{lab}(412)$ and the highest S^{lab} in HJB (Table S4.2).

Surface waters in southern Hudson Bay were saltier than those in the southwest, due to contributions from mid-sized rivers such as the Severn and Winisk. The lower $a_{CDOM}^{lab}(412)$ in this region was likely influenced by dilution from sea-ice melt (SIM) (Table S4.2). Central Hudson Bay had relatively fresh surface waters, with $a_{CDOM}^{lab}(412)$ similar to those in the northwest (Table S4.2). In southeastern Hudson Bay, $a_{CDOM}^{lab}(412)$ was lower than in James Bay, while S^{lab} was higher (Table S4.2), suggesting the transport of RW from James Bay into Hudson Bay (Figure S4.3). Farther north along the northeastern coast, the lowest $a_{CDOM}^{lab}(412)$ in HJB, along with increasing S^{lab} (Table S4.2), reflects a combination of factors including, dilution of RW transported from southeastern Hudson Bay, microbial and photodegradation of CDOM (Kazmiruk et al., 2021; Helms et al., 2008), and minimal CDOM input from small rivers such as the Nastapoca (Figure 4.1a).

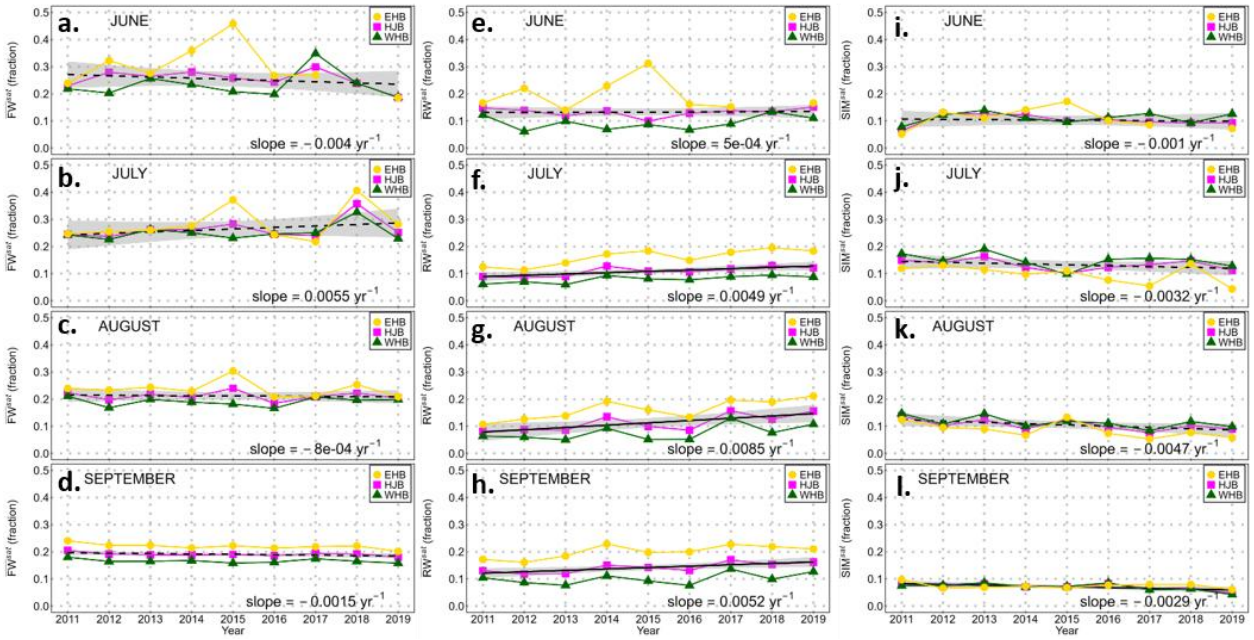


Figure S4.1. Satellite-derived mean fractions of a–d. freshwater ($\overline{\mathrm{FW}}^{\mathrm{sat}}$); g–h. river water ($\overline{\mathrm{RW}}^{\mathrm{sat}}$); i–l. sea-ice melt ($\overline{\mathrm{SIM}}^{\mathrm{sat}}$), in Hudson and James Bay (HJB), western Hudson Bay (WHB) and eastern Hudson Bay (EHB) from 2011 to 2019 for the months of June, July, August and September.

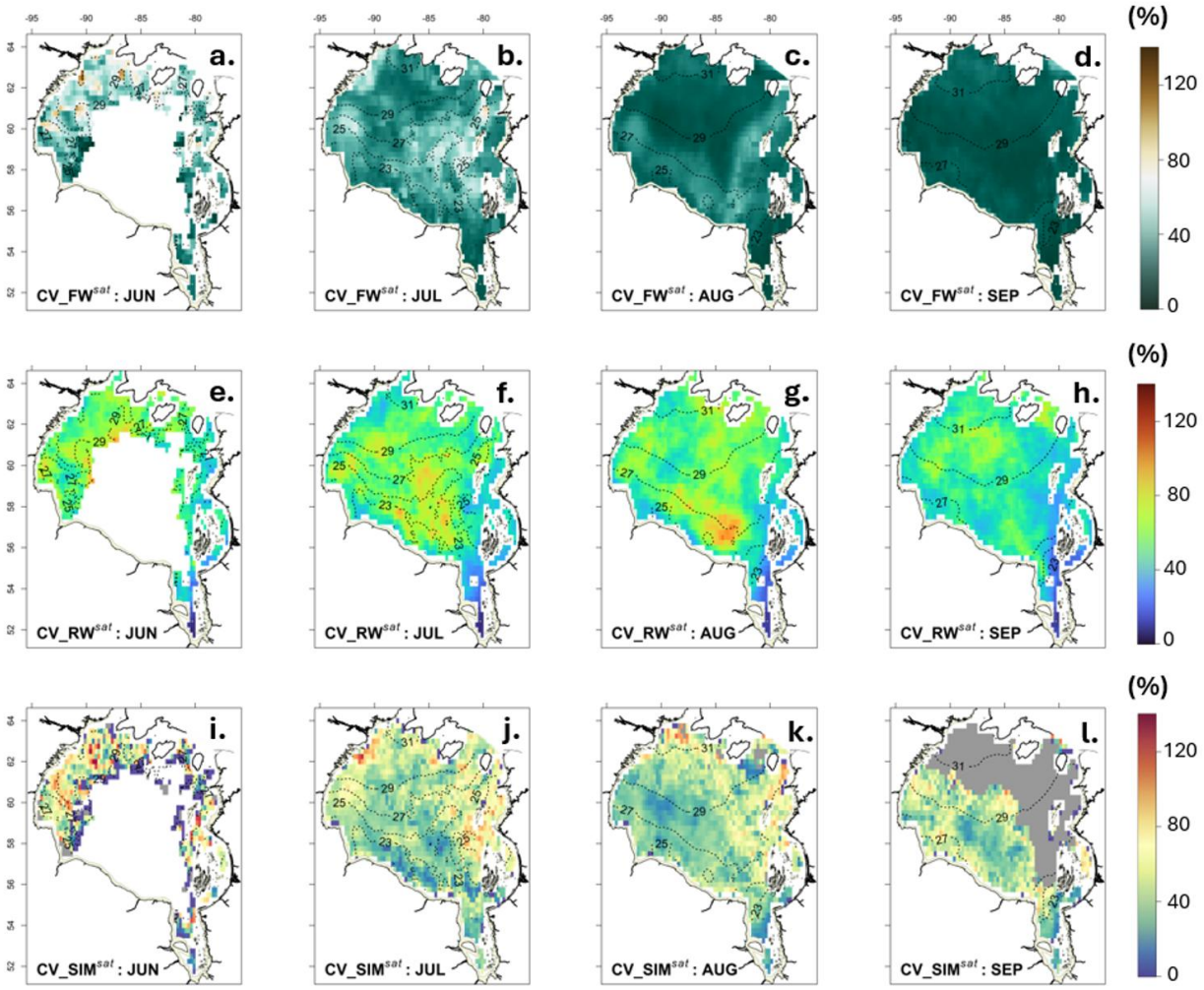


Figure S4.2. Per-pixel coefficient of variation (2011–2019) of satellite-derived fractions of a–d. freshwater (FW^{sat}), e–h. river water (RW^{sat}) and i–l. sea-ice melt (SIM^{sat}) in Hudson and James Bay (HJB) for June (JUN), July (JUL), August (AUG) and September (SEP). Dotted contours show satellite-derived salinity (S^{sat}). White and grey areas indicate missing data and $-SIM^{sat}$ pixels, respectively. Coastal pixels < 10 m depth are masked (beige).

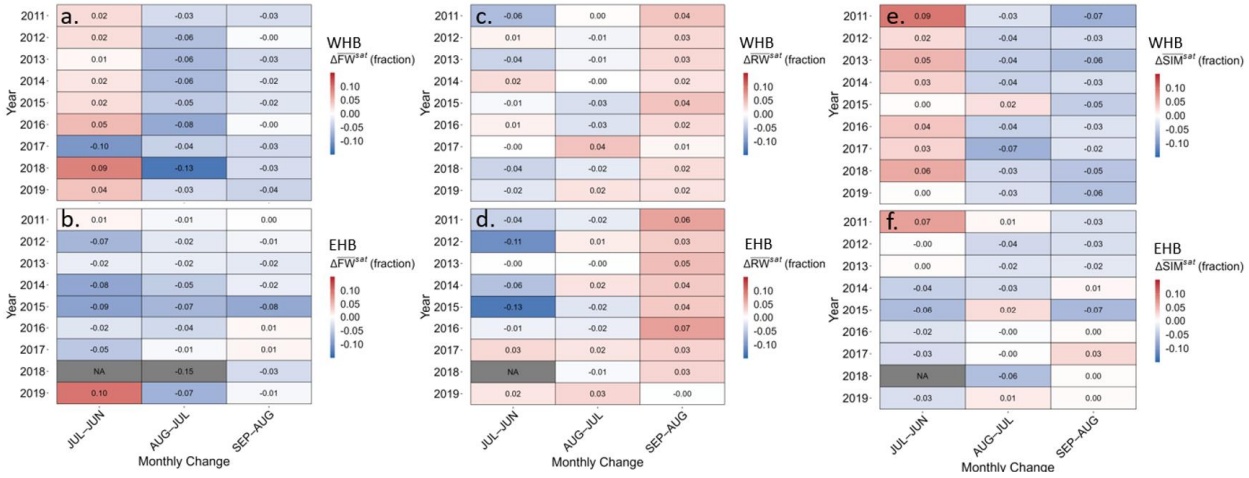


Figure S4.3. Monthly changes in mean satellite-derived fractions of a–b. freshwater ($\overline{\mathrm{FW}}^{\mathrm{sat}}$), e–f. river water ($\overline{\mathrm{RW}}^{\mathrm{sat}}$) and g–h. sea-ice melt ($\overline{\mathrm{SIM}}^{\mathrm{sat}}$) in July (JUL), August (AUG) and September (SEP) from their preceding month for western and eastern Hudson Bay (WHB and EHB), respectively, from 2011–2019.

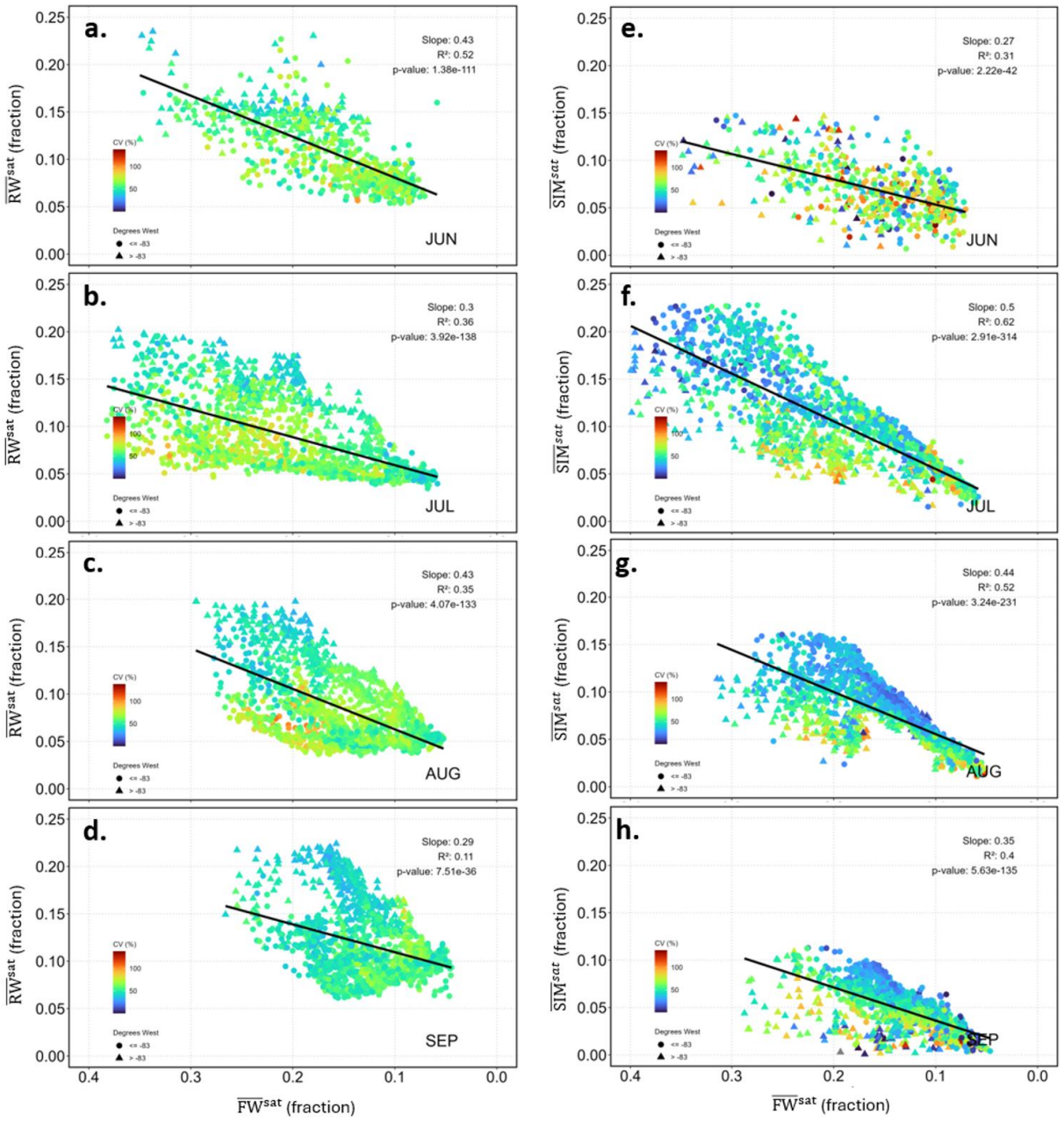


Figure S4.4. Relationship (solid black line) between satellite-derived per pixel mean (2011–2019) freshwater fractions ($\overline{\mathrm{FW}}^{\mathrm{sat}}$) and satellite-derived per pixel mean (2011–2019) fractions of a–d. river water ($\overline{\mathrm{RW}}^{\mathrm{sat}}$) and e–h. sea-ice melt ($\overline{\mathrm{SIM}}^{\mathrm{sat}}$) for June (JUN), July (JUL), August (AUG) and September (SEP) for all pixels of western (when latitude $>$ 83° W) and eastern Hudson Bay (when latitude $\leq$ 83° W), color coded by coefficient of variance (CV %)

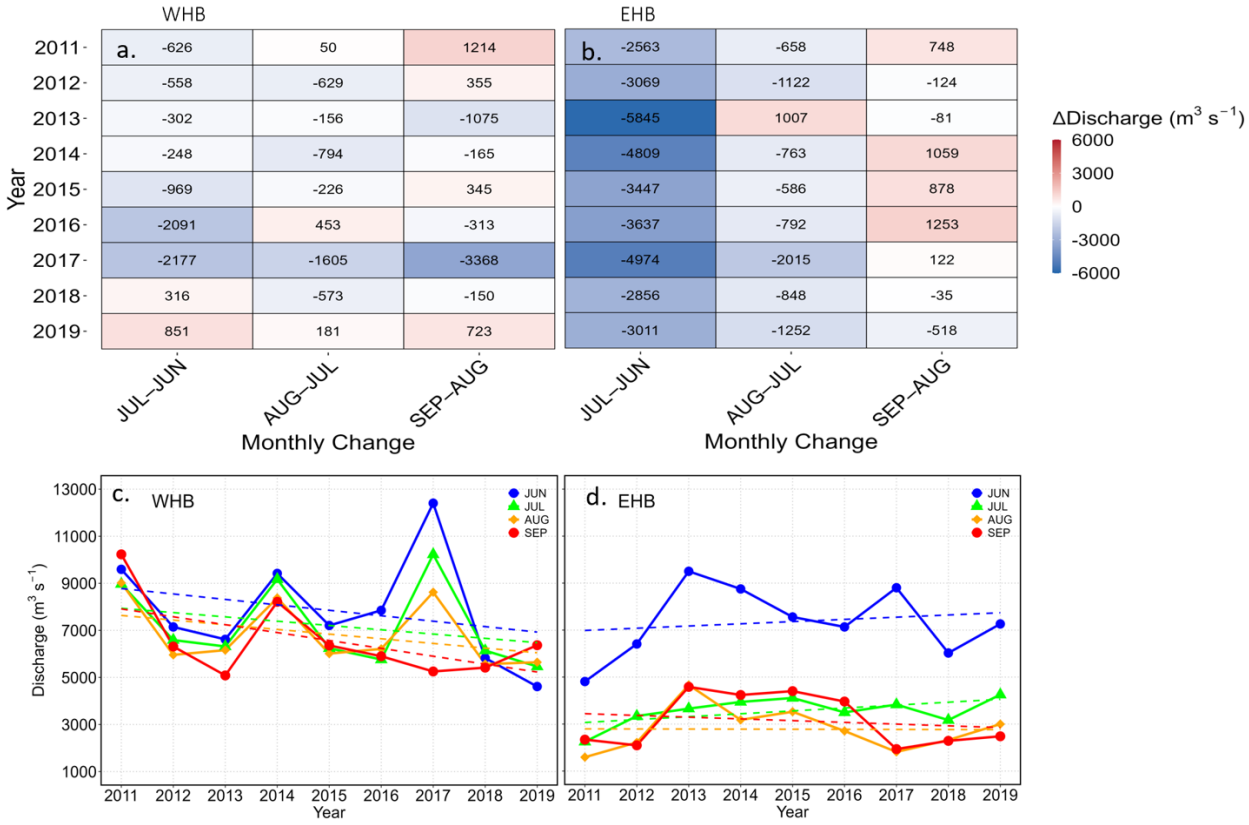


Figure S4.5. a–b. Monthly changes in river discharge change in July (JUL), August (AUG) and September (SEP) from their preceding month for western and eastern Hudson Bay (WHB and EHB) from 2011–2019. c–d. River discharge for June to September from 2011–2019. dashed lines represent non-significant ($p > 0.05$) trends.

Table S4.1. Statistics of match-up analysis.

Matchup	n	RMSE	MAPE (%)	Slope	Intercept	Bias	Percent Bias (%)	Correlation	Coefficient of Determination
BR	26	0.47	142.90	0.67	0.62	0.35	33.92	0.85	0.72
BR*	26	0.35	42.05	0.94	0.09	0.02	2.39	0.85	0.72
QAA	26	0.63	61.43	0.34	0.25	-0.39	-40.01	0.58	0.34
MLR	26	0.96	70.22	0.09	0.09	-0.78	-80.86	0.79	0.62
S^{sat}	32	1.68	4.39	0.57	13.02	0.23	0.78	0.92	0.85
RW^{sat}	31	0.08	121.74	0.98	0.03	0.03	27.84	0.77	0.60
$RW^{sat\#}$	19	0.02	31.10	1.10	0.00	0.00	9.75	0.88	0.78
$SIM^{sat\#}$	19	0.01	12.82	0.99	0.00	0.00	-4.98	0.92	0.85

* Corrected

June to September

BR : Band Ratio algorithm

QAA : Quasi Analytical Algorithm Version 6

MLR : Multiple Linear Regression algorithm

RW: River water fraction

SIM : Sea Icel melt Fraction

sat : Satellite derived

S : Sea surface salinity

Table S4.2. Laboratory measured absorption of chromophoric dissolved organic matter (CDOM) and salinity in Hudson and James Bay (HJB)

Region	in situ CDOM[a]	in situ Salinity[b]	No. of Station
Hudson Bay (HB)[c]	0.42 ± 0.46	27.3 ± 5.7	81
James Bay	3.90 ± 4.90	19.5 ± 5.4	29
HJB[d]	1.31 ± 2.90	25.3 ± 6.6	110
Southwestern HB	0.58 ± 0.60	26.2 ± 7.8	33
Southern HB	0.38 ± 3.80	28.7 ± 2.5	14
Northwestern HB	0.22 ± 0.06	32.3 ± 0.07	3
Central HB	0.23 ± 0.12	27.9 ± 4.1	12
Western HB[e]	0.46 ± 0.49	27.4 ± 6.4	64
Southeastern HB	0.35 ± 0.32	26.5 ± 1.5	13
Northeastern HB	0.20 ± 0.10	28.9 ± 2.5	6
Eastern HB[f]	2.46 ± 4.13	22.5 ± 5.8	48

[a]average in situ $a_{CDOM}^{lab}(412)$ (m^{-1})

[b]average in situ salinity

[c]includes southwestern, southern, northwestern, central, southeastern and northeastern Hudson Bay

[d]includes Hudson Bay and James Bay

[e]includes southwestern, southern, northwestern and central Hudson Bay

[f]includes southeastern, northeastern Hudson Bay and James Bay

Table S4.3. Monthly River discharge (m^3s^{-1}) stations (2011–2019) for western and eastern Hudson Bay (WHB and EHB) (https://wateroffice.ec.gc.ca/search/historical_e.html).

WHB		EHB	
River	**Station code**	**River**	**Station code**
Brown	06OA007	Winisk	04DC001
Thelon	06JC002	Albany	04HA002
Thlewiazza	06HB002	Attawapiskat	04FC001
Seal	06GD001	Moose	04LG004
Churchill	06FD001	Pontax	03BF001
Nelson	05UF007	Ekwan	04EA001
Hayes	04AB001	Abitibi	04ME003
Severn	04CA002	Harricana	04NA001
		Great Whale	03ED001

5. Chapter – River water control of stratification in Arctic marginal seas

This manuscript is submitted as a research paper in a peer-reviewed journal for publication.

Abstract

Freshwater-driven stratification regulates vertical exchanges of heat and nutrients in Arctic marginal seas, yet the relative roles of river water and sea-ice melt, the two main freshwater sources, remain uncertain. Using salinity and oxygen-isotope observations from the seasonally ice-covered sub-Arctic inland seas, Hudson Bay and James Bay (HJB), we show that river water dominates seasonal stratification not only in coastal regions but also in offshore and northern areas, where sea-ice meltwater has traditionally been assumed to dominate. Moreover, enhanced late-fall discharge from regulated rivers may introduce stratification during ice formation, potentially limiting deep-water renewal. These findings suggest a more persistent, river-dominated stratification regime in HJB, with implications for winter ventilation, biogeochemical cycling, and ecosystem sensitivity under continued Arctic warming.

5.1. Introduction

Stratification, the density-driven layering of seawater, regulates vertical exchanges of heat, momentum, gases, and nutrients in the water column, thereby shaping marine ecosystems. Seawater density is controlled by gradients in temperature and salinity (Carmack, 2007). In Arctic marginal seas, including Hudson Bay and James Bay (HJB), vertical stratification is predominantly salinity-driven, reflecting a freshwater system shaped by large riverine inputs and seasonal sea ice processes that concentrate buoyant freshwater in surface layers (Granskog et al., 2011; Basu et al., 2023).

Recent satellite observations of HJB indicate increasing river-water contributions and declining surface sea-ice meltwater, resulting in altered salinity distributions and ocean color patterns (Basu et al., 2026). These shifts point to evolving controls on stratification and highlight the need for depth-resolved assessments of freshwater source types when evaluating their influence on vertical density structure in HJB (e.g., Ahmed et al., 2020).

Previous studies of the FW budget in HJB have primarily emphasized lateral transports and exports (Straneo and Saucier, 2008; McCullough et al., 2019; Ridenour et al., 2021), while vertical exchanges and the potential incorporation of FW into deeper layers remain less well constrained. Salinity–oxygen isotope ($\delta^{18}O$) analyses by Granskog et al. (2009, 2011) were limited to September–October 2005, excluding the June freshet and coinciding with an anomalously high runoff year (Shook, 2016). Other isotopic studies were regional in scope, focusing on southwestern (Kuzyk et al., 2008), southeastern Hudson Bay (Eastwood et al., 2020), and coastal James Bay (Guzzi et al., 2024), thereby limiting basin-wide and seasonal interpretation.

Several investigations have examined how stratification influences the distribution of marine biota in HJB; however, these studies were largely confined to late spring conditions (Morency et al., 2022; Schembri et al., 2023; Jacquemot et al., 2024). Although satellite- and model-based studies have characterized the surface distribution of FW across HJB (Ridenour et al., 2019a; Barbedo et al., 2022), the relative contributions of river water and sea-ice melt to vertical stratification remain poorly studied, primarily due to the scarcity of depth-resolved field observations spanning multiple seasons.

Here, we use multi-year salinity, temperature, and $\delta^{18}O$ measurements collected from late spring through fall to (1) quantify the relative contributions of salinity and temperature gradients to vertical density stratification; (2) determine river water and sea-ice melt fractions throughout the water column; and (3) evaluate how distinct freshwater sources control seasonal stratification within the HJB water column.

5.2. Data and methods

This study determined the salinity and temperature controls on the HJB stratification by deriving the gradients of potential density ($\Delta\rho_\theta/\Delta z$; kg m^{-3} m^{-1}), potential temperature ($\Delta\theta/\Delta z$; °C m^{-1}) and salinity ($\Delta S/\Delta z$; S m^{-1}) between depth-resolved seawater samples for each of the 72 stations (i.e., 336 samples in total) collected from several ship-based expeditions: CCGS Amundsen (September 2005; July 2010; June–July, 2018), CCGS Des Groseilliers (September–October, 2016) and R/V William Kennedy (August 2017, 2019, 2021; September 2017) (Figure 5.1). Potential temperature (θ; °C) and potential density (ρ_θ; kg m^{-3}) were calculated from discrete salinity (S) samples, measured on an Autosal 8400B salinometer calibrated to IAPSO Standard

Seawater, and CTD-based temperature (T; ℃) using TEOS-10 Gibbs Seawater formulations (McDougall and Barker, 2011).

The seasonal control of salinity and temperature on vertical density stratification was first quantified using simple linear regressions of $\Delta\rho_\theta/\Delta z$ on individual thermohaline gradients ($\Delta\theta/\Delta z$ and $\Delta S/\Delta z$). Because salinity and temperature covary in the water column, a multiple linear regression model was applied to isolate their independent contribution on $\Delta\rho_\theta/\Delta z$, using partial coefficients of determination, obtained from

$$\Delta\rho_\theta/\Delta z = \gamma + \beta(\Delta S/\Delta z) - \alpha(\Delta\theta/\Delta z), \quad (5.1)$$

where α (kg m^{-3} °C^{-1}) and β (kg m^{-3} S^{-1}) represent thermal expansion and haline contraction of seawater, γ is the y-intercept (kg m^{-3} m^{-1}), and z is the sample depth (m).

Furthermore, river-water (RW), sea-ice melt (SIM), and seawater (SW) fractions were derived for 472 seawater samples from 150 stations with measured salinity and $\delta^{18}O$, the latter analyzed using a Picarro L-2120i cavity ring-down spectrometer. This yielded a total of 808 seawater samples from 222 stations across HJB for which RW, SIM, and SW fractions were obtained using a standard three-component mixing model (equations 5.2–5.4) (Östlund and Hut, 1984), widely applied across polar regions (e.g., Yamamoto-Kawai et al., 2005; Granskog et al., 2011). Briefly,

$$RW + SIM + SW = 1 \quad (5.2)$$

$$RW\ S_{RW} + SIM\ S_{SIM} + SW\ S_{SW} = S \quad (5.3)$$

$$RW\ \delta^{18}O_{RW} + SIM\ \delta^{18}O_{SIM} + SW\ \delta^{18}O_{SW} = \delta^{18}O. \quad (5.4)$$

Equations 5.2–5.4 were solved using the SW endmember (salinity: 32.5; $\delta^{18}O$: –2.16‰) obtained from the linear fit $\delta^{18}O = 0.32\ S - 12.66$ (Figure 1b in Basu et al., 2026). The RW $\delta^{18}O$ endmember salinity of 0 was –12.66‰, corresponding to the y-intercept of this fit. SIM endmember values (salinity: 1.4 ± 0.5; $\delta^{18}O$: –0.8 ± 0.2‰) were adopted from Ahmed et al. (2020) based on samples of melting sea ice collected during June 2018 in southern Hudson Bay. Negative SIM solutions derived from equations (5.2–5.4) indicate a freshwater deficit associated with brine injection in the water column during sea ice formation, while negative RW solutions reveal the presence of water masses that fall outside the endmember framework adopted in this study (Granskog et al., 2011).

The seasonal control of river- and sea ice-sourced freshwater on stratification was evaluated at the depth of maximum salinity gradient (z_{SGM}; m) using simple linear regression between $\Delta S/\Delta z$ and the freshwater gradients ($|\Delta RW/\Delta z|$ and $|\Delta SIM/\Delta z|$; fraction m^{-1}). These gradients were computed durin early summer (June–July), late summer (August–September), and fall (October) (Figure 5.1). Because RW and SIM covary in the water column, a multiple linear regression model (equation 5.5) was applied to isolate their independent contributions on $\Delta S/\Delta z$:

$$\Delta S/\Delta z = \lambda + \beta_{RW}(\Delta RW/\Delta z) + \beta_{SIM}(|\Delta SIM/\Delta z|), \quad (5.5)$$

where β_{RW} (S fraction^{-1}) and β_{SIM} (S fraction^{-1}) are the haline contraction coefficients of freshwater sourced from rivers and sea ice, respectively, λ is the y-intercept (S m^{-1}), and z is the sample depth (m). The relative influence of $|\Delta RW/\Delta z|$ and $|\Delta SIM/\Delta z|$ on haline stratification was quantified using partial coefficients of determination, obtained from equation (5.5). Two late-summer coastal stations (Station 5 and BS07; Figure 5.1), strongly influenced by tidal forcing and spatio-temporal variability, exhibited negative $\Delta S/\Delta z$ and were therefore excluded from analyses (Figure 1).

Finally, freshwater fractions (RW and SIM) and their vertical gradients, together with the salinity gradient at z_{SGM}, were used to characterize the halocline across HJB. Here, the halocline is defined by upper and lower boundaries identified by tracking the decay of $\Delta S/\Delta z$ above and below z_{SGM} to a threshold of -0.0001 S m^{-1} and separated by a salinity difference (ΔS).

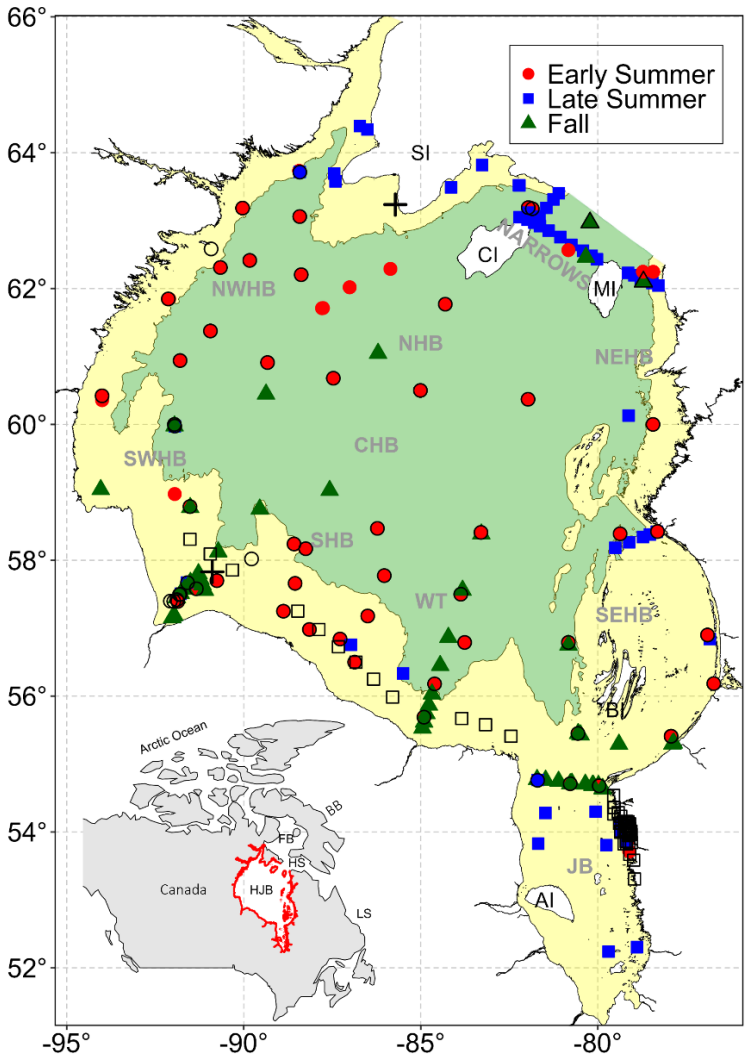


Figure 5.1: Hudson and James Bay (HJB) study area. Discrete water-sampling stations in coastal (<100 m deep; pale yellow) and offshore (≥100 m deep; light green) waters during early summer (June–July), late summer (August–September), and fall (October) are shown in the map. Stations with ≥ 3 depth samples are shown with filled symbols, whereas stations with fewer samples are shown with transparent symbols. Stations with both salinity and temperature measurements are marked with black outline. Samples from southern regions include James Bay (JB), southeastern Hudson Bay (SEHB), Winisk Trough (WT), southern Hudson Bay (SHB), southwestern Hudson Bay (SWHB), and central Hudson Bay (CHB). Samples from northern regions include northwestern Hudson Bay (NWHB), northern Hudson Bay (NHB), northeastern Hudson Bay (NEHB), and the Narrows. Major islands shown include Southampton Island (SI), Coats Island (CI), and Mansel Island (MI) in the north, as well as the Belcher Islands (BI) in SEHB and Akimiski Island (AI) in JB. Subsurface waters at station 5 near SI and station BS07 in SWHB,

indicated by black plus symbols, exhibit negative salinity gradients during late summer. The inset map highlights the HJB study area (red outline) within Canada, with Foxe Basin (FB) to the north, connected to the Arctic Ocean, and Hudson Strait (HS) to the northeast, linking HJB to the Labrador Sea (LS) in the North Atlantic Ocean and to Baffin Bay (BB), which also connects to the Arctic Ocean.

5.3. Results

5.3.1. Salinity and temperature controls on density stratification

Across all seasons, vertical density stratification in HJB is primarily controlled by salinity gradients, which explain 93–98% of the variance in potential density gradients (Table 5.1). High partial coefficients of determination (0.98–0.99) and large haline contraction coefficients (0.77–0.78 kg m^{-3} S^{-1}) further confirm that salinity governs density stratification after accounting for temperature effects (Table S5.1).

In contrast, potential temperature gradients explain only 25–66% of the seasonal variance in potential density gradients, with a modest contribution in fall (Table 5.1). Despite relatively high partial coefficients of determination (0.92–0.97), small negative thermal expansion coefficients indicate that temperature has little independent influence and mainly covaries with salinity (Table S5.1). Accordingly, combined salinity and temperature gradients explain 99% of the total variance in vertical density stratification across HJB (Table S5.1).

Table 5.1. Seasonal contribution of salinity gradient ($\Delta S/\Delta z$; S m^{-1}) and temperature gradient ($\Delta\theta/\Delta z$; °C m^{-1}) to potential density gradient ($\Delta\rho_\theta/\Delta z$; kg m^{-3} m^{-1}) across water columns of Hudson and James Bays (HJB), evaluated using simple linear regression analyses.

Season	Stations	Samples	Variable	Slope	Intercept[c]	r^2	*p*-value
Early Summer	58	301	$\Delta S/\Delta z$	0.87[a]	0.00	0.98	< 0.001
Late Summer	12	16		0.79[a]	0.01	0.99	< 0.001
Fall	2	19		1.01[a]	0.00	0.93	< 0.001
All	72	336		0.81[a]	0.01	0.99	< 0.001
Early Summer	58	301	$\Delta\theta/\Delta z$	−0.37[b]	0.02	0.50	< 0.001
Late Summer	12	16		−1.13[b]	0.30	0.25	< 0.01
Fall	2	19		−0.23[b]	0.02	0.66	< 0.001
All	72	336		−0.59[b]	0.02	0.27	< 0.001

[a]kg m^{-3} S^{-1}

[b]kg m^{-3} °C^{-1}

[c]kg m^{-3} m^{-1}

5.3.2. Sources of freshwater and their control on haline stratification

During summer, haline stratification in HJB is primarily controlled by RW gradients, which explain 86–92% of the variance in salinity gradients (Table 5.2). Partial R^2 values (0.84–0.89) confirm that RW is the dominant driver of salinity gradients at z_{SGM}, while sea ice-derived freshwater provides a secondary (Partial R^2 = 0.29–0.53) but significant contribution during summer (Table S5.2).

In contrast, SIM gradients dominate haline stratification in fall, accounting for 66% of salinity-gradient variability (Table 5.2) and 92% after accounting for RW (Table S5.2). Nevertheless, RW retains a strong and independent influence at z_{SGM} in fall (partial R^2 = 0.88) (Table S5.2). Together, RW and SIM gradients explain 94% of the total variance in salinity-driven stratification across HJB, with the remaining 6% likely reflecting saline inflows from Hudson Strait and Foxe Basin (Table S5.2).

Table 5.2. Seasonal contribution of river water (|ΔRW/Δz|; fraction m^{-1}) and sea-ice melt (|ΔSIM/Δz|; fraction m^{-1}) gradients to salinity gradients ($\Delta S/\Delta z$; S m^{-1}) at the depth of maximum salinity gradient (z_{SGM}; m), across the Hudson and James Bay (HJB) evaluated using simple linear regression analyses.

Season	Stations	Variable	Slope[a]	Intercept[b]	r^2	*p*-value
Early Summer	69	|ΔRW/Δz|	29.8	0.05	0.86	< 0.001
Late Summer	54		31.2	0.02	0.92	< 0.001
Fall	48		34.7	0.07	0.44	< 0.001
All	171		31.1	0.05	0.78	< 0.001
Early Summer	69	|ΔSIM/Δz|	63.8	0.03	0.38	< 0.001
Late Summer	54		97.9	0.00	0.65	< 0.001
Fall	48		32.7	0.11	0.62	< 0.001
All	171		46.8	0.09	0.46	< 0.001

[a]S fraction^{-1}

[b]S m^{-1}

5.3.3. Regional variability of freshwater sources and their control on haline stratification

Salinity-driven stratification and freshwater sources within the halocline vary across HJB. In early summer, water columns south of 60° N are dominated by RW. Southern HJB is characterized by shallow haloclines (z_{SGM} = 14–18 m; ΔS = 1.2–3.4) with steep salinity gradient maxima (0.17–0.64 S m^{-1}) (Figures 5.2a, d, g; Figures 5.3a–d; Table S5.3). In central Hudson Bay, stratification is instead controlled by negative SIM fractions (i.e., brine), yielding weaker salinity contrasts in the halocline (ΔS = 0.6) and reduced salinity gradient maxima (0.06 S m^{-1}) at comparable depths (z_{SGM} = 17 m) (Figures 5.2d, g; Table S5.3).

North of 60° N, early summer haloclines are deeper (z_{SGM} = 34–68 m; ΔS = 0.6–2.4) characterized by weaker salinity gradient maxima (0.02–0.16 S m^{-1}) (Figures 5.2a, d; Table S5.4). Negative SIM fractions increase with depth in northern HJB (Figures S5.2c–d; Figures S5.3a–d), yet RW remains the dominant contributor to stratification (Figures 5.2d, g; Table S5.4). Stratification is relatively strong in northeastern Hudson Bay, due to combined RW and SIM inputs in the halocline (z_{SGM} = 43 m; ΔS = 2) (Figures 5.2d, g; Figures 5.3e-f; Table S5.4).

During late summer, stratification intensifies in northern HJB (Figure 5.2e). Stratification remains RW-dominated in northwestern Hudson Bay. Here, RW remains confined to a near-surface halocline (z_{SGM} = 14–35 m; ΔS = 0.4–3.6), generating steep salinity gradient maxima (0.11–0.55 S m^{-1}) (Figures 5.2b, e; Figures 5.3e–5.3f; Figures S5.3a–d). Negative RW fractions in the Narrows indicate water masses not represented by the endmember framework (Figures 5.2e, h; Figures S5.3a–d; Table S5.4). SIM dominates stratification in northeastern Hudson Bay (Figures 5.2e, h; Table S5.4).

In contrast, southern HJB exhibits weaker salinity gradient maxima (0.04–0.07 S m^{-1}) associated with reduced RW and a deeper halocline (z_{SGM} = 33–48 m; ΔS = 0.6–3.2) (Figures 5.2b, e; Figures 5.3c–d; Figures S5.1a–f; Table S5.3), although RW gradients dominate stratification across southern HJB (Figure 5.2h). In James Bay, the salinity gradient maxima (0.65 S m^{-1}) remain comparable to early summer, with enhanced RW likely reflecting nearshore sampling (Figure 5.1; Figures 5.2b, e, h; Figures 5.3a–b; Table S5.3). Overall, the halocline remains influenced by both RW and SIM across HJB, in contrast to early summer when SIM was largely confined to the surface mixed layer.

Despite reduced river discharge, stratification re-intensifies in southern HJB in fall, with increased RW and steep salinity gradient maxima (0.13–0.40 S m^{-1}) within the halocline (z_{SGM}= 28–35 m; ΔS = 2.7–3.4) (Figures 5.2c, f; Figures 5.3c-d, Figures S5.1a-f). Coastal stratification remains RW-driven, whereas offshore stratification is controlled by negative SIM fractions (Figure 5.2i; Table S5.3). In James Bay, stratification weakens along with RW and SIM within the halocline (z_{SGM}= 35 m; ΔS = 4.6). Northern and northeastern Hudson Bay also remain weakly stratified (z_{SGM}= 30–50 m; ΔS = 1.4–3.4), although RW continues to dominate stratification (Figure 5.2i; Figures 5.3e–f; Figures S5.2c–d; Table S5.1).

By contrast, halocline shoaling in the Narrows between Coats and Mansel Islands (z_{SGM}= 25 m; ΔS = 1.2) indicates renewed near-surface RW influence and eastward redistribution of freshwater from west of Coats Island since late summer (Figures 5.2f, i; Figures S5.3c–d; Tables S5.3, S5.4).

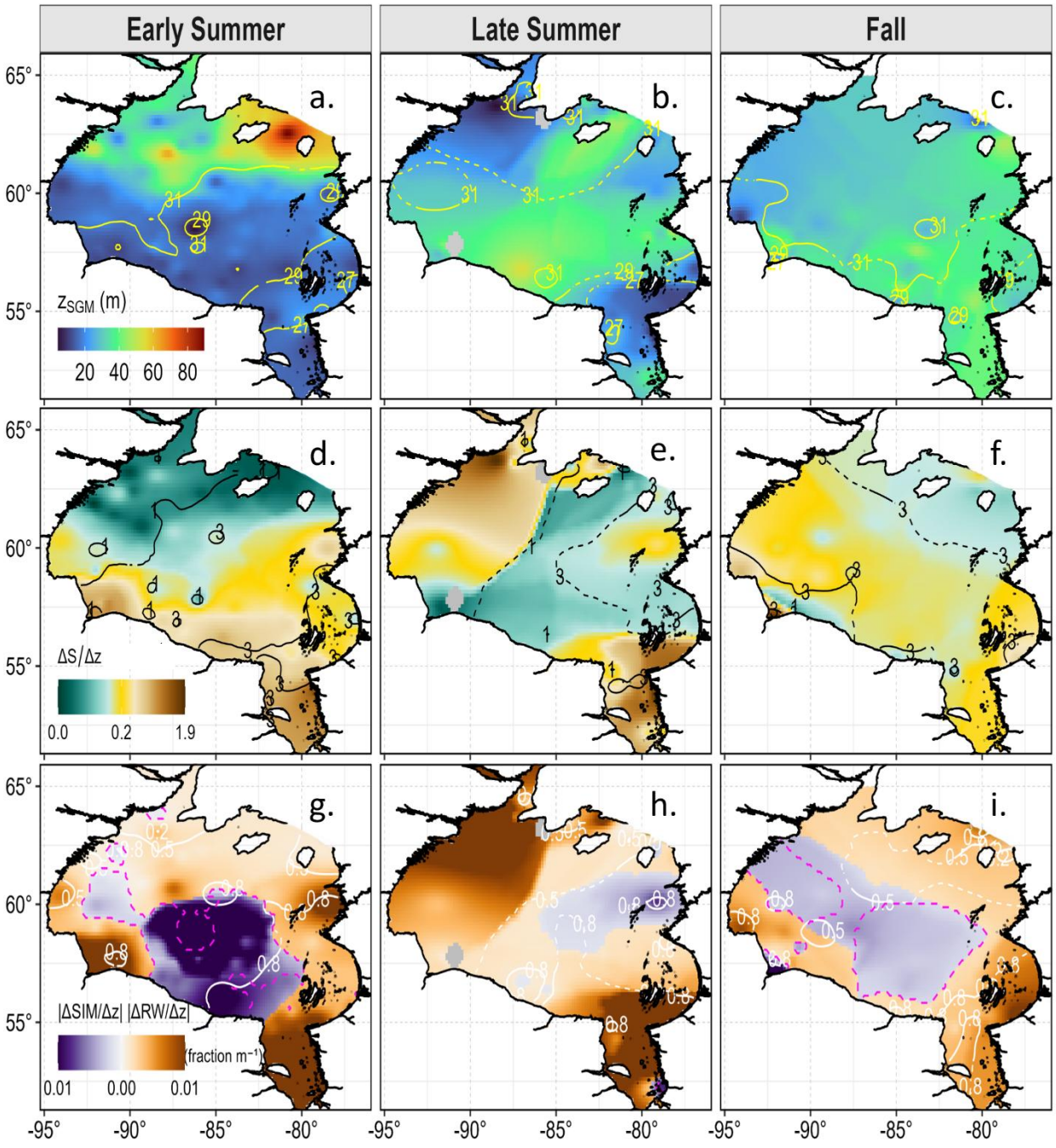


Figure 5.2. a–c. z_{SGM}, with the yellow contours showing the salinity. d–f. Salinity gradient ($\Delta S/\Delta z$; S m^{-1}), with the black contours indicating the salinity difference (ΔS) between the halocline top and bottom boundaries. g–i. Larger of absolute values of river water gradients ($|\Delta RW/\Delta z|$; fraction m^{-1}) and sea-ice melt gradients ($|\Delta SIM/\Delta z|$; fraction m^{-1}) determine dominance on haline stratification. White contours in panels g–i show the apparent river water influence (i.e., |RW|/(|RW| + |SIM|), and pink dashed contours mark regions with negative SIM,

whereas the remaining |ΔSIM/Δz|-dominated regions correspond to positive sea-ice melt contribution. In panels a–i, solid contours (yellow, black, and white) denote areas well supported by observations, whereas dashed contours indicate extrapolated regions obtained using inverse-distance-weighted interpolation (1.5° radius) and subsequently smoothed with a 3×3 kernel. Grey masks in panels b, e, h indicate subsurface waters at station 5 near SI and station BS07 in southwestern Hudson Bay that exhibit negative salinity gradients and were therefore excluded from the gridded fields.

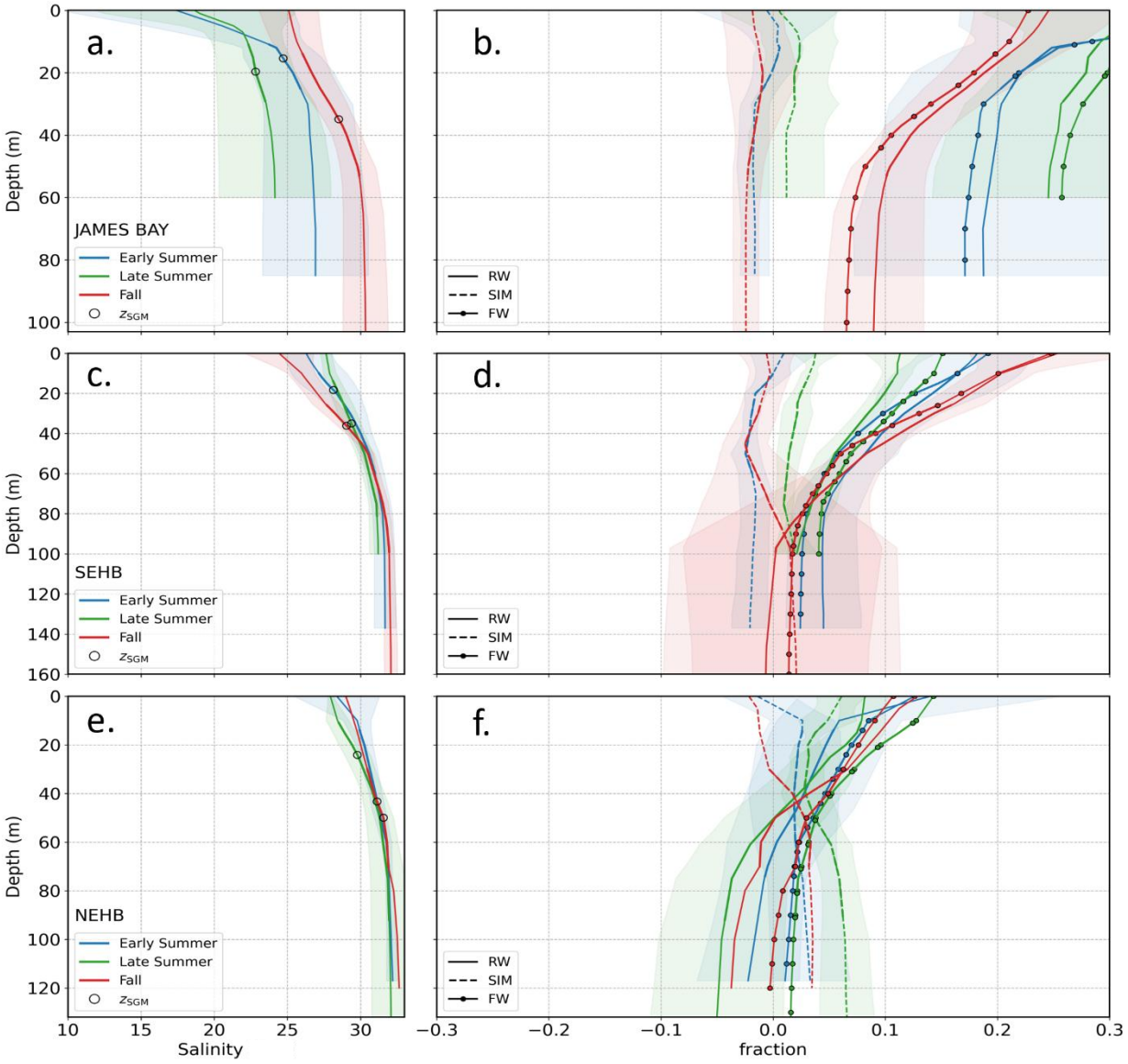


Figure 5.3. Examples of vertical profiles of salinity, river water (RW), sea-ice melt (SIM), and freshwater (FW = RW + SIM) across Hudson Bay and James Bay (HJB) during early summer,

late summer, and fall. a–b. James Bay, c–d. southeastern Hudson Bay (SEHB), and e–f. northeastern Hudson Bay (NEHB). Shaded envelopes show ±1 standard deviations for each variable. Thick segments within vertical profiles denote the halocline layer. Black circles in panels a., c., and e. mark the depth of the maximum salinity gradient (z_{SGM}; m).

5.4. Discussion

Regional salinity profiles indicate that the sub-surface layer of HJB is stably stratified, with freshwater, primarily river runoff, controlling salinity-driven stratification in summer (Figure 5.3; Figures S5.1–S5.3; Table 5.1; Table S5.1). In early summer, a fresh surface layer overlies saltier marine waters south of 60°N, forming shallow haloclines, particularly in James Bay and southeastern Hudson Bay, where buoyant RW overlies brine-enriched subsurface waters (Figures 5.2a, d, g; Figures 5.3a–d; Table S5.3).

The resulting, RW-driven, sea surface height gradient between southeastern and southwestern Hudson Bay drives a westward geostrophic current that strengthens haline stratification along the southern coast (Figures 5.2d, g; Ridenour et al., 2019a). Wind-driven anticyclonic circulation over southeastern Hudson Bay further reinforces stratification by advecting RW southward and southwestward (Figures 5.2d, g; Saucier et al., 2004; Ridenour et al., 2019a). This promotes freshwater convergence and downwelling in the Winisk Trough and southern and central Hudson Bay, where z_{SGM} is governed by residual brine (negative SIM fraction), indicating vertical mixing of surface freshwater (Figures 5.2d, g; Figures S5.1a–d; Figures S5.2a–b).

Comparatively deeper and saltier haloclines in northern HJB reflect weaker stratification due to reduced runoff and stronger influence of brine and saline inflows from Foxe Basin and Hudson Strait (Figures 5.2a, d; Figures 5.3e–f; Figures S5.2c–d; Figures S5.3a–d; Table S5.4; Jones and Anderson, 1994; Granskog et al., 2011). Nevertheless, RW continues to control z_{SGM}, implying northward advection from southern source regions driven by Coriolis deflection and mesoscale circulation features (Figure 5.2g; Table S5.4; Ridenour et al., 2019a).

In late summer, the northward transport through interior and coastal pathways becomes evident, intensifying RW-driven stratification in the northwest and SIM-driven stratification in the northeast (Figures 5.2e, h; Table S5.4; Ridenour et al., 2019a). This leads to a shallower halocline

in the north compared to southern HJB, where weaker stratification reflects declining river discharge and a subdued anticyclonic circulation cell (Figures 5.2b, e, h; Ridenour et al., 2019a).

However, in fall, wind-driven cyclonic circulation across HJB redirects freshwater from the interior toward the coast, augmenting coastal RW despite reduced discharge (St-Laurent et al., 2011; Dmitrenko et al., 2020; Basu et al., 2026). Coastal downwelling vertically redistributes this RW, deepening haloclines along the southern and eastern coasts and strengthening stratification (Figures 5.2c, f, i; Figures 5.3c–f; Figures S5.1a–f). Conversely, upwelling in freshwater-depleted offshore waters produces shallower haloclines, where stratification is governed by residual brine (Figures 5.2c, f, i; Tables 5.2, S5.2).

Nevertheless, RW continues to control stratification in northern HJB during fall, particularly in the Narrows and northeastern Hudson Bay, implying export of RW and SIM from weakly stratified James Bay along the eastern coast into the Labrador Sea via southern Hudson Strait (Figures 5.2f, i; Table S5.3; Straneo and Saucier, 2008). Thus, these seasonal patterns show that salinity-driven density stratification across HJB is not set by runoff and geostrophic circulation alone but also by its wind-driven redistribution.

As river discharge continues to rise and winds get stronger in HJB (Fazel-Rastgar et al., 2020; Feng et al., 2021), the projected increase in fall and winter runoff (Déry et al., 2016; Macdonald et al., 2018) is likely to further intensify stratification. Compounding this, hydroelectric regulation of major rivers has shifted freshwater delivery toward late fall and winter (Déry et al., 2016; McCullough et al, 2019), adding buoyancy during sea ice formation that can suppress ice production and further stabilize the water column. Such strengthened stratification is expected to impede deep-water formation in HJB and nutrient replenishment to the surface layer, thereby constraining primary production (Matthes et al., 2021; Barbedo et al., 2022) in the oligotrophic HJB (Lee et al., 2023; Guzzi et al., 2024).

5.5. Conclusion

We have a poor understanding of HJB deep-water renewal, which is thought to result from the inflow of Arctic/Atlantic water through the Hudson Strait and Foxe Basin, and from heat loss and brine rejection in coastal polynyas (Bruneau et al. 2021), but we do not know their relative importance. Our results demonstrate that HJB is fundamentally a salinity-dominated system, in

which near-freezing temperatures generate negative thermal expansion coefficients that reinforce, rather than erode, stratification for salinity < 24.7, while Arctic–Atlantic inflow exerts a minor influence. We show that river runoff sustains year-round stratification in HJB.

Contrary to the prevailing understanding, RW control on density stratification extends beyond coastal corridors into offshore and northern regions, where ice-driven convection should be most effective, suggesting a potential impediment to deep-water renewal during winter. As HJB becomes increasingly stratified and less ventilated, driven by rising runoff (Feng et al., 2021), regulated river flows (Déry et al., 2011), stronger winds (Fazel-Rastgar et al., 2020), longer ice-free seasons (Crawford et al., 2021; Stroeve at al., 2024), and more frequent cyclonic storms (Dmitrenko et al., 2021; Zhang et al., 2023) it may export greater volumes of fresh water to the North Atlantic.

Data availability

In situ data for salinity, oxygen isotope ratio, derived river water, sea-ice melt and sea water fractions for Hudson and James Bays were obtained from Basu and Guzzi, (2025).

Supplementary materials

Table S5.1: Seasonal contribution of salinity gradient ($\Delta S/\Delta z$; S m^{-1}) and temperature gradient ($\Delta\theta/\Delta z$; °C m^{-1}) to potential density gradient ($\Delta\rho_\theta/\Delta z$; kg m^{-3} m^{-1}) across water columns of Hudson and James Bays (HJB), evaluated using multiple linear regression analysis.

Season	Stations	Samples	α^a	β^b	γ^c	R^2 (model)	R^2 ($\Delta S/\Delta z$)	R^2 ($\Delta\theta/\Delta z$)	p-value	p-value ($\Delta S/\Delta z$)	p-value ($\Delta\theta/\Delta z$)
Early Summer	58	301	-0.07	0.78	0.00	0.99	0.99	0.90	< 0.001	< 0.001	< 0.001
Late Summer	12	16	-0.11	0.77	0.00	0.99	0.99	0.97	< 0.001	< 0.001	< 0.001
Fall	2	19	-0.09	0.78	0.00	0.99	0.98	0.92	< 0.001	< 0.001	< 0.001
All	72	336	-0.08	0.78	0.00	0.99	0.99	0.91	< 0.001	< 0.001	< 0.001

[a]Thermal expansion coefficient (kg m^{-3} °C^{-1})

[b]Haline contraction coefficient (kg m^{-3} S^{-1})

[c]y-intercept (kg m^{-3} m^{-1})

Table S5.2. Seasonal contribution of river water ($|\Delta RW/\Delta z|$; fraction m^{-1}) and sea-ice melt ($|\Delta SIM/\Delta z|$; fraction m^{-1}) gradients to salinity gradients ($\Delta S/\Delta z$; S m^{-1}) at the depth of maximum salinity gradient (z_{SGM}; m), across the Hudson and James Bay (HJB) evaluated using multiple linear regression analyses.

Season	Stations	β_{RW}^a	β_{SIM}^b	λ^c	R^2 (model)	R^2 ($\lvert\Delta RW/\Delta z\rvert$)	R^2 ($\lvert\Delta SIM/\Delta z\rvert$)	p-value (model)	p-value ($\lvert\Delta RW/\Delta z\rvert$)	p-value ($\lvert\Delta SIM/\Delta z\rvert$)
Early Summer	69	26.0	30.5	-0.01	0.94	0.89	0.53	< 0.001	< 0.001	< 0.001
Late Summer	54	25.9	27.3	-0.01	0.94	0.84	0.29	< 0.001	< 0.001	< 0.001
Fall	48	30.4	30.1	-0.02	0.95	0.88	0.92	< 0.001	< 0.001	< 0.001
All	171	26.1	29.9	-0.01	0.94	0.89	0.74	< 0.001	< 0.001	< 0.001

[a]Haline contraction coefficient: river water component (S fraction^{-1})

[b]Haline contraction coefficient: sea-ice melt component (S fraction^{-1})

[c]y-intercept (S m^{-1})

Table S5.3: Seasonal characteristics of the halocline in James Bay and south of 60° N in Hudson Bay.

Halocline Characteristics	Season	JB[a]		SEHB[b]		WT[c]		SHB[d]		SWHB[e]		CHB[f]	
		Mean	SD	Mean	SD	Mean	SD	Mean	SD	Mean	SD	Mean	SD
z_{SGM}[g] (m)	Early Summer	15.4	9.8	18.3	6.1	16.0	5.5	15.8	6.6	14.5	5.7	17.0	6.1
	Late Summer	19.7	13.6	35.0	23.5	–	–	48.0	11.3	33.3	15.3	–	–
	Fall	34.9	15.8	36.2	14.6	35.0	15.9	–	–	27.8	15.7	35.0	–
	All	24.9	15.9	28.2	16.8	28.2	15.9	23.9	16.5	23.5	14.3	21.5	10.3
S_{SGM}[h]	Early Summer	25.3	3.8	28.3	1.6	30.0	1.0	30.7	0.3	30.5	1.6	32.0	0.1
	Late Summer	23.0	3.8	29.6	1.1	–	–	31.4	0.5	30.4	1.1	–	–
	Fall	29.3	1.5	29.2	1.8	30.5	2.4	–	–	29.6	3.2	32.2	–
	All	25.9	4.2	28.9	1.6	30.3	2.0	30.9	0.4	30.0	2.6	32.0	0.2
ΔS[i]	Early Summer	2.8	–	3.4	–	2.9	–	1.7	–	1.2	–	0.6	–
	Late Summer	2.1	–	3.2	–	–	–	1.6	–	0.6	–	–	–
	Fall	4.6	–	3.0	–	3.4	–	–	–	2.7	–	2.8	–
	All	3.2	–	3.2	–	3.2	–	1.7	–	1.9	–	1.2	–
RW_{SGM}[j] (fraction)	Early Summer	0.221	0.123	0.139	0.052	0.096	0.010	0.091	0.037	0.085	0.035	0.058	0.015
	Late Summer	0.279	0.106	0.070	0.026	–	–	0.031	0.017	0.005	0.034	–	–
	Fall	0.119	0.041	0.121	0.040	0.095	0.057	–	–	0.102	0.118	0.007	–
	All	0.206	0.114	0.114	0.050	0.096	0.045	0.076	0.042	0.086	0.093	0.045	0.028
SIM_{SGM}[k] (fraction)	Early Summer	−0.001	0.012	−0.011	0.012	−0.018	0.032	−0.038	0.031	−0.024	0.032	−0.043	0.017
	Late Summer	0.013	0.037	0.021	0.012	–	–	0.004	0.002	0.064	0.005	–	–
	Fall	−0.021	0.018	−0.021	0.025	−0.034	0.020	–	–	−0.013	0.047	0.001	–
	All	−0.003	0.031	−0.005	0.023	−0.028	0.025	−0.027	0.033	−0.009	0.046	−0.032	0.026
$\lvert\Delta RW\rvert/(\lvert\Delta RW\rvert + \lvert\Delta SIM\rvert)_{SGM}$[l]	Early Summer	0.96	–	0.91	–	0.76	–	0.71	–	0.74	–	0.57	–
	Late Summer	0.92	–	0.77	–	–	–	0.88	–	0.30	–	–	–
	Fall	0.83	–	0.83	–	0.74	–	–	–	0.79	–	0.85	–
	All	0.90	–	0.86	–	0.75	–	0.72	–	0.73	–	0.58	–
$(\Delta S/\Delta z)_{SGM}$[m] (psu m^{-1})	Early Summer	0.64	0.63	0.17	0.09	0.33	0.17	0.24	0.13	0.40	0.47	0.06	0.05
	Late Summer	0.65	0.88	0.07	0.01	–	–	0.06	0.00	0.04	0.04	–	–
	Fall	0.15	0.08	0.20	0.17	0.13	0.04	–	–	0.40	0.73	0.12	–
	All	0.45	0.66	0.15	0.11	0.20	0.14	0.20	0.14	0.36	0.60	0.08	0.05
$(\Delta RW/\Delta z)_{SGM}$[n] (fraction m^{-1})	Early Summer	−0.0206	0.0242	−0.0032	0.0009	−0.0019	0.0011	−0.0031	0.0017	−0.0102	0.0127	−0.0004	0.0007
	Late Summer	−0.0215	0.0318	−0.0023	0.0013	–	–	−0.0007	0.0000	−0.0020	0.0017	–	–
	Fall	−0.0043	0.0027	−0.0062	0.0073	−0.0018	0.0011	–	–	−0.0062	0.0137	0.0012	–
	All	−0.0146	0.0239	−0.0038	0.0041	−0.0018	0.0011	−0.0025	0.0018	−0.0072	0.0126	−0.0000	0.0010
$(\Delta SIM/\Delta z)_{SGM}$[o] (fraction m^{-1})	Early Summer	0.0011	0.0066	−0.0019	0.0025	−0.0085	0.0045	−0.0046	0.0026	−0.0023	0.0027	−0.0016	0.0010
	Late Summer	0.0017	0.0072	−0.0001	0.0013	–	–	−0.0012	0.0000	0.0007	0.0014	–	–
	Fall	−0.0003	0.0010	0.0001	0.0023	−0.0022	0.0012	–	–	−0.0063	0.0183	−0.0052	–
	All	0.0008	0.0054	−0.0008	0.0023	−0.0045	0.0041	−0.0038	0.0027	−0.0042	0.0135	−0.0025	0.0020

[a]James Bay

[b]Southeastern Hudson Bay

[c]Winisk Trough

[d]Southern Hudson Bay

[e]Southwestern Hudson Bay

[f]Central Hudson Bay

[g]depth at salinity gradient maximum

[h]salinity at z_{SGM}

[i]salinity difference between top and bottom boundaries of the halocline

[j]river water fraction at z_{SGM}

[k]sea-ice melt fraction at z_{SGM}

[l]apparent river water influence

[m]vertical salinity gradient at z_{SGM}

[n]vertical river water gradient at z_{SGM}

[o]vertical sea-ice melt gradient at z_{SGM}

Table S5.4: Seasonal characteristics of the halocline north of 60° N in Hudson Bay and for Hudson Bay combined north and south.

Halocline Characteristics	Season	NHB[a]		NEHB[b]		NWHB[c]		NAR[d]		HB[e]	
		Mean	SD	Mean	SD	Mean	SD	Mean	SD	Mean	SD
z_{SGM}[f] (m)	Early Summer	40.0	26.5	43.3	28.9	33.8	20.3	67.5	25.0	27.3	20.6
	Late Summer	–	–	24.2	9.7	14.4	11.0	35.2	17.2	31.6	17.5
	Fall	30.0	0.0	50.0	–	–	–	25.0	21.2	31.7	15.0
	All	36.0	19.5	32.5	18.9	29.9	20.2	39.4	21.8	29.7	18.4
S_{SGM}[g]	Early Summer	31.2	1.8	30.8	2.0	32.4	0.6	32.4	0.3	31.0	1.8
	Late Summer	–	–	29.9	0.7	31.3	0.8	31.9	0.7	31.1	1.2
	Fall	32.0	0.2	31.6	–	–	–	31.5	0.9	30.1	2.6
	All	31.5	1.4	30.3	1.2	32.2	0.8	31.9	0.7	30.8	1.9
ΔS[h]	Early Summer	2.4	–	2.0	–	0.6	–	1.1	–	1.6	–
	Late Summer	–	–	3.6	–	0.4	–	1.5	–	1.8	–
	Fall	3.4	–	1.4	–	–	–	1.3	–	2.8	–
	All	2.8	–	2.9	–	0.5	–	1.4	–	2.0	–
RW_{SGM}[i] (fraction)	Early Summer	0.044	0.055	0.029	0.096	0.026	0.020	0.004	0.038	0.065	0.055
	Late Summer	–	–	0.058	0.011	0.017	0.016	−0.005	0.025	0.020	0.037
	Fall	0.007	0.018	0.002	–	–	–	0.012	0.055	0.088	0.091
	All	0.029	0.045	0.044	0.050	0.024	0.020	−0.003	0.029	0.058	0.067
SIM_{SGM}[j] (fraction)	Early Summer	−0.004	0.008	0.025	0.036	−0.025	0.026	−0.002	0.032	−0.019	0.029
	Late Summer	–	–	0.022	0.023	0.020	0.010	0.026	0.013	0.026	0.018
	Fall	0.009	0.024	0.028	–	–	–	0.019	0.027	−0.015	0.037
	All	0.001	0.015	0.024	0.024	−0.016	0.030	0.021	0.020	−0.005	0.035
$\lvert\Delta RW\rvert/(\lvert\Delta RW\rvert + \lvert\Delta SIM\rvert)_{SGM}$[k]	Early Summer	0.90	–	0.65	–	0.49	–	0.55	–	0.71	–
	Late Summer	–	–	0.70	–	0.47	–	0.44	–	0.56	–
	Fall	0.43	–	0.06	–	–	–	0.67	–	0.77	–
	All	0.77	–	0.66	–	0.48	–	0.48	–	0.70	–
$(\Delta S/\Delta z)_{SGM}$[l] (psu m^{-1})	Early Summer	0.09	0.05	0.16	0.22	0.05	0.05	0.02	0.01	0.17	0.25
	Late Summer	–	–	0.13	0.06	0.55	1.14	0.11	0.28	0.15	0.43
	Fall	0.09	0.01	0.06	–	–	–	0.10	0.08	0.25	0.50
	All	0.09	0.04	0.13	0.12	0.15	0.51	0.09	0.24	0.19	0.38
$(\Delta RW/\Delta z)_{SGM}$[m] (fraction m^{-1})	Early Summer	−0.0039	0.0043	−0.0061	0.0090	−0.0016	0.0023	−0.0012	0.0008	−0.0037	0.0064
	Late Summer	–	–	−0.0015	0.0019	−0.0114	0.0237	−0.0028	0.0061	−0.0034	0.0091
	Fall	−0.0010	0.0011	−0.0030	–	–	–	−0.0046	0.0024	−0.0045	0.0095
	All	−0.0028	0.0035	−0.0030	0.0050	−0.0036	0.0107	−0.0027	0.0054	−0.0038	0.0081
$(\Delta SIM/\Delta z)_{SGM}$[n] (fraction m^{-1})	Early Summer	0.0014	0.0044	0.0011	0.0022	0.0002	0.0014	0.0006	0.0006	−0.0016	0.0035
	Late Summer	–	–	−0.0027	0.0039	−0.0056	0.0120	−0.0007	0.0027	−0.0014	0.0048
	Fall	−0.0019	0.0007	0.0011	–	–	–	0.0015	0.0001	−0.0034	0.0122
	All	0.0001	0.0036	−0.0012	0.0037	−0.0009	0.0056	−0.0003	0.0025	−0.0020	0.0071

[a]Northern Hudson Bay

[b]Northeastern Hudson Bay

[c]Northwestern Hudson Bay

[d]Narrows

[e]Hudson Bay

[f]depth at salinity gradient maximum

[g] salinity at z_{SGM}

[h]salinity difference between top and bottom boundaries of the halocline

[i]river water fraction at z_{SGM}

[j]sea-ice melt fraction at z_{SGM}

[k]apparent river water influence

[l]vertical salinity gradient at z_{SGM}

[m]vertical river water gradient at z_{SGM}

[n]vertical sea-ice melt gradient at z_{SGM}

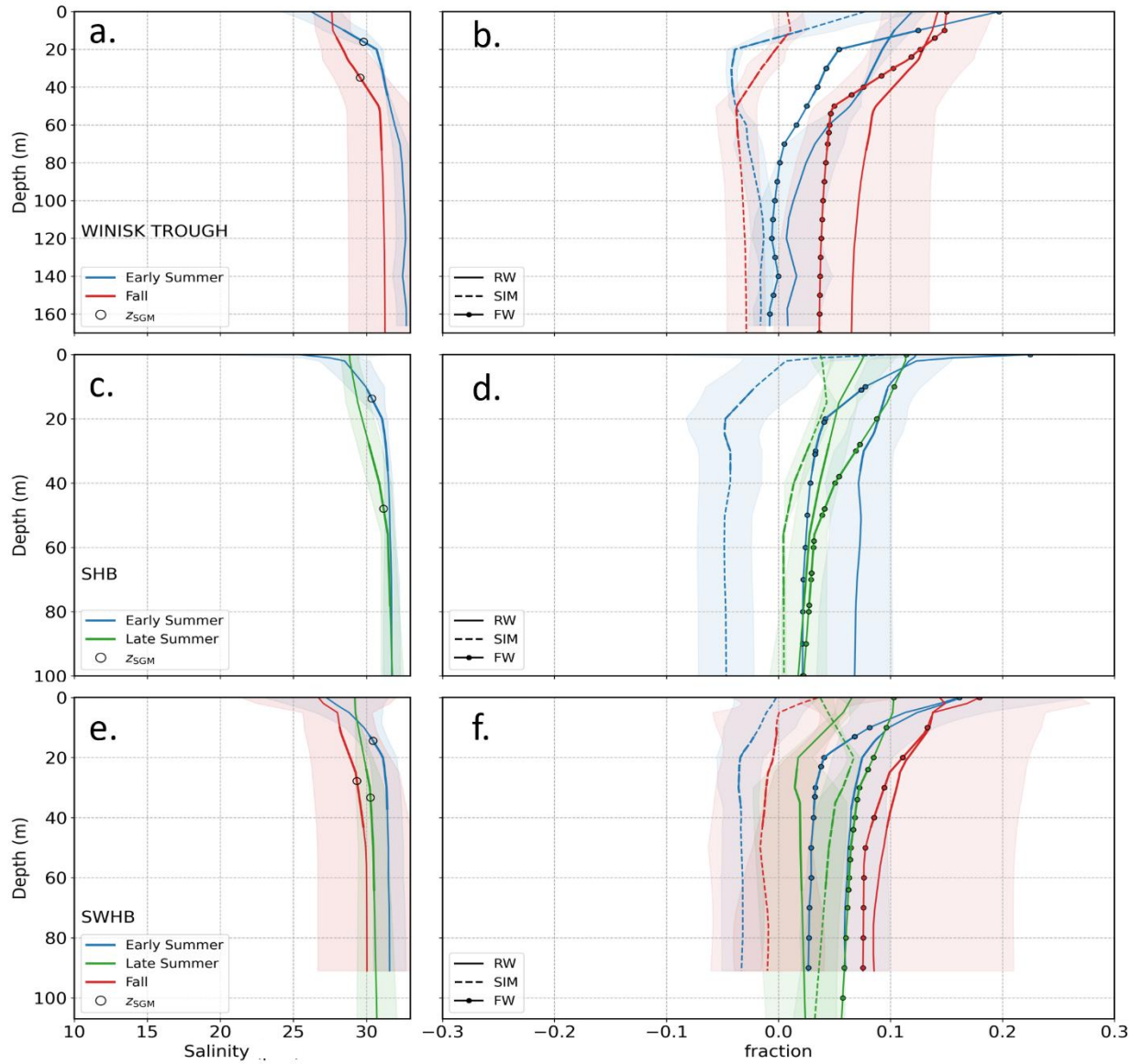


Figure S5.1: Vertical profiles of salinity, river water (RW), sea-ice melt (SIM), and freshwater (FW = RW + SIM) during early summer, late summer, and fall in a–b. Winisk Trough, c–d. southern Hudson Bay (SHB), and e–f. southwestern Hudson Bay (SWHB). Shaded envelopes show ±1 standard deviations for each variable. Thick segments within vertical profiles denote the halocline layer. Black circles in panels a, c, and e. mark the depth of the salinity gradient maximum (z_{SGM}; m).

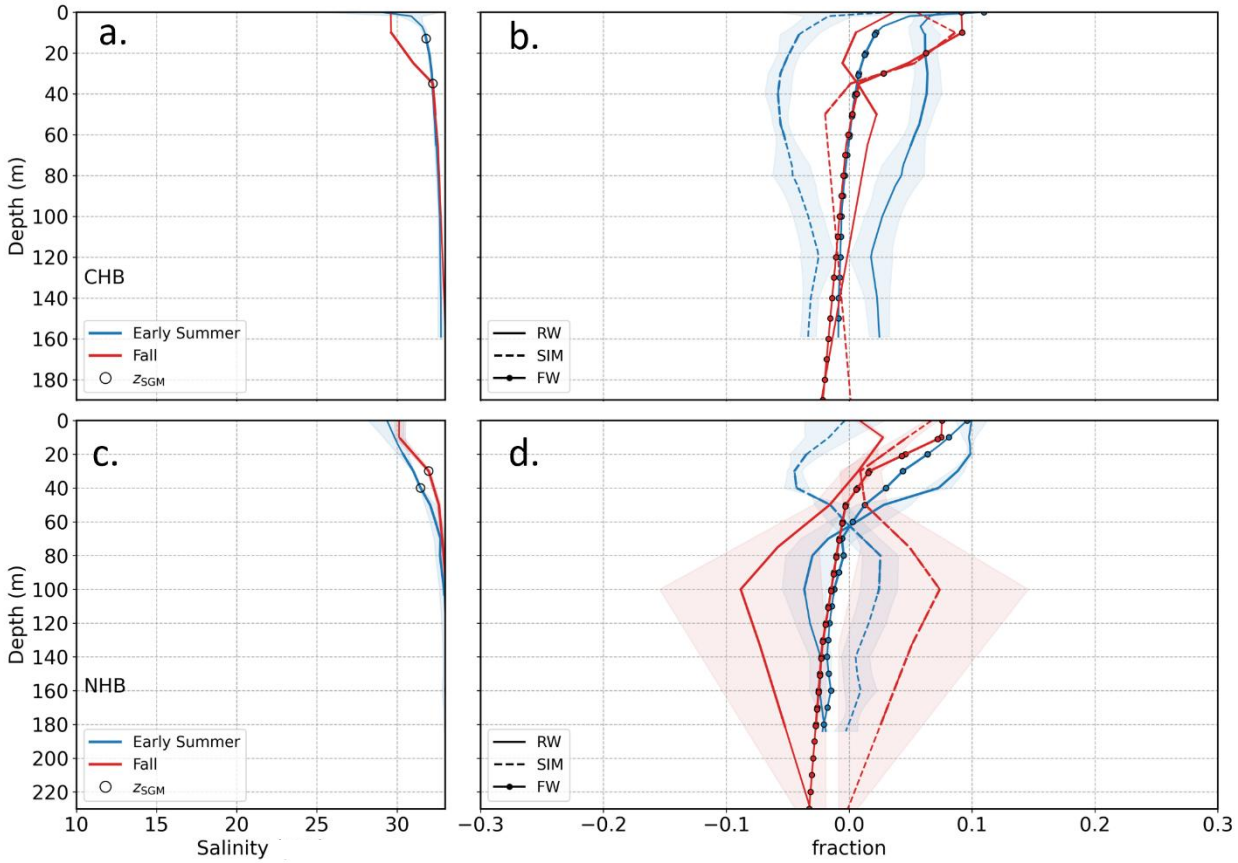


Figure S5.2: Vertical profiles of salinity, river water (RW), sea-ice melt (SIM), and freshwater (FW = RW + SIM) during early summer, late summer, and fall in a–b. central Hudson Bay (CHB), and c–d. northern Hudson Bay (NHB). Shaded envelopes show ±1 standard deviations for each variable. Thick segments within vertical profiles denote the halocline layer. Black circles in panels a, and c mark the depth of the salinity gradient maximum (z_{SGM}; m).

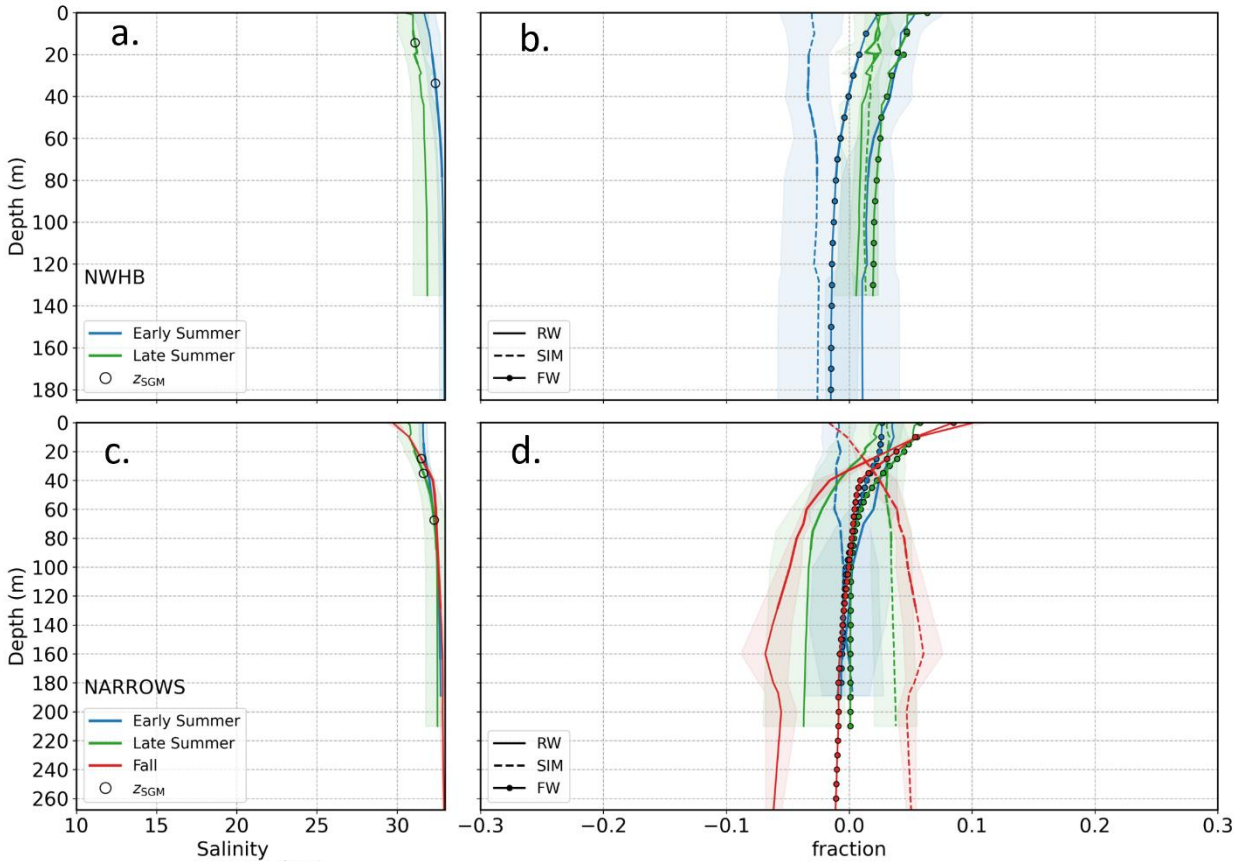


Figure S5.3: Vertical profiles of salinity, river water (RW), sea-ice melt (SIM), and freshwater (FW = RW + SIM) during early summer, late summer, and fall in a–b. northwestern Hudson Bay (NWHB), and c–d. Narrows. Shaded envelopes show ±1 standard deviations for each variable. Thick segments within vertical profiles denote the halocline layer. Black circles in panels a, and c mark the depth of the salinity gradient maximum (z_{SGM}; m).

6. Chapter – Summary and conclusions

6.1. Importance and main contribution

River water entering Hudson Bay and James Bay (HJB) accounts for approximately 10% of total Pan-Arctic river discharge, while runoff yield per unit area is about three times greater than that of the Arctic Ocean. Furthermore, increasing river discharge and hydropower regulation (Stadnyk et al., 2020), together with declining sea-ice cover (Stroeve et al., 2024), are altering the magnitude and seasonality of freshwater inputs to HJB. These changes in freshwater inputs influence the structure and stability of the water column, with implications for primary productivity, circulation, and water-mass exchange processes, underscoring the need to monitor freshwater sources within HJB.

The goal of this thesis is to advance understanding of freshwater sources, their seasonal distribution, and their role in controlling stratification in HJB. Existing field-based measurements of freshwater tracers, including salinity, temperature, total alkalinity, oxygen isotopes, chromophoric dissolved organic matter, and suspended solids, remain sparse and are restricted to ice-free periods during late summer and fall, typically from August onwards. Therefore, this thesis used satellite- and field-based approaches to quantify the contributions of river water and sea-ice melt and assess their influence on water-column stratification across HJB from early summer through fall.

This thesis demonstrated how river discharge, winds, and tidal processes transport and redistribute freshwater through estuaries and into the broader HJB marine system. Notably, anticyclonic winds redistributed freshwater offshore along eastern HJB, analogous to the freshwater accumulation associated with the Beaufort High circulation system in the western Arctic Ocean (Proshutinsky et al., 2009; Ridenour et al., 2019a). The results revealed increasing river water contributions and declining sea-ice melt contributions in surface waters during 2011–2019, establishing a robust baseline against which future changes in these Arctic marginal seas can be assessed.

A significant contribution of this thesis is the development of satellite-based approaches to distinguish and monitor river water and sea ice melt in HJB. These approaches provide improved capability for estuarine-, coastal- and basin-scale monitoring of freshwater dispersion in polar marine systems where field observations remain sparse. This thesis established that the seasonal

distribution of river water and sea-ice meltwater can be effectively captured using ocean color satellite observations in HJB.

This thesis also addressed a key research question of the Hudson Bay System Study (BaySys), a collaborative project involving the University of Manitoba, Manitoba Hydro, and NSERC: whether river water or sea-ice meltwater primarily controls stratification in Hudson Bay. The results demonstrate that RW, rather than SIM, is the primary freshwater control on water-column stratification across HJB, both in coastal regions and in northern Hudson Bay, where sea-ice processes were previously considered to play a greater role in stratification.

By improving understanding of freshwater sources and distribution in the understudied HJB, this thesis contributes to Pan-Arctic freshwater research. The findings provide important insight into how freshwater shifts in HJB may influence stratification, thus sea-ice variability, nutrient supply, and marine ecosystems. Hence, this thesis contributes to United Nations Sustainable Development Goal 14 by enhancing capacity for sustainable ocean observation through satellite- and field-based monitoring of freshwater and supporting the Ocean Decade (2021–2030) Challenge 2, focused on protecting and restoring marine ecosystems (Ausen et al., 2023).

6.2. Summary

6.2.1. Plume dispersion from the Nelson and Hayes rivers into Hudson Bay using satellite remote sensing of CDOM and suspended sediment

Chapter 3 of this thesis uses satellite observations of chromophoric dissolved organic matter (CDOM) and total suspended solids (TSS) derived from the blue and red bands of the Aqua-Moderate Resolution Imaging Spectroradiometer (MODIS) to trace the extent and transport direction of the combined Nelson River and Hayes River plume. A satellite-based approach was developed for plume delineation, thereby addressing thesis objectives i and ii.

This chapter demonstrated that satellite-derived CDOM varied in a conservative manner with Nelson/Hayes River discharge, which accounts for 14% of the basin's total annual river discharge (Déry et al., 2011, 2016). TSS originated from both riverine and coastal sources, making TSS unsuitable as an optical tracer of river runoff.

The mixing of Nelson River/Hayes River water within the plume was defined using quantile concentrations ($Q_{0.05}$–$Q_{0.95}$) rather than mean CDOM concentrations along the river-to-sea

gradient, because mean values limit the separation of riverine and marine water contributions within the plume. These quantile concentrations of riverine CDOM decreased exponentially from the Nelson/Hayes River mouth and approached an asymptotic limit that defined the offshore plume extent.

This dilution of riverine CDOM in southwestern Hudson Bay decreased with increasing river discharge, corresponding to the offshore spread of the Nelson/Hayes River plume, and vice versa. The CDOM asymptote of the 95th quantile was then used to estimate that 75% dilution of river water occurs within 125 km of the Nelson/Hayes River mouth, which varied by ±35 km between flood and ebb tides.

In addition, CDOM-weighted bearings along the freshwater-marine gradient demonstrated that anticyclonic winds exported the Nelson/Hayes River plume at an angle of 10°–50° towards central HJB, while cyclonic winds directed it eastward along the coast at an azimuth of 50°–80° from the river mouth. Thus, Chapter 3 of this thesis established an estuarine- and coastal-scale methodology for tracking river plume dispersion from satellites using CDOM as a freshwater tracer.

6.2.2. Satellite data trace seasonal freshwater dispersion in Hudson and James Bays

Since CDOM-rich river runoff can be tracked using Aqua-MODIS, Chapter 4 combined this approach with satellite-derived salinity from the Soil Moisture and Ocean Salinity (SMOS) mission to distinguish river water from sea-ice meltwater, which contains negligible CDOM. The CDOM-derived RW fraction was subtracted from the total freshwater fraction derived from SMOS salinity to estimate the SIM fraction. This approach enabled both river water and sea-ice meltwater to be mapped across HJB, thereby addressing thesis objective iii.

Satellite retrievals of RW and SIM were consistent with observed freshwater patterns in HJB. High RW fractions occurred in the southern and eastern regions due to large river inputs from the Hudson Bay Lowlands and James Bay, while SIM dominated central Hudson Bay and declined through summer, thereby addressing thesis objective iv.

The presence of river water in offshore HJB during summer suggests transport driven by anticyclonic circulation, similar to that observed for the Nelson River/Hayes River plume in

Chapter 3. However, in the fall, river water increased in the surface water along the southern and eastern coasts despite lower river discharge relative to summer.

Over the period 2011–2019, river water contributions in the surface waters of HJB increased by 0.5% yr^{-1}, while sea-ice meltwater declined by 0.3% yr^{-1}, indicating a shift in the freshwater regime across HJB and addressing thesis objective v. Thus, satellite observations in Chapter 4 captured the seasonal evolution and interannual changes of freshwater in the surface waters of HJB.

6.2.3. River water control of stratification in Arctic marginal seas

Evidence of rising river water fractions and declining sea-ice melt fractions in HJB surface waters was investigated in Chapter 5 to determine their control on stratification using in situ salinity and oxygen-isotope ratio ($\delta^{18}O$) profiles. River water gradients were found to control salinity gradients and thus stratification across seasons, whereas sea-ice melt gradients exerted a secondary, regionally variable influence, thereby addressing the final thesis objectives vi and vii.

In early summer, shallow river water-rich haloclines (15–18 m) occur in southern HJB, while northern haloclines (43–78 m) remain river water-depleted. By late summer, river- and sea-ice-melt-driven stratification develops in northern Hudson Bay, whereas southern regions become freshwater-depleted and less strongly stratified. Thus, from early to late summer, anticyclonic winds are likely to redistribute freshwater northward, leading to weaker stratification in the south than in the north.

However, in the fall, river water concentrates along the southern and eastern coasts, strengthening stratification, consistent with satellite observations in Chapter 4. This re-emergence of freshwater-driven stratification suggests that cyclonic winds drive offshore waters toward the coast, forming an alongshore river water corridor (Granskog et al., 2009; Dmitrenko et al., 2020). This onshore transport explains the increase in surface RW despite reduced summer discharge observed in Chapter 4.

In contrast, northern HJB remains relatively freshwater-depleted in fall, with a deep halocline (180 m) compared to shallow, freshwater-dominated haloclines (30 m) in southern HJB. Nevertheless, RW dominates stratification in northern Hudson Bay across all seasons, contrary to the traditional view of sea-ice-driven control.

The findings of Chapter 5 suggest that projected increases in winter river discharge, both natural and regulated (Macdonald et al., 2018; Stadnyk et al., 2020), are likely to enhance stratification and may impact deep-water formation, with implications for nutrient supply, primary productivity, carbon cycling, and freshwater export from HJB to the Labrador Sea.

6.3. Limitations and future works

- **Use state-of-the-art satellite observations** from Sentinel-2/3, PACE, and SWOT to improve surface freshwater-source discrimination and quantify river-water and sea-ice-meltwater volumes, storage, and transport at high spatial and temporal resolution.
- **Better characterize uncertainties in satellite-derived freshwater tracers** through CDOM degradation experiments, high-latitude atmospheric correction, improved cold-water salinity retrievals, multi-sensor data fusion and machine learning for gap filling due to clouds/sea ice, and robust end-member representation for isotope-based freshwater estimates.
- **Expand year-round in situ observations** of freshwater tracers and hydrography throughout the water column to overcome the surface limitation of satellites, particularly during fall and winter, to investigate the freshwater cycle, deep-water formation using moorings, ice-tethered profilers, and autonomous platforms such as Biogeochemical-Argo floats.
- **Use coupled hydrodynamic–biogeochemical models** along with observations to determine how changing hydrography and river regulation affect stratification, deep-water renewal, nutrient supply, and primary productivity.

References

Aagaard, K., & Carmack, E. C. (1989). The role of sea ice and other fresh water in the Arctic circulation. *Journal of Geophysical Research: Oceans*, *94*(C10), 14485–14498. https://doi.org/10.1029/JC094iC10p14485

Aagaard, K., Coachman, L. K., & Carmack, E. (1981). On the halocline of the Arctic Ocean. *Deep Sea Research Part A. Oceanographic Research Papers*, *28*(6), 529–545. https://doi.org/10.1016/0198-0149(81)90115-1

Ahmed, M. M. M., Else, B. G. T., Butterworth, B., Capelle, D. W., Guéguen, C., Miller, L. A., Meilleur, C., & Papakyriakou, T. (2021). Widespread surface water *p* CO2 undersaturation during ice-melt season in an Arctic continental shelf sea (Hudson Bay, Canada). *Elementa: Science of the Anthropocene*, *9*(1), 00130. https://doi.org/10.1525/elementa.2020.00130

Ahmed, M. M. M., Else, B. G. T., Capelle, D., Miller, L. A., & Papakyriakou, T. (2020). Underestimation of surface *p* CO2 and air-sea CO2 fluxes due to freshwater stratification in an Arctic shelf sea, Hudson Bay. *Elementa: Science of the Anthropocene*, *8*(1), 084. https://doi.org/10.1525/elementa.084

Anderson, L. G., Jutterström, S., Kaltin, S., Jones, E. P., & Björk, G. (2004). Variability in river runoff distribution in the Eurasian Basin of the Arctic Ocean. *Journal of Geophysical Research: Oceans*, *109*(C1), 2003JC001773. https://doi.org/10.1029/2003JC001773

Andrews, J., Babb, D., & Barber, D. G. (2018). Climate change and sea ice: Shipping in Hudson Bay, Hudson Strait, and Foxe Basin (1980–2016). *Elementa: Science of the Anthropocene*, *6*, 19. https://doi.org/10.1525/elementa.281

Ardyna, M., & Arrigo, K. R. (2020). Phytoplankton dynamics in a changing Arctic Ocean. *Nature Climate Change*, *10*(10), 892–903. https://doi.org/10.1038/s41558-020-0905-y

Ardyna, M., Babin, M., Gosselin, M., Devred, E., Rainville, L., & Tremblay, J. (2014). Recent Arctic Ocean sea ice loss triggers novel fall phytoplankton blooms. *Geophysical Research Letters*, *41*(17), 6207–6212. https://doi.org/10.1002/2014GL061047

Armitage, T. W. K., Bacon, S., Ridout, A. L., Thomas, S. F., Aksenov, Y., & Wingham, D. J. (2016). Arctic sea surface height variability and change from satellite radar altimetry and GRACE, 2003–2014. *Journal of Geophysical Research: Oceans*, *121*(6), 4303–4322. https://doi.org/10.1002/2015JC011579

Arrigo, K. R., Van Dijken, G., & Pabi, S. (2008). Impact of a shrinking Arctic ice cover on marine primary production. *Geophysical Research Letters*, *35*(19), 2008GL035028. https://doi.org/10.1029/2008GL035028

Ausen, E. L., Barber, D. G., Basu, A., Ehn, J., Walker, D., Dalman, L., & Marcoux, M. (2023). River-influenced beluga (*Delphinapterus leucas)* summer habitat use in western Hudson Bay, Canada. *Arctic Science*, *9*(4), 869–885. https://doi.org/10.1139/as-2022-0040

Babin, M., Stramski, D., Ferrari, G. M., Claustre, H., Bricaud, A., Obolensky, G., & Hoepffner, N. (2003). Variations in the light absorption coefficients of phytoplankton, nonalgal particles, and dissolved organic matter in coastal waters around Europe. *Journal of Geophysical Research: Oceans*, *108*(C7), 2001JC000882. https://doi.org/10.1029/2001JC000882

Bailey, S. W., & Werdell, P. J. (2006). A multi-sensor approach for the on-orbit validation of ocean color satellite data products. *Remote Sensing of Environment*, *102*(1–2), 12–23. https://doi.org/10.1016/j.rse.2006.01.015

Bainbridge, Z. T., Wolanski, E., Álvarez-Romero, J. G., Lewis, S. E., & Brodie, J. E. (2012). Fine sediment and nutrient dynamics related to particle size and floc formation in a Burdekin River flood plume, Australia. *Marine Pollution Bulletin*, *65*(4–9), 236–248. https://doi.org/10.1016/j.marpolbul.2012.01.043

Balasubramanian, S. V., Pahlevan, N., Smith, B., Binding, C., Schalles, J., Loisel, H., Gurlin, D., Greb, S., Alikas, K., Randla, M., Bunkei, M., Moses, W., Nguyễn, H., Lehmann, M. K., O'Donnell, D., Ondrusek, M., Han, T.-H., Fichot, C. G., Moore, T., & Boss, E. (2020). Robust algorithm for estimating total suspended solids (TSS) in inland and nearshore coastal waters. *Remote Sensing of Environment*, *246*, 111768. https://doi.org/10.1016/j.rse.2020.111768

Bamber, J. L., Westaway, R. M., Marzeion, B., & Wouters, B. (2018). The land ice contribution to sea level during the satellite era. *Environmental Research Letters*, *13*(6), 063008. https://doi.org/10.1088/1748-9326/aac2f0

Barbedo, L., Bélanger, S., Lukovich, J. V., Myers, P. G., & Tremblay, J.-É. (2022). Atmospheric forcing and photo-acclimation of phytoplankton fall blooms in Hudson Bay. *Elementa: Science of the Anthropocene*, *10*(1), 00067. https://doi.org/10.1525/elementa.2021.00067

Barber, D. G., Harasyn, M. L., Babb, D. G., Capelle, D., McCullough, G., Dalman, L. A., Matthes, L. C., Ehn, J. K., Kirillov, S., Kuzyk, Z., Basu, A., Fayak, M., Schembri, S., Papkyriakou, T., Ahmed, M. M. M., Else, B., Guéguen, C., Meilleur, C., Dmitrenko, I., … Sydor, K. (2021). Sediment-laden sea ice in southern Hudson Bay: Entrainment, transport, and biogeochemical implications. *Elementa: Science of the Anthropocene*, *9*(1), 00108. https://doi.org/10.1525/elementa.2020.00108

Barrett, A. P., Stroeve, J. C., & Serreze, M. C. (2020). Arctic Ocean Precipitation From Atmospheric Reanalyses and Comparisons With North Pole Drifting Station Records. *Journal of Geophysical Research: Oceans*, *125*(1), e2019JC015415. https://doi.org/10.1029/2019JC015415

Basu, A., Bélanger, S., Kuzyk, Z. Z. A., Singh, R. K., Mukherjee, S., Larouche, P., Guzzi, A. C., Ausen, E. L., McCullough, G., & Ehn, J. K. (2026). Satellite Data Trace Seasonal Freshwater Dispersion in Hudson and James Bays. *Geophysical Research Letters*, *53*(2), e2025GL116442. https://doi.org/10.1029/2025GL116442

Basu, A., & Guzzi, A. (2025). *Satellite Data Trace Seasonal Freshwater Dispersion in Hudson and James Bays: Field and Matchup Data* [Dataset]. University of Manitoba. https://doi.org/10.34992/330G-2C55

Basu, A., McCullough, G., Bélanger, S., Mukhopadhyay, A., Doxaran, D., Sydor, K., Barber, D., & Ehn, J. (2023). Plume dispersion from the Nelson and Hayes rivers into Hudson Bay using satellite remote sensing of CDOM and suspended sediment. *Elementa: Science of the Anthropocene*, *11*(1), 00076. https://doi.org/10.1525/elementa.2022.00076

Bélanger, S., Babin, M., & Larouche, P. (2008). An empirical ocean color algorithm for estimating the contribution of chromophoric dissolved organic matter to total light absorption in optically

complex waters. *Journal of Geophysical Research: Oceans*, *113*(C4), 2007JC004436. https://doi.org/10.1029/2007JC004436

Bélanger, S., Ehn, J. K., & Babin, M. (2007). Impact of sea ice on the retrieval of water-leaving reflectance, chlorophyll a concentration and inherent optical properties from satellite ocean color data. *Remote Sensing of Environment*, *111*(1), 51–68. https://doi.org/10.1016/j.rse.2007.03.013

Bergeron, M., & Tremblay, J.-É. (2014). Shifts in biological productivity inferred from nutrient drawdown in the southern Beaufort Sea (2003-2011) and northern Baffin Bay (1997-2011), Canadian Arctic. *Geophysical Research Letters*, *41*(11), 3979–3987. https://doi.org/10.1002/2014GL059649

Bevis, M., Harig, C., Khan, S. A., Brown, A., Simons, F. J., Willis, M., Fettweis, X., Van Den Broeke, M. R., Madsen, F. B., Kendrick, E., Caccamise, D. J., Van Dam, T., Knudsen, P., & Nylen, T. (2019). Accelerating changes in ice mass within Greenland, and the ice sheet's sensitivity to atmospheric forcing. *Proceedings of the National Academy of Sciences*, *116*(6), 1934–1939. https://doi.org/10.1073/pnas.1806562116

Bhatia, M. P., Das, S. B., Kujawinski, E. B., Henderson, P., Burke, A., & Charette, M. A. (2011). Seasonal evolution of water contributions to discharge from a Greenland outlet glacier: Insight from a new isotope-mixing model. *Journal of Glaciology*, *57*(205), 929–941. https://doi.org/10.3189/002214311798043861

Bhatia, M. P., Das, S. B., Xu, L., Charette, M. A., Wadham, J. L., & Kujawinski, E. B. (2013). Organic carbon export from the Greenland ice sheet. *Geochimica et Cosmochimica Acta*, *109*, 329–344. https://doi.org/10.1016/j.gca.2013.02.006

Bintanja, R., & Andry, O. (2017). Towards a rain-dominated Arctic. *Nature Climate Change*, *7*(4), 263–267. https://doi.org/10.1038/nclimate3240

Bintanja, R., Van Der Wiel, K., Van Der Linden, E. C., Reusen, J., Bogerd, L., Krikken, F., & Selten, F. M. (2020). Strong future increases in Arctic precipitation variability linked to poleward moisture transport. *Science Advances*, *6*(7), eaax6869. https://doi.org/10.1126/sciadv.aax6869

Biskaborn, B. K., Smith, S. L., Noetzli, J., Matthes, H., Vieira, G., Streletskiy, D. A., Schoeneich, P., Romanovsky, V. E., Lewkowicz, A. G., Abramov, A., Allard, M., Boike, J., Cable, W. L.,

Christiansen, H. H., Delaloye, R., Diekmann, B., Drozdov, D., Etzelmüller, B., Grosse, G., … Lantuit, H. (2019). Permafrost is warming at a global scale. *Nature Communications*, *10*(1), 264. https://doi.org/10.1038/s41467-018-08240-4

Bricaud, A., & Morel, A. (1986). Light attenuation and scattering by phytoplanktonic cells: A theoretical modeling. *Applied Optics*, *25*(4), 571. https://doi.org/10.1364/AO.25.000571

Bricaud, A., Morel, A., & Prieur, L. (1981). Absorption by dissolved organic matter of the sea (yellow substance) in the UV and visible domains1. *Limnology and Oceanography*, *26*(1), 43–53. https://doi.org/10.4319/lo.1981.26.1.0043

Brown, K. A., Holding, J. M., & Carmack, E. C. (2020). Understanding Regional and Seasonal Variability Is Key to Gaining a Pan-Arctic Perspective on Arctic Ocean Freshening. *Frontiers in Marine Science*, *7*, 606. https://doi.org/10.3389/fmars.2020.00606

Bruneau, J., Babb, D., Chan, W., Kirillov, S., Ehn, J., Hanesiak, J., & Barber, D. G. (2021). The ice factory of Hudson Bay. *Elementa: Science of the Anthropocene*, *9*(1), 00168. https://doi.org/10.1525/elementa.2020.00168

Burban, P., Lick, W., & Lick, J. (1989). The flocculation of fine-grained sediments in estuarine waters. *Journal of Geophysical Research: Oceans*, *94*(C6), 8323–8330. https://doi.org/10.1029/JC094iC06p08323

Cai, W.-J., Chen, L., Chen, B., Gao, Z., Lee, S. H., Chen, J., Pierrot, D., Sullivan, K., Wang, Y., Hu, X., Huang, W.-J., Zhang, Y., Xu, S., Murata, A., Grebmeier, J. M., Jones, E. P., & Zhang, H. (2010). Decrease in the CO_2 Uptake Capacity in an Ice-Free Arctic Ocean Basin. *Science*, *329*(5991), 556–559. https://doi.org/10.1126/science.1189338

Campanelli, A., Pascucci, S., Betti, M., Grilli, F., Marini, M., Pignatti, S., & Guicciardi, S. (2017). An Empirical Ocean Colour Algorithm for Estimating the Contribution of Coloured Dissolved Organic Matter in North-Central Western Adriatic Sea. *Remote Sensing*, *9*(2), 180. https://doi.org/10.3390/rs9020180

Capelle, D. W., Kuzyk, Z. Z. A., Papakyriakou, T., Guéguen, C., Miller, L. A., & Macdonald, R. W. (2020). Effect of terrestrial organic matter on ocean acidification and CO2 flux in an Arctic shelf sea. *Progress in Oceanography*, *185*, 102319. https://doi.org/10.1016/j.pocean.2020.102319

Carmack, E. C. (2007). The alpha/beta ocean distinction: A perspective on freshwater fluxes, convection, nutrients and productivity in high-latitude seas. *Deep Sea Research Part II: Topical Studies in Oceanography*, *54*(23–26), 2578–2598. https://doi.org/10.1016/j.dsr2.2007.08.018

Carmack, E. C., Williams, W. J., Zimmermann, S. L., & McLaughlin, F. A. (2012). The Arctic Ocean warms from below. *Geophysical Research Letters*, *39*(7), 2012GL050890. https://doi.org/10.1029/2012GL050890

Carmack, E. C., Yamamoto-Kawai, M., Haine, T. W. N., Bacon, S., Bluhm, B. A., Lique, C., Melling, H., Polyakov, I. V., Straneo, F., Timmermans, M. -L., & Williams, W. J. (2016). Freshwater and its role in the Arctic Marine System: Sources, disposition, storage, export, and physical and biogeochemical consequences in the Arctic and global oceans. *Journal of Geophysical Research: Biogeosciences*, *121*(3), 675–717. https://doi.org/10.1002/2015JG003140

Carmack, E., & Wassmann, P. (2006). Food webs and physical–biological coupling on pan-Arctic shelves: Unifying concepts and comprehensive perspectives. *Progress in Oceanography*, *71*(2–4), 446–477. https://doi.org/10.1016/j.pocean.2006.10.004

Carmack, E., Winsor, P., & Williams, W. (2015). The contiguous panarctic Riverine Coastal Domain: A unifying concept. *Progress in Oceanography*, *139*, 13–23. https://doi.org/10.1016/j.pocean.2015.07.014

Carton, J. A., Ding, Y., & Arrigo, K. R. (2015). The seasonal cycle of the Arctic Ocean under climate change. *Geophysical Research Letters*, *42*(18), 7681–7686. https://doi.org/10.1002/2015GL064514

Cast, Z. I., Serreze, M. C., Cassano, E. N., & Barrett, A. P. (2026). Seasonal characteristics and trends in precipitation partitioning in the Arctic. *The Cryosphere*, *20*(4), 2127–2141. https://doi.org/10.5194/tc-20-2127-2026

Castro De La Guardia, L., Hu, X., & Myers, P. G. (2015). Potential positive feedback between Greenland Ice Sheet melt and Baffin Bay heat content on the west Greenland shelf. *Geophysical Research Letters*, *42*(12), 4922–4930. https://doi.org/10.1002/2015GL064626

Challet, F., Herbaut, C., Houssais, M. -N., & Meneghello, G. (2025). Weakened Stratification Across the Eurasian Basin Enables Enhanced Vertical Spreading of Atlantic Water. *Journal of Geophysical Research: Oceans*, *130*(11), e2025JC022632. https://doi.org/10.1029/2025JC022632

Charette, M. A., Kipp, L. E., Jensen, L. T., Dabrowski, J. S., Whitmore, L. M., Fitzsimmons, J. N., Williford, T., Ulfsbo, A., Jones, E., Bundy, R. M., Vivancos, S. M., Pahnke, K., John, S. G., Xiang, Y., Hatta, M., Petrova, M. V., Heimbürger-Boavida, L., Bauch, D., Newton, R., … Zhang, R. (2020). The Transpolar Drift as a Source of Riverine and Shelf-Derived Trace Elements to the Central Arctic Ocean. *Journal of Geophysical Research: Oceans*, *125*(5), e2019JC015920. https://doi.org/10.1029/2019JC015920

Cheng, K., Shu, Q., Wang, Q., Song, Z., He, Y., Wang, S., Pan, R., Bi, H., & Qiao, F. (2025). Distinct Impacts of Increased Atlantic and Pacific Ocean Heat Transport on Arctic Ocean Warming and Sea Ice Decline. *Journal of Geophysical Research: Oceans*, *130*(3), e2024JC021178. https://doi.org/10.1029/2024JC021178

Clair, T. A., Ehrman, J., & Higuchi, K. (1998). Changes to the runoff of Canadian ecozones under a doubled CO_2 atmosphere. *Canadian Journal of Fisheries and Aquatic Sciences*, *55*(11), 2464–2477. https://doi.org/10.1139/f98-129

Coachman, L. K., & Aagaard, K. (1966). ON THE WATER EXCHANGE THROUGH BERING STRAIT. *Limnology and Oceanography*, *11*(1), 44–59. https://doi.org/10.4319/lo.1966.11.1.0044

Crawford, A., Stroeve, J., Smith, A., & Jahn, A. (2021). Arctic open-water periods are projected to lengthen dramatically by 2100. *Communications Earth & Environment*, *2*(1), 109. https://doi.org/10.1038/s43247-021-00183-x

Danielson, S. L., Ahkinga, O., Ashjian, C., Basyuk, E., Cooper, L. W., Eisner, L., Farley, E., Iken, K. B., Grebmeier, J. M., Juranek, L., Khen, G., Jayne, S. R., Kikuchi, T., Ladd, C., Lu, K., McCabe, R. M., Moore, G. W. K., Nishino, S., Ozenna, F., … Weingartner, T. J. (2020). Manifestation and consequences of warming and altered heat fluxes over the Bering and Chukchi Sea continental shelves. *Deep Sea Research Part II: Topical Studies in Oceanography*, *177*, 104781. https://doi.org/10.1016/j.dsr2.2020.104781

De Andrés, E., Umbert, M., Sánchez-Urrea, M., González-Gambau, V., Olmedo, E., Gabarró, C., & Elosegui, P. (2025). Sea Ice Meltwater in the Beaufort Gyre: A Comprehensive Analysis Using Sea Surface Salinity Data From SMOS. *Journal of Geophysical Research: Oceans*, *130*(3), e2023JC020733. https://doi.org/10.1029/2023JC020733

Déry, S. J., Mlynowski, T. J., Hernández-Henríquez, M. A., & Straneo, F. (2011). Interannual variability and interdecadal trends in Hudson Bay streamflow. *Journal of Marine Systems*, *88*(3), 341–351. https://doi.org/10.1016/j.jmarsys.2010.12.002

Déry, S. J., Stadnyk, T. A., MacDonald, M. K., & Gauli-Sharma, B. (2016). Recent trends and variability in river discharge across northern Canada. *Hydrology and Earth System Sciences*, *20*(12), 4801–4818. https://doi.org/10.5194/hess-20-4801-2016

Déry, S. J., Stadnyk, T. A., MacDonald, M. K., Koenig, K. A., & Guay, C. (2018). Flow alteration impacts on Hudson Bay river discharge. *Hydrological Processes*, *32*(24), 3576–3587. https://doi.org/10.1002/hyp.13285

Déry, S. J., & Wood, E. F. (2005). Decreasing river discharge in northern Canada. *Geophysical Research Letters*, *32*(10), 2005GL022845. https://doi.org/10.1029/2005GL022845

Deschepper, I., Myers, P. G., Lavoie, D., Papakyriakou, T., & Maps, F. (2023). Understanding the Physical Forcings Behind the Biogeochemical Productivity of the Hudson Bay Complex. *Journal of Geophysical Research: Biogeosciences*, *128*(6), e2022JG007294. https://doi.org/10.1029/2022JG007294

Dmitrenko, I. A., Kirillov, S. A., Babb, D. G., Kuzyk, Z. Z. A., Basu, A., Ehn, J. K., Sydor, K., & Barber, D. G. (2021). Storm-driven hydrography of western Hudson Bay. *Continental Shelf Research*, *227*, 104525. https://doi.org/10.1016/j.csr.2021.104525

Dmitrenko, I. A., Myers, P. G., Kirillov, S. A., Babb, D. G., Volkov, D. L., Lukovich, J. V., Tao, R., Ehn, J. K., Sydor, K., & Barber, D. G. (2020). Atmospheric vorticity sets the basin-scale circulation in Hudson Bay. *Elementa: Science of the Anthropocene*, *8*(1), 049. https://doi.org/10.1525/elementa.049

Dorji, P., & Fearns, P. (2017). Impact of the spatial resolution of satellite remote sensing sensors in the quantification of total suspended sediment concentration: A case study in turbid waters of

Northern Western Australia. *PLOS ONE*, *12*(4), e0175042. https://doi.org/10.1371/journal.pone.0175042

Dou, T. F., Pan, S. F., Bintanja, R., & Xiao, C. D. (2022). More Frequent, Intense, and Extensive Rainfall Events in a Strongly Warming Arctic. *Earth's Future*, *10*(10), e2021EF002378. https://doi.org/10.1029/2021EF002378

Doxaran, D., Cherukuru, R. C. N., & Lavender, S. J. (2005). Use of reflectance band ratios to estimate suspended and dissolved matter concentrations in estuarine waters. *International Journal of Remote Sensing*, *26*(8), 1763–1769. https://doi.org/10.1080/01431160512331314092

Doxaran, D., Ehn, J., Bélanger, S., Matsuoka, A., Hooker, S., & Babin, M. (2012). Optical characterisation of suspended particles in the Mackenzie River plume (Canadian Arctic Ocean) and implications for ocean colour remote sensing. *Biogeosciences*, *9*(8), 3213–3229. https://doi.org/10.5194/bg-9-3213-2012

Dunbar, M. J. (1993). Hudson Bay has too much fresh water. *The Center for Climate and Global Change Research–McGill University*, *4*, 12-13.

Eastwood, R. A., Macdonald, R. W., Ehn, J. K., Heath, J., Arragutainaq, L., Myers, P. G., Barber, D. G., & Kuzyk, Z. A. (2020). Role of River Runoff and Sea Ice Brine Rejection in Controlling Stratification Throughout Winter in Southeast Hudson Bay. *Estuaries and Coasts*, *43*(4), 756–786. https://doi.org/10.1007/s12237-020-00698-0

Ehn, J. K., Reynolds, R. A., Stramski, D., Doxaran, D., Lansard, B., & Babin, M. (2019). Patterns of suspended particulate matter across the continental margin in the Canadian Beaufort Sea during summer. *Biogeosciences*, *16*(7), 1583–1605. https://doi.org/10.5194/bg-16-1583-2019

Ekwurzel, B., Schlosser, P., Mortlock, R. A., Fairbanks, R. G., & Swift, J. H. (2001). River runoff, sea ice meltwater, and Pacific water distribution and mean residence times in the Arctic Ocean. *Journal of Geophysical Research: Oceans*, *106*(C5), 9075–9092. https://doi.org/10.1029/1999JC000024

Else, B. G. T., Galley, R. J., Lansard, B., Barber, D. G., Brown, K., Miller, L. A., Mucci, A., Papakyriakou, T. N., Tremblay, J. -É., & Rysgaard, S. (2013). Further observations of a decreasing

atmospheric CO_2 uptake capacity in the Canada Basin (Arctic Ocean) due to sea ice loss. *Geophysical Research Letters*, *40*(6), 1132–1137. https://doi.org/10.1002/grl.50268

Else, B. G. T., Papakyriakou, T. N., Granskog, M. A., & Yackel, J. J. (2008). Observations of sea surface $f\,CO_2$ distributions and estimated air-sea CO_2 fluxes in the Hudson Bay region (Canada) during the open water season. *Journal of Geophysical Research: Oceans*, *113*(C8), 2007JC004389. https://doi.org/10.1029/2007JC004389

Else, B. G. T., Yackel, J. J., & Papakyriakou, T. N. (2008). Application of satellite remote sensing techniques for estimating air–sea CO2 fluxes in Hudson Bay, Canada during the ice-free season. *Remote Sensing of Environment*, *112*(9), 3550–3562. https://doi.org/10.1016/j.rse.2008.04.013

Environment Canada and Department of Fisheries and Oceans. (1992). Federal Ecological Monitoring Program Final Report (vol. 1). Environment Canada, Conservation and Protection Western and Northern Region, and Department of Fisheries and Oceans, Central and Arctic Region: 1–58.

Estrada, R., Harvey, M., Gosselin, M., Starr, M., Galbraith, P. S., & Straneo, F. (2012). Late-summer zooplankton community structure, abundance, and distribution in the Hudson Bay system (Canada) and their relationships with environmental conditions, 2003–2006. *Progress in Oceanography*, *101*(1), 121–145. https://doi.org/10.1016/j.pocean.2012.02.003

Évrard, A., Fink-Mercier, C., Galindo, V., Neumeier, U., Gosselin, M., & Xie, H. (2023). Regulated vs. unregulated rivers: Impacts on CDOM dynamics in the eastern James Bay. *Marine Chemistry*, *256*, 104309. https://doi.org/10.1016/j.marchem.2023.104309

Fazel-Rastgar, F. (2020). Seasonal Analysis of Atmospheric Changes in Hudson Bay during 1998-2018. *American Journal of Climate Change*, *09*(02), 100–122. https://doi.org/10.4236/ajcc.2020.92008

Feng, D., Gleason, C. J., Lin, P., Yang, X., Pan, M., & Ishitsuka, Y. (2021). Recent changes to Arctic river discharge. *Nature Communications*, *12*(1), 6917. https://doi.org/10.1038/s41467-021-27228-1

Fichot, C. G., Kaiser, K., Hooker, S. B., Amon, R. M. W., Babin, M., Bélanger, S., Walker, S. A., & Benner, R. (2013). Pan-Arctic distributions of continental runoff in the Arctic Ocean. *Scientific Reports*, *3*(1), 1053. https://doi.org/10.1038/srep01053

Foss, Ø., Maton, J., Moholdt, G., Schmidt, L. S., Sutherland, D. A., Fer, I., Nilsen, F., Kohler, J., & Sundfjord, A. (2024). Ocean warming drives immediate mass loss from calving glaciers in the high Arctic. *Nature Communications*, *15*(1), 10460. https://doi.org/10.1038/s41467-024-54825-7

Fournier, S., & Lee, T. (2021). Seasonal and Interannual Variability of Sea Surface Salinity Near Major River Mouths of the World Ocean Inferred from Gridded Satellite and In-Situ Salinity Products. *Remote Sensing*, *13*(4), 728. https://doi.org/10.3390/rs13040728

Fu, L., Pavelsky, T., Cretaux, J., Morrow, R., Farrar, J. T., Vaze, P., Sengenes, P., Vinogradova-Shiffer, N., Sylvestre-Baron, A., Picot, N., & Dibarboure, G. (2024). The Surface Water and Ocean Topography Mission: A Breakthrough in Radar Remote Sensing of the Ocean and Land Surface Water. *Geophysical Research Letters*, *51*(4), e2023GL107652. https://doi.org/10.1029/2023GL107652

Gagnon, A. S., & Gough, W. A. (2002). Hydro-Climatic Trends in the Hudson Bay Region, Canada. *Canadian Water Resources Journal*, *27*(3), 245–262. https://doi.org/10.4296/cwrj2703245

Galbraith, P. S., & Larouche, P. (2011). Sea-surface temperature in Hudson Bay and Hudson Strait in relation to air temperature and ice cover breakup, 1985–2009. *Journal of Marine Systems*, *88*(3), 463–475. https://doi.org/10.1016/j.jmarsys.2011.06.006

Gangloff, A., Verney, R., Doxaran, D., Ody, A., & Estournel, C. (2017). Investigating Rhône River plume (Gulf of Lions, France) dynamics using metrics analysis from the MERIS 300m Ocean Color archive (2002–2012). *Continental Shelf Research*, *144*, 98–111. https://doi.org/10.1016/j.csr.2017.06.024

Gardner, A. S., Moholdt, G., Wouters, B., Wolken, G. J., Burgess, D. O., Sharp, M. J., Cogley, J. G., Braun, C., & Labine, C. (2011). Sharply increased mass loss from glaciers and ice caps in the Canadian Arctic Archipelago. *Nature*, *473*(7347), 357–360. https://doi.org/10.1038/nature10089

Garvine, R. W. (1995). A dynamical system for classifying buoyant coastal discharges. *Continental Shelf Research*, *15*(13), 1585–1596. https://doi.org/10.1016/0278-4343(94)00065-U

Garvine, R. W. (1999). Penetration of Buoyant Coastal Discharge onto the Continental Shelf: A Numerical Model Experiment. *Journal of Physical Oceanography*, *29*(8), 1892–1909. https://doi.org/10.1175/1520-0485(1999)029%253C1892:POBCDO%253E2.0.CO;2

Giles, K. A., Laxon, S. W., Ridout, A. L., Wingham, D. J., & Bacon, S. (2012). Western Arctic Ocean freshwater storage increased by wind-driven spin-up of the Beaufort Gyre. *Nature Geoscience*, *5*(3), 194–197. https://doi.org/10.1038/ngeo1379

Goharrokhi, M., McCullough, G. K., Lobb, D. A., Owens, P. N., & Koiter, A. J. (2022). Sediment sources and transport dynamics in large, regulated river systems with multiple lakes and reservoirs in the subarctic region of Canada. *Hydrological Processes*, *36*(9), e14675. https://doi.org/10.1002/hyp.14675

Gordon, H. R., Brown, O. B., Evans, R. H., Brown, J. W., Smith, R. C., Baker, K. S., & Clark, D. K. (1988). A semianalytic radiance model of ocean color. *Journal of Geophysical Research: Atmospheres*, *93*(D9), 10909–10924. https://doi.org/10.1029/JD093iD09p10909

Gordon, H. R., Brown, O. B., & Jacobs, M. M. (1975). Computed Relationships Between the Inherent and Apparent Optical Properties of a Flat Homogeneous Ocean. *Applied Optics*, *14*(2), 417. https://doi.org/10.1364/AO.14.000417

Gough, W. A. (2024). Reconstructing and Hindcasting Sea Ice Conditions in Hudson Bay Using a Thermal Variability Framework. *Climate*, *12*(10), 165. https://doi.org/10.3390/cli12100165

Granskog, M. A. (2012). Changes in spectral slopes of colored dissolved organic matter absorption with mixing and removal in a terrestrially dominated marine system (Hudson Bay, Canada). *Marine Chemistry*, *134–135*, 10–17. https://doi.org/10.1016/j.marchem.2012.02.008

Granskog, M. A., Kuzyk, Z. Z. A., Azetsu-Scott, K., & Macdonald, R. W. (2011). Distributions of runoff, sea-ice melt and brine using δ18O and salinity data—A new view on freshwater cycling in Hudson Bay. *Journal of Marine Systems*, *88*(3), 362–374. https://doi.org/10.1016/j.jmarsys.2011.03.011

Granskog, M. A., Macdonald, R. W., Kuzyk, Z. Z. A., Senneville, S., Mundy, C., Barber, D. G., Stern, G. A., & Saucier, F. (2009). Coastal conduit in southwestern Hudson Bay (Canada) in summer: Rapid transit of freshwater and significant loss of colored dissolved organic matter. *Journal of Geophysical Research: Oceans*, *114*(C8), 2009JC005270. https://doi.org/10.1029/2009JC005270

Granskog, M. A., Macdonald, R. W., Mundy, C.-J., & Barber, D. G. (2007). Distribution, characteristics and potential impacts of chromophoric dissolved organic matter (CDOM) in Hudson Strait and Hudson Bay, Canada. *Continental Shelf Research*, *27*(15), 2032–2050. https://doi.org/10.1016/j.csr.2007.05.001

Gray, P., Boss, E., Prochaska, X., Kerner, H., Demeaux, C., & Lehahn, Y. (2024). The Promise and Pitfalls of Machine Learning in Ocean Remote Sensing. *Oceanography*, *37*(3). https://doi.org/10.5670/oceanog.2024.511

Grebmeier, J. M., Overland, J. E., Moore, S. E., Farley, E. V., Carmack, E. C., Cooper, L. W., Frey, K. E., Helle, J. H., McLaughlin, F. A., & McNutt, S. L. (2006). A Major Ecosystem Shift in the Northern Bering Sea. *Science*, *311*(5766), 1461–1464. https://doi.org/10.1126/science.1121365

Griffith, D. R., McNichol, A. P., Xu, L., McLaughlin, F. A., Macdonald, R. W., Brown, K. A., & Eglinton, T. I. (2012). Carbon dynamics in the western Arctic Ocean: Insights from full-depth carbon isotope profiles of DIC, DOC, and POC. *Biogeosciences*, *9*(3), 1217–1224. https://doi.org/10.5194/bg-9-1217-2012

Guay, C. K. H., McLaughlin, F. A., & Yamamoto-Kawai, M. (2009). Differentiating fluvial components of upper Canada Basin waters on the basis of measurements of dissolved barium combined with other physical and chemical tracers. *Journal of Geophysical Research: Oceans*, *114*(C1), 2008JC005099. https://doi.org/10.1029/2008JC005099

Guay, C. K., & Kenison Falkner, K. (1997). Barium as a tracer of Arctic halocline and river waters. *Deep Sea Research Part II: Topical Studies in Oceanography*, *44*(8), 1543–1569. https://doi.org/10.1016/S0967-0645(97)00066-0

Guéguen, C., Granskog, M. A., McCullough, G., & Barber, D. G. (2011). Characterisation of colored dissolved organic matter in Hudson Bay and Hudson Strait using parallel factor analysis. *Journal of Marine Systems*, *88*(3), 423–433. https://doi.org/10.1016/j.jmarsys.2010.12.001

Guéguen, C., Mokhtar, M., Perroud, A., McCullough, G., & Papakyriakou, T. (2016). Mixing and photoreactivity of dissolved organic matter in the Nelson/Hayes estuarine system (Hudson Bay, Canada). *Journal of Marine Systems*, *161*, 42–48. https://doi.org/10.1016/j.jmarsys.2016.05.005

Guzzi, A. C., Ehn, J. K., Michel, C., Tremblay, J.-É., Heath, J. P., & Kuzyk, Z. Z. A. (2024). Influence of altered freshwater discharge on the seasonality of nutrient distributions near La Grande River, northeastern James Bay, Québec. *Elem Sci Anth*, *12*(1), 00133. https://doi.org/10.1525/elementa.2023.00133

Haine, T. W. N., Curry, B., Gerdes, R., Hansen, E., Karcher, M., Lee, C., Rudels, B., Spreen, G., De Steur, L., Stewart, K. D., & Woodgate, R. (2015). Arctic freshwater export: Status, mechanisms, and prospects. *Global and Planetary Change*, *125*, 13–35. https://doi.org/10.1016/j.gloplacha.2014.11.013

Helms, J. R., Stubbins, A., Ritchie, J. D., Minor, E. C., Kieber, D. J., & Mopper, K. (2008). Absorption spectral slopes and slope ratios as indicators of molecular weight, source, and photobleaching of chromophoric dissolved organic matter. *Limnology and Oceanography*, *53*(3), 955–969. https://doi.org/10.4319/lo.2008.53.3.0955

Hetland, R. D. (2005). Relating River Plume Structure to Vertical Mixing. *Journal of Physical Oceanography*, *35*(9), 1667–1688. https://doi.org/10.1175/JPO2774.1

Hochheim, K. P., & Barber, D. G. (2014). An Update on the Ice Climatology of the Hudson Bay System. *Arctic, Antarctic, and Alpine Research*, *46*(1), 66–83. https://doi.org/10.1657/1938-4246-46.1.66

Holmes, R. M., McClelland, J. W., Peterson, B. J., Tank, S. E., Bulygina, E., Eglinton, T. I., Gordeev, V. V., Gurtovaya, T. Y., Raymond, P. A., Repeta, D. J., Staples, R., Striegl, R. G., Zhulidov, A. V., & Zimov, S. A. (2012). Seasonal and Annual Fluxes of Nutrients and Organic Matter from Large Rivers to the Arctic Ocean and Surrounding Seas. *Estuaries and Coasts*, *35*(2), 369–382. https://doi.org/10.1007/s12237-011-9386-6

Hopkins, J., Lucas, M., Dufau, C., Sutton, M., Stum, J., Lauret, O., & Channelliere, C. (2013). Detection and variability of the Congo River plume from satellite derived sea surface temperature, salinity, ocean colour and sea level. *Remote Sensing of Environment*, *139*, 365–385. https://doi.org/10.1016/j.rse.2013.08.015

Horner-Devine, A. R., Hetland, R. D., & MacDonald, D. G. (2015). Mixing and Transport in Coastal River Plumes. *Annual Review of Fluid Mechanics*, *47*(1), 569–594. https://doi.org/10.1146/annurev-fluid-010313-141408

Hsiao, S. S.-Y., Hsu, T.-C., Liu, J. -w., Xie, X., Zhang, Y., Lin, J., Wang, H., Yang, J.-Y. T., Hsu, S.-C., Dai, M., & Kao, S.-J. (2014). Nitrification and its oxygen consumption along the turbid Chang Jiang River plume. *Biogeosciences*, *11*(7), 2083–2098. https://doi.org/10.5194/bg-11-2083-2014

Hugelius, G., Strauss, J., Zubrzycki, S., Harden, J. W., Schuur, E. A. G., Ping, C.-L., Schirrmeister, L., Grosse, G., Michaelson, G. J., Koven, C. D., O'Donnell, J. A., Elberling, B., Mishra, U., Camill, P., Yu, Z., Palmtag, J., & Kuhry, P. (2014). Estimated stocks of circumpolar permafrost carbon with quantified uncertainty ranges and identified data gaps. *Biogeosciences*, *11*(23), 6573–6593. https://doi.org/10.5194/bg-11-6573-2014

Ikeda, M., Tanaka, S. S., & Watanabe, Y. W. (2018). Circulation patterns in the lower Arctic Ocean derived from geochemical data. *Journal of Oceanography*, *74*(5), 453–470. https://doi.org/10.1007/s10872-018-0472-2

Ingram, R. G., & Larouche, P. (1987). Variability of an under-ice river plume in Hudson Bay. *Journal of Geophysical Research: Oceans*, *92*(C9), 9541–9547. https://doi.org/10.1029/JC092iC09p09541

IOCCG Protocol Series. (2018). Inherent optical property measurements and protocols: Absorption coefficient. In A. R. Neeley & A. Mannino (Eds.), IOCCG ocean optics and biogeochemistry protocols for satellite ocean colour sensor validation (Vol. 1). IOCCG.

IOCCG Algorithms for Ocean-Colour Algorithms. (2014). Chapter 10: Quasi-analytical algorithm by ZhongPing Lee, Kendall Carder and Robert Arnone), version 6.

Ivanova, D., Bhattacharyya, S., Strawa, A., Zornetzer, S., Olinger, S., Field, L., Ivanov, A., Kusnadi, E., & Kim, J. (2026). Evaluating the impacts of localized artificial enhancement of sea ice albedo over Beaufort Gyre towards restoring Arctic Sea Ice. *Cold Regions Science and Technology*, *241*, 104657. https://doi.org/10.1016/j.coldregions.2025.104657

Jacquemot, L., Kalenitchenko, D., Matthes, L. C., Vigneron, A., Mundy, C. J., Tremblay, J.-É., & Lovejoy, C. (2021). Protist communities along freshwater–marine transition zones in Hudson Bay (Canada). *Elementa: Science of the Anthropocene*, *9*(1), 00111. https://doi.org/10.1525/elementa.2021.00111

Jacquemot, L., Tremblay, J.-É., Morency, C., & Lovejoy, C. (2024). Stratification and summer protist communities in the Arctic influenced coastal systems of Nunavik (Québec, Canada). *Frontiers in Marine Science*, *11*, 1321604. https://doi.org/10.3389/fmars.2024.1321604

Jacquemot, L., Vigneron, A., Tremblay, J.-É., & Lovejoy, C. (2022). Contrasting sea ice conditions shape microbial food webs in Hudson Bay (Canadian Arctic). *ISME Communications*, *2*(1), 104. https://doi.org/10.1038/s43705-022-00192-7

Jakobsson, M., Mayer, L., Coakley, B., Dowdeswell, J. A., Forbes, S., Fridman, B., Hodnesdal, H., Noormets, R., Pedersen, R., Rebesco, M., Schenke, H. W., Zarayskaya, Y., Accettella, D., Armstrong, A., Anderson, R. M., Bienhoff, P., Camerlenghi, A., Church, I., Edwards, M., … Weatherall, P. (2012). The International Bathymetric Chart of the Arctic Ocean (IBCAO) Version 3.0. *Geophysical Research Letters*, *39*(12), 2012GL052219. https://doi.org/10.1029/2012GL052219

Jia, C., & Minnett, P. J. (2020). High latitude sea surface temperatures derived from MODIS infrared measurements. *Remote Sensing of Environment*, *251*, 112094. https://doi.org/10.1016/j.rse.2020.112094

Jones, E. P., & Anderson, L. G. (1994). Northern hudson bay and foxe basin: Water masses, circulation and productivity. *Atmosphere-Ocean*, *32*(2), 361–374. https://doi.org/10.1080/07055900.1994.9649502

Jones, E. P., Rudels, B., & Anderson, L. G. (1995). Deep waters of the Arctic Ocean: Origins and circulation. *Deep Sea Research Part I: Oceanographic Research Papers*, *42*(5), 737–760. https://doi.org/10.1016/0967-0637(95)00013-V

Kåresdotter, E., Destouni, G., Ghajarnia, N., Hugelius, G., & Kalantari, Z. (2021). Mapping the Vulnerability of Arctic Wetlands to Global Warming. *Earth's Future*, *9*(5), e2020EF001858. https://doi.org/10.1029/2020EF001858

Kattsov, V. M., Walsh, J. E., Chapman, W. L., Govorkova, V. A., Pavlova, T. V., & Zhang, X. (2007). Simulation and Projection of Arctic Freshwater Budget Components by the IPCC AR4 Global Climate Models. *Journal of Hydrometeorology*, *8*(3), 571–589. https://doi.org/10.1175/JHM575.1

Kazmiruk, Z. V., Capelle, D. W., Kamula, C. M., Rysgaard, S., Papakyriakou, T., & Kuzyk, Z. A. (2021). High biodegradability of riverine dissolved organic carbon in late winter in Hudson Bay, Canada. *Elementa: Science of the Anthropocene*, *9*(1), 00123. https://doi.org/10.1525/elementa.2020.00123

King, M. D., Howat, I. M., Jeong, S., Noh, M. J., Wouters, B., Noël, B., & Van Den Broeke, M. R. (2018). Seasonal to decadal variability in ice discharge from the Greenland Ice Sheet. *The Cryosphere*, *12*(12), 3813–3825. https://doi.org/10.5194/tc-12-3813-2018

Kipp, L. E., Kadko, D. C., Pickart, R. S., Henderson, P. B., Moore, W. S., & Charette, M. A. (2019). Shelf-Basin Interactions and Water Mass Residence Times in the Western Arctic Ocean: Insights Provided by Radium Isotopes. *Journal of Geophysical Research: Oceans*, *124*(5), 3279–3297. https://doi.org/10.1029/2019JC014988

Kirillov, S., Babb, D., Dmitrenko, I., Landy, J., Lukovich, J., Ehn, J., Sydor, K., Barber, D., & Stroeve, J. (2020). Atmospheric Forcing Drives the Winter Sea Ice Thickness Asymmetry of Hudson Bay. *Journal of Geophysical Research: Oceans*, *125*(2), e2019JC015756. https://doi.org/10.1029/2019JC015756

Kitching, E. H., Michel, C., Matthes, L. C., Castro De La Guardia, L., Kuzyk, Z. Z. A., Limoges, A., Ehn, J. K., Papakyriakou, T. N., & Mundy, C. J. (2026). Local primary production hotspot in

the coastal waters of Southampton Island, Nunavut, Canada, in summer 2019. *Arctic Science*, *12*, 1–20. https://doi.org/10.1139/as-2025-0015

Kjeldsen, K. K., Korsgaard, N. J., Bjørk, A. A., Khan, S. A., Box, J. E., Funder, S., Larsen, N. K., Bamber, J. L., Colgan, W., Van Den Broeke, M., Siggaard-Andersen, M.-L., Nuth, C., Schomacker, A., Andresen, C. S., Willerslev, E., & Kjær, K. H. (2015). Spatial and temporal distribution of mass loss from the Greenland Ice Sheet since AD 1900. *Nature*, *528*(7582), 396–400. https://doi.org/10.1038/nature16183

Kong, B., Gao, L., Wang, S., & Guo, G. (2025). Cooling and Sinking of the Atlantic Water in the Eurasian Basin Since 1990s. *Geophysical Research Letters*, *52*(9), e2025GL114720. https://doi.org/10.1029/2025GL114720

Kowal, S., Gough, W. A., & Butler, K. (2017). Temporal evolution of Hudson Bay Sea Ice (1971–2011). *Theoretical and Applied Climatology*, *127*(3–4), 753–760. https://doi.org/10.1007/s00704-015-1666-9

Kranck, K. (1984). THE ROLE OF FLOCCULATION IN THE FILTERING OF PARTICULATE MATTER IN ESTUARIES. In *The Estuary As a Filter* (pp. 159–175). Elsevier. https://doi.org/10.1016/B978-0-12-405070-9.50014-1

Kuzyk, Z. A., Macdonald, R. W., Granskog, M. A., Scharien, R. K., Galley, R. J., Michel, C., Barber, D., & Stern, G. (2008). Sea ice, hydrological, and biological processes in the Churchill River estuary region, Hudson Bay. *Estuarine, Coastal and Shelf Science*, *77*(3), 369–384. https://doi.org/10.1016/j.ecss.2007.09.030

Kuzyk, Z. Z. A., Macdonald, R. W., Johannessen, S. C., Gobeil, C., & Stern, G. A. (2009). Towards a sediment and organic carbon budget for Hudson Bay. *Marine Geology*, *264*(3–4), 190–208. https://doi.org/10.1016/j.margeo.2009.05.006

Kwok, R., Kacimi, S., Markus, T., Kurtz, N. T., Studinger, M., Sonntag, J. G., Manizade, S. S., Boisvert, L. N., & Harbeck, J. P. (2019). ICESat-2 Surface Height and Sea Ice Freeboard Assessed With ATM Lidar Acquisitions From Operation IceBridge. *Geophysical Research Letters*, *46*(20), 11228–11236. https://doi.org/10.1029/2019GL084976

Kwok, R., & Morison, J. (2011). Dynamic topography of the ice-covered Arctic Ocean from ICESat: DYNAMIC TOPOGRAPHY OF ARCTIC OCEAN. *Geophysical Research Letters*, *38*(2), n/a-n/a. https://doi.org/10.1029/2010GL046063

Kwok, R., & Morison, J. (2016). Sea surface height and dynamic topography of the ice-covered oceans from CryoSat-2: 2011–2014. *Journal of Geophysical Research: Oceans*, *121*(1), 674–692. https://doi.org/10.1002/2015JC011357

Laidre, K. L., Stern, H., Kovacs, K. M., Lowry, L., Moore, S. E., Regehr, E. V., Ferguson, S. H., Wiig, Ø., Boveng, P., Angliss, R. P., Born, E. W., Litovka, D., Quakenbush, L., Lydersen, C., Vongraven, D., & Ugarte, F. (2015). Arctic marine mammal population status, sea ice habitat loss, and conservation recommendations for the 21st century: Arctic Marine Mammal Conservation. *Conservation Biology*, *29*(3), 724–737. https://doi.org/10.1111/cobi.12474

Landy, J. C., Ehn, J. K., Babb, D. G., Thériault, N., & Barber, D. G. (2017). Sea ice thickness in the Eastern Canadian Arctic: Hudson Bay Complex & Baffin Bay. *Remote Sensing of Environment*, *200*, 281–294. https://doi.org/10.1016/j.rse.2017.08.019

Lansard, B., Mucci, A., Miller, L. A., Macdonald, R. W., & Gratton, Y. (2012). Seasonal variability of water mass distribution in the southeastern Beaufort Sea determined by total alkalinity and δ^{18} O. *Journal of Geophysical Research: Oceans*, *117*(C3), 2011JC007299. https://doi.org/10.1029/2011JC007299

Lapoussière, A., Michel, C., Gosselin, M., & Poulin, M. (2009). Spatial variability in organic material sinking export in the Hudson Bay system, Canada, during fall. *Continental Shelf Research*, *29*(9), 1276–1288. https://doi.org/10.1016/j.csr.2009.02.004

Laxon, S. W., Giles, K. A., Ridout, A. L., Wingham, D. J., Willatt, R., Cullen, R., Kwok, R., Schweiger, A., Zhang, J., Haas, C., Hendricks, S., Krishfield, R., Kurtz, N., Farrell, S., & Davidson, M. (2013). CryoSat-2 estimates of Arctic sea ice thickness and volume. *Geophysical Research Letters*, *40*(4), 732–737. https://doi.org/10.1002/grl.50193

Lee, J., Tefs, A., Galindo, V., Stadnyk, T., Gosselin, M., & Tremblay, J.-É. (2023). Nutrient inputs from subarctic rivers into Hudson Bay. *Elem Sci Anth*, *11*(1), 00085. https://doi.org/10.1525/elementa.2021.00085

Lee, Z., Carder, K. L., & Arnone, R. A. (2002). Deriving inherent optical properties from water color: A multiband quasi-analytical algorithm for optically deep waters. *Applied Optics*, *41*(27), 5755. https://doi.org/10.1364/AO.41.005755

Lewis, K. M., Van Dijken, G. L., & Arrigo, K. R. (2020). Changes in phytoplankton concentration now drive increased Arctic Ocean primary production. *Science*, *369*(6500), 198–202. https://doi.org/10.1126/science.aay8380

Li, S. S., & Ingram, R. G. (2007). Isopycnal deepening of an under-ice river plume in coastal waters: Field observations and modeling. *Journal of Geophysical Research: Oceans*, *112*(C7), 2006JC003883. https://doi.org/10.1029/2006JC003883

Lin, P., Pickart, R. S., Cyr, F., Snook, S., Bahr, F., & Déry, S. J. (2026). The Labrador Boundary Current System in Summer and Fall: Mean, Variability, and Influence on Cross-Shelf Exchange. *Journal of Physical Oceanography*, *56*(10), 2311–2326. https://doi.org/10.1175/JPO-D-25-0224.1

Loisel, H., Vantrepotte, V., Jamet, C., & Ngoc Dat, D. (2013). Challenges and New Advances in Ocean Color Remote Sensing of Coastal Waters. In E. Zambianchi (Ed.), *Topics in Oceanography*. InTech. https://doi.org/10.5772/56414

MacDonald, M. K., Stadnyk, T. A., Déry, S. J., Braun, M., Gustafsson, D., Isberg, K., & Arheimer, B. (2018). Impacts of 1.5 and 2.0 °C Warming on Pan-Arctic River Discharge Into the Hudson Bay Complex Through 2070. *Geophysical Research Letters*, *45*(15), 7561–7570. https://doi.org/10.1029/2018GL079147

Macdonald, R. W., Paton, D. W., Carmack, E. C., & Omstedt, A. (1995). The freshwater budget and under-ice spreading of Mackenzie River water in the Canadian Beaufort Sea based on salinity and $^{18}O/^{16}O$ measurements in water and ice. *Journal of Geophysical Research: Oceans*, *100*(C1), 895–919. https://doi.org/10.1029/94JC02700

Mankoff, K. D., Colgan, W., Solgaard, A., Karlsson, N. B., Ahlstrøm, A. P., Van As, D., Box, J. E., Khan, S. A., Kjeldsen, K. K., Mouginot, J., & Fausto, R. S. (2019). Greenland Ice Sheet solid ice discharge from 1986 through 2017. *Earth System Science Data*, *11*(2), 769–786. https://doi.org/10.5194/essd-11-769-2019

Manning, A. J., Langston, W. J., & Jonas, P. J. C. (2010). A review of sediment dynamics in the Severn Estuary: Influence of flocculation. *Marine Pollution Bulletin*, *61*(1–3), 37–51. https://doi.org/10.1016/j.marpolbul.2009.12.012

Mannino, A., Novak, M. G., Hooker, S. B., Hyde, K., & Aurin, D. (2014). Algorithm development and validation of CDOM properties for estuarine and continental shelf waters along the northeastern U.S. coast. *Remote Sensing of Environment*, *152*, 576–602. https://doi.org/10.1016/j.rse.2014.06.027

Manucharyan, G. E., & Spall, M. A. (2016). Wind-driven freshwater buildup and release in the Beaufort Gyre constrained by mesoscale eddies. *Geophysical Research Letters*, *43*(1), 273–282. https://doi.org/10.1002/2015GL065957

Many, G., Bourrin, F., Durrieu De Madron, X., Pairaud, I., Gangloff, A., Doxaran, D., Ody, A., Verney, R., Menniti, C., Le Berre, D., & Jacquet, M. (2016). Particle assemblage characterization in the Rhone River ROFI. *Journal of Marine Systems*, *157*, 39–51. https://doi.org/10.1016/j.jmarsys.2015.12.010

Maritorena, S., Siegel, D. A., & Peterson, A. R. (2002). Optimization of a semianalytical ocean color model for global-scale applications. *Applied Optics*, *41*(15), 2705. https://doi.org/10.1364/AO.41.002705

Martínez, J., Gabarró, C., Turiel, A., González-Gambau, V., Umbert, M., Hoareau, N., González-Haro, C., Olmedo, E., Arias, M., Catany, R., Bertino, L., Raj, R. P., Xie, J., Sabia, R., & Fernández, D. (2022). Improved BEC SMOS Arctic Sea Surface Salinity product v3.1. *Earth System Science Data*, *14*(1), 307–323. https://doi.org/10.5194/essd-14-307-2022

Martini, I. P. (1986). Chapter 7 Coastal Features of Canadian Inland Seas. In *Elsevier Oceanography Series* (Vol. 44, pp. 117–142). Elsevier. https://doi.org/10.1016/S0422-9894(08)70900-0

Martín-Neira, M., Oliva, R., Corbella, I., Torres, F., Duffo, N., Durán, I., Kainulainen, J., Closa, J., Zurita, A., Cabot, F., Khazaal, A., Anterrieu, E., Barbosa, J., Lopes, G., Tenerelli, J., Díez-García, R., Fauste, J., Martín-Porqueras, F., González-Gambau, V., … Suess, M. (2016). SMOS

instrument performance and calibration after six years in orbit. *Remote Sensing of Environment*, *180*, 19–39. https://doi.org/10.1016/j.rse.2016.02.036

Matsuoka, A., Babin, M., & Devred, E. C. (2016). A new algorithm for discriminating water sources from space: A case study for the southern Beaufort Sea using MODIS ocean color and SMOS salinity data. *Remote Sensing of Environment*, *184*, 124–138. https://doi.org/10.1016/j.rse.2016.05.006

Matsuoka, A., Boss, E., Babin, M., Karp-Boss, L., Hafez, M., Chekalyuk, A., Proctor, C. W., Werdell, P. J., & Bricaud, A. (2017). Pan-Arctic optical characteristics of colored dissolved organic matter: Tracing dissolved organic carbon in changing Arctic waters using satellite ocean color data. *Remote Sensing of Environment*, *200*, 89–101. https://doi.org/10.1016/j.rse.2017.08.009

Matsuoka, A., Bricaud, A., Benner, R., Para, J., Sempéré, R., Prieur, L., Bélanger, S., & Babin, M. (2012). Tracing the transport of colored dissolved organic matter in water masses of the Southern Beaufort Sea: Relationship with hydrographic characteristics. *Biogeosciences*, *9*(3), 925–940. https://doi.org/10.5194/bg-9-925-2012

Matsuoka, A., Hill, V., Huot, Y., Babin, M., & Bricaud, A. (2011). Seasonal variability in the light absorption properties of western Arctic waters: Parameterization of the individual components of absorption for ocean color applications. *Journal of Geophysical Research*, *116*(C2), C02007. https://doi.org/10.1029/2009JC005594

Matsuoka, A., Hooker, S. B., Bricaud, A., Gentili, B., & Babin, M. (2013). Estimating absorption coefficients of colored dissolved organic matter (CDOM) using a semi-analytical algorithm for southern Beaufort Sea waters: Application to deriving concentrations of dissolved organic carbon from space. *Biogeosciences*, *10*(2), 917–927. https://doi.org/10.5194/bg-10-917-2013

Matthes, L. C., Ehn, J. K., Dalman, L. A., Babb, D. G., Peeken, I., Harasyn, M., Kirillov, S., Lee, J., Bélanger, S., Tremblay, J.-É., Barber, D. G., & Mundy, C. J. (2021). Environmental drivers of spring primary production in Hudson Bay. *Elementa: Science of the Anthropocene*, *9*(1), 00160. https://doi.org/10.1525/elementa.2020.00160

McClelland, J. W., Holmes, R. M., Peterson, B. J., Raymond, P. A., Striegl, R. G., Zhulidov, A. V., Zimov, S. A., Zimov, N., Tank, S. E., Spencer, R. G. M., Staples, R., Gurtovaya, T. Y., & Griffin, C. G. (2016). Particulate organic carbon and nitrogen export from major Arctic rivers. *Global Biogeochemical Cycles*, *30*(5), 629–643. https://doi.org/10.1002/2015GB005351

McCrystall, M. R., Stroeve, J., Serreze, M., Forbes, B. C., & Screen, J. A. (2021). New climate models reveal faster and larger increases in Arctic precipitation than previously projected. *Nature Communications*, *12*(1), 6765. https://doi.org/10.1038/s41467-021-27031-y

McCullough, G. K., Kuzyk, Z. Z., Ehn, J., Babb, D. G., Ridenour, N., Myers, P. G., et al. (2019). Chapter 3, Freshwater-marine interactions in the greater Hudson Bay marine region. In Z. A. Kuzyk & L. M. Candlish (Eds.), From science to policy in the greater Hudson Bay marine region: An integrated regional impact study (IRIS) of climate change and modernization (p. 424). ArcticNet.

McDougall, T.J. and P.M. Barker, 2011: Getting started with TEOS-10 and the Gibbs Seawater (GSW) Oceanographic Toolbox, 28pp., SCOR/IAPSO WG127, ISBN 978-0-646-55621-5.

McGeachy, D., Lunn, N. J., Richardson, E. S., & Derocher, A. E. (2024). Sea ice influence on male polar bear survival in Hudson Bay. *Arctic Science*, *10*(3), 483–498. https://doi.org/10.1139/as-2023-0045

Meilleur, C., Kamula, M., Kuzyk, Z. A., & Guéguen, C. (2023). Insights into surface circulation and mixing in James Bay and Hudson Bay from dissolved organic matter optical properties. *Journal of Marine Systems*, *238*, 103841. https://doi.org/10.1016/j.jmarsys.2022.103841

Mensah, V., Chen, Y.-C., Nomura, D., Ueno, H., Chien, H., & Ohshima, K. I. (2025). Multidecadal decline in sea ice meltwater volume and Pacific Winter Water salinity in the Bering Sea revealed by ocean observations. *Progress in Oceanography*, *230*, 103377. https://doi.org/10.1016/j.pocean.2024.103377

Messier, D., Ingram, R. G., & Roy, D. (1986). Chapter 20 Physical and Biological Modifications in Response to LA Grande Hydroelectric Complex. In *Elsevier Oceanography Series* (Vol. 44, pp. 403–424). Elsevier. https://doi.org/10.1016/S0422-9894(08)70913-9

Middag, R., De Baar, H. J. W., Laan, P., & Bakker, K. (2009). Dissolved aluminium and the silicon cycle in the Arctic Ocean. *Marine Chemistry*, *115*(3–4), 176–195. https://doi.org/10.1016/j.marchem.2009.08.002

Moholdt, G., Wouters, B., & Gardner, A. S. (2012). Recent mass changes of glaciers in the Russian High Arctic. *Geophysical Research Letters*, *39*(10), 2012GL051466. https://doi.org/10.1029/2012GL051466

Morel, A. (1987). Chlorophyll-specific scattering coefficient of phytoplankton. A simplified theoretical approach. *Deep Sea Research Part A. Oceanographic Research Papers*, *34*(7), 1093–1105. https://doi.org/10.1016/0198-0149(87)90066-5

Morel, A., & Prieur, L. (1977). Analysis of variations in ocean color. *Limnology and Oceanography*, *22*(4), 709–722. https://doi.org/10.4319/lo.1977.22.4.0709

Morency, C., Jacquemot, L., Potvin, M., & Lovejoy, C. (2022). A microbial perspective on the local influence of Arctic rivers and estuaries on Hudson Bay (Canada). *Elementa: Science of the Anthropocene*, *10*(1), 00009. https://doi.org/10.1525/elementa.2021.00009

Morison, J., Kwok, R., Peralta-Ferriz, C., Alkire, M., Rigor, I., Andersen, R., & Steele, M. (2012). Changing Arctic Ocean freshwater pathways. *Nature*, *481*(7379), 66–70. https://doi.org/10.1038/nature10705

Mukherjee, S., Mabit, R., & Bélanger, S. (2026). A semi-analytical Bayesian estimate retrieval algorithm for the inversion of remote-sensing reflectance in optically deep and shallow waters. *Limnology and Oceanography: Methods*, *24*(1), e70004. https://doi.org/10.1002/lom3.70004

Mundy, C. J., Gosselin, M., Starr, M., & Michelc, C. (2010). Riverine export and the effects of circulation on dissolved organic carbon in the Hudson Bay system, Canada. *Limnology and Oceanography*, *55*(1), 315–323. https://doi.org/10.4319/lo.2010.55.1.0315

Nechad, B., Ruddick, K. G., & Park, Y. (2010). Calibration and validation of a generic multisensor algorithm for mapping of total suspended matter in turbid waters. *Remote Sensing of Environment*, *114*(4), 854–866. https://doi.org/10.1016/j.rse.2009.11.022

Nghiem, S. V., Hall, D. K., Mote, T. L., Tedesco, M., Albert, M. R., Keegan, K., Shuman, C. A., DiGirolamo, N. E., & Neumann, G. (2012). The extreme melt across the Greenland ice sheet in

2012. *Geophysical Research Letters*, *39*(20), 2012GL053611. https://doi.org/10.1029/2012GL053611

Noël, B., Jakobs, C. L., Van Pelt, W. J. J., Lhermitte, S., Wouters, B., Kohler, J., Hagen, J. O., Luks, B., Reijmer, C. H., Van De Berg, W. J., & Van Den Broeke, M. R. (2020). Low elevation of Svalbard glaciers drives high mass loss variability. *Nature Communications*, *11*(1), 4597. https://doi.org/10.1038/s41467-020-18356-1

Notz, D., & SIMIP, S. (2020). Arctic Sea Ice in CMIP6. *Geophysical Research Letters*, *47*(10), e2019GL086749. https://doi.org/10.1029/2019GL086749

Oliva, R., Daganzo, E., Kerr, Y. H., Mecklenburg, S., Nieto, S., Richaume, P., & Gruhier, C. (2012). SMOS Radio Frequency Interference Scenario: Status and Actions Taken to Improve the RFI Environment in the 1400–1427-MHz Passive Band. *IEEE Transactions on Geoscience and Remote Sensing*, *50*(5), 1427–1439. https://doi.org/10.1109/TGRS.2012.2182775

Osadchiev, A. A., Izhitskiy, A. S., Zavialov, P. O., Kremenetskiy, V. V., Polukhin, A. A., Pelevin, V. V., & Toktamysova, Z. M. (2017). Structure of the buoyant plume formed by O b and Y enisei river discharge in the southern part of the K ara S ea during summer and autumn. *Journal of Geophysical Research: Oceans*, *122*(7), 5916–5935. https://doi.org/10.1002/2016JC012603

Osadchiev, A., Frey, D., Spivak, E., Shchuka, S., Tilinina, N., & Semiletov, I. (2021). Structure and Inter-Annual Variability of the Freshened Surface Layer in the Laptev and East-Siberian Seas During Ice-Free Periods. *Frontiers in Marine Science*, *8*, 735011. https://doi.org/10.3389/fmars.2021.735011

Osadchiev, A., & Sedakov, R. (2019). Spreading dynamics of small river plumes off the northeastern coast of the Black Sea observed by Landsat 8 and Sentinel-2. *Remote Sensing of Environment*, *221*, 522–533. https://doi.org/10.1016/j.rse.2018.11.043

Osadchiev, A., Zabudkina, Z., Rogozhin, V., Frey, D., Gordey, A., Spivak, E., Salyuk, A., Semiletov, I., & Sedakov, R. (2023). Structure of the Ob-Yenisei plume in the Kara Sea shortly before autumn ice formation. *Frontiers in Marine Science*, *10*, 1129331. https://doi.org/10.3389/fmars.2023.1129331

Osburn, C. L., Retamal, L., & Vincent, W. F. (2009). Photoreactivity of chromophoric dissolved organic matter transported by the Mackenzie River to the Beaufort Sea. *Marine Chemistry*, *115*(1–2), 10–20. https://doi.org/10.1016/j.marchem.2009.05.003

Östlund, H. G., & Hut, G. (1984). Arctic Ocean water mass balance from isotope data. *Journal of Geophysical Research: Oceans*, *89*(C4), 6373–6381. https://doi.org/10.1029/JC089iC04p06373

Otero, P., Ruiz-Villarreal, M., & Peliz, Á. (2009). River plume fronts off NW Iberia from satellite observations and model data. *ICES Journal of Marine Science*, *66*(9), 1853–1864. https://doi.org/10.1093/icesjms/fsp156

Oziel, L., Neukermans, G., Ardyna, M., Lancelot, C., Tison, J., Wassmann, P., Sirven, J., Ruiz-Pino, D., & Gascard, J. (2017). Role for A tlantic inflows and sea ice loss on shifting phytoplankton blooms in the B arents S ea. *Journal of Geophysical Research: Oceans*, *122*(6), 5121–5139. https://doi.org/10.1002/2016JC012582

Palacios, S. L., Peterson, T. D., & Kudela, R. M. (2012). Optical characterization of water masses within the Columbia River plume. *Journal of Geophysical Research: Oceans*, *117*(C11), 2012JC008005. https://doi.org/10.1029/2012JC008005

Peacock, N. R., & Laxon, S. W. (2004). Sea surface height determination in the Arctic Ocean from ERS altimetry. *Journal of Geophysical Research: Oceans*, *109*(C7), 2001JC001026. https://doi.org/10.1029/2001JC001026

Peck, C. J., Kuzyk, Z. Z. A., Heath, J. P., Lameboy, J., & Ehn, J. K. (2022). Under-Ice Hydrography of the La Grande River Plume in Relation to a Ten-Fold Increase in Wintertime Discharge. *Journal of Geophysical Research: Oceans*, *127*(10), e2021JC018341. https://doi.org/10.1029/2021JC018341

Pelletier, B. R. (1986). Chapter 8 Seafloor Morphology and Sediments. In *Elsevier Oceanography Series* (Vol. 44, pp. 143–162). Elsevier. https://doi.org/10.1016/S0422-9894(08)70901-2

Pemberton, P., & Nilsson, J. (2016). The response of the central Arctic O cean stratification to freshwater perturbations. *Journal of Geophysical Research: Oceans*, *121*(1), 792–817. https://doi.org/10.1002/2015JC011003

Peralta-Ferriz, C., & Woodgate, R. A. (2015). Seasonal and interannual variability of pan-Arctic surface mixed layer properties from 1979 to 2012 from hydrographic data, and the dominance of stratification for multiyear mixed layer depth shoaling. *Progress in Oceanography*, *134*, 19–53. https://doi.org/10.1016/j.pocean.2014.12.005

Perovich, D., Smith, M., Light, B., & Webster, M. (2021). Meltwater sources and sinks for multiyear Arctic sea ice in summer. *The Cryosphere*, *15*(9), 4517–4525. https://doi.org/10.5194/tc-15-4517-2021

Peterson, B. J., Holmes, R. M., McClelland, J. W., Vörösmarty, C. J., Lammers, R. B., Shiklomanov, A. I., Shiklomanov, I. A., & Rahmstorf, S. (2002). Increasing River Discharge to the Arctic Ocean. *Science*, *298*(5601), 2171–2173. https://doi.org/10.1126/science.1077445

Pimenta, F. M., Kirwan, A. D., & Huq, P. (2011). On the Transport of Buoyant Coastal Plumes. *Journal of Physical Oceanography*, *41*(3), 620–640. https://doi.org/10.1175/2010JPO4473.1

Polyakov, I. V., Alkire, M. B., Bluhm, B. A., Brown, K. A., Carmack, E. C., Chierici, M., Danielson, S. L., Ellingsen, I., Ershova, E. A., Gårdfeldt, K., Ingvaldsen, R. B., Pnyushkov, A. V., Slagstad, D., & Wassmann, P. (2020). Borealization of the Arctic Ocean in Response to Anomalous Advection From Sub-Arctic Seas. *Frontiers in Marine Science*, *7*, 491. https://doi.org/10.3389/fmars.2020.00491

Polyakov, I. V., Pnyushkov, A. V., Charette, M., Cho, K.-H., Jung, J., Kipp, L., Muilwijk, M., Whitmore, L., Yang, E. J., & Yoo, J. (2025). Atlantification advances into the Amerasian Basin of the Arctic Ocean. *Science Advances*, *11*(8), eadq7580. https://doi.org/10.1126/sciadv.adq7580

Polyakov, I. V., Pnyushkov, A. V., & Timokhov, L. A. (2012). Warming of the Intermediate Atlantic Water of the Arctic Ocean in the 2000s. *Journal of Climate*, *25*(23), 8362–8370. https://doi.org/10.1175/JCLI-D-12-00266.1

Pope, R. M., & Fry, E. S. (1997). Absorption spectrum (380–700 nm) of pure water II Integrating cavity measurements. *Applied Optics*, *36*(33), 8710. https://doi.org/10.1364/AO.36.008710

Prinsenberg, S. J. (1986a). Chapter 9 Salinity and Temperature Distributions of Hudson Bay and James Bay. In *Elsevier Oceanography Series* (Vol. 44, pp. 163–186). Elsevier. https://doi.org/10.1016/S0422-9894(08)70902-4

Prinsenberg, S. J. (1986b). Chapter 10 The Circulation Pattern and Current Structure of Hudson Bay. In *Elsevier Oceanography Series* (Vol. 44, pp. 187–204). Elsevier. https://doi.org/10.1016/S0422-9894(08)70903-6

Proshutinsky, A., Krishfield, R., Timmermans, M., Toole, J., Carmack, E., McLaughlin, F., Williams, W. J., Zimmermann, S., Itoh, M., & Shimada, K. (2009). Beaufort Gyre freshwater reservoir: State and variability from observations. *Journal of Geophysical Research: Oceans*, *114*(C1), 2008JC005104. https://doi.org/10.1029/2008JC005104

Proshutinsky, A. Y., & Johnson, M. A. (1997). Two circulation regimes of the wind-driven Arctic Ocean. *Journal of Geophysical Research: Oceans*, *102*(C6), 12493–12514. https://doi.org/10.1029/97JC00738

Rantanen, M., Karpechko, A. Yu., Lipponen, A., Nordling, K., Hyvärinen, O., Ruosteenoja, K., Vihma, T., & Laaksonen, A. (2022). The Arctic has warmed nearly four times faster than the globe since 1979. *Communications Earth & Environment*, *3*(1), 168. https://doi.org/10.1038/s43247-022-00498-3

Raymond, P. A., McClelland, J. W., Holmes, R. M., Zhulidov, A. V., Mull, K., Peterson, B. J., Striegl, R. G., Aiken, G. R., & Gurtovaya, T. Y. (2007). Flux and age of dissolved organic carbon exported to the Arctic Ocean: A carbon isotopic study of the five largest arctic rivers. *Global Biogeochemical Cycles*, *21*(4), 2007GB002934. https://doi.org/10.1029/2007GB002934

Ridenour, N. A., Hu, X., Sydor, K., Myers, P. G., & Barber, D. G. (2019a). Revisiting the Circulation of Hudson Bay: Evidence for a Seasonal Pattern. *Geophysical Research Letters*, *46*(7), 3891–3899. https://doi.org/10.1029/2019GL082344

Ridenour, N. A., Hu, X., Jafarikhasragh, S., Landy, J. C., Lukovich, J. V., Stadnyk, T. A., Sydor, K., Myers, P. G., & Barber, D. G. (2019b). Sensitivity of freshwater dynamics to ocean model resolution and river discharge forcing in the Hudson Bay Complex. *Journal of Marine Systems*, *196*, 48–64. https://doi.org/10.1016/j.jmarsys.2019.04.002

Ridenour, N. A., Straneo, F., Holte, J., Gratton, Y., Myers, P. G., & Barber, D. G. (2021). Hudson Strait Inflow: Structure and Variability. *Journal of Geophysical Research: Oceans*, *126*(9), e2020JC017089. https://doi.org/10.1029/2020JC017089

Rooijakkers, F., Poulsen, E., Ruiz-Castillo, E., & Rysgaard, S. (2025). Meltwater from the Greenland ice sheet and its water isotope distribution in Dickson Fjord, East Greenland. *The Cryosphere*, *19*(8), 2881–2894. https://doi.org/10.5194/tc-19-2881-2025

Rosenberg, D. M., Chambers, P. A., Culp, J. M., Franzin, W. G., Nelson, P. A., Salki, A. G., Stainton, M. P., Bodaly, R. A., & Newbury, R. W. (2005). NELSON AND CHURCHILL RIVER BASINS. In *Rivers of North America* (pp. 852–901). Elsevier. https://doi.org/10.1016/B978-012088253-3/50022-5

Ruddick, K. G., De Cauwer, V., Park, Y.-J., & Moore, G. (2006). Seaborne measurements of near infrared water-leaving reflectance: The similarity spectrum for turbid waters. *Limnology and Oceanography*, *51*(2), 1167–1179. https://doi.org/10.4319/lo.2006.51.2.1167

Ruddick, K. G., Ovidio, F., & Rijkeboer, M. (2000). Atmospheric correction of SeaWiFS imagery for turbid coastal and inland waters. *Applied Optics*, *39*(6), 897. https://doi.org/10.1364/AO.39.000897

Rudels, B. (2012). Arctic Ocean circulation and variability – advection and external forcing encounter constraints and local processes. *Ocean Science*, *8*(2), 261–286. https://doi.org/10.5194/os-8-261-2012

Rudels, B., Anderson, L. G., & Jones, E. P. (1996). Formation and evolution of the surface mixed layer and halocline of the Arctic Ocean. *Journal of Geophysical Research: Oceans*, *101*(C4), 8807–8821. https://doi.org/10.1029/96JC00143

Rudels, B., & Carmack, E. (2022). Arctic Ocean Water Mass Structure and Circulation. *Oceanography*. https://doi.org/10.5670/oceanog.2022.116

Saha, M., Stroeve, J., Isleifson, D., Yackel, J., Nandan, V., Landy, J. C., & Lam, H. M. (2025). Snow depth estimation on leadless landfast ice using Cryo2Ice satellite observations. *The Cryosphere*, *19*(1), 325–346. https://doi.org/10.5194/tc-19-325-2025

Sathyendranath, S., Prieur, L., & Morel, A. (1989). A three-component model of ocean colour and its application to remote sensing of phytoplankton pigments in coastal waters. *International Journal of Remote Sensing*, *10*(8), 1373–1394. https://doi.org/10.1080/01431168908903974

Saucier, F. J., Senneville, S., Prinsenberg, S., Roy, F., Smith, G., Gachon, P., Caya, D., & Laprise, R. (2004). Modelling the sea ice-ocean seasonal cycle in Hudson Bay, Foxe Basin and Hudson Strait, Canada. *Climate Dynamics*, *23*(3–4), 303–326. https://doi.org/10.1007/s00382-004-0445-6

Schembri, S., Bouchard, C., Jones, L., Baumann, H., & Maps, F. (2025). Larval and juvenile fish assemblages in the Hudson Bay system. *Polar Biology*, *48*(2), 58. https://doi.org/10.1007/s00300-025-03377-7

Schembri, S., Bouchard, C., Pontbriand, T., & Maps, F. (2023). Seasonality of zooplankton communities in the Hudson Bay system. *Elem Sci Anth*, *11*(1), 00113. https://doi.org/10.1525/elementa.2022.00113

Schembri, S., Deschepper, I., Myers, P. G., Sirois, P., Fortier, L., Bouchard, C., & Maps, F. (2022). Arctic cod (*Boreogadus saida*) hatching in the Hudson Bay system. *Elementa: Science of the Anthropocene*, *9*(1), 00042. https://doi.org/10.1525/elementa.2021.00042

Schroeder, T., Devlin, M. J., Brando, V. E., Dekker, A. G., Brodie, J. E., Clementson, L. A., & McKinna, L. (2012). Inter-annual variability of wet season freshwater plume extent into the Great Barrier Reef lagoon based on satellite coastal ocean colour observations. *Marine Pollution Bulletin*, *65*(4–9), 210–223. https://doi.org/10.1016/j.marpolbul.2012.02.022

Schuur, E. A. G., McGuire, A. D., Schädel, C., Grosse, G., Harden, J. W., Hayes, D. J., Hugelius, G., Koven, C. D., Kuhry, P., Lawrence, D. M., Natali, S. M., Olefeldt, D., Romanovsky, V. E., Schaefer, K., Turetsky, M. R., Treat, C. C., & Vonk, J. E. (2015). Climate change and the permafrost carbon feedback. *Nature*, *520*(7546), 171–179. https://doi.org/10.1038/nature14338

Schweiger, A., Lindsay, R., Zhang, J., Steele, M., Stern, H., & Kwok, R. (2011). Uncertainty in modeled Arctic sea ice volume. *Journal of Geophysical Research*, *116*, C00D06. https://doi.org/10.1029/2011JC007084

Serreze, M. C., Barrett, A. P., Slater, A. G., Woodgate, R. A., Aagaard, K., Lammers, R. B., Steele, M., Moritz, R., Meredith, M., & Lee, C. M. (2006). The large-scale freshwater cycle of the Arctic. *Journal of Geophysical Research: Oceans*, *111*(C11), 2005JC003424. https://doi.org/10.1029/2005JC003424

Serreze, M. C., & Barry, R. G. (2011). Processes and impacts of Arctic amplification: A research synthesis. *Global and Planetary Change*, *77*(1–2), 85–96. https://doi.org/10.1016/j.gloplacha.2011.03.004

Sharp, J. H., Benner, R., Bennett, L., Carlson, C. A., Fitzwater, S. E., Peltzer, E. T., & Tupas, L. M. (1995). Analyses of dissolved organic carbon in seawater: The JGOFS EqPac methods comparison. *Marine Chemistry*, *48*(2), 91–108. https://doi.org/10.1016/0304-4203(94)00040-K

Sharp, J. H., Carlson, C. A., Peltzer, E. T., Castle-Ward, D. M., Savidge, K. B., & Rinker, K. R. (2002). Final dissolved organic carbon broad community intercalibration and preliminary use of DOC reference materials. *Marine Chemistry*, *77*(4), 239–253. https://doi.org/10.1016/S0304-4203(02)00002-6

Shepherd, A., Ivins, E. R., A, G., Barletta, V. R., Bentley, M. J., Bettadpur, S., Briggs, K. H., Bromwich, D. H., Forsberg, R., Galin, N., Horwath, M., Jacobs, S., Joughin, I., King, M. A., Lenaerts, J. T. M., Li, J., Ligtenberg, S. R. M., Luckman, A., Luthcke, S. B., … Zwally, H. J. (2012). A Reconciled Estimate of Ice-Sheet Mass Balance. *Science*, *338*(6111), 1183–1189. https://doi.org/10.1126/science.1228102

Shimada, K., Itoh, M., Nishino, S., McLaughlin, F., Carmack, E., & Proshutinsky, A. (2005). Halocline structure in the Canada Basin of the Arctic Ocean. *Geophysical Research Letters*, *32*(3), 2004GL021358. https://doi.org/10.1029/2004GL021358

Shook, K. (2016). The 2005 flood events in the Saskatchewan River Basin: Causes, assessment and damages. *Canadian Water Resources Journal / Revue Canadienne Des Ressources Hydriques*, *41*(1–2), 94–104. https://doi.org/10.1080/07011784.2014.1001439

Shu, Q., Qiao, F., Song, Z., Zhao, J., & Li, X. (2018). Projected Freshening of the Arctic Ocean in the 21st Century. *Journal of Geophysical Research: Oceans*, *123*(12), 9232–9244. https://doi.org/10.1029/2018JC014036

Singh, R. K., & Shanmugam, P. (2014). A novel method for estimation of aerosol radiance and its extrapolation in the atmospheric correction of satellite data over optically complex oceanic waters. *Remote Sensing of Environment*, *142*, 188–206. https://doi.org/10.1016/j.rse.2013.12.001

Singh, R. K., Shanmugam, P., He, X., & Schroeder, T. (2019). UV-NIR approach with non-zero water-leaving radiance approximation for atmospheric correction of satellite imagery in inland and coastal zones. *Optics Express*, *27*(16), A1118. https://doi.org/10.1364/OE.27.0A1118

Solomon, A., Heuzé, C., Rabe, B., Bacon, S., Bertino, L., Heimbach, P., Inoue, J., Iovino, D., Mottram, R., Zhang, X., Aksenov, Y., McAdam, R., Nguyen, A., Raj, R. P., & Tang, H. (2021). Freshwater in the Arctic Ocean 2010–2019. *Ocean Science*, *17*(4), 1081–1102. https://doi.org/10.5194/os-17-1081-2021

Stadnyk, T. A., MacDonald, M. K., Tefs, A., Déry, S. J., Koenig, K., Gustafsson, D., Isberg, K., & Arheimer, B. (2020). Hydrological modeling of freshwater discharge into Hudson Bay using HYPE. *Elem Sci Anth*, *8*, 43. https://doi.org/10.1525/elementa.439

State of Lake Winnipeg. (2020). Environment and Change Canada. (2nd ed). Manitoba, Canada: Manitoba Agriculture and Resource Development.

Stedmon, C. A., Amon, R. M. W., Bauch, D., Bracher, A., Gonçalves-Araujo, R., Hoppmann, M., Krishfield, R., Laney, S., Rabe, B., Reader, H., & Granskog, M. A. (2021). Insights Into Water Mass Origins in the Central Arctic Ocean From In-Situ Dissolved Organic Matter Fluorescence. *Journal of Geophysical Research: Oceans*, *126*(7), e2021JC017407. https://doi.org/10.1029/2021JC017407

Steele, M., & Boyd, T. (1998). Retreat of the cold halocline layer in the Arctic Ocean. *Journal of Geophysical Research: Oceans*, *103*(C5), 10419–10435. https://doi.org/10.1029/98JC00580

Steele, M., Morison, J., Ermold, W., Rigor, I., Ortmeyer, M., & Shimada, K. (2004). Circulation of summer Pacific halocline water in the Arctic Ocean. *Journal of Geophysical Research: Oceans*, *109*(C2), 2003JC002009. https://doi.org/10.1029/2003JC002009

Stern, H. L. (2025). Regime Shift in Arctic Ocean Sea-Ice Extent. *Geophysical Research Letters*, *52*(8), e2024GL114546. https://doi.org/10.1029/2024GL114546

St-Laurent, P., Straneo, F., Dumais, J.-F., & Barber, D. G. (2011). What is the fate of the river waters of Hudson Bay? *Journal of Marine Systems*, *88*(3), 352–361. https://doi.org/10.1016/j.jmarsys.2011.02.004

Stramski, D., Boss, E., Bogucki, D., & Voss, K. J. (2004). The role of seawater constituents in light backscattering in the ocean. *Progress in Oceanography*, *61*(1), 27–56. https://doi.org/10.1016/j.pocean.2004.07.001

Straneo, F., & Saucier, F. (2008). The outflow from Hudson Strait and its contribution to the Labrador Current. *Deep Sea Research Part I: Oceanographic Research Papers*, *55*(8), 926–946. https://doi.org/10.1016/j.dsr.2008.03.012

Stroeve, J., Crawford, A., Ferguson, S., Stirling, I., Archer, L., York, G., Babb, D., & Mallett, R. (2024). Ice-free period too long for Southern and Western Hudson Bay polar bear populations if global warming exceeds 1.6 to 2.6 °C. *Communications Earth & Environment*, *5*(1), 296. https://doi.org/10.1038/s43247-024-01430-7

Stroeve, J., & Notz, D. (2018). Changing state of Arctic sea ice across all seasons. *Environmental Research Letters*, *13*(10), 103001. https://doi.org/10.1088/1748-9326/aade56

Supply, A., Boutin, J., Vergely, J.-L., Kolodziejczyk, N., Reverdin, G., Reul, N., & Tarasenko, A. (2020). New insights into SMOS sea surface salinity retrievals in the Arctic Ocean. *Remote Sensing of Environment*, *249*, 112027. https://doi.org/10.1016/j.rse.2020.112027

Syed, T. H., Famiglietti, J. S., Zlotnicki, V., & Rodell, M. (2007). Contemporary estimates of Pan-Arctic freshwater discharge from GRACE and reanalysis. *Geophysical Research Letters*, *34*(19), 2007GL031254. https://doi.org/10.1029/2007GL031254

Tang, W., Yueh, S. H., Yang, D., Mcleod, E., Fore, A., Hayashi, A., Olmedo, E., Martínez, J., & Gabarró, C. (2020). The Potential of Space-Based Sea Surface Salinity on Monitoring the Hudson Bay Freshwater Cycle. *Remote Sensing*, *12*(5), 873. https://doi.org/10.3390/rs12050873

Tank, S. E., Raymond, P. A., Striegl, R. G., McClelland, J. W., Holmes, R. M., Fiske, G. J., & Peterson, B. J. (2012). A land-to-ocean perspective on the magnitude, source and implication of DIC flux from major Arctic rivers to the Arctic Ocean. *Global Biogeochemical Cycles*, *26*(4), 2011GB004192. https://doi.org/10.1029/2011GB004192

Tapley, B. D., Bettadpur, S., Ries, J. C., Thompson, P. F., & Watkins, M. M. (2004). GRACE Measurements of Mass Variability in the Earth System. *Science*, *305*(5683), 503–505. https://doi.org/10.1126/science.1099192

Tian, S., Li, D., Zhang, T., McClelland, J. W., Overeem, I., Lane, S. N., Spencer, R. G. M., Wohl, E., Sha, A., Zhao, Y., Miao, C., Ning, M., Yuan, L., & Ni, J. (2026). Increasing river sediment concentration and flux across the pan-Arctic. *Nature Geoscience*, *19*(5), 565–572. https://doi.org/10.1038/s41561-026-01960-z

Timmermans, M., & Marshall, J. (2020). Understanding Arctic Ocean Circulation: A Review of Ocean Dynamics in a Changing Climate. *Journal of Geophysical Research: Oceans*, *125*(4), e2018JC014378. https://doi.org/10.1029/2018JC014378

Tivy, A., Howell, S. E. L., Alt, B., McCourt, S., Chagnon, R., Crocker, G., Carrieres, T., & Yackel, J. J. (2011). Trends and variability in summer sea ice cover in the Canadian Arctic based on the Canadian Ice Service Digital Archive, 1960–2008 and 1968–2008. *Journal of Geophysical Research*, *116*(C3), C03007. https://doi.org/10.1029/2009JC005855

Twardowski, M. S., Claustre, H., Freeman, S. A., Stramski, D., & Huot, Y. (2007). Optical backscattering properties of the "clearest" natural waters. *Biogeosciences*, *4*(6), 1041–1058. https://doi.org/10.5194/bg-4-1041-2007

van der Linde, DW. (1998). Protocol for the determination of total suspended matter in oceans and coastal zones (Technical note I 98.182). Joint Research Centre, Ispra.

Van Donk, J., & Mathieu, G. (1969). Oxygen isotope compositions of foraminifera and water samples from the Arctic Ocean. *Journal of Geophysical Research*, *74*(13), 3396–3407. https://doi.org/10.1029/JC074i013p03396

Vavrus, S. J., Holland, M. M., Jahn, A., Bailey, D. A., & Blazey, B. A. (2012). Twenty-First-Century Arctic Climate Change in CCSM4. *Journal of Climate*, *25*(8), 2696–2710. https://doi.org/10.1175/JCLI-D-11-00220.1

Vihma, T., Screen, J., Tjernström, M., Newton, B., Zhang, X., Popova, V., Deser, C., Holland, M., & Prowse, T. (2016). The atmospheric role in the Arctic water cycle: A review on processes, past and future changes, and their impacts. *Journal of Geophysical Research: Biogeosciences*, *121*(3), 586–620. https://doi.org/10.1002/2015JG003132

Voelker, A. H. L., Colman, A., Olack, G., Waniek, J. J., & Hodell, D. (2015). Oxygen and hydrogen isotope signatures of Northeast Atlantic water masses. *Deep Sea Research Part II: Topical Studies in Oceanography*, *116*, 89–106. https://doi.org/10.1016/j.dsr2.2014.11.006

Vonk, J. E., Mann, P. J., Davydov, S., Davydova, A., Spencer, R. G. M., Schade, J., Sobczak, W. V., Zimov, N., Zimov, S., Bulygina, E., Eglinton, T. I., & Holmes, R. M. (2013). High biolability of ancient permafrost carbon upon thaw. *Geophysical Research Letters*, *40*(11), 2689–2693. https://doi.org/10.1002/grl.50348

Wahr, J., Swenson, S., Zlotnicki, V., & Velicogna, I. (2004). Time-variable gravity from GRACE: First results. *Geophysical Research Letters*, *31*(11), 2004GL019779. https://doi.org/10.1029/2004GL019779

Walsh, J. E., Bigalke, S., McAfee, S. A., Lader, R., Serreze, M. C., & Ballinger, T. J. (2023). NOAA Arctic Report Card 2023: Precipitation. *NOAA Technical Report OAR ARC; 23-04*. https://doi.org/10.25923/HCM7-AZ41

Wang, M., & Shi, W. (2007). The NIR-SWIR combined atmospheric correction approach for MODIS ocean color data processing. *Optics Express*, *15*(24), 15722. https://doi.org/10.1364/OE.15.015722

Wang, Q., Shu, Q., Wang, S., Li, X., Danilov, S., Qiao, F., Song, Z., Wang, F., & Jung, T. (2025). Dominant inflation of the Arctic Ocean's Beaufort Gyre in a warming climate. *Communications Earth & Environment*, *6*(1), 40. https://doi.org/10.1038/s43247-025-02028-3

Wang, R., McCullough, G. K., Gunn, G. G., Hochheim, K. P., Dorostkar, A., Sydor, K., & Barber, D. G. (2012). An observational study of ice effects on Nelson River estuarine variability, Hudson Bay, Canada. *Continental Shelf Research*, *47*, 68–77. https://doi.org/10.1016/j.csr.2012.06.014

Wang, X., Liu, Y., Key, J. R., & Dworak, R. (2022). A New Perspective on Four Decades of Changes in Arctic Sea Ice from Satellite Observations. *Remote Sensing*, *14*(8), 1846. https://doi.org/10.3390/rs14081846

Wassmann, P., & Reigstad, M. (2011). Future Arctic Ocean Seasonal Ice Zones and Implications for Pelagic-Benthic Coupling. *Oceanography*, *24*(3), 220–231. https://doi.org/10.5670/oceanog.2011.74

Werdell, P. J., Franz, B. A., Bailey, S. W., Feldman, G. C., Boss, E., Brando, V. E., Dowell, M., Hirata, T., Lavender, S. J., Lee, Z., Loisel, H., Maritorena, S., Mélin, F., Moore, T. S., Smyth, T. J., Antoine, D., Devred, E., d'Andon, O. H. F., & Mangin, A. (2013). Generalized ocean color inversion model for retrieving marine inherent optical properties. *Applied Optics*, *52*(10), 2019. https://doi.org/10.1364/AO.52.002019

Wiken, E. B. (1986). Terrestrial ecozones of Canada. Ecological land classification, Series no. 19. Environment Canada.

Woodgate, R. A. (2018). Increases in the Pacific inflow to the Arctic from 1990 to 2015, and insights into seasonal trends and driving mechanisms from year-round Bering Strait mooring data. *Progress in Oceanography*, *160*, 124–154. https://doi.org/10.1016/j.pocean.2017.12.007

Woodgate, R. A., & Aagaard, K. (2005). Revising the Bering Strait freshwater flux into the Arctic Ocean. *Geophysical Research Letters*, *32*(2), 2004GL021747. https://doi.org/10.1029/2004GL021747

Woodgate, R. A., Weingartner, T., & Lindsay, R. (2010). The 2007 Bering Strait oceanic heat flux and anomalous Arctic sea-ice retreat. *Geophysical Research Letters*, *37*(1), 2009GL041621. https://doi.org/10.1029/2009GL041621

Woosley, R. J., & Millero, F. J. (2020). Freshening of the western Arctic negates anthropogenic carbon uptake potential. *Limnology and Oceanography*, *65*(8), 1834–1846. https://doi.org/10.1002/lno.11421

Wu, Z., Yin, Q., Ganopolski, A., Berger, A., & Guo, Z. (2023). Effect of Hudson Bay closure on global and regional climate under different astronomical configurations. *Global and Planetary Change*, *222*, 104040. https://doi.org/10.1016/j.gloplacha.2023.104040

Xi, H., Larouche, P., Tang, S., & Michel, C. (2013). Seasonal variability of light absorption properties and water optical constituents in Hudson Bay, Canada. *Journal of Geophysical Research: Oceans*, *118*(6), 3087–3102. https://doi.org/10.1002/jgrc.20237

Xi, H., Larouche, P., Tang, S., & Michel, C. (2014). Characterization and variability of particle size distributions in Hudson Bay, Canada. *Journal of Geophysical Research: Oceans*, *119*(6), 3392–3406. https://doi.org/10.1002/2013JC009542

Yamamoto-Kawai, M., McLaughlin, F. A., Carmack, E. C., Nishino, S., & Shimada, K. (2009). Aragonite Undersaturation in the Arctic Ocean: Effects of Ocean Acidification and Sea Ice Melt. *Science*, *326*(5956), 1098–1100. https://doi.org/10.1126/science.1174190

Yamamoto-Kawai, M., Tanaka, N., & Pivovarov, S. (2005). Freshwater and brine behaviors in the Arctic Ocean deduced from historical data of δ^{18} O and alkalinity (1929–2002 A.D.). *Journal of Geophysical Research: Oceans*, *110*(C10), 2004JC002793. https://doi.org/10.1029/2004JC002793

Yang, X., & Cessi, P. (2024). The Bering Strait Throughflow Component of the Global Mass, Heat and Freshwater Transport. *Journal of Geophysical Research: Oceans*, *129*(10), e2024JC021463. https://doi.org/10.1029/2024JC021463

Zhang, X., Tang, H., Zhang, J., Walsh, J. E., Roesler, E. L., Hillman, B., Ballinger, T. J., & Weijer, W. (2023). Arctic cyclones have become more intense and longer-lived over the past seven decades. *Communications Earth & Environment*, *4*(1), 348. https://doi.org/10.1038/s43247-023-01003-0

Zhuk, V. R., & Kubryakov, A. A. (2021). Interannual Variability of the Lena River Plume Propagation in 1993–2020 during the Ice-Free Period on the Base of Satellite Salinity, Temperature, and Altimetry Measurements. *Remote Sensing*, *13*(21), 4252. https://doi.org/10.3390/rs13214252

Contribution of collaborating authors

Manuscript 1 / Chapter 3: Basu, A., McCullough, G., Bélanger, S., Mukhopadhyay, A., Doxaran, D., Sydor, K., et al. (2023). Plume dispersion from the Nelson and Hayes rivers into Hudson Bay using satellite remote sensing of CDOM and suspended sediment. *Elementa: Science of the Anthropocene*, 11(1), 00076.

The above study was conceived by Atreya Basu. Atreya Basu contributed to the development of the methodology. The study was conducted under the supervision of Jens Ehn, Simon Bélanger. and David Doxaran. Funding for this study was provided by Jens Ehn, and the project under which it was conducted was administered by late David Barber. Data processing and analysis was conducted by Atreya Basu, Anirban Mukhopadhyay. Data curation was carried out by Atreya Basu. Resources were contributed by Greg McCullough, Jens Ehn, and Kevin Sydor. The original draft of the manuscript was written by Atreya Basu, and review and editing were contributed by all authors of the manuscript.

Manuscript 2 / Chapter 4: Basu, A., Bélanger, S., Kuzyk, Z. Z. A., Singh, R. K., Mukherjee, S., Larouche, P., Guzzi, A. C., Ausen, E. L., McCullough, G., & Ehn, J. K. (2026). Satellite data trace seasonal freshwater dispersion in Hudson and James Bays. *Geophysical Research Letters*, 53(2).

The above study was conceived by Atreya Basu and Jens Ehn. Atreya Basu contributed to the development of the methodology. The study was conducted under the supervision of Jens Ehn and Simon Bélanger. Funding for this study was provided by Jens Ehn and Zou Zou Kuzyk, and the project under which it was conducted was coordinated by Alessia Guzzi. Data processing was conducted by Atreya Basu, Rakesh K. Singh, Soham Mukherjee, Alessia Guzzi, and Emma Ausen. The data analysis was performed by Atreya Basu, Alessia Guzzi, Soham Mukherjee and Emma Ausen. Data curation was carried out by Atreya Basu and Alessia Guzzi. Resources were contributed by Zou Zou Kuzyk, Rakesh Singh, Pierre Larouche, Alessia Guzzi, Greg McCullough, and Jens Ehn. The original draft of the manuscript was written by Atreya Basu, and review and editing were contributed by all authors of the manuscript.

Manuscript 3 (submitted for publication) / Chapter 5: Basu, A., Kuzyk, Z. Z., McCullough, G., Bélanger, S., Guzzi, A., & Ehn, J. River water control of stratification in Arctic marginal seas.

The above study was conceived by Atreya Basu and Jens Ehn. Atreya Basu contributed to the development of the methodology. The study was conducted under the supervision of Jens Ehn and Zou Zou Kuzyk. Funding for this study was provided by Jens Ehn and Zou Zou Kuzyk, and the project under which it was conducted was coordinated by Alessia Guzzi. Data processing was conducted by Atreya Basu and Alessia Guzzi. The analysis and investigation of the data were performed by Atreya Basu. Data curation was carried out by Atreya Basu and Alessia Guzzi. Resources were contributed by Zou Zou Kuzyk, Alessia Guzzi, and Jens Ehn. The original draft of the manuscript/chapter was written by Atreya Basu, and review and editing were contributed by Jens Ehn, Zou Zou Kuzyk, Simon Bélanger, Greg McCullough, and Alessia Guzzi.